

***IN-SITU* GAMMA-RAY MAPPING OF ENVIRONMENTAL  
RADIOACTIVITY AT iTHEMBA LABS AND ASSOCIATED RISK  
ASSESSMENT**

Israel Nkululeko Hlatshwayo

A thesis presented in partial fulfilment of the requirements for the degree of Master of Sciences in the Department of Physics and Engineering at the University of Zululand

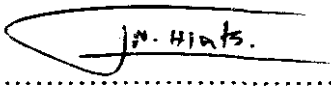
Internal Supervisor: Prof. O. M. Ndwandwe  
Dept. of Physics and Engineering  
University of Zululand

External supervisor: Dr. R. T. Newman  
Physics Group  
iThemba LABS

February 2007

## DECLARATION

I, the undersigned, hereby declare that the work contained in this thesis is my own original work and that I have not previously in its entirety or in part submitted it at any university for a degree.

  
.....

Date: 26/03/2007

Israel Nkululeko Hlatshwayo

## ***In-situ* gamma-ray mapping of environmental radioactivity at iThemba LABS and associated risk assessment**

Israel Nkululeko Hlatshwayo

### **Abstract**

In February and July 2005, following up on June 2004, the Environmental Radioactivity Laboratory (ERL) of iThemba LABS performed *in-situ* and *ex-situ* measurements of environmental radioactivity on the iThemba LABS (iTL) site. The ERL's Multi-Element-Detector-for-Underwater-Sediment-Activity (MEDUSA) and high-purity germanium (HPGe) detector systems were used to make *in-situ* and *ex-situ* measurements, respectively. MEDUSA consists of a CsI(Na) crystal (length 15 cm, diameter 7 cm) for  $\gamma$ -ray detection. MEDUSA was mounted ~ 0.5 m above the ground on the front of a 4x4 vehicle to traverse [at ~ 2 m.s<sup>-1</sup>] the accessible portions of the iTL site. Spatial data (via a GPS receiver mounted above the crystal) were acquired every 1 s, and  $\gamma$ -ray spectra (0 – 3 MeV) every 2 s. Maps of count rate were produced from the MEDUSA data to show the spatial distribution of radioactivity on the site. The lead-shielded HPGe detector is a Canberra p-type model with built-in pre-amplifier, crystal diameter 62.5 mm, and length 59.9 mm. The HPGe was used to measure the radioactivity in soil (and also in some grass) samples collected at particular spots on the iTL site. The sampled spots include six identified high activity spots (“hotspots”) and two “calibration spots”.

The activity concentration results that were obtained for the naturally occurring radioactive materials (NORM) [from both HPGe and MEDUSA data from off-road iTL site sections] have the ranges 7.8 – 39.0, 5.9 – 21.4, and 29.8 – 63.3 Bq.kg<sup>-1</sup> for <sup>238</sup>U, <sup>232</sup>Th, and <sup>40</sup>K, respectively. The absorbed and effective doses (from external gamma irradiation) that were calculated for the NORM radionuclides have the ranges 10.4 – 27.2 nGy.h<sup>-1</sup> and 12.8 – 33.4  $\mu$ Sv.y<sup>-1</sup>, respectively. The average NORM activity

concentration results (from February and July 2005) for the *i*TL road are 30.3, 29.6, and 345.0 Bq.kg<sup>-1</sup> for <sup>238</sup>U, <sup>232</sup>Th, and <sup>40</sup>K, respectively. When averaging over the off-road sections of the *i*TL site, and excluding data from the hotspots, the average results obtained are 10.6, 8.5, and 42.4 Bq.kg<sup>-1</sup>. When averaging over the off-road sections plus hotspots, the average results are 23.1, 8.0, and 50.4 Bq.kg<sup>-1</sup>.

The activity concentration results that were obtained for the anthropogenic radionuclides have the ranges 1.2 – 6533.5, 0 – 100.8, 0 – 20.6, 0 – 0.7, and 0.2 – 192.5 Bq.kg<sup>-1</sup> for <sup>68</sup>Ga, <sup>65</sup>Zn, <sup>22</sup>Na, <sup>137</sup>Cs, and <sup>54</sup>Mn, respectively. The absorbed and effective doses (from external gamma irradiation) due to anthropogenic sources were calculated for two plane source depth locations, namely, 1 and 10 cm. The absorbed and effective dose results that were obtained at 1 cm plane source depth have the ranges 0.2 – 152.7 nGy.h<sup>-1</sup> and 0 – 187.3 μSv.y<sup>-1</sup>. The absorbed and effective dose results that were obtained at 10 cm plane source depth have the ranges 0 – 38.1 nGy.h<sup>-1</sup> and 0 – 46.7 μSv.y<sup>-1</sup>.

The count rate maps showed that the six identified hotspots consistently appear at the same locations for June 2004, and February and July 2005 maps. The maps also showed that the radionuclide deposition at the hotspots is not a typical result of radionuclide spread via irrigation. The activity concentration results showed that the radioactivity level due to NORM sources on the *i*Themba LABS grounds is below the world average of 35, 30, and 400 Bq.kg<sup>-1</sup> for <sup>238</sup>U, <sup>232</sup>Th, and <sup>40</sup>K, respectively. The effective dose results showed that the maximum effective dose to humans on the *i*Themba LABS grounds as a result of external exposure to natural and anthropogenic radionuclides is well below the regulatory 1 mSv per year per member of public.

## **ACKNOWLEDGEMENTS**

For the accomplishment of this work, my sincere thanks go to

- the **Father**, from whom the whole family in heaven and on earth derives its name (Ephesians 3:14-15).
- **Prof. O. M. Ndwandwe**, my internal supervisor and the visionary (together with the late **Dr. T. K. Marais**) of the MANUS/MatSci postgraduate programme, for keeping me motivated and focused throughout this work. Thank you sir for allowing me to be part of the MANUS/MatSci postgraduate programme.
- **Dr. Richard T. Newman**, my external supervisor, for going beyond the call of duty to mentor me for excellence in the field of research. Thank you sir for your unwavering professionalism.
- **Dr. Atulya K. Mohanty, Prof. Robbie Lindsay, and Prof. Rob J. de Meijer** for their insight and willingness to transfer apt knowledge to guide me during the course of this work.
- The former and current **ERL students and staff**, namely, **Pogisho Maine, Wesley Damon, Angelo Joseph, Wilcot Speelman, Eric Mudau, Katse Maphoto, Tiro Modisane, Peane Maleka, Siddig Talha, Nolasco Mlwilo, Nkanyiso Mbatha, Ramudzuli Manavhela**, for informed advice and support.
- The **University of Zululand, iThemba LABS, the University of the Western Cape**, and the **NRF** for accommodating and financing me through the MANUS/MatSci postgraduate programme.
- My pastor in Restoration Life Ministry (RLM), **Dr. Charmaine Pienaar**, for being my extraordinary supervisor for this work.
- Finally, my **family, friends, prayer partners, and brethren**, without whom I am to be pitied, for their love and understanding.

# CONTENTS

<b>CHAPTER 1</b>	<b><i>Introduction</i></b>	<b>1</b>
1.1	Radioisotope production at <i>iThemba LABS</i>	3
1.2	The motivation for this study	5
1.3	Hypothesis and problems to be investigated	8
1.4	Scope of this study	8
1.5	The dissertation plan	9
<b>CHAPTER 2</b>	<b><i>Background theory: Radioactivity in the environment</i></b>	<b>11</b>
2.1	Radionuclides	11
2.1.1	Properties of radionuclides	12
2.1.2	Forms of radiation from radionuclides	17
2.1.2.1	$\gamma$ -radiation and its interaction with matter	18
2.1.3	Detection of ionizing radiation: Detector characteristics	24
2.1.3.1	Detection of $\gamma$ -radiation	28
2.2	Environmental radioactivity	38
2.2.1	Primordial and anthropogenic environmental radionuclides	39
2.2.2	Pathways of radionuclides in the environment	41
2.2.3	<i>In-situ</i> radiometric mapping	433
2.2.4	Human exposure to environmental radiation	44
2.2.5	Measurement techniques for environmental <i>gamma</i> -radiation: <i>Ex-situ</i> vs. <i>in-situ gamma</i> -ray spectrometry	488
2.3	Literature review: Some studies on <i>in-situ</i> $\gamma$ -ray mapping of environmental radioactivity	4949
<b>CHAPTER 3</b>	<b><i>Methodology</i></b>	<b>52</b>
3.1	Experiments	52
3.2	<i>In-situ</i> procedure	52
3.2.1	Overview of the <i>iThemba LABS</i> MEDUSA system	52
3.2.2	February and July 2005 surveys	56
3.3	<i>Ex-situ</i> procedure	61
3.3.1	Overview of the ERL HPGe detector system	61
3.3.2	Sample collection, preparation, and measurements	63
<b>CHAPTER 4</b>	<b><i>Data Analysis</i></b>	<b>68</b>
4.1	Analysis of the <i>in-situ</i> data	68
4.1.1	Full-spectrum (FSA) spectral analysis method	68
4.1.2	The actual analysis	69
4.2	Analysis of the <i>ex-situ</i> data	75
4.2.1	Peak area analysis methods	75
4.2.2	The actual analysis	78
4.2.2.1	Determination of absolute efficiency	81
4.3	Calculation of Dose	83
<b>CHAPTER 5</b>	<b><i>Findings and discussion</i></b>	<b>86</b>

<b>5.1</b>	<b><i>In-situ</i> findings</b>	<b>86</b>
5.1.1	February 2005 survey	87
5.1.2	July 2005 survey	96
<b>5.2</b>	<b><i>Ex-situ</i> findings</b>	<b>103</b>
<b>5.3</b>	<b>Normalised <i>in-situ</i> findings</b>	<b>114</b>
<b>5.4</b>	<b>Comparison of results</b>	<b>117</b>
5.4.1	Current vs. June 2004 count rate maps	117
5.4.2	HPGe vs. normalised MEDUSA	120
<b>CHAPTER 6</b>	<b><i>Summary and conclusion</i></b>	<b>125</b>
<b>6.1</b>	<b>Summary</b>	<b>125</b>
<b>6.2</b>	<b>Conclusion</b>	<b>129</b>
<b>6.3</b>	<b>Outlook</b>	<b>131</b>
<b>APPENDICES</b>		<b>134</b>
	<b>Overview of the patent of the MEDUSA system</b>	<b>134</b>
	<b>Decay schemes of the anthropogenic radionuclides identified on the iThemba LABS site</b>	<b>138</b>
	<b><sup>68</sup>Ge-<sup>68</sup>Ga secular equilibrium</b>	<b>139</b>
	<b>Absolute efficiency parameters and the IAEA intercomparison</b>	<b>140</b>
	<b>HPGe count rate, activity concentration, and dose in each sample</b>	<b>142</b>
	<b>Half-life prediction decay curves</b>	<b>148</b>
	<b>Testing of normalisation factors</b>	<b>151</b>
<b>REFERENCES</b>		<b>153</b>

## LIST OF FIGURES

Figure 1-1: The map of parts of the Western Cape province of South Africa showing the location of Faure. ....	1
Figure 1-2: The location of the <i>i</i> Themba LABS site in Faure in Western Cape, South Africa .....	2
Figure 1-3: Aerial photograph of the <i>i</i> Themba LABS site, taken in the winter of 1991. ....	2
Figure 1-4: Schematic diagram of the <i>i</i> Themba LABS site.....	3
Figure 1-5: A bar graph representing the results of the activity of some anthropogenic radionuclides identified in one of the holding dams on the <i>i</i> TL site in 2003.. .....	6
Figure 1-6: Map showing MEDUSA detection count rate obtained during the June 2004 survey.....	7
Figure 1-7: A flow-chart illustrating the scope of this study of the <i>i</i> Themba LABS site .....	9
Figure 2-1: A graphical illustration of the radioactive decay of a three nucleus chain. ....	16
Figure 2-2: A diagram showing the domination of the photoelectric effect, Compton effect, and pair production in the three areas separated by the lines showing the values of $Z$ and photon energy $E$ .....	18
Figure 2-3: A plot showing a calculated photoelectric cross section for lead.. .....	20
Figure 2-4: A diagram illustrating the kinematics of Compton scattering.. .....	22
Figure 2-5: A schematic diagram of the features of a scintillation counter.....	29
Figure 2-6: Temperature dependence of light output from inorganic crystals.. .....	32
Figure 2-7: A plot showing $\gamma$ -ray absorption coefficients for NaI and NE102A plastic scintillator.. .....	33
Figure 2-8: A diagram showing the np junction with no external voltage applied.....	35
Figure 2-9: A plot showing the depletion depth as a function of impurity concentration and applied voltage for planar diodes of high-purity germanium.....	37
Figure 2-10: A demonstration of how the $^{60}\text{Co}$ spectrum compares when taken with a NaI detector and a germanium detector .....	38
Figure 2-11: A graphical illustration of the uranium and thorium series.. .....	40
Figure 2-12: A diagram illustrating the pathways to man, followed by radioactive materials released to surface and ground water.. .....	41
Figure 2-13: A diagram illustrating the pathways to man, followed by radioactive materials released through air. ....	42
Figure 2-14: A simplified illustration of one possible pathway of effluent-released radionuclides to humans in the event of an uncontrolled environmental release of radioactivity. ....	42
Figure 2-15: A diagram illustrating the pathways down to the resulting health effects, followed by radioactive sources released into the environment .....	43
Figure 2-16: Pie chart showing the average contributions made by natural and anthropogenic radiation sources to the total effective radiation dose to the population.. .....	44
Figure 3-1: A schematic diagram showing the derivation of sediment composition from $\gamma$ -ray measurements with the MEDUSA system. ....	54
Figure 3-2: A schematic diagram showing the components of the encased probe part of the MEDUSA system.....	55



Figure 3-3: Digital photos showing physical features of some of the units encased in the aluminium/stainless steel tube. ....	55
Figure 3-4: A schematic diagram showing the interlinking between the units of the iThemba LABS MEDUSA system. ....	56
Figure 3-5: A photograph showing the physical features of the interlinking between units of the MEDUSA system. ....	57
Figure 3-6: Photographs showing the setup on the 4x4 of the probe, Aladin box and laptop computer, and GPS receiver. ....	57
Figure 3-7: Photographs showing the battery used to supply the MS with required voltage via the DC/AC power inverter, and external GPS antenna mounted directly above the detection crystal in the probe. ....	58
Figure 3-8: Photographs showing locations where stationary measurements were made. ....	60
Figure 3-9: Schematic diagram showing how the components of the ERL HPGe system interlink. ....	61
Figure 3-10: Photograph showing a top view of the ERL HPGe setup located in the ERL. ....	62
Figure 3-11: Photograph showing the lead castle of the ERL HPGe system, with the LN <sub>2</sub> dewar protruding underneath. ....	63
Figure 3-12: Schematic top-view representation of the sampling strategy used at the spots CS1, NCS1, and HS1. ....	64
Figure 3-13: The geometry of the Marinelli beaker used for holding environmental samples for laboratory measurements with the HPGe detector. ....	66
Figure 3-14: Photograph showing the sealed soil sample in a labeled Marinelli beaker. ....	66
Figure 4-1: Flow diagram showing how, and in which file format, the MEDUSA-acquired data went from one software program to another during the analysis. .	70
Figure 4-2: Flow diagram showing the procedure that was followed during the synchronization of the MEDUSA-acquired data of this study, using the MDS software program. ....	70
Figure 4-3: Flow diagram showing the procedure that was followed during the extraction of activity concentration of radionuclides from the synchronized MEDUSA data of this study, using the MPA software program. ....	72
Figure 4-4: MCNPX-simulated $\gamma$ -ray spectrum of radionuclide <sup>40</sup> K used in FSA. ....	73
Figure 4-5: MCNPX-simulated $\gamma$ -ray spectrum of radionuclide <sup>232</sup> Th used in FSA. ..	73
Figure 4-6: MCNPX-simulated $\gamma$ -ray spectrum of radionuclide <sup>238</sup> U used in FSA. ....	74
Figure 4-7: MCNPX-simulated $\gamma$ -ray spectrum of radionuclide <sup>22</sup> Na used in FSA. A source depth of 15 cm was considered in the simulation. ....	74
Figure 4-8: Background spectrum measured at Theewaterskloof Dam and used in FSA. ....	75
Figure 4-9: An illustration showing the linear background being less than the step background on the left side of the multiplet and greater than the step background on the right side. ....	78
Figure 4-10: Flow diagram showing the spectra analysis by means of the OxfordWin-MCA software in the ERL. ....	79
Figure 4-11: Absolute efficiency curve for $\gamma$ -ray energies used to identify radionuclides in this study. ....	82
Figure 4-12: Flow diagram showing how the units evolved during the determination of absorbed dose by anthropogenic radionuclides via the model used. ....	85
Figure 4-13: Schematic diagram showing features of the assumed slab of soil. ....	85

Figure 5-1: Map showing the altitude (m) of all locations surveyed in February 2005 (also in July 2005).....	87
Figure 5-2: Map showing the temperature variation at sections surveyed on the site in February 2005.....	88
Figure 5-3: Map showing MEDUSA count rate obtained during the February 2005 survey.....	89
Figure 5-4: Map showing MEDUSA count rate obtained during the February 2005 survey.....	90
Figure 5-5: The raw <i>gamma</i> -ray spectrum acquired with MEDUSA in a stationary position over calibration spot CS1 in February 2005. ....	92
Figure 5-6: The raw <i>gamma</i> -ray spectrum acquired with MEDUSA in a stationary position over hotspot HS1 in February 2005. ....	92
Figure 5-7: The raw <i>gamma</i> -ray spectrum acquired with MEDUSA in a stationary position over hotspot HS2 in February 2005. ....	93
Figure 5-8: The raw <i>gamma</i> -ray spectrum acquired with MEDUSA in a stationary position over hotspot HS3 in February 2005. ....	93
Figure 5-9: Map showing the temperature variation at sections surveyed on the site in July 2005.....	97
Figure 5-10: Map showing MEDUSA count rate obtained during the July 2005 survey. ....	98
Figure 5-11: Map showing MEDUSA count rate obtained during the July 2005 survey. ....	99
Figure 5-12: The raw <i>gamma</i> -ray spectrum acquired with MEDUSA in a stationary position over hotspot NHS4 in July 2005.....	100
Figure 5-14: Spectrum showing energy peaks (range = 0 – 2700 keV) identified with the HPGe detector in soil CS1, S1.....	104
Figure 5-15: Spectrum showing energy peaks (range = 0 – 2700 keV) identified with the HPGe detector in soil HS1, S1.....	105
Figure 5-16: Spectrum showing energy peaks (range = 0 – 2700 keV) identified with the HPGe detector in soil HS2, S1.....	106
Figure 5-17: Spectrum showing energy peaks (range = 0 – 2700 keV) identified with the HPGe detector in soil HS3, S1.....	107
Figure 5-18: Spectrum showing energy peaks (range = 0 – 2700 keV) identified with the HPGe detector in soil NHS4, S1.....	108
Figure 5-19: Spectrum showing energy peaks (range = 0 – 2700 keV) identified with the HPGe detector in soil NHS5, S1.....	109
Figure 5-20: Spectrum showing that energy peaks 834.9 and 1115.5 keV, from <sup>54</sup> Mn and <sup>65</sup> Zn, respectively, identified with the HPGe detector in soil HS1, S1, are affected by nearby peaks.....	114
Figure 5-21: Sections of MEDUSA count rate maps obtained during the June 2004, July 2005, and February 2005 surveys. ....	118
Figure 5-22: Sections of MEDUSA count rate maps obtained during the June 2004, July 2005, and February 2005 surveys. ....	119
Figure 5-23: Sections of MEDUSA count rate maps obtained during the June 2004, July 2005, and February 2005 surveys. ....	120
Figure 5-24: Bar graphs showing the comparison of activity concentration results obtained with MEDUSA and HPGe for the NORM sources in February and July 2005.....	121

Figure 5-25: Bar graph showing the comparison of activity concentration results obtained with MEDUSA and HPGe for the anthropogenic sources in February and July 2005.....	122
Figure 5-26: Bar graph showing the comparison of absorbed dose results obtained with MEDUSA and HPGe for the NORM sources in February and July 2005....	123
Figure 6-1: A photograph showing some of the wild animals that live, and eat of the grass on the iTL site.....	132
Figure 6-2: Spectrum showing energy peaks (range = 0 – 2700 keV) identified with the HPGe detector in grass sample taken from location NHS4 during the July 2005 survey.....	133
Figure 0-1: Schematic diagram showing the components of the MEDUSA system according to the invention as patented by the Nuclear Geophysics Division (NGD) of the KVI.....	134
Figure 0-2: A plot of count rate versus energy showing the spectrum of energy peaks as produced in computer unit 26.....	136
Figure 0-3: Decay schemes of the anthropogenic radionuclides identified in the surveys.....	138
Figure 0-4: Curve showing that a minimum period of 2 days is required for secular equilibrium to be reached between $^{68}\text{Ge}$ and $^{68}\text{Ga}$ .....	139
Figure 0-5: Count rate decay curve of the 1077.4 keV line measured and re-measured in hotspot sample HS1, S1.....	149
Figure 0-6: Count rate decay curve of the 1115.55 keV line measured and re-measured in hotspot sample HS1, S1.....	149
Figure 0-7: Count rate decay curve of the 834.848 keV line measured and re-measured in hotspot sample HS1, S1.....	150
Figure 0-8: Bar graphs showing results obtained for normalisation of CS1 and NCS1 MEDUSA results using NCS1 and CS1 normalisation factors, respectively....	152

## **LIST OF TABLES**

Table 1-1: Useful radioisotopes produced at iThemba LABS.....	4
Table 1-2: Anthropogenic radioisotopes released as waste products [into two holding dams] at iThemba LABS. ....	5
Table 2-1: Equations associated with a radioactive decay chain of nuclides <i>A</i> , <i>B</i> , and <i>C</i> .....	15
Table 2-2: Equations associated with a radioactive decay chain of nuclides <i>A</i> , <i>B</i> , and <i>C</i> .....	16
Table 2-3: A list of some of the primordial, or terrestrial, radionuclides, together with their abundance and half-life.. ....	40
Table 2-4: A list of radiation weighting factors for different radiation types.....	46
Table 2-5: A list of tissue weighting factors for different tissues.....	46
Table 2-6: Activity concentration of natural radionuclides in soil and associated absorbed dose rate in air.. ....	48
Table 3-1: Locations where stationary MEDUSA measurements were made during the February and July 2005 surveys.. ....	59
Table 3-2: Information about the samples collected at spots of interest regarding receipt, labelling, and measurement.....	67
Table 4-1: MDS settings and acquisition rates of the different data sets accommodated in the MEDUSA in the MEDUSA detection system. ....	71
Table 4-2: <i>Gamma</i> -ray lines, their branching ratios, and their absolute efficiencies, with uncertainties, used to obtain the activity concentrations of their respective source radionuclides.....	82
Table 4-3: Dose conversion factors for NORM radionuclides used in this study. ....	84
Table 5-1: “Manual Stabilization” fits for the February 2005 survey. ....	95
Table 5-2: February 2005 MEDUSA “Sum & Analyze” results.. ....	96
Table 5-3: “Manual stabilization” fits for the July 2005 survey.....	101
Table 5-4: July 2005 MEDUSA “Sum & Analyze” results.....	102
Table 5-5: HPGe count rate reported for the February 2005 calibration spot and hotspot samples.....	111
Table 5-6: Average HPGe count rate reported for the July 2005 calibration spot and hotspot samples.....	111
Table 5-7: Activity concentrations, from HPGe data, calculated for the naturally occurring radioactive materials (NORM) identified in the surveys.....	112
Table 5-8: Activity concentrations, from HPGe data, calculated for the anthropogenic radionuclides identified in February and July 2005.....	112
Table 5-9: Absorbed and effective dose, from HPGe data, calculated for the NORM and anthropogenic radionuclides identified in February and July 2005.....	112
Table 5-10: Normalization factors used for the February and July 2005 MEDUSA activity concentration results. ....	115
Table 5-11: Normalized activity concentrations, from MEDUSA data, extracted for the NORM radionuclides identified in the surveys. ....	115
Table 5-12: Normalized activity concentrations, from MEDUSA data, extracted for the anthropogenic radionuclides identified in the surveys.....	116
Table 5-13: Absorbed and effective dose, from MEDUSA data. calculated for the NORM and anthropogenic radionuclides identified in the surveys.....	116

Table 5-14: Comparison of activity concentration results obtained with MEDUSA and HPGe for the NORM sources February and July 2005. ....	121
Table 5-15: Comparison of activity concentration results obtained with MEDUSA and HPGe for the anthropogenic sources in February and July 2005. ....	121
Table 5-16: Comparison of absorbed and effective dose results obtained with MEDUSA and HPGe for the NORM sources in February and July 2005.....	122
Table 5-17: Percentage differences from the comparison of activity concentration results obtained with MEDUSA and HPGe for NORM plus $^{22}\text{Na}$ in February and July 2005.....	124
Table 5-18: Percentage differences from the comparison of absorbed and effective dose results obtained with MEDUSA and HPGe for the NORM sources in February and July 2005.....	124
Table 6-1: A summary of the radionuclide contamination identified on the <i>i</i> TL grounds.....	130
Table 0-1: Parameters ( <i>a</i> and <i>b</i> ) and their uncertainties for the absolute FEP efficiency for Simonsig Wine Farm samples.....	140
Table 0-2: Results of the comparison of the ERL to the IAEA-recommended activity concentrations, for the validation of the method used in this study to obtain absolute efficiencies.....	141
Table 0-3: HPGe count rate reported for the 5 locations of calibration spot CS1 in February 2005.....	142
Table 0-4: HPGe count rate reported the 5 locations of hotspot HS1 in February 2005.....	143
Table 0-5: HPGe count rate reported for the 5 locations of calibration spot NCS1 in July 2005.....	143
Table 0-6: Activity concentrations, absorbed and effective dose, from HPGe data, calculated for the naturally occurring radioactive materials (NORM) identified in the surveys. ....	144
Table 0-7: Activity concentrations, from HPGe data, calculated for the anthropogenic radioactive materials identified in the surveys.....	144
Table 0-8: Absorbed and effective dose, from HPGe data, calculated for the anthropogenic radioactive materials identified in the surveys.....	145
Table 0-9: Activity concentrations, from HPGe data for the 5 locations of calibration spot CS1, shown for the individual energy lines used for the thorium and uranium series. ....	145
Table 0-10: Activity concentrations, from HPGe data for the 5 locations of hotspot HS1, shown for the individual energy lines used for the thorium and uranium series. ....	146
Table 0-11: Activity concentrations, from HPGe data for the 5 locations of calibration spot NCS1, shown for the individual energy lines used for the thorium and uranium series. ....	146
Table 0-12: Activity concentrations, from HPGe data for the rest of the hotspots, shown for the individual energy lines used for the thorium and uranium series. ....	147
Table 0-13: Half-life prediction results from decay measurements of the 1077.4 keV line of $^{68}\text{Ga}$ in hotspot sample HS1, S1. ....	148
Table 0-14: Half-life prediction results from decay measurements of the 1115.55 keV line of $^{63}\text{Zn}$ in hotspot sample HS1, S1.....	149
Table 0-15: Half-life prediction results from decay measurements of the 834.848 keV line of $^{54}\text{Mn}$ in hotspot sample HS1, S1. ....	150

Table 0-16: Normalisation factors obtained from calibration spot NCS1. .... 151  
Table 0-17: Results obtained for normalisation of CS1 and NCS1 MEDUSA results  
using NCS1 and CS1 normalisation factors, respectively. .... 152

# CHAPTER 1 INTRODUCTION

The *i*Themba Laboratory for Accelerator Based Sciences (LABS) (formerly the National Accelerator Centre (NAC)) produces radioisotopes for use in nuclear medicine and research. This multidisciplinary research laboratory also provides facilities for basic and applied research using particle beams, and particle radiotherapy for the treatment of cancer. These sciences are “accelerator-based”, and *i*Themba runs four particle accelerators, namely, the main 200 MeV separated sector cyclotron (SSC), two smaller injector cyclotrons (SPC1 and SPC2), and the 6 MeV Van de Graaf electrostatic accelerator [vRo04]. The site of *i*Themba LABS (*i*TL) is situated in Faure, approximately 32 km from Cape Town (Figure 1-1 to Figure 1-3).

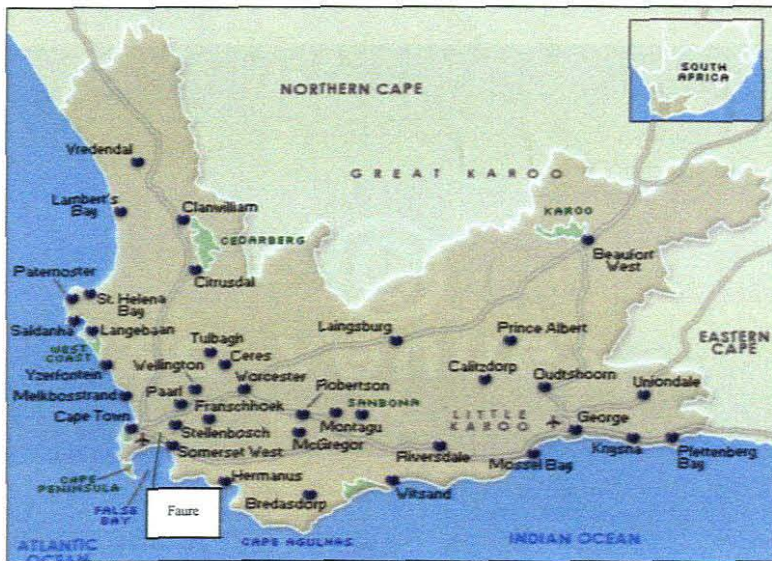


Figure 1-1: The map of parts of the Western Cape province of South Africa showing the location of Faure [Www01].

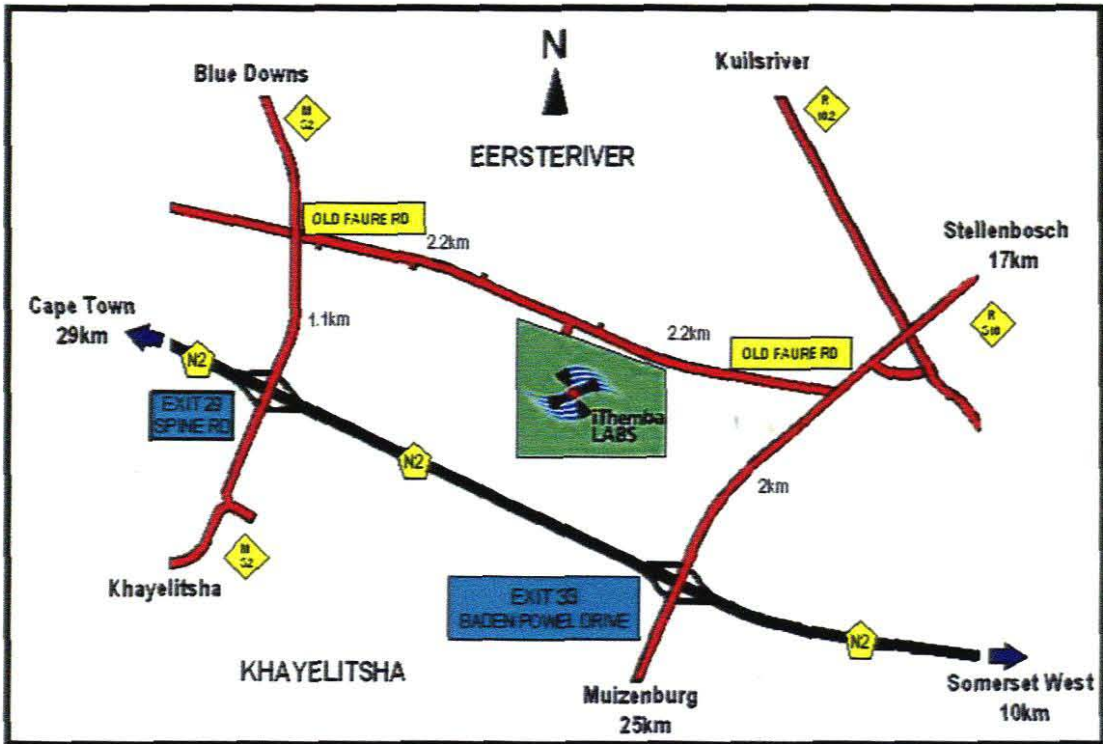


Figure 1-2: The location of the iThemba LABS site in Faure in Western Cape, South Africa



Figure 1-3: Aerial photograph of the iThemba LABS site, taken in the winter of 1991 [vRo04].

The landscape of the iTL site is largely flat, although there are some uneven sections. A large area of the site is covered with grass, as well as some bushes and trees. The holding dams are located South-West of the site (Figure 1-4). Access to the



various buildings on the site is by means of a tarred road network. All the portions of the site (except the dams and bushes) that have no building on them can be accessed with a 4x4 vehicle. The perimeter of the entire site is also accessible with the vehicle.

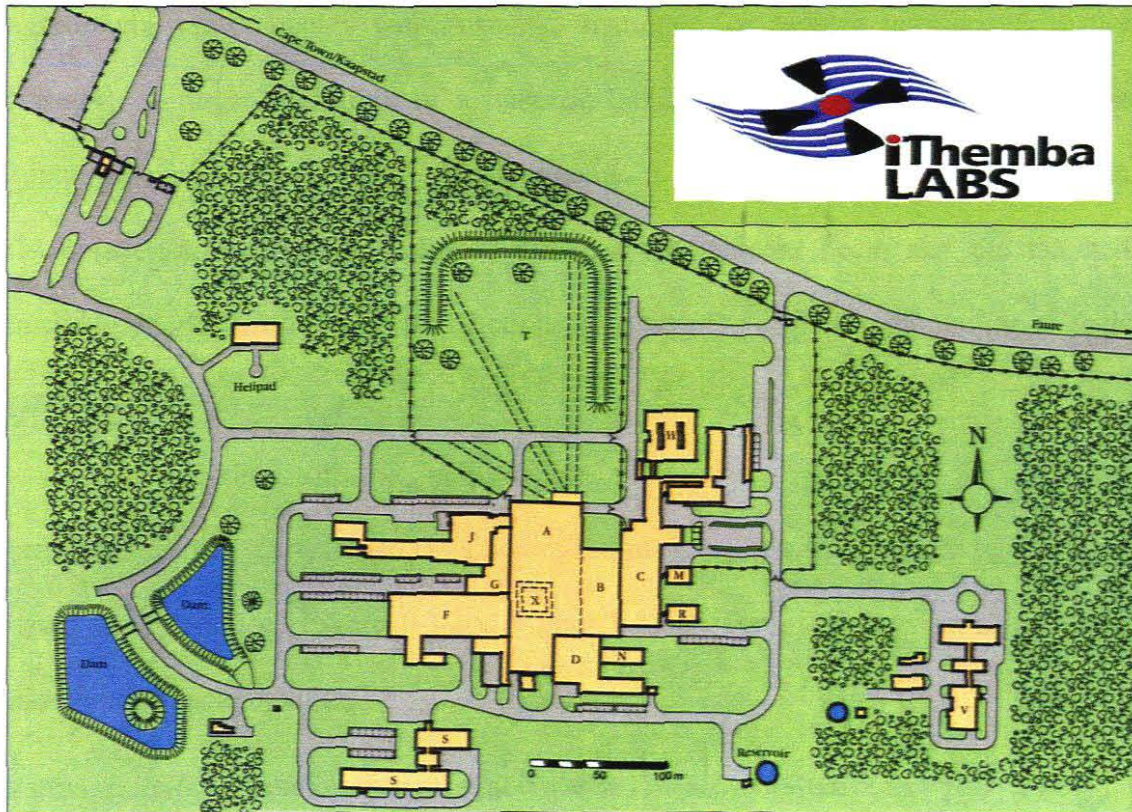


Figure 1-4: Schematic diagram of the iThemba LABS site. (A = Accelerator hall, B = Radiotherapy vaults, C = Patient handling, D = Radioisotope production, F = Workshop and services, G = Control and data, H = Hospital, J = Offices and laboratories, M = Medical Physics, N = Nuclear Medicine, R = Radiobiology, S = Service laboratories, V = Van de Graaff accelerator, and X = Separated-sector cyclotron)

## 1.1 Radioisotope production at iThemba LABS

The iTL Radionuclide Production Group (RPG) produces radionuclides to meet the entire country's demand for certain important radio-pharmaceuticals. More than 1000 deliveries are made to more than thirty institutions throughout South Africa. These batches are used for nearly 10 000 patients each year [vRo04]. A number of long-lived, non-medical radionuclides, mainly  $^{22}\text{Na}$ , are produced, on request, for use

in research and industry. In Table 1-1 is contained the list of useful radionuclides produced at iTL.

The process of radionuclide production involves the bombardment of appropriate target nuclei with, usually, hydrogen or helium accelerated nuclei [vRo04]. A target consisting of a material (solid, liquid or gaseous) that has the appropriate nuclide as one of its constituents, is irradiated with a 66 MeV proton (hydrogen ion) beam. The collision between the incident beam and the targeted nuclide material leads to nuclear reactions that have the desired radionuclide as their product [vRo04].

A by-product of the radioisotope production process is the artificial radionuclides that are released [in a controlled manner] as waste into the two holding dams on the site (see Figure 1-3 and Figure 1-4). In Table 1-2 is given a list of the contributing radionuclides.

**Table 1-1: Useful radioisotopes produced at iThemba LABS. (Abbreviations: a ≡ year; d ≡ day; h ≡ hour; m ≡ minute; s ≡ second.) (Adapted from [vRo04].)**

Isotope	Symbol	Half-life	Application
Gallium-67	<sup>67</sup> Ga	78.0 h	Medical
Fluorine-18	<sup>18</sup> F	110.0 m	Medical
Cerium-139	<sup>139</sup> Ce	138.0 d	Medical/Industrial
Strontium-82	<sup>82</sup> Sr	25.5 d	Medical/Industrial
Rubidium-81	<sup>81</sup> Rb	4.6 h	Medical: Production of <sup>81m</sup> Kr in Rb-Kr-generator
Krypton-81m	<sup>81m</sup> Kr	13.0 s	Medical
Indium-111	<sup>111</sup> In	3.0 d	Medical
Iodine-123	<sup>123</sup> I	13.0 h	Medical
Thallium-201	<sup>201</sup> Tl	73 h	Medical
Sodium-22	<sup>22</sup> Na	2.6 a	Industrial
Iron-55	<sup>55</sup> Fe	2.7 a	Industrial
Cobalt-57	<sup>57</sup> Co	271 d	Industrial

**Table 1-2: Anthropogenic radioisotopes released as waste products [into two holding dams] at iThemba LABS. (Adapted from [vRo04].)**

Isotope	Symbol	Half-life
Sodium-22	<sup>22</sup> Na	2.6 a
Sodium-24	<sup>24</sup> Na	15 h
Manganese-54	<sup>54</sup> Mn	312 d
Zinc-65	<sup>65</sup> Zn	244 d
Rubidium-83	<sup>83</sup> Rb	86 d
Rubidium-84	<sup>84</sup> Rb	33 d
Cobalt-57	<sup>57</sup> Co	271 d
Cobalt-58	<sup>58</sup> Co	71 d
Germanium-68	<sup>68</sup> Ge	288 d
Tin-113	<sup>113</sup> Tin	115 d
Strontium-83	<sup>83</sup> Sr	32 d
Strontium-85	<sup>85</sup> Sr	65 d
Xenon-123	<sup>123</sup> Xe	2.1 h
Indium-114m	<sup>114m</sup> In	50 d

## 1.2 The motivation for this study

The extensive lawns around the iTL site are irrigated using water from the two holding ponds. In Figure 1-5 is shown a bar graph representing the results of the activity of some anthropogenic radionuclides identified in one of the holding dams on the iTL site in 2003. There is [reasonable] interest in knowing how much anthropogenic radionuclide contamination could be on the site as a result of this irrigation practice. This interest led to the first *in-situ gamma-ray* radiometric mapping of the iTL grounds being carried out by the Environmental Radioactivity Laboratory (ERL) in June 2004. The ERL is run by the Physics Group of iThemba LABS. In carrying out the mapping, a detection system called *Multi-Element Detector for Underwater Sediment Activity* (or MEDUSA) was used.

The June 2004 survey did a lot to inform the ERL about the radioactivity profile of the iTL grounds. Of particular note were the regions of higher count rates that can be observed on the map shown in Figure 1-6 below. The map shows the iTL grounds in terms of the [colour-coded] count rate levels that were recorded during the survey. The colour-code range (or scale) of 100 - 1100 counts per second is used for

better contrast of the colours; the actual recorded count rate level range is 51 - 5318 counts per second.

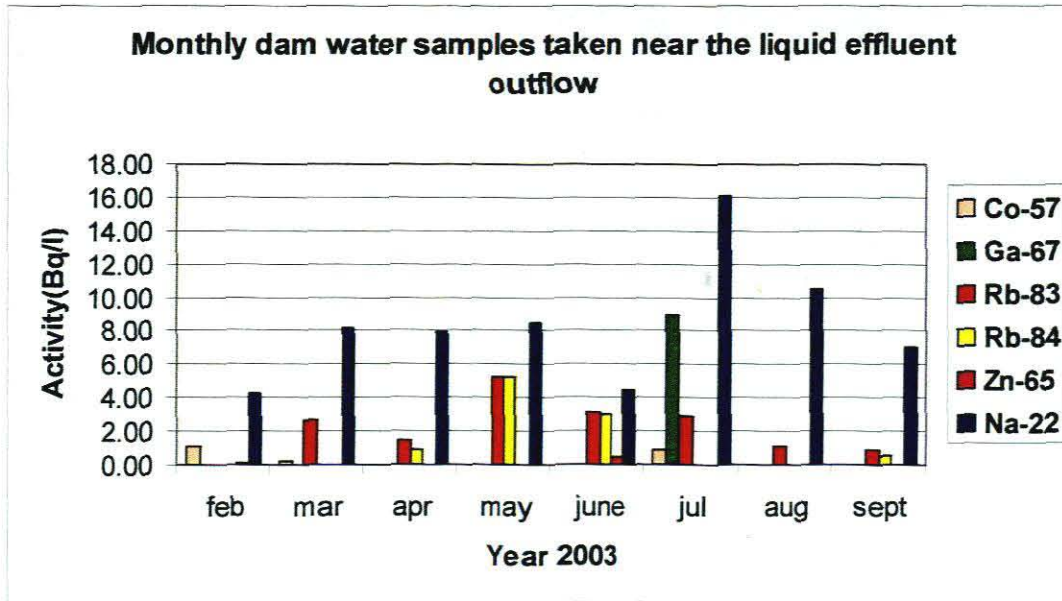


Figure 1-5: A bar graph representing the results of the activity of some anthropogenic radionuclides identified in one of the holding dams on the iTL site in 2003. (Adapted from [New04c]).

The information that was provided by the June 2004 survey will be used to further extract the activity concentration of the anthropogenic radionuclides responsible for the observed enhancement in detection count rate. The MEDUSA system runs on a suite of software programs that allows for the activity concentration to be extracted, only with a precondition that a standard spectrum associated with each of the observed radionuclides be used in the analysis (see Section 4.1.2). This condition was not met at the time of the June 2004 survey [New04a]. In 2005, however, a set of new simulated spectra was obtained and the ERL could then continue with a survey (this study) similar to that of June 2004, only this time more information could be obtained from it, including the activity concentration of the anthropogenic radionuclide  $^{22}\text{Na}$ .



Figure 1-6: Map showing MEDUSA detection count rate obtained during the June 2004 survey. The range of the count rate is 100 – 1100 counts per second, and is shown on the top-right corner on the map.

### ***1.3 Hypothesis and problems to be investigated***

The hypothesis stated for this project is the following:

*The maximum effective dose to humans on the iThemba LABS grounds as a result of external gamma-ray exposure to natural and anthropogenic radionuclides is orders of magnitude below 1 mSv per year<sup>1</sup>.*

The following are the main questions that the study tries to address:

- what is the radioactivity level (due to both natural and anthropogenic  $\gamma$ -ray emitting radionuclides) on the iThemba LABS grounds?
- where are the most radioactive spots (“hotspots”) on the grounds?
- what radionuclides contribute to radiation in these spots?
- what are the activity concentrations of the radionuclides?
- does the “hotspot” spatial distribution change with time?
- what are the associated effective doses from the “hotspots” to humans on the site?

### ***1.4 Scope of this study***

The scope of this study [as initially envisaged] is illustrated in the diagram shown in Figure 1-7 below. The focus here is on the profiling of the iTL site in terms of environmental radioactivity, and then using a simple model to arrive at the health effects due to the identified anthropogenic contamination on site.

---

<sup>1</sup> The *International Commission on Radiological Protection* (ICRP) has set a recommended dose limit on effective dose of 1 mSv per year per individual member of public [vRo04].

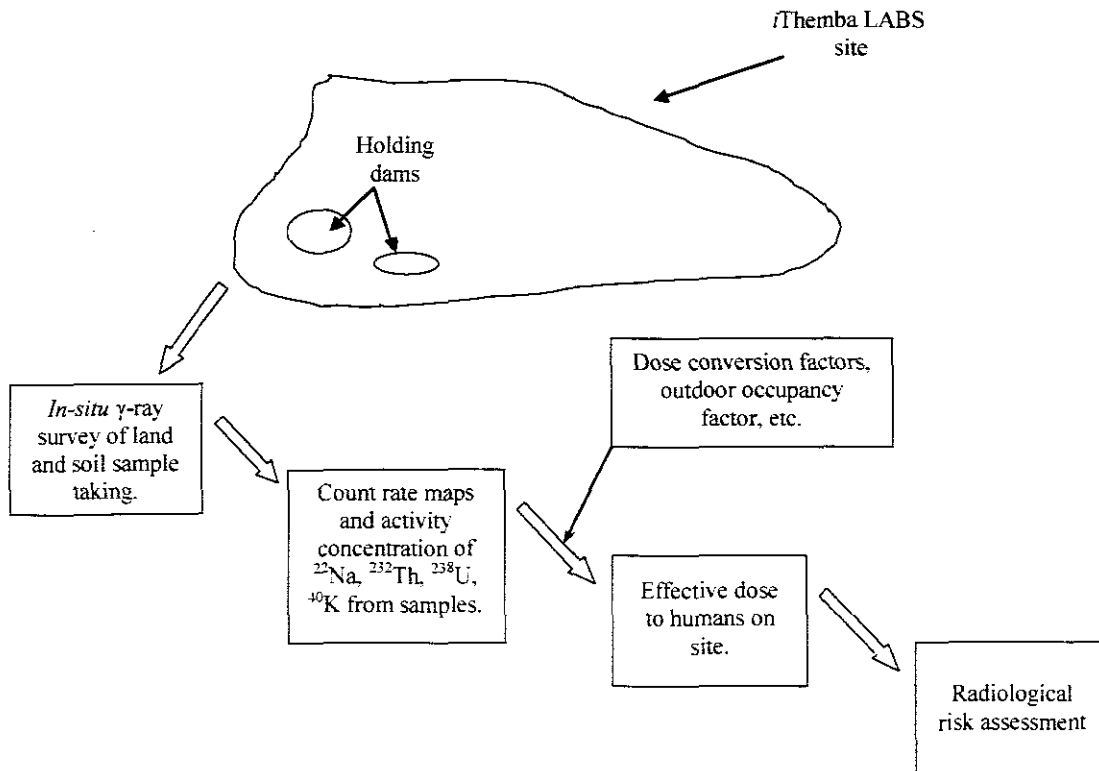


Figure 1-7: A flow-chart illustrating the scope of this study of the iThemba LABS site

This *in-situ* radiometric mapping is limited to (i) the area within the boundaries of the iThemba LABS site, (ii) the areas that are accessible with the 4x4 vehicle, and (iii) the radiological risks to human beings due to external exposure to environmental *gamma*-radiation on site (non-human biota is excluded).

### 1.5 The dissertation plan

This dissertation has been organized as follows:

- in Chapter Two there is a discussion the background theory on Environmental Radioactivity, as well as a literature review focusing on *in-situ* radiometric mapping studies;
- in Chapter Three there is a discussion of the methodology used in carrying out the experimental aspects of this study;

- in Chapter Four there is an expansion on the methods of analyzing the data collected during this study;
- in Chapter Five there is a presentation and discussion of the findings of this study, and
- in Chapter Six the conclusion and outlook of this study are given.



## CHAPTER 2 BACKGROUND THEORY: RADIOACTIVITY IN THE ENVIRONMENT

In this chapter a detailed discussion of the subject of environmental radioactivity is given. This begins with the basic theory on radionuclides, their properties and the radiation associated with them. The discussion is narrowed down to be specific to  $\gamma$ -radiation, its characteristics and how it is detected. In the discussion the theory on radiation protection vis-à-vis the impacts that environmental radioactivity has on humans is also addressed.

### 2.1 Radionuclides

The term *radioactivity* is used to refer to the spontaneous emission of subatomic particles and high-frequency electromagnetic *radiation* by radioactive elements [Tyk95]. This phenomenon was given its name by Marie Curie of Poland a few years after Henri Becquerel of France discovered it in 1896 [Tyk95, Kat84].

*Radiation* can be defined as energy propagated through space or material medium [vRo04]. There are three main forms of radiation that are emitted by radioactive elements, namely *alpha* ( $\alpha$ ), *beta* ( $\beta$ ) and *gamma* ( $\gamma$ ) [Mar79].

Radioactive elements are referred to as *radionuclides* [Tyk95]. The term *nuclide* refers to any species of atom having in its nucleus certain numbers of protons and neutrons, and where the sum of the numbers of protons and neutrons denotes the mass number of the nuclide [Tyk95]. Initially, the different elements were recognized by some of their specific properties and characteristics, e.g., state, colour, density, etc. Elements, however, could further be characterized by their physical and chemical properties and parameters. They were then subdivided into nuclides [Tyk95].

A radionuclide is an unstable nuclide, that is, it undergoes spontaneous transformation into a different atom of lower atomic mass, because it emits subatomic particles and/or high-frequency electromagnetic radiation, according to Einstein's mass-energy equation, in order to assume better nuclear stability [Mar79, Tyk95].

Radionuclides are found almost all around us, but the radiation that they produce can neither be seen with the naked eye, nor can it be smelt, heard, tasted, and felt by touching. Its manifestation is observed from its characteristic behaviours that are revealed by using the correct nuclear instruments. These nuclear instruments, called *detectors*, make use of nuclear physics principles that govern the interaction of radiation with matter.

In the following sub-sections to 2.1, the subject of radionuclides is going to be explored even further by looking at properties of radionuclides (2.1.1), forms of radiation from radionuclides (2.1.2), interaction of  $\gamma$ - radiation with matter (2.1.2.1), as well as detection of radiation from radionuclides, with emphasis on  $\gamma$ - radiation (2.1.3 and 2.1.3.1).

### 2.1.1 Properties of radionuclides

One or more radionuclides may be contained in a radioactive substance or material [Tyk95]. The number of radioactive transformations of these radionuclides are statistical, that is, it cannot be predicted which of the radionuclides will undergo radioactive transformation, because there is an equal probability for any radionuclide in the material to undergo radioactive transformation. The statistical fluctuations in the number of radioactive transformations occurring within radioactive material follow a Poisson distribution. The strength or *activity* of radioactive material is denoted by the *mean value* of the number of radioactive transformations occurring within the material per unit time [Hal97, Tyk95]. Mathematically it means

$$A = \frac{dN}{dt}$$

**Equation 2-1**

where  $A$  is the activity,  $dN$  is the mean value of the number of radioactive transformations that occurred over time interval  $dt$  [Leo87, Tyk95].

It was observed by experiment that activity decays exponentially in time, and that the decay equals to the decay rate of the radionuclide concerned [Leo87, Tyk95]. As an example, consider radioactive material consisting of  $N$  amount of nuclear species of a particular radionuclide whose transformation probability per unit time equals to  $\lambda$ . This means that the following relationship between activity and decay rate holds:

$$\frac{dN}{dt} = -\lambda N$$

**Equation 2-2**

where  $\lambda$  is called the *decay constant* of the radionuclide and  $t$  is the same as in Equation 2-1. When Equation 2-2 is integrated over time, the result gives the so-called *radioactive decay law* equation in the form

$$N_t = N_0 e^{-\lambda t}$$

**Equation 2-3**

in which  $N_0$  is the number of nuclear species of the radionuclide at reference time  $t = 0$ ,  $N_t$  is their number remaining at some time  $t$  later, and  $e$  is the base of the natural logarithms. It follows from Equation 2-1 and Equation 2-2 that the exponential decay relationship also holds for the activity, that is,

$$A_t = A_0 e^{-\lambda t}$$

**Equation 2-4**

where  $A_0$  and  $A_t$  denote the activity at  $t = 0$  and  $t$ , respectively [Tyk95, Leo87, Hal97].

In practice, a radionuclide's *half-life*, instead of its decay constant, is used for the characterization of the radionuclide [Tyk95]. Half-life refers to the time required for one half of the nuclear species of the radionuclide to decay within the radioactive material [Mar79]. Using again the example of the radioactive material in Equation 2-2 and putting  $N_t = N_0/2$  in Equation 2-3, the half-life ( $T_{1/2}$ ) of the radionuclide is defined as follows:

$$N_0 / 2 = N_0 e^{-\lambda T_{1/2}}$$

divided by  $N_0$  and followed by the taking of logs this becomes

$$\ln(1/2) = -\lambda T_{1/2}$$

and therefore

$$T_{1/2} = \frac{\ln 2}{\lambda} = \tau_m \ln 2$$

**Equation 2-5**

where  $\tau_m$  is called the *mean lifetime* of the radionuclide in the radioactive material, and it represents the time it takes for the radioactive material to decay to  $1/e$  of its original activity [Leo87, Tyk95].

As mentioned earlier, the number of radioactive transformations that occur within radioactive material follows the statistical Poisson probability distribution. To illustrate this, let  $\Delta t$  represent a time interval shorter than the half-life of the radionuclide. Now, if repeated measurements of the number of radioactive transformations, call it  $n$ , are taken in the interval  $\Delta t$ , fluctuations will be observed from one measurement to another. In each of the measurements the probability of detecting  $n$  counts of radioactive transformations in the time interval  $\Delta t$  is equal to

$$P(n, \Delta t) = \frac{m^n}{n!} e^{-m}$$

**Equation 2-6**

where  $m$  is the average number of counts in the time interval  $\Delta t$ . This distribution has a standard deviation,  $\sigma$ , given by

$$\sigma = \sqrt{m}.$$

**Equation 2-7**

Characteristic also to radionuclides are the radioactive decay chains that are formed when a radionuclide transforms into another radionuclide, meaning that both the parent (the original) and the daughter (the product) nuclides are unstable. So far we've only looked at an unstable parent nuclide that transforms into a stable daughter nuclide. Amongst numerous others, nuclides such as  $^3\text{H}$ ,  $^{14}\text{C}$ ,  $^{32}\text{P}$ ,  $^{35}\text{S}$ ,  $^{36}\text{Cl}$ ,  $^{45}\text{Ca}$ , and  $^{131}\text{I}$ , transform by this simple parent – stable daughter association [LAN98]. However, there are numerous other radionuclides used as *tracers*<sup>2</sup> that transform by producing further radioactive nuclides and thus form the characteristic radioactive decays.

In a radioactive decay chain where parent radionuclide  $A$  transforms to daughter radionuclide  $B$ , and daughter  $B$  further decays to stable nuclide  $C$ , the radioactive decay law when applied yields the equations given in Table 2-1.

**Table 2-1: Equations associated with a radioactive decay chain of nuclides  $A$ ,  $B$ , and  $C$ .**

$\frac{dN_a}{dt} = -\lambda_a N_a$
$\frac{dN_b}{dt} = \lambda_a N_a - \lambda_b N_b$
$\frac{dN_c}{dt} = \lambda_b N_b$

Here  $\lambda_a$  and  $\lambda_b$  represent the decay constants of nuclides  $A$  and  $B$ , respectively. The results follow the same principle when longer radioactive decays are considered. Assuming an initial condition of  $N_{a0} = N_{c0} = 0$ , then the solution to the equations in Table 2-1 is given in Table 2-2.

---

<sup>2</sup> When one or more radionuclides are intentionally introduced into an experimental system, their distribution can be determined to obtain an illustration of the course of particular studied phenomena [Tyk95]. These radionuclides are given the term *radiotracers*.

**Table 2-2: Equations associated with a radioactive decay chain of nuclides A, B, and C.**

$$\begin{aligned}
 N_{at} &= N_{a0}e^{-\lambda_a t} \\
 N_{bt} &= N_{a0} \frac{\lambda_a}{\lambda_b - \lambda_a} (e^{-\lambda_a t} - e^{-\lambda_b t}) \\
 N_{ct} &= N_{a0} \left[ 1 + \frac{1}{\lambda_b - \lambda_a} (\lambda_a e^{-\lambda_b t} - \lambda_b e^{-\lambda_a t}) \right]
 \end{aligned}$$

A graphical illustration of the behaviour in time of the three species of nuclides is given in Figure 2-1 below. The activity of B shown here is given by  $\lambda_b N_b$  instead of  $dN_b/dt$ , since the latter now includes the rate of B created by A [Leo87]. Nuclide B goes to a maximum in which, when the derivative is set to zero, we find

$$t_m = \frac{\ln(\lambda_b / \lambda_a)}{\lambda_b - \lambda_a}$$

**Equation 2-8**

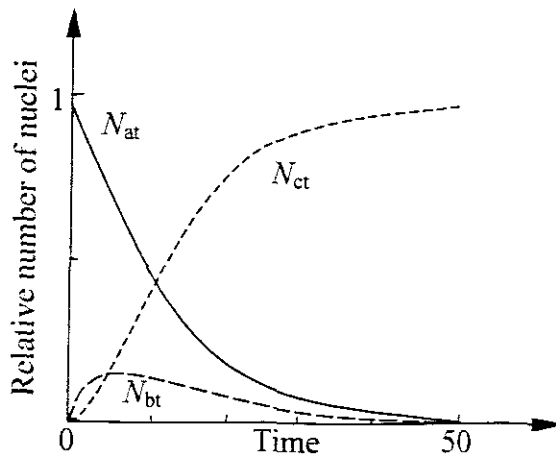


**Figure 2-1: A graphical illustration of the radioactive decay of a three nucleus chain. (Adapted from [Leo87])**

It follows from Table 2-2 that  $t_m$  is the point at which the activity of B reaches a maximum equal to

$$\lambda_b N_{bt_m} = \lambda_a N_{at_m}$$

**Equation 2-9**

This is termed *ideal equilibrium*. Except for the point at ideal equilibrium, the ratio of the activities of any parent (in this case,  $A$ ) and its daughter (in this case,  $B$ ) changes with time according to

$$\frac{\lambda_b N_b}{\lambda_a N_a} = \frac{\lambda_b}{\lambda_b - \lambda_a} \left[ 1 - e^{(\lambda_b - \lambda_a)t} \right].$$

**Equation 2-10**

For this ratio there are three cases of note, namely (1)  $\lambda_a > \lambda_b$ , (2)  $\lambda_b > \lambda_a$ , and (3)  $\lambda_b \gg \lambda_a$ . In case (1), the ratio increases with time. In case (2), called *transient equilibrium*, the ratio becomes almost constant  $> 1$  at large  $t$ . In case (3), called *secular equilibrium*, the ratio rapidly levels off to  $\approx 1$  [Leo87].

The SI unit of activity ( $A$ ) is the *becquerel* (abbreviated Bq). One Bq corresponds to one radioactive transformation per second, i.e.  $1 \text{ Bq} = 1 \text{ s}^{-1}$  [Tyk95]. The former unit of activity is the *curie* (Ci), which is related to the transformation rate of 1 gram of  $^{226}\text{Ra}$  equal to nearly  $3.7 \times 10^{10} \text{ s}^{-1}$  [Tyk95].

### 2.1.2 Forms of radiation from radionuclides

Radiation can be ionizing and/or non-ionizing. Ionizing radiation produces ion pairs when traveling through matter, while non-ionizing radiation does not. Only the former form will be discussed in this section. A distinction is often made between particulate and non-particulate forms of radiation [LAn98]. The particulate are those that may have a definite rest mass, while the non-particulate or electromagnetic forms may not. Radiation emissions either come directly from the nucleus of the radionuclide or from its electron structure [LAn98].

The particulate forms of ionizing radiation include alpha ( $\alpha$ ) and beta ( $\beta$ ) particles, which are emitted from the nuclei of radionuclides, *internal conversion electrons*, and *Auger electrons*. The non-particulate forms of ionizing radiation

include *bremsstrahlung*, *X-radiation*, and *gamma* ( $\gamma$ ) radiation [vRo04, LAn98]. The focus of this section is going to be on  $\gamma$ -radiation and its interaction with matter; this is the main form of ionizing radiation that the study was based on.

### 2.1.2.1 $\gamma$ - radiation and its interaction with matter

Here we deal with the processes that make detection and measurement of  $\gamma$ -radiation possible [Tyk95, Tso83].  $\gamma$ -radiation is deficient of electric charge and so does not interact via inelastic collisions with atomic electrons, as is characteristic of charged radiation forms [Leo87]. There are three main processes with which  $\gamma$ -radiation interacts with matter, namely, (1) the *photoelectric effect*, (2) *Compton scattering*, and (3) *pair production*.

In Figure 2-2 is shown a diagram that illustrates the regions of the atomic number  $Z$  and the  $\gamma$ -ray energy  $E = h\nu$  (in MeV) where each of the processes predominates [Tyk95]. According to the illustration, the photoelectric effect is more dominant for low-energy  $\gamma$ -rays, while the Compton scattering and pair production are dominant for medium and high-energy  $\gamma$ -rays, respectively [Tyk95].

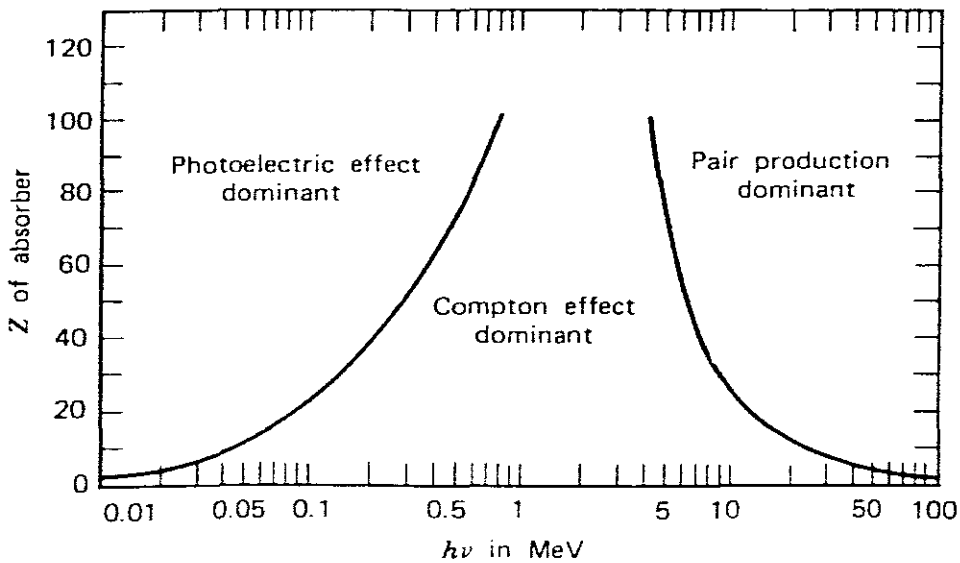


Figure 2-2: A diagram showing the domination of the photoelectric effect, Compton effect, and pair production in the three areas separated by the lines showing the values of  $Z$  and photon energy  $E$ . (Adapted from [Tyk95]).



An acquaintance with these processes reveals a unique qualitative feature of  $\gamma$ -radiation, that is, a beam of  $\gamma$ -rays is not degraded in energy as it passes through a thickness of matter, only attenuated in intensity [Leo87]. This is so because for all the three processes, the  $\gamma$ -ray is removed from the beam entirely, either by scattering or absorption. This means that the  $\gamma$ -rays that pass through have not suffered any interactions at all; they have kept their original energy. As a result of the specific amount of  $\gamma$ -rays that have interacted, however, the number of  $\gamma$ -rays in the beam (the intensity) is reduced by the same amount. It can be shown that the relationship of attenuation to thickness is exponential as follows:

$$I(x) = I_0 \exp(-\mu x)$$

**Equation 2-11**

where  $I_0$  = incident beam intensity,  $x$  = thickness of material,  $\mu$  = absorption coefficient associated with material [Leo87]. The following sub-sections are going to look at the three processes of  $\gamma$ -ray interaction with matter.

#### **2.1.2.1.1 Photoelectric effect**

This is a process of a  $\gamma$ -ray interacting by transferring all of its energy to a bound atomic electron, thus leading to the electron being ejected from the atom. The ejected electron has a kinetic energy,  $E$ , given by

$$E = h\nu - E_{be}$$

**Equation 2-12**

where  $h$  = Planck constant,  $\nu$  = frequency of light wave associated with  $\gamma$ -ray, and  $E_{be}$  = binding energy of the electron [Hal97]. The emphasis is put on the fact that the absorbing electron can only be amongst the bound atomic electrons because the free electrons cannot absorb a  $\gamma$ -ray and conserve momentum as well; the nucleus absorbs

the recoil momentum when the electron is bound [Leo87]. In the case where the ejected electron is from the inner bound  $K$  or  $L$  atomic shells, the outer bound electrons fall from their states to fill the resulting vacancy, thus leading to energy being emitted in the form of  $X$ -radiation [LAn98].

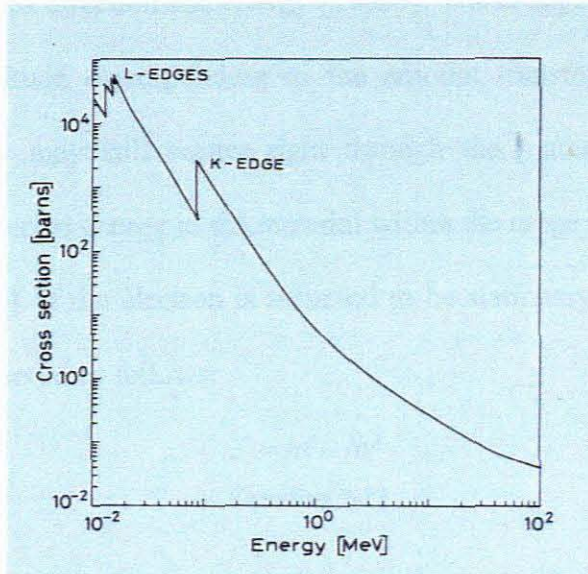


Figure 2-3: A plot showing a calculated photoelectric cross section for lead. (Adapted from [Leo87]).

In Figure 2-3 is shown how the *photoelectric cross section* (pcs) behaves when plotted against incident  $\gamma$ -ray energy. Moving from high incident energy to low, it is shown that the pcs increases drastically for energies corresponding to the binding energies of the different atomic shells. The sharp drop that follows exists because incident  $\gamma$ -ray energy is not high enough for the photoelectric effect to occur with the shell electrons, i.e.  $h\nu < E_{be}$  [Leo87].

The pcs depends on the atomic number  $Z$  of the absorbing material, such that at MeV levels of energy, this dependence goes as  $Z^4$  or  $Z^5$ . This makes the higher  $Z$  materials to be the most favoured for photoelectric absorption, as well as an important consideration when  $\gamma$ -ray detectors are chosen [Leo87].

### 2.1.2.1.2 Compton scattering

This is a process of a  $\gamma$ -ray colliding elastically with a loosely bound (regarded as free) electron. An illustration of the collision is shown in Figure 2-4 below. It can be observed from the illustration that the  $\gamma$ -ray does not disappear in this scattering process, only changes direction and energy [Tso83]. The change in energy equals to a reduction in magnitude corresponding to the amount transferred to the scattered electron. The  $\gamma$ -ray may still scatter right through the material, but the electron dissipates the transferred energy in the material within the range the electron travels in the material [Tso83]. If the electron is assumed to be stationary before the collision, then energy is conserved as follows:

$$T = hv - hv'$$

Equation 2-13

When momentum conservation is accounted for, then we get the expression for the kinetic energy of the scattered  $\gamma$ -ray in terms of the scattering angle  $\theta$  as follows:

$$hv' = \frac{hv}{1 + (1 - \cos\theta)hv / mc^2}$$

Equation 2-14

At this point the kinetic energy of the scattered electron can be derived to be

$$T = hv \frac{(1 - \cos\theta)hv / mc^2}{1 + (1 - \cos\theta)hv / mc^2}$$

Equation 2-15

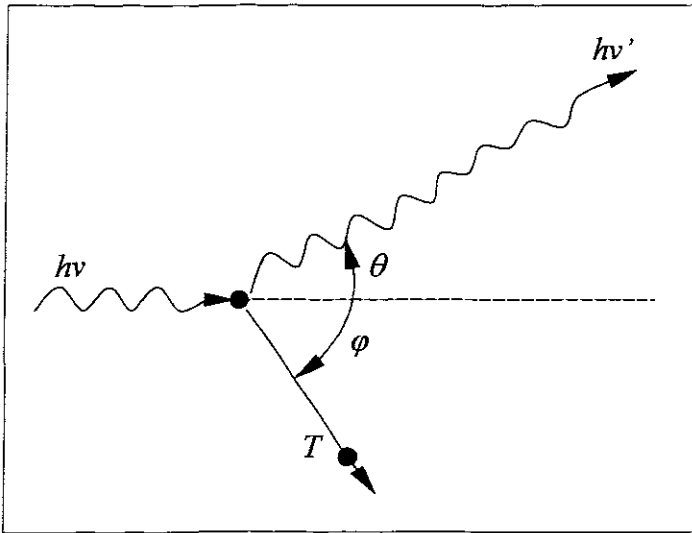


Figure 2-4: A diagram illustrating the kinematics of Compton scattering. (Adapted from [Leo87]).

The minimum and the maximum kinetic energy of the  $\gamma$ -ray and the electron after collision can be obtained by considering specific values of  $\theta$ . The minimum kinetic energy of the scattered  $\gamma$ -ray results when  $\theta = 180^\circ$  and it corresponds to the maximum energy of the electron. At this point Equation 2-14 gives

$$hv'_{\min} = \frac{hv}{1 + 2hv/mc^2}$$

Equation 2-16

and

$$T_{\max} = hv \frac{2hv/mc^2}{1 + 2hv/mc^2}$$

Equation 2-17

The maximum kinetic energy of the scattered  $\gamma$ -ray results when  $\theta = 0^\circ$ , that is, where the collision did not occur at all. Here Equation 2-14 gives  $hv'_{\max} = hv$  and  $T_{\min} = 0$ .

From the result in Equation 2-16, it is deducible that the minimum  $\gamma$ -ray energy in Compton Scattering can never be zero, that is, a total energy transfer from the  $\gamma$ -ray to the electron is impossible [Tso83].

### 2.1.2.1.3 Pair production

In this process a  $\gamma$ -ray interacts with the coulombic field of an atomic nucleus and produces two (a pair of) nuclear particles, namely, an electron (negatron) and a positron [LAn98]. This is a demonstration of mass being created from energy in accordance with Einstein's energy-mass equation  $E = mc^2$ , where  $E$  = energy,  $m$  = mass, and  $c$  = speed of light. In the case of an electron being created from energy, a certain quantum of  $\gamma$ -ray energy that will be sufficient for the process to occur can be calculated (using  $E = mc^2$ ) as follows:

$$(9.11 \times 10^{-31} \text{ kg})(2.99 \times 10^8 \text{ m.s}^{-1})^2 = 8.14 \times 10^{-14} \text{ J}$$

where substitutions have been made for  $m$  and  $c$ , of  $9.11 \times 10^{-31} \text{ kg}$  and  $2.99 \times 10^8 \text{ m.s}^{-1}$ , respectively. In units of *electron volts* (eV) this becomes

$$(8.14 \times 10^{-14} \text{ J}) \left( \frac{1 \text{ eV}}{1.602 \times 10^{-19}} \right) = 5.08 \times 10^5 \text{ eV}$$

or

$$E = 0.51 \text{ MeV}$$

The creation of an antiparticle to the electron (the positron) requires an equal minimum quantum of  $\gamma$ -ray energy, i.e.  $E = 0.51 \text{ MeV}$ . This means that in order for the electron-positron pair to result from pair production, there has to be a  $\gamma$ -ray of minimum energy equal to

$$2 \times 0.51 \text{ MeV} = 1.02 \text{ MeV}.$$

There is another feature to pair production that it may also involve a  $\gamma$ -ray of energy above 1.02 MeV that originates from the transitions in the nucleus itself [LAn98]. The latter is termed *internal pair production*, and its existence competes to a small extent with the emission of  $\gamma$ -radiation [LAn98].

In Figure 2-2 it is shown that pair production is the dominant mechanism of interaction for  $\gamma$ -ray energies of 5 MeV and above. A  $\gamma$ -ray of energy in excess of 1.02 MeV that undergoes the pair production interaction distributes its kinetic energy as follows:

$$h\nu = 2mc^2 + E_{e^-} + E_{e^+}$$

where  $h\nu$  = energy of  $\gamma$ -ray,  $2mc^2 = 1.02$  MeV, and  $E_{e^-}$  and  $E_{e^+}$  are electron and positron kinetic energies produced, respectively [LAn98].

### 2.1.3 Detection of ionizing radiation: Detector characteristics

To avoid repetition, it has been mentioned earlier that an understanding of the mechanisms by which radiation interacts with matter leads to an understanding of how radiation detectors function [Tso83]. Put differently, the interaction of radiation with detector material (the matter) gives a basis for the detection and interpretation of the nature of the radiation concerned. This section is therefore not going to deliberate on any exclusive theory regarding radiation detection, but rather it is a discussion of the general features common to radiation detectors.

The fundamental principle in the operation of any detector is one, namely, the transfer of part or all of the radiation energy to the detector mass where it is converted into some other form more accessible to human perception [Leo87]. Reference to “detectors” in this context applies both to the detection unit as well as the accompanying electronics that are used to transform the information from the detector unit into electrical impulses that can be treated with accuracy and speed [Leo87].

Characteristic of any detector is firstly its *sensitivity*, that is, the capability that the detector has of producing a usable signal for a given type of radiation and energy [Leo87]. Sensitivity, therefore, is a function of the energy of the incident radiation and

it depends on certain factors, namely, (1) the cross section for ionizing reactions in the detector, (2) the detector mass, (3) the inherent detector noise, and (4) the protective material surrounding the detection volume [Leo87].

The second factor to consider is the *response* of the detector. For a detector whose output electrical signal provides information on the energy of the incident radiation, detector “response” refers to the relationship between the incident radiation energy and its equivalent in the output signal [Leo87]. For detectors that give output pulses as current, an equivalent of the incident radiation energy equals to the amount of charge that is contained in the current signal, that is, the integral of the pulse with respect to time [Leo87]. The integral of the pulse is directly proportional to the amplitude or pulse height of the signal when it is assumed that the shape of the pulse is not changing from one event to the other. An ideal detector response, therefore, equals to a linear relationship between the incident radiation energy and the total charge or pulse height of the output signal [Leo87].

Next in detector characteristics is the *energy resolution*, which is defined as the extent to which the detector can distinguish between two close lying energies [Leo87]. This feature is usually presented as the full-width-at-half-maximum of the energy peak (FWHM). Here “energy peak” refers to the Gaussian-shaped peak structure with finite width, which represents the detector’s response to particular incident radiation energy. If two closely lying energies lie within the energy resolution of the detector, they are considered as irresolvable [Leo87]. The relative resolution of energy  $E$  is usually expressed in percent as  $\Delta E/E$ , where  $\Delta E = \text{FWHM}$  of the energy peak. This resolution ratio improves with higher energy, i.e. the resolution is a function of the incident energy [Leo87]. Because of the Poisson-like statistical nature of ionization and excitation, there is a fixed amount,  $w$ , of average energy required to produce an

ionization, and it is dependent only on the material [Leo87]. Therefore, since  $J = E/w$  gives the average number of ionizations ( $E$  is the incident energy), it follows that as energy increases, the number of ionization events increases, and the relative fluctuations are reduced [Leo87].

The fluctuations are considered for, (1) the detector in which the radiation energy is not totally absorbed, and (2) one in which the full energy is absorbed [Leo87]. For the first detector, the number of events is given by a Poisson distribution, with the variance given by  $\sigma^2 = J$ . The resolution varies inversely as the square root of the energy as follows:

$$R = 2.35 \frac{\sqrt{J}}{J} = 2.35 \sqrt{\frac{w}{E}},$$

Equation 2-18

where the factor 2.35 relates the standard deviation of a Gaussian to its FWHM [Leo87]. For the second detector, the Poisson distribution is not applicable, and according to Fano, the variance here is  $\sigma^2 = FJ$ , where  $F$  is the so-called Fano factor [Leo87]. The resolution here is given by

$$R = 2.35 \frac{\sqrt{FJ}}{J} = 2.35 \sqrt{\frac{Fw}{E}}.$$

Equation 2-19

Another important factor in dealing with detectors is the *response function* of the detector, which is defined as the spectrum of pulse heights observed from the detector when it is bombarded by a monoenergetic beam of the given radiation [Leo87]. Ideally, this function corresponds to a Dirac delta function (or Gaussian peak with zero width) that gives, for a fixed incident energy, an output signal which has a single, fixed amplitude [Leo87]. In reality, the Gaussian peak is not always realized because the response function at a given energy is determined by the different



interactions that the radiation can undergo in the detector and its design and geometry [Leo87].

The *response time* of the detector is important to the timing properties of the detector, because when a good response time is achieved, then quick sharp pulses are formed to mark precisely the moment in time in the signal when the event occurred. Response time refers to the time that the detector takes to form the signal after the arrival of the radiation [Leo87]. Another aspect to this detector feature is the duration of the signal, that is, the period (known as *dead time*) over which the detector does not accept the second event because of the detector's insensitivity and/or to prevent the piling up of the second signal on the first [Leo87].

Dead time is the finite time that the detector requires to process an event [Leo87]. During this period the detector can either still be sensitive to the next event, resulting in the piling up of the two events, or it can be insensitive to the next event, but whichever way, in both cases the information in the signal is lost [Leo87]. Dead time effects can be avoided by keeping the counting rate of the detector sufficiently low such that the probability of a second event occurring during a dead time period is small [Leo87].

*Efficiency* is another characteristic associated with radiation detectors. Efficiency has two types, namely absolute (or total) and intrinsic detection efficiency [Leo87]. The absolute efficiency of a detector is defined as that fraction of events emitted by the source, which is actually registered by the detector, or

$$\epsilon_{\text{abs}} = \frac{\text{events registered}}{\text{events emitted by source}}$$

The absolute efficiency therefore becomes a function of the detector geometry and the probability of an interaction in the detector [Leo87]. The two variables can be

expressed, after certain considerations, in terms of geometrical efficiency and intrinsic efficiency, respectively. This defines the absolute efficiency as

$$\mathcal{E}_{\text{abs}} \approx \mathcal{E}_{\text{int}} \mathcal{E}_{\text{geom}}$$

where  $\mathcal{E}_{\text{int}}$  and  $\mathcal{E}_{\text{geom}}$  represent the intrinsic and geometrical efficiencies, respectively [Leo87]. The intrinsic efficiency is defined as that fraction of events actually hitting the detector which is registered, or

$$\mathcal{E}_{\text{int}} = \frac{\text{events registered}}{\text{events impinging on detector}}.$$

The intrinsic efficiency therefore becomes a function of the type and energy of the radiation in question, as well as the material of the detector [Leo87]. Geometrical efficiency, on the other hand, refers to that fraction of the source radiation that is geometrically intercepted by the detector [Leo87]. This efficiency is simply a function of the geometrical design of the detector.

### 2.1.3.1 Detection of $\gamma$ -radiation

This section covers the detection of  $\gamma$ -radiation by means of scintillation and semiconductor detectors, sections 2.1.3.1.1 and 2.1.3.1.2, respectively.

#### 2.1.3.1.1 Detection with scintillation detectors

The passage of ionizing radiation through a *scintillation* material is signaled by the formation of sparks (or scintillations) of light within the material [Tso83, Leo87]. The earliest use of scintillation material for nuclear particle detection dates as far back as 1903 where it was employed to detect  $\alpha$ -particles [Leo87]. Scintillators are also accredited with being the first solid materials to be used for nuclear particle detection [Tso83]. By the late 1980s, scintillation detectors were recognized as the most often and widely used particle detection devices in nuclear and particle physics [Leo87].

The main steps involved in particle detection via scintillation detectors are: (1) the absorption of incident radiation by the material, followed by the production of visible light, and (2) the amplification of the light by a *photomultiplier tube* (PMT), followed by the production of the output electrical pulse [Tso83].

A schematic diagram showing the basic elements of a scintillation detector is given in Figure 2-5 below. In the diagram, the scintillator is optically coupled to a PMT to allow for the optimal transmission of the produced light from the former to the latter [Leo87, Tso83]. The light is produced when radiation passes through the scintillator and excites the atoms and molecules making up the scintillator. The PMT converts the light into a weak current of so-called photoelectrons. This current signal is amplified via an electronic multiplier system, and then goes further for analysis by an electronic system [Leo87].

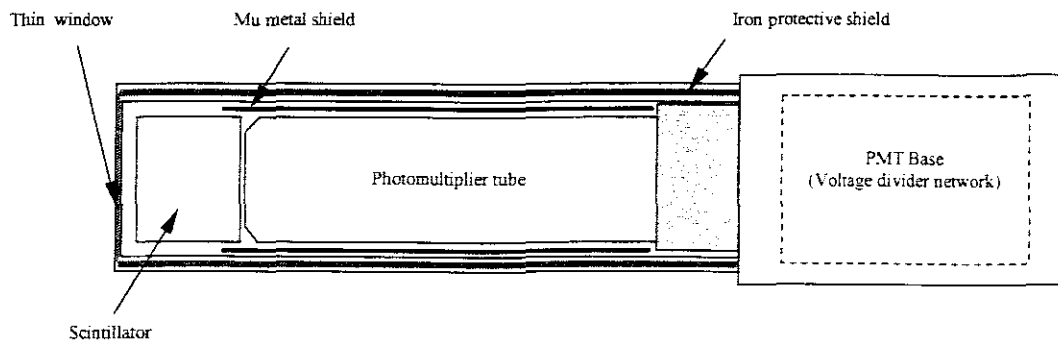


**Figure 2-5: A schematic diagram of the features of a scintillation counter. (Adapted from [Leo87]).**

A variety of information can be obtained from scintillator signals because of features such as (1) sensitivity to energy, (2) fast time response, and (3) pulse shape discrimination, in these signals [Leo87]. Sensitivity to energy has to do with the quality that most scintillators behave almost linearly for incident radiation of energy above a certain threshold. Fast time response recognizes the ability of scintillators to give timing information because of their short response and recovery times as compared to other types of detectors. And finally, pulse shape discrimination refers to

the ability of certain scintillators to distinguish between different types of particles by analyzing the shape of the emitted light pulses [Leo87].

The process of light production in scintillating materials derives from the luminescence characteristic of these materials [Leo87]. This means that when scintillating materials are exposed to certain forms of energy, in this case nuclear radiation, they absorb and re-emit the energy in the form of visible light. Re-emission can either occur immediately after absorption, fluorescence, or it can be delayed, phosphorescence, depending on the material being used. Delay times may range from a few microseconds to hours [Leo87].

A good scintillation detector is one that complies with a list of some four requirements, namely, (1) high efficiency for conversion of exciting energy to fluorescent radiation, (2) transparency to its fluorescent radiation so as to allow transmission of the light, (3) emission in a spectral range consistent with the spectral response of existing photomultipliers, as well as (4) a short decay constant<sup>3</sup> [Leo87]. Varying types of scintillation materials are in use, but this section focuses only on one such material, namely, inorganic crystals. Other available types include organic crystals, organic liquids, plastics, gases and glasses [Leo87].

The inorganic scintillators are mainly crystals of alkali metals, in particular alkali iodides, that contain a small concentration of an activator impurity [Tso83, Leo87]. Among these can be mentioned NaI(Tl), the most commonly used crystal in which thallium (Tl) is the impurity, also CsI(Tl), CsF<sub>2</sub>, CsI(Na), KI(Tl), and LiI(Eu) among others. Some of the useful non-alkali materials include Bi<sub>4</sub>Ge<sub>3</sub>O<sub>12</sub> (bismuth germanate or BGO), BaF<sub>2</sub>, ZnS(Ga), CaWO<sub>4</sub> among others [Leo87, Tso83]. The

---

<sup>3</sup> In the first approximation equation for the time development during reemission,  $N = (N_0/\tau) \exp(-t/\tau)$ , the  $N$  stands for the number of photons emitted at time  $t$ ,  $N_0$  is the total number of photons emitted, and  $\tau$  the decay constant [Leo87].

activator impurity is responsible for the luminescence of the inorganic scintillator crystal [Tso83].

Scintillation in the inorganic crystals is characterized by the electronic band structure [Leo87, Tso83]. The process of scintillation of inorganic crystals involves the following events: (1) ionizing radiation passes through the crystal, (2) electrons are raised to the conduction band, (3) holes are created in the valence band, (4) *excitons*<sup>4</sup> are formed, (5) impurity states are raised to the excited states by absorbing electrons, holes, and excitons, and (6) de-excitation, if allowed, is followed by the emission of a photon [Tso83, Leo87].

The most important quantity, when dealing with scintillators, is the *light output response* (LOR), which is defined as the efficiency of the scintillator for converting ionization energy to photons [Leo87]. This quantity is particularly significant because it determines the efficiency and resolution of the scintillator. The LOR of a scintillator is related to factors such as linearity, temperature dependence, and pulse shape discrimination [Leo87].

Linearity, that is, a linear response of scintillators with respect to the exciting energy, is not truly characteristic of scintillators [Leo87]. With NaI (and CsI), for example, a linear response to  $\gamma$ -radiation is maintained down to energy of about 400 keV where non-linearity occurs. This behaviour should therefore be taken into account to avoid poor accuracy for work done in this energy region [Leo87]. Temperature dependence of the LOR occurs in most scintillators, and should be considered if a scintillator is being used at temperatures that are very different from normal. In Figure 2-6 below is shown the strong variations that occur in the relative

---

<sup>4</sup> Sometimes the incident radiation does not give sufficient energy to raise an electron all the way to the conduction band. In this case the electron remains electrostatically bound to its hole in the valence band to form an electron-hole pair called an *exciton*. The exciton state results from an elevation of the electron up to a state above the valence band, but just below the conduction band (and coinciding with the lower level of the conduction band) [Tso83].

light output percentage of some inorganic crystals [Leo87]. Pulse shape discrimination (PSD) has already been defined above as the capability of certain scintillators of distinguishing between different types of incident particles by the shape of the emitted light pulse [Leo87].

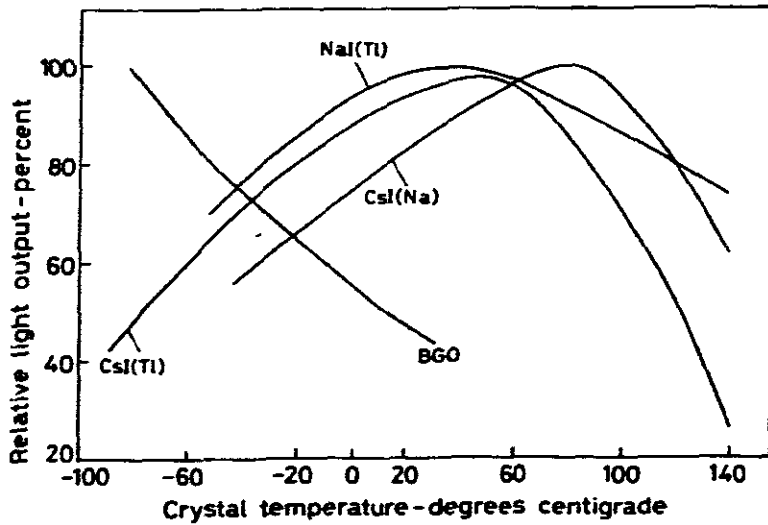


Figure 2-6: Temperature dependence of light output from inorganic crystals. (Adapted from [Leo87]).

Not all scintillator materials are suitable for efficiently detecting a particular type of incident radiation [Leo87]. Some factors that need to be considered when deciding on the most suitable type of scintillation detector have already been discussed; for example, the mechanisms by which the radiation interacts with the molecules of that particular scintillator material (see Section 2.1.2.1). The other factors include the probability of the interactions to occur within the volume of the scintillator detector, and of course the LOR of the scintillator [Leo87]. This subject deals with the *intrinsic detection efficiency* of the scintillator to various radiation types. This section will look at the intrinsic efficiency of scintillators for detecting  $\gamma$ -radiation.

The three processes by which  $\gamma$ -rays interact with matter require that the scintillator material used for detecting  $\gamma$ -radiation be of a high atomic number,  $Z$

[Leo87]. This follows from the fact that both the photoelectric and pair production processes result in the complete absorption of the  $\gamma$ -ray within the material, whereas Compton scattering can allow the  $\gamma$ -ray to escape after interaction (Section 2.1.2.1), and therefore a high- $Z$  material will favour the former two processes over the latter<sup>5</sup> [Leo87]. An illustration in Figure 2-7 shows that the high  $Z$  inorganic scintillator crystals (e.g. NaI in the diagram) are more favourable for  $\gamma$ -ray detection compared to the other materials (e.g. NE102A plastic in the diagram), because the former have higher photoelectric and pair production cross sections [Leo87]. Amongst the other inorganic crystals mentioned in this section, certain important properties of NaI(Tl) and CsI(Na) will be mentioned.

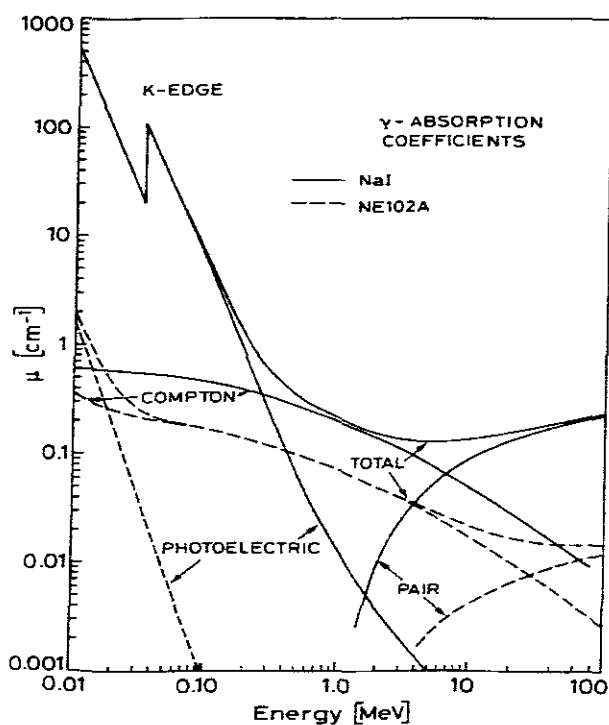


Figure 2-7: A plot showing  $\gamma$ -ray absorption coefficients for NaI and NE102A plastic scintillator. (Adapted from [Leo87]).

NaI(Tl) is the most commonly used scintillator for  $\gamma$ -ray detection, and is very useful in experiments where large detector volumes are needed [Tso83]. This crystal

<sup>5</sup> The photoelectric and pair production cross sections increase with increasing  $Z$  as  $Z^2$  and  $Z^2$ , respectively, whereas the Compton scattering cross section only varies linearly with  $Z$ .

has very high efficiency due to its relatively high density ( $3.67 \times 10^3 \text{ kg.m}^{-3}$ ) and high  $Z$ . The NaI(Tl) crystal also has the highest LOR amongst all the inorganic crystals. Although NaI(Tl) is adorned with all the abovementioned qualities, it still has some undesirable properties such as its brittleness, sensitivity to temperature, thermal shocks, hygroscopic nature, and content of small amounts of potassium that create a certain background due to the radioactive  $^{40}\text{K}$  [Tso83]. The CsI(Na) crystal has a higher  $\gamma$ -ray detection efficiency than NaI(Tl) because CsI(Na) has a density ( $4.51 \times 10^3 \text{ kg.m}^{-3}$ ) and  $Z$  that are higher than those for NaI(Tl) [Tso83]. The LOR of CsI(Na) is about 85% of that for NaI(Tl) at room temperature. The CsI(Na) crystal is only slightly hygroscopic, and does not contain potassium [Tso83].

#### ***2.1.3.1.2 Detection with semiconductor detectors***

The response of a semiconductor (or solid-state) material when penetrated by ionizing radiation is the formation of electron-hole pairs [Leo87, LAn98, Tso83]. Detection of ionizing radiation using a semiconductor detector (SCD) is achieved by collecting by an electric field the produced electron-hole pairs [Leo87]. The development and earliest usage of SCDs (particularly silicon (Si) and germanium (Ge)) is traceable back to the 1930s. Their application has been in nuclear physics research, and further work was started developing SCDs into detectors for future high energy experiments [Leo87]. The latter is a prospect deriving from the known superiority that SCDs have over other types of detectors when it comes to energy resolution capabilities [Tso83].

SCDs are also praised for other qualities such as their (1) linear response over a wide energy range, (2) higher efficiency for a given size due to high density, (3) ability to operate in vacuum, and (4) insensitivity to magnetic fields [Tso83]. They do also have their limitations such as (1) the general need for SCDs to be operated at low



temperatures and thus requiring an additional cryogenic system in their design features, and (2) their great sensitivity to radiation damage impinging upon their long term use [Tso83].

The operation of SCDs is based on the properties of the *np junction* associated with semiconductors [Tso83, Leo87]. The np junction is so called because it is formed by a juxtaposition of the n- and p-type semiconductor materials<sup>6</sup> (Figure 2-8) [Tso83, Leo87]. This configuration of the semiconductor materials results in the flow of electrons and holes from areas of high concentration to areas of low concentration, until an equilibrium in concentrations is reached. With this flow of charge carriers having taken place between the two materials, the n- and p-type materials have become positively and negatively charged, respectively. The np junction is therefore made up of a juxtaposition of the n- and p-type semiconductor materials with a certain potential difference  $V_0$  in between them [Tso83].

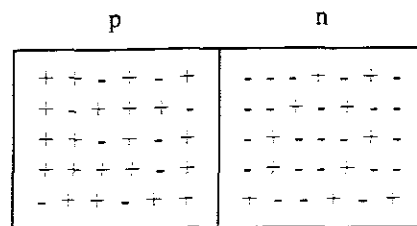


**Figure 2-8: A diagram showing the np junction with no external voltage applied. (Adapted from [Tso83]).**

An external voltage ( $V_b$ ), called the reverse bias, is applied to the np junction by connecting the positive pole to the n-type side. This increases the total potential across the junction to  $V_0 + V_b$ . The increased potential difference restrains the motion of charge carriers (electrons and holes), as well as widens the region (of width  $X_0$ ) that is devoid of mobile charge carriers, the so-called depletion zone [Tso83, Leo87]. The depletion zone is the region of changing potential in which an electric field  $E = -$

<sup>6</sup> The n- and p-type semiconductor materials have an excess of electron carriers and holes, respectively.

$\partial V/\partial x$  exists [Tso83]. The electric field in the depletion zone is responsible for sweeping out any electron or hole that enters this region [Leo87].

In an SCD setting, electron-hole pairs that are liberated by ionizing radiation are swept out by the electric field to produce a current signal, proportional to the ionization, for detection via the electrical contacts attached on either sides of the SCD junction [Leo87]. SCDs can be reviewed by looking at characteristics such as (1) average energy per electron-hole pair, (2) linearity, (3) intrinsic energy resolution, (4) leakage current, and (5) intrinsic efficiency [Leo87]. These are discussed here.

On average, a very small amount of energy is needed to create an electron-hole pair in SCDs, thus the better energy resolution [Leo87]. The *average energy per electron-hole pair* depends only on the type of material used, and not on the type and energy of the incident radiation [Leo87]. The response of SCDs to incident ionizing radiation is perfectly *linear* provided that the SCD depletion region is thick enough to allow for a total absorption of the radiation particle in the region [Leo87]. The *intrinsic energy resolution* depends on the number of charge carriers and the Fano Factor, and is given by Equation 2-19. The energy resolution of semiconductors is greatly enhanced due to low Fano factor values on the order of 0.12. *Leakage current* is a small fluctuating current that flows through SCD junctions when bias voltage is applied [Leo87]. This “noise current” has several sources and has a magnitude range from nanoamperes per  $\text{cm}^2$  up to a few microamperes per  $\text{cm}^2$ , depending on the source [Leo87]. The *intrinsic efficiency* of SCDs for charged particles is close to 100%, and has a limit of noise from the leakage current and the associated electronics [Leo87].

SCDs of germanium are preferred over those of silicon for the detection of  $\gamma$ -rays, because they have greater efficiency [Leo87]. With an atomic number  $Z_{\text{Ge}} = 32$ ,

germanium has a photoelectric cross section that is about 60 times greater than that of Si ( $Z_{Si} = 14$ ) [Leo87]. On the low side, germanium has a smaller band gap, and thus requires that the detector be operated at low temperatures [Leo87]. The *high purity germanium* (or HPGe) detectors are on the increase in use recently, gradually replacing the *Lithium-drifted germanium* (Ge(Li)) detectors [Leo87]. This section will only discuss the HPGe detectors.

HPGe detectors are constructed by a process similar to that used to construct Ge(Li) detectors, only there is not the lithium-drifting step. The HPGe detector is simply an application of a reverse bias across a piece of germanium that has an impurity concentration of less than  $10^{10}$  atoms.cm<sup>-3</sup> [Leo87, Tso83]. The depletion region of an HPGe detector is a function of the impurity concentration and the applied voltage, as shown in Figure 2-9 [Tso83]. The operation of HPGe detectors is also the same as that of the Ge(Li) detectors, only the former do not need to be kept at low temperatures at all times. The cooling of HPGe detectors is necessary only when a high voltage is applied [Leo87].

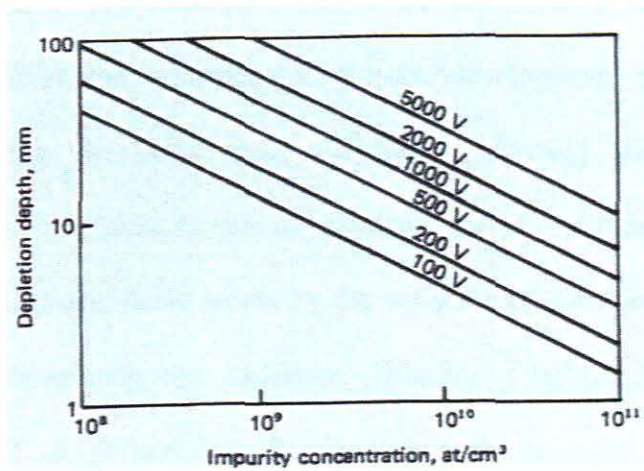
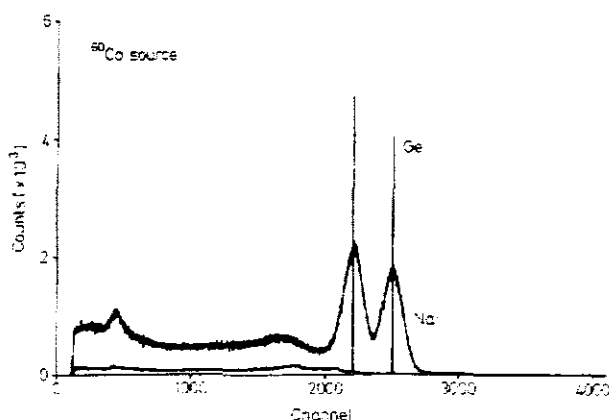


Figure 2-9: A plot showing the depletion depth as a function of impurity concentration and applied voltage for planar diodes of high-purity germanium. (Adapted from [Tso83])

Germanium detectors are mainly applied in  $\gamma$ -ray spectroscopy, where they are credited with offering the highest resolution available for  $\gamma$ -ray energies from a few

keV up to 10 MeV [Leo87]. In Figure 2-10, a comparison is made between a NaI-measured spectrum of  $^{60}\text{Co}$  and an HPGe-measured spectrum of  $^{60}\text{Co}$ . At 1.33 MeV, the HPGe resolution is about 0.15 %, while that of the NaI one is about 8 % [Leo87]. Germanium detectors also have a greater peak-to-Compton ratio because of their high photoelectric cross section [Leo87].



**Figure 2-10: A demonstration of how the  $^{60}\text{Co}$  spectrum compares when taken with a NaI detector and a germanium detector (Adapted from [Leo87])**

## 2.2 Environmental radioactivity

Environment, in this context, refers to the combination of external physical conditions that affect and influence the growth, development, and survival of an organism, including air, water, soil, and trees [Www01]. The environment is radioactive, i.e. it contains atoms of elements whose unstable nuclei undergo transformation into more stable atoms by the emission of subatomic particles and/or high-frequency electromagnetic radiation [Mar79, Tyk95]. Hans Geitel from Germany and C. T. R. Wilson from Scotland observed evidence for radioactivity in the environment. They discovered, in 1900, that an electroscope could be discharged simply from the air inside it, and not from insulator leakage as had previously been thought to be the case. The discovery led to a conclusion that the air contained radioactive components [Kat84].

### 2.2.1 Primordial and anthropogenic environmental radionuclides

Radionuclides are practically found all around us, in soil, rocks, air, water, plants, animals, and our own human bodies [Kat84]. They are found in our surroundings in different amounts and kinds, either as naturally-occurring, or as a result of human activity (these are called *anthropogenic* radionuclides). By 1995 more than 2500 radionuclides of various elements were known, in which approximately 80 could be found in nature, and the rest were directly or indirectly produced artificially [Tyk95]. Some of the naturally-occurring radionuclides are believed to have been created together with the earth more than  $3 \times 10^9$  years ago [Tyk95]. These are considered as naturally-occurring parent radionuclides, and are termed *primordial* radionuclides [Tyk95].

Some of the primordial, or *terrestrial*, radionuclides, together with their abundance and half-life, are listed in Table 2-3. Amongst these, the most abundant and important are  $^{40}\text{K}$ ,  $^{87}\text{Rb}$ , as well as the three radioactive series headed by  $^{238}\text{U}$ ,  $^{235}\text{U}$ , and  $^{232}\text{Th}$  [Tyk95]. For the purposes of this study only the  $^{238}\text{U}$  and  $^{232}\text{Th}$  series are considered. The  $^{238}\text{U}$  and  $^{232}\text{Th}$  series are usually called the *uranium* and *thorium series*, respectively, and are illustrated in Figure 2-11. Transfer mechanisms such as dust deposition, wash-out, weathering, sedimentation, and other processes are responsible for the expected presence of primordial radionuclides in environmental samples [Tyk95].

Anthropogenic radiation sources can be categorized as (1) technologically enhanced natural radiations (TENR), (2) consumer products, (3) fallout from nuclear explosives and weapons tests, (4) nuclear power, (5) medical radiation, and (6) occupational exposure [Kat84]. The TENR category refers to the possible increase in radioactivity levels as a result of the modification of the natural environment by

human activity, such as mining operations. *Consumer products* such as smoke and fire detectors, ceramics and U-Th alloys, etc., emit ionizing radiations.

**Table 2-3: A list of some of the primordial, or terrestrial, radionuclides, together with their abundance and half-life. (Adapted from [Tyk95]).**

Radio-nuclide	Abundance (%)	Half-life (years)
$^{40}\text{K}$	0.012	$1.26 \times 10^9$
$^{82}\text{Se}$	9.19	$1.40 \times 10^{20}$
$^{87}\text{Rb}$	27.85	$5.00 \times 10^{11}$
$^{115}\text{Cd}$	12.26	$9.30 \times 10^{15}$
$^{115}\text{In}$	95.72	$5.10 \times 10^{14}$
$^{138}\text{La}$	0.09	$1.10 \times 10^{11}$
$^{144}\text{Nd}$	23.85	$\approx 5.00 \times 10^{15}$
$^{147}\text{Sm}$	15.10	$1.06 \times 10^{11}$
$^{148}\text{Sm}$	11.30	$1.20 \times 10^{13}$
$^{152}\text{Gd}$	0.20	$1.10 \times 10^{14}$
$^{176}\text{Lu}$	2.60	$3.00 \times 10^{10}$
$^{174}\text{Hf}$	0.18	$2.00 \times 10^{15}$
$^{187}\text{Re}$	62.60	$7.00 \times 10^{10}$
$^{190}\text{Pt}$	0.013	$7.00 \times 10^{11}$
$^{232}\text{Th}$	100.00	$1.41 \times 10^{10}$
$^{235}\text{U}$	0.72	$7.10 \times 10^8$
$^{238}\text{U}$	99.28	$4.51 \times 10^9$

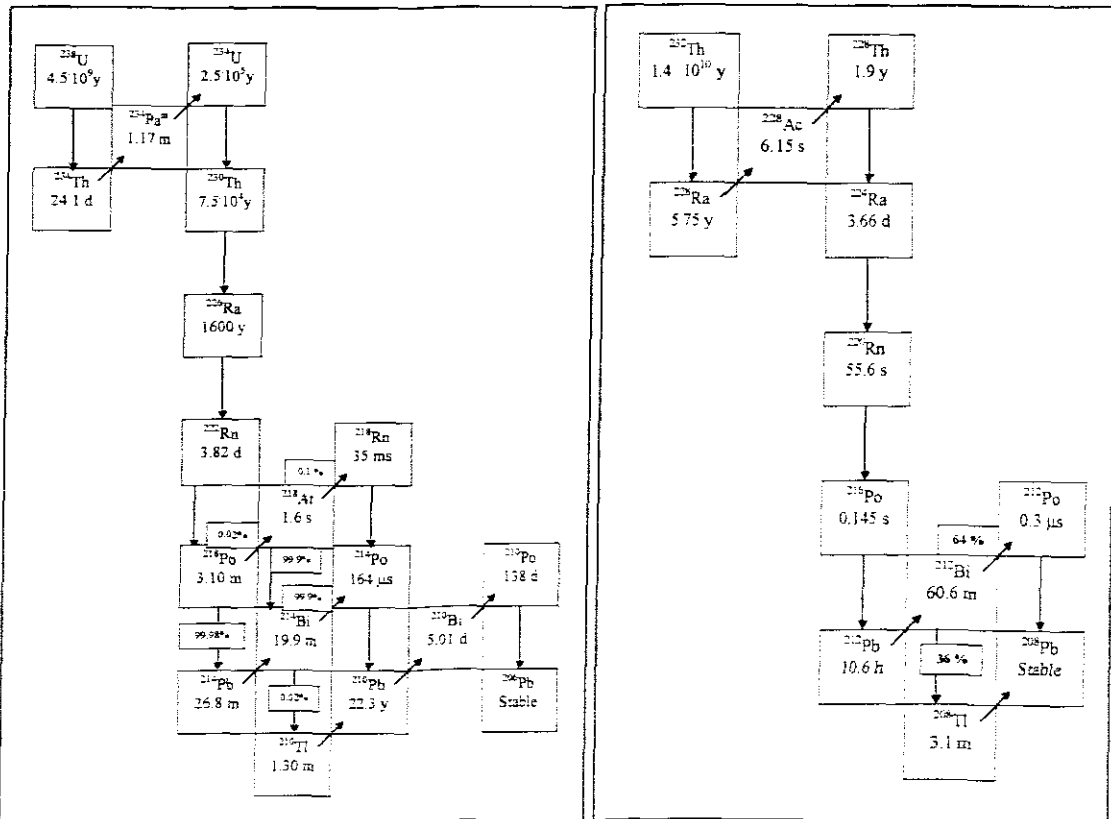


**Figure 2-11: A graphical illustration of the uranium and thorium series. Radionuclides  $^{226}\text{Ra}$ ,  $^{214}\text{Pb}$ , and  $^{214}\text{Bi}$  are the  $\gamma$ -ray emitters in the uranium series. In the thorium series the  $\gamma$ -ray emitters are  $^{228}\text{Ac}$ ,  $^{212}\text{Pb}$ , and  $^{208}\text{Tl}$ . (Adapted from [Mod05]).**

## 2.2.2 Pathways of radionuclides in the environment

Various radioactive materials get released into the environment from activities such as the generation of electricity, the applications of radionuclides in industry, technology, science, medicine, consumer products, and the tests of nuclear weapons [Tyk95]. These materials usually follow two general categories of environmental transport pathways, namely (1) transport and entry of radionuclides into the foodstuffs through ground and surface waters (Figure 2-12), and (2) radionuclides introduced into the environment via the atmosphere (Figure 2-13) [Tyk95]. For the purposes of this study, a simplified illustration of the pathway of interest is shown in Figure 2-14. The assessment of the impact of the radionuclides in the environment according to their transport pathways follows the major steps shown in Figure 2-15.

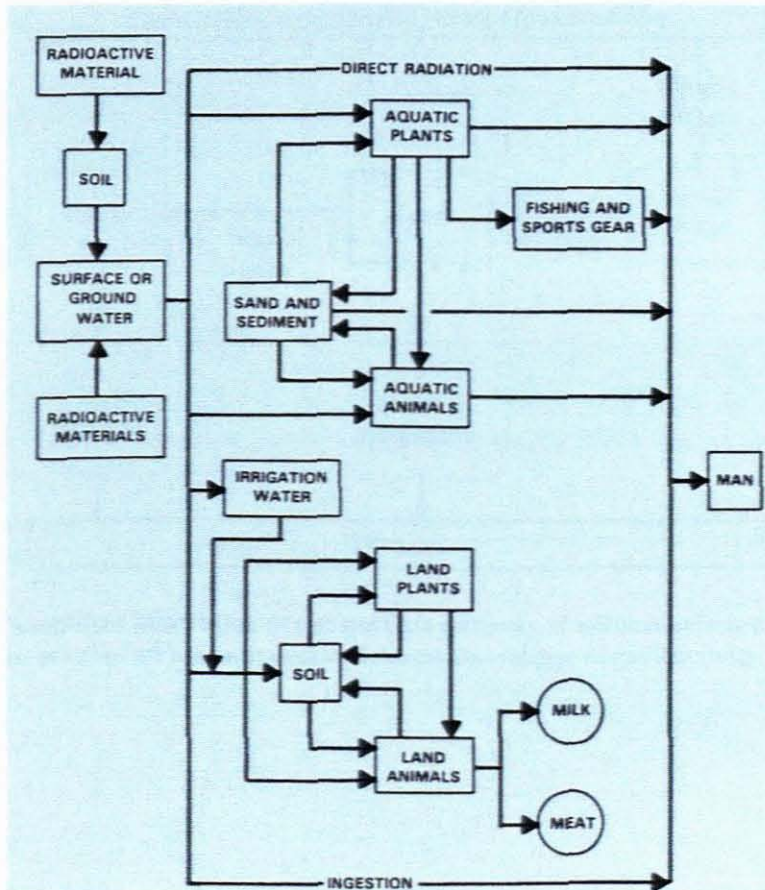


Figure 2-12: A diagram illustrating the pathways to man, followed by radioactive materials released to surface and ground water. (Adapted from [Kat84]).

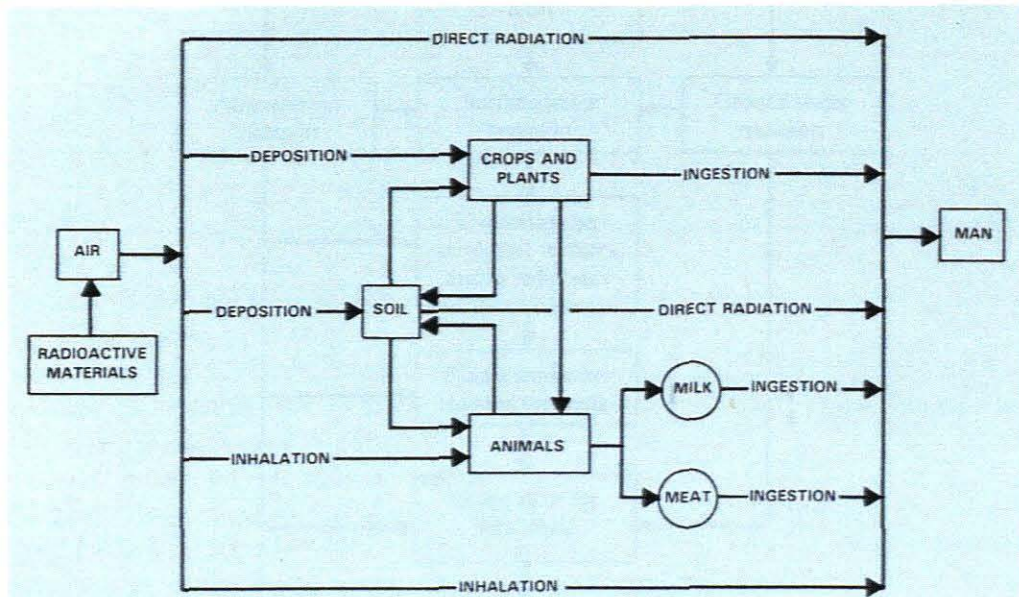


Figure 2-13: A diagram illustrating the pathways to man, followed by radioactive materials released through air. (Adapted from [Kat84])

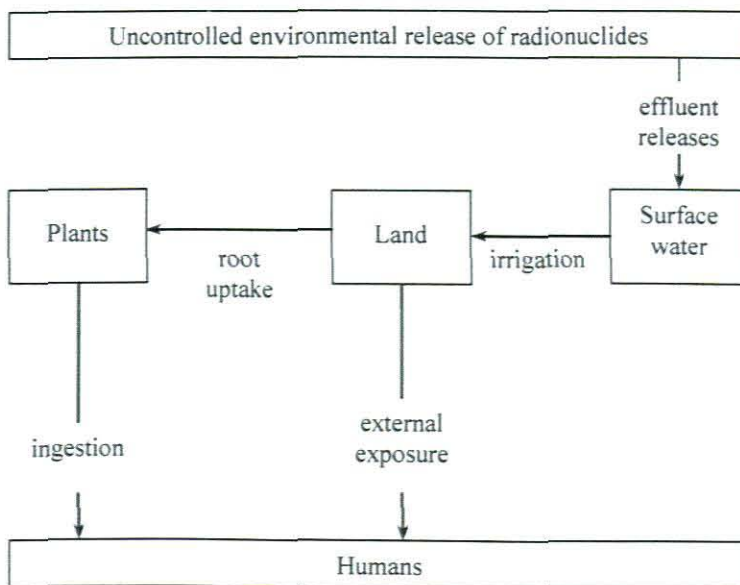
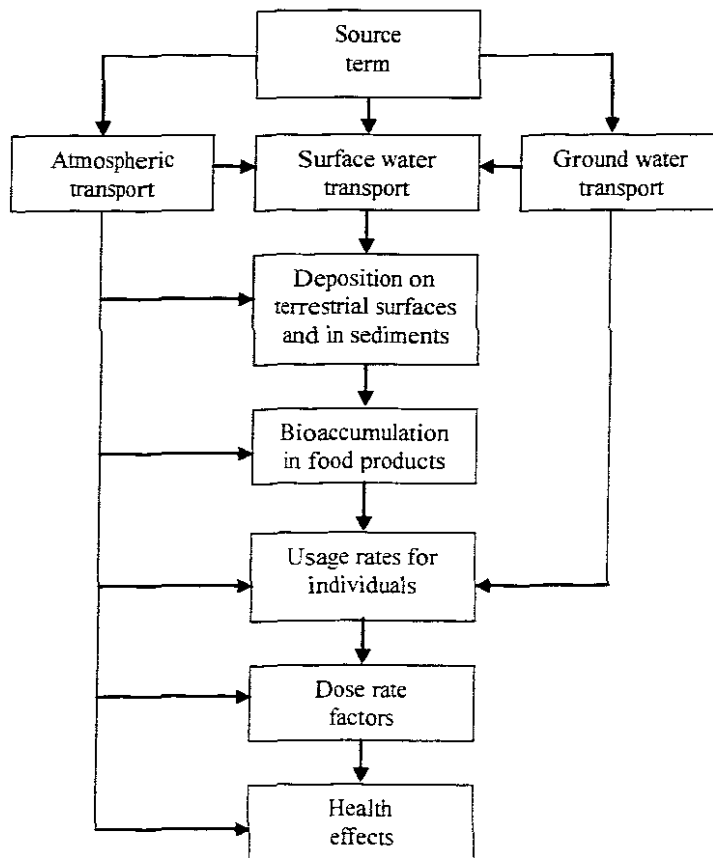


Figure 2-14: A simplified illustration of one possible pathway of effluent-released radionuclides to humans in the event of an uncontrolled environmental release of radioactivity. (Adapted from [Sed03].)





**Figure 2-15: A diagram illustrating the pathways down to the resulting health effects, followed by radioactive sources released into the environment (Adapted from [Tyk95])**

### 2.2.3 *In-situ* radiometric mapping

Over time, the successful use of *in-situ*  $\gamma$ -ray spectrometry for rapid and accurate assessment of radionuclides in the environment has been witnessed [Map04]. Along with airborne  $\gamma$ -ray spectrometry, the *in-situ* technique has been shown to provide rapid and spatially representative estimates of environmental radioactivity across a range of landscapes [Tyl04].

The technique of *in-situ* radiometric mapping is defined as the practice of scanning a radiation sensor over a surface suspected to contain radioactive materials, such as the ground, so that spatial variations of the radiation field may be measured [Jos98]. In Section 2.2.5 is given further definition of this technique used in this study.

## 2.2.4 Human exposure to environmental radiation

In Figure 2-16 is shown a graphical illustration of the average contributions made by natural and anthropogenic radiation sources to the total effective radiation dose to the population. The total effective radiation dose to the population is 3.6 mSv per person per year [vRo04]. According to the chart, approximately 15% of this is contributed by medical radiation, 84% by natural background, and less than 1% by the nuclear industry [vRo04].

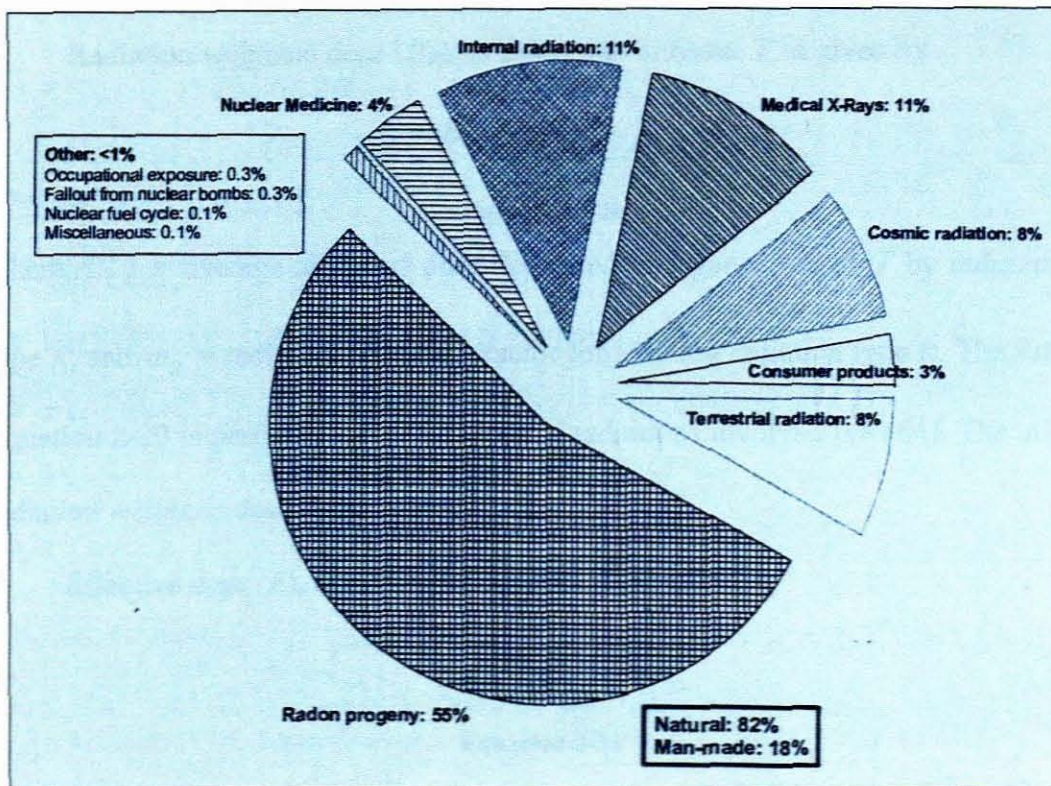


Figure 2-16: Pie chart showing the average contributions made by natural and anthropogenic radiation sources to the total effective radiation dose to the population. (Adapted from [vRo04]).

Radiological protection seeks to provide a suitable standard of protection for humanity and the ecosystem with no excessive limit put on the beneficial actions giving rise to radiation exposure. Dosimetric quantities are used to assess (or quantify) the radiation exposures of humans as well as other organisms [vRo04]. According to the 2005 recommendations of the *International Commission on Radiological*

Protection (ICRP), the quantities mentioned include *absorbed dose*, *radiation weighted dose*, and *effective dose*.

Absorbed dose ( $D$ ) is the quotient of mean energy,  $d\bar{E}$ , imparted by ionizing radiation in a volume element and the mass  $dm$  of the matter in that element [vRo04]. Therefore,  $D = d\bar{E}/dm$ , and has the SI unit  $\text{J}\cdot\text{kg}^{-1}$ , called the *gray* (Gy). In practice, the absorbed dose values are averaged over larger tissue (or organ) volumes, based on the *Linear, no-Threshold* (LNT) hypothesis, which assumes a linear dose-response relationship with no threshold [vRo04].

Radiation weighted dose ( $H_T$ ), in any organ or tissue  $T$ , is given by

$$H_T = \sum_R \omega_R D_{T,R}$$

**Equation 2-20**

where  $D_{T,R}$  = average absorbed dose deposited in organ or tissue  $T$  by radiation of type  $R$ , and  $\omega_R$  = radiation weighting factor for ionizing radiation type  $R$ . The sum of Equation 2-20 is performed over all types of radiations involved [vRo04]. The unit of radiation weighted dose is the *sievert* (Sv).

Effective dose ( $E$ ), in any organ or tissue  $T$ , is given by

$$E = \sum_T \omega_T \sum_R \omega_R D_{T,R}$$

**Equation 2-21**

where  $\omega_T$  = tissue weighting factor for tissue or organ  $T$ . The unit of the effective dose is also the *sievert* (Sv). An important consideration is that effective dose is used for regulatory purposes, and not for assessing risks of stochastic effects in retrospective situations of exposures in identified individuals, nor in epidemiological evaluations of human exposure. Effective dose is a non-measurable quantity, which is estimated by applying *conversion coefficients* that relate the effective dose of a person to other measurable quantities, e.g. air kerma or particle fluence in case of external

exposure, or activity concentrations etc. in case of [both] external and internal exposure [vRo04].

Radiation weighting factors relate to the characteristics of the type and energy of the ionizing radiation incident on the human body (or emitted by a source within the body). In Table 2-4 is given the list of radiation weighting factors for some of the radiation types, as they are used in radiological protection.

**Table 2-4: A list of radiation weighting factors for different radiation types. (Adapted from [vRo04])**

Radiation type	Radiation weighting factor
Photons	1
Electrons and muons	1
Protons	2
Alpha particles, fission fragments, heavy nuclei	20

Tissue weighting factors relate to cancer incidence data, where account is taken of the lethality rate, the years of life lost, and a weighted contribution from the nonfatal cancers and from hereditary disorders [vRo04]. A list of values of tissue weighting factors [that are normalized to give a total of 1] for some tissue is given in Table 2-5. The values listed are averaged over both genders and all ages.

**Table 2-5: A list of tissue weighting factors for different tissues. (Adapted from [vRo04])**

Tissue	$\omega_T$	$\sum_T \omega_T$
Bone marrow, Breast, Colon, Lung, Stomach	0.12	0.60
Bladder, Oesophagus, Gonads, Liver, Thyroid	0.05	0.25
Bone surface, Brain, Kidneys, Salivary glands, Skin	0.01	0.05

Radiological protection seeks to control exposures to low radiation doses that give rise to stochastic<sup>7</sup> effects, as well as to prevent exposures that give rise to

<sup>7</sup> Stochastic effects are health effects that occur randomly and for which the probability of the effect occurring, rather than its severity, is assumed to be a linear function of dose without threshold [vRo04].

deterministic<sup>8</sup> effects [vRo04]. The dosimetric quantities that are employed to accomplish this are defined by the ICRP and the ICRU (*International Commission on Radiation Units and Measurement*). The quantities introduced by the ICRU for area and individual monitoring of radiation sources external to the body are collectively called Operational Quantities. *Ambient dose equivalent* and *directional dose equivalent* are ICRU quantities used for monitoring.

To control stochastic risk, the *annual effective dose* is assessed as the sum of the effective dose from external exposure in that year and the *committed effective dose* from intakes of radionuclides in that year. Using Operational Quantities, the effective dose,  $E$ , is estimated by

$$E = H_p(10) + \sum_j [e_{j,\text{inh}}(50)I_{j,\text{inh}}] + \sum_j [e_{j,\text{ing}}(50)I_{j,\text{ing}}]$$

**Equation 2-22**

where

$H_p(10)$  = personal dose equivalent resulting from exposures to external radiation fields,

$e_{j,\text{inh}}(50)$  = committed effective dose conversion coefficient for activity intakes via inhalation of radionuclide  $j$ ,

$I_{j,\text{inh}}$  = activity intake of radionuclide  $j$  by inhalation,

$e_{j,\text{ing}}(50)$  = committed effective dose conversion coefficient for activity intakes via ingestion of radionuclide  $j$ , and

$I_{j,\text{ing}}$  = activity intake of radionuclide  $j$  by ingestion.

---

<sup>8</sup> Deterministic effects are health effects, the severity of which varies with the dose and for which a threshold is believed to exist [vRo04].

The commitment period of 50 years is a rounded value that relates to the life expectancy of a young person entering the workforce [vRo04]. The dose limit is 20 mSv per year and 1 mSv per year for radiation workers and the public, respectively.

To control *tissue reactions*, classified as deterministic effects, the spatial and temporal distributions of absorbed dose have to be qualitatively judged since tissue reactions depend heavily on them. On the whole, apart from some exposures of medical patients and some serious emergency situations that have to be managed separately, the occurrence of most, and probably all, tissue reactions will be avoided by the control of stochastic effects [vRo04].

Naturally-occurring radionuclides are by far the largest contributor to radiation doses received by human beings [Tyk95]. This serves as a good reference with which evaluation of the significance of human exposures to artificial  $\gamma$ -ray emitting radionuclides can be made. In Table 2-6 are shown some data acquired from the USA illustrating *absorbed dose* rate values in air resulting from a contamination by some primordial radionuclides in the soil.

**Table 2-6: Activity concentration of natural radionuclides in soil and associated absorbed dose rate in air. (Adapted from [Tyk95]).**

Radionuclide	Concentration (Bq.kg <sup>-1</sup> )		Dose Rate (nGy.h <sup>-1</sup> )	
	Average	Range	Average	Range
<sup>40</sup> K	370	100-700	15	4-29
<sup>232</sup> Th series	35	4-130	22	2-81
<sup>238</sup> U series	35	4-140		
<sup>226</sup> Ra sub-series	40	8-160	18	4-74

### 2.2.5 Measurement techniques for environmental *gamma*-radiation: *Ex-situ* vs. *in-situ gamma*-ray spectrometry

*Ex-situ* means to be “moved from its original place; excavated; removed or recovered from the sub-surface” [Www03]. *Ex-situ*  $\gamma$ -ray spectrometry refers to the

technique by which a field is surveyed for  $\gamma$ -radiation by means of taking samples and analyzing them in the laboratory, away from the field in question. As can be observed, this technique only identifies what is contained in the sampled material, such that for fields that do not have uniform radiation distributions, some hot spot areas could be missed [Can96]. It is also evident that there is a lot of labour involved in this technique.

*In-situ* means to be “in its original place; unmoved; unexcavated; remaining at the site or in the subsurface’ [Www04]. *In-situ*  $\gamma$ -ray spectrometry, or  $\gamma$ -radiation mapping, refers to the technique by which a field is surveyed for  $\gamma$ -radiation by means of scanning a detector over a surface suspected to contain radioactive materials, such as the ground, so that spatial variations of the radiation field may be measured [Jos98]. In this technique, there is a very high probability that no spot will be missed in the surveyed field, because with it even radioactivity that is buried below the surface of the soil can be detected, provided it emits penetrating high energy radiation. This technique is also able to provide results immediately with equivalent or better accuracy, and with less labour than with the *ex-situ* technique [Can96]. The following section looks at some studies that have been conducted using *in-situ*  $\gamma$ -ray spectrometry.

### ***2.3 Literature review: Some studies on in-situ $\gamma$ -ray mapping of environmental radioactivity***

A range of approaches have been used to carry out *in-situ* radiation surveys. These include motorized vehicles, manually pushed carts, remotely controlled trolleys, heavy construction equipment, and forklifts [Jos98]. In the study conducted at the ARA-23 site of the Idaho National Engineering Laboratory (INEEL), an all-terrain vehicle equipped with GPS was used [Jos98]. A light four-wheel drive vehicle

was used at Maralinga in South Australia [Lon04]. At the Miami-Erie Canal in Ohio, the INEEL Warthog excavation monitoring system was used for the survey. The latter system attaches to a standard heavy duty excavator and allows for mapping scans to be made without human entry onto the site [Jos98]. The detection systems that have been used for *in-situ* surveying also vary. The ARA-23, Maralinga, and Miami-Erie Canal studies used 1200 cm<sup>2</sup> plastic scintillators, 128 mm diameter by 1.6 mm thick NaI crystal, and six 7.5 cm × 7.5 cm thin film CaF<sub>2</sub> crystals, respectively [Jos98, Lon04].

The problems that were being tackled in these studies varied from one study to another. The ARA-23 and Miami-Erie Canal studies gave information on radioactive source distribution, location of hotspots, and the suggested mode of contaminant deposition at these sites [Jos98]. The Maralinga measurements had to ensure that no radioactive particle exceeding 100 kBq of <sup>241</sup>Am activity, and no area of 1 ha exceeding 3 kBq.m<sup>-2</sup> of <sup>241</sup>Am activity, remained in the rehabilitated area [Lon04]. Another relevant requirement in the Maralinga study was that the area had to be scanned at a demanding rate of approximately 3 ha.day<sup>-1</sup> [Lon04].

The reported performance of some of the *in-situ* systems used in various studies should be reviewed. According to [Jos98], a detector deployed from a vehicle moving at 1.5 m.s<sup>-1</sup> will collect a 1.5 m × 1.5 m grid (> 1700 points) of independent radiation field measurements at a 0.4 ha site in about 30 minutes. The ARA-23 and Miami-Erie Canal studies showed that *in-situ* mapping results a) reveal high fidelity details of the contaminant distribution that give insight into the mode of deposition, b) show the precise position and relative size of hotspots, c) give clear indications of the outer boundary of the contaminated areas, and d) provide a high level of confidence that no contamination has been “missed” because of the completeness of data coverage



[Jos98]. These studies further showed that a comparison of *in-situ* count rates to sampling activity concentration results gives a good correlation. There were, nonetheless, some significant digressions from ideal correlations in the results. The digressions have to do with the fact that *in-situ* detectors perform average or “bulk” measurements that fail to capture detailed variations in the measured soil, whereas sampling does capture these but fails to provide full assurance for a safe extrapolation between widely spaced sampling points. The two were seen to be agreeing closely in areas where contamination was relatively uniform [Jos98].

Studies such as the ARA-23 and Miami-Erie Canal were able to make a conclusion that continuing research on quantitative analysis methods could lead to more rigorous use of *in-situ* radiation mapping data [Jos98]. As far as the Maralinga study was concerned, recent advances in technology, particularly in the areas of electrical cooling of detectors, heads-up displays, global positioning systems and integrated electronics could be incorporated into future designs [of *in-situ* radiation mapping equipment] to provide more refined and effective systems [Lon04].

## CHAPTER 3 METHODOLOGY

In this chapter the methodology used to acquire the data used in this study is discussed. An outline is given of the *in-situ* procedure (3.2) by looking at an overview of the MEDUSA system (3.2.1) as well as the February and July 2005 surveys (3.2.2), the *ex-situ* procedure (3.3) looks at an overview of the *iThemba LABS* HPGe detector system (3.3.1) and the sample collection, preparation, and measurements (3.3.2).

### 3.1 Experiments

Two field trips were undertaken within the duration of this study. Both trips were taken around the grounds on the site of *iThemba LABS* (*iTL*) as shown in Figure 1-4. Each trip entailed a thorough survey of most of the accessible areas on the grounds by, scanning over them with a  $\gamma$ -ray detector, taking some samples, and making radiometric measurements. The techniques used to acquire data are called (1) *in-situ*, and (2) *ex-situ*,  $\gamma$ -ray spectrometry.

### 3.2 In-situ procedure

A motorized [4x4] vehicle was used for *in-situ* surveys that were conducted in this study. The vehicle gave easier mobility over the rough (and sometimes sandy) surface on the grounds. On the vehicle was appropriately set up the detection system called *Multi-Element Detector for Underwater Sediment Activity* or simply *MEDUSA*.

#### 3.2.1 Overview of the *iThemba LABS* MEDUSA system

As part of their aim to participate in multi-disciplinary research projects involving the transfer of nuclear physics techniques to disciplines in geosciences, the Nuclear Geophysics Division (NGD) of the Nuclear Accelerator Institute (abbreviated

KVI, which stands for Kernfysisch Versneller Instituut) at the University of Groningen (RuG) in the Netherlands then designed, built, tested and used the MEDUSA system (MS) for doing *in-situ* measurements of environmental radioactivity [deM97, Lim00]. They patented the MS internationally and gave ownership of the patent to MEDUSA Explorations BV, their spin-off company [New04b]. NGD worked in collaboration with the British Geological Survey (BGS) to develop the MS. The MS contains a number of modified components of an earlier “EEL” system [Jon94], but has an added improvement of roughly an order of magnitude on sensitivity to  $^{238}\text{U}$  and  $^{232}\text{Th}$  measurements than the “EEL” system [Lim00, deM97].

The MS, as the name suggests, was invented with an initial purpose of mapping out the distribution of the natural radionuclides  $^{40}\text{K}$ ,  $^{238}\text{U}$ , and  $^{232}\text{Th}$  underwater only. It, however, found useful application in performing the same task on land as well [Lim00, Mod05]. Moreover, the system would not only serve as a rather more efficient *in-situ* detector of natural radioactivity, but it has developed into a collection of hardware and software apparatus that are used to (1) measure, (2) process, and (3) translate into sediment composition the data for natural radioactivity (see Figure 3-1) [Lim00].

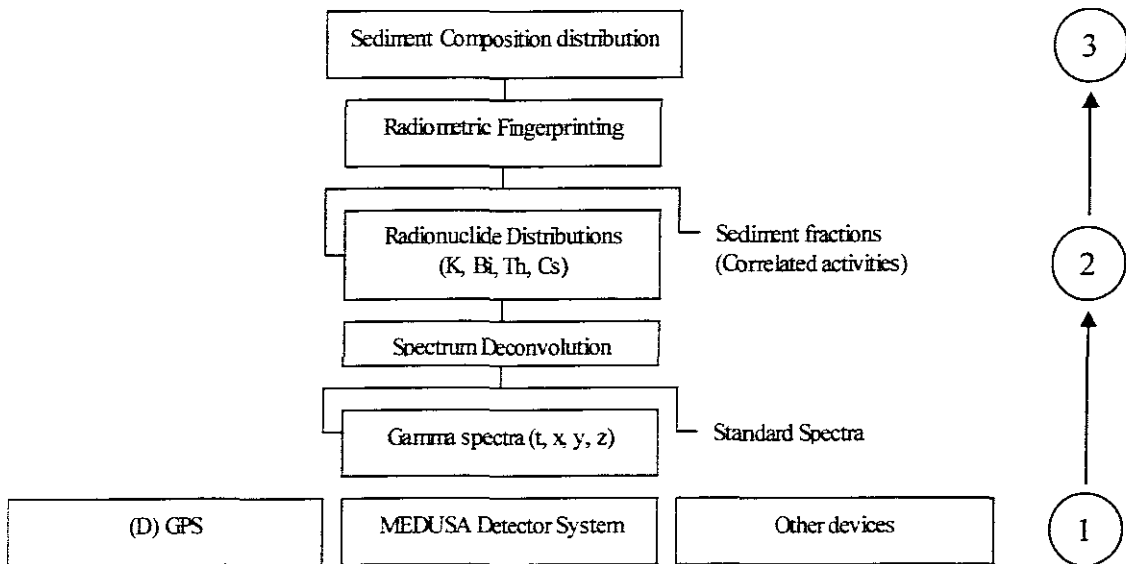


**Figure 3-1: A schematic diagram showing the derivation of sediment composition from  $\gamma$ -ray measurements with the MEDUSA system. Radiometric fingerprinting is a technique by which the MEDUSA system is used to identify a sediment's "fingerprint", that is, a signature vector that differentiates the sediment in terms of the  $^{40}\text{K}$ ,  $^{238}\text{U}$ , and  $^{232}\text{Th}$  concentrations [Lim00]. (Adapted from [Lim00].)**

The MS is divided into mainly two parts. The first, shown in Figure 3-2, is encased in an aluminium/stainless steel tube and it consists of the detector crystal (labeled CsI(Na) in the diagram), photomultiplier tube (PMT), high-voltage generator (HVG), spectroscopic amplifier (Amp), temperature sensor (AD590), microphone, and pressure sensor. The iThemba LABS MEDUSA system, as illustrated in Figure 3-2, uses the cesium iodide doped with sodium (CsI(Na)) detection crystal and not the bismuth germanium oxide (or BGO) as per the original preference in the patent of the MS (see Appendix 1 for a detailed description of MS components according to the patent)<sup>9</sup>. The second part of the MS consists of a detector telemetry board (see Figure 3-2), and an interface panel/power supply (labeled Aladin interface box in Figure 3-4). The latter is equipped with a detector power supply board, and a probe electronics board (see Figure 3-3a-c for photos of some of the MS components encased in the aluminium/stainless steel tube).

<sup>9</sup> The change was introduced after observations were made that the CsI(Na) crystal: (1) gives better results because of its high energy resolution when compared to BGO, and (2) has a light output that doesn't drop off severely with increasing temperature, as does that of BGO (see Figure 2-6) [Mod05].

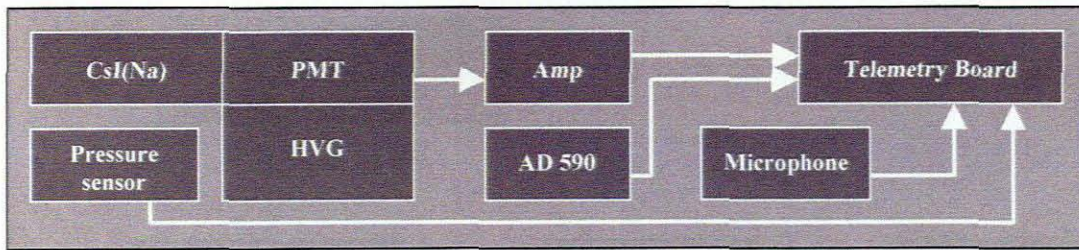


Figure 3-2: A schematic diagram showing the components of the encased probe part of the MEDUSA system.

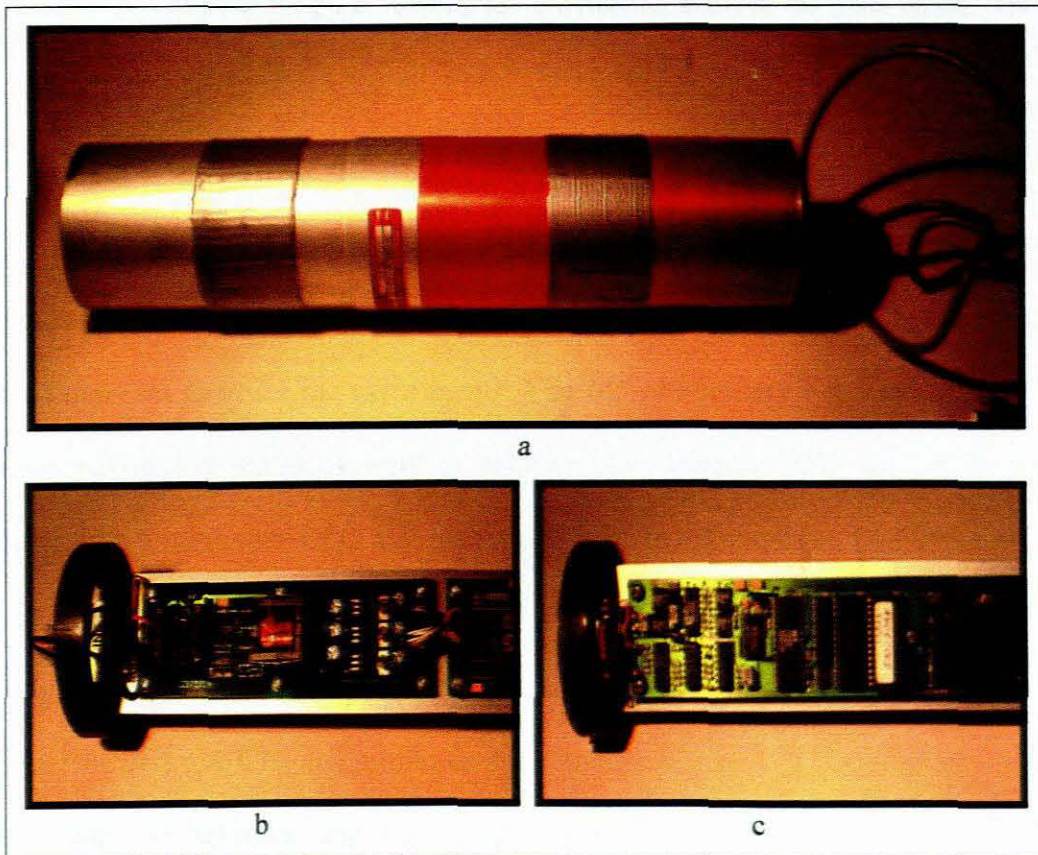


Figure 3-3: Digital photos showing physical features of some of the units encased in the aluminium/stainless steel tube, namely, (a) the CsI(Na) crystal, (b) the detector power supply board, and (c) the probe electronics board.

A complete experimental setup of the *i*TL MEDUSA system is illustrated in the diagram in Figure 3-4. The setup consists of the probe (the aluminium/stainless steel encased part), the Aladin interface box, the laptop computer, and the GPS (Global Positioning System) device (see also photo in Figure 3-5).

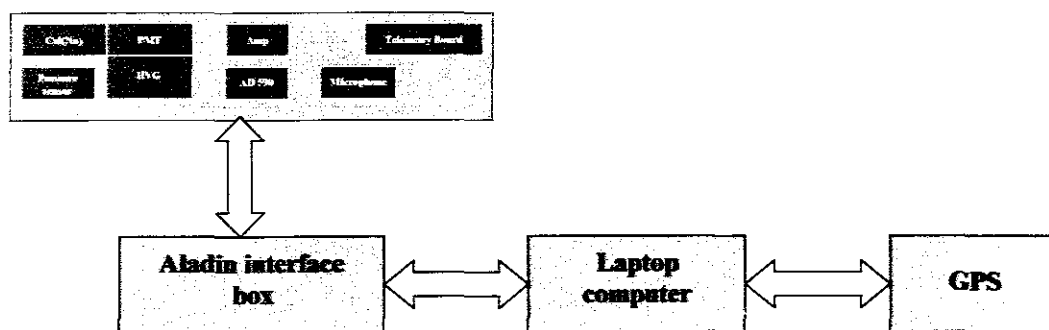


Figure 3-4: A schematic diagram showing the interlinking between the units of the iThemba LABS MEDUSA system.

### 3.2.2 February and July 2005 surveys

After the official weather forecasts had been acquired for the potential days of conducting experiments, the 23<sup>rd</sup> and the 14<sup>th</sup> of February and July 2005, respectively, were finally set apart for the experiments. The 24<sup>th</sup> of February was used as well. The forecasted weather statistics were as follows: 23 February 2005 was to be partly cloudy with a minimum 18°C and maximum 27°C in temperature, 24 February 2005 to be partly cloudy with 30% chances of rain by evening and minimum 18°C and maximum 24°C in temperature, and 14 July 2005 to be partly cloudy with few thundershowers (30°C) and a minimum 14°C and maximum 17°C in temperature.

Both the February and July 2005 surveys took approximately six hours to finish, per individual day used. The required apparatus were assembled and prepared for use each day before 10h00 in the morning. At 10h00 the logging of the official data commenced for each of the three days used. By this time the MS (see Figure 3-5) had to have been powered and tested in the ERL, a process known as the bench test, to ensure that it functioned properly before its deployment as shown in the photos of Figure 3-6 below. The battery (see Figure 3-7) had to have been charged up to full capacity and ready for use on the field.

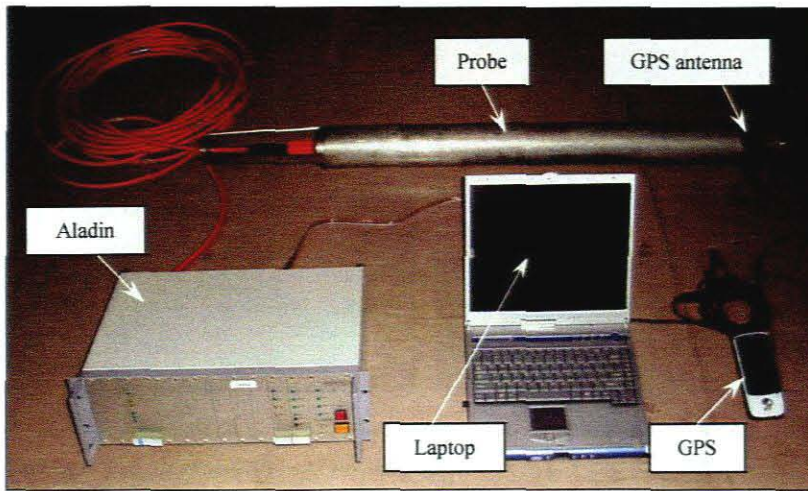


Figure 3-5: A photograph showing the physical features of the interlinking between units of the MEDUSA system.

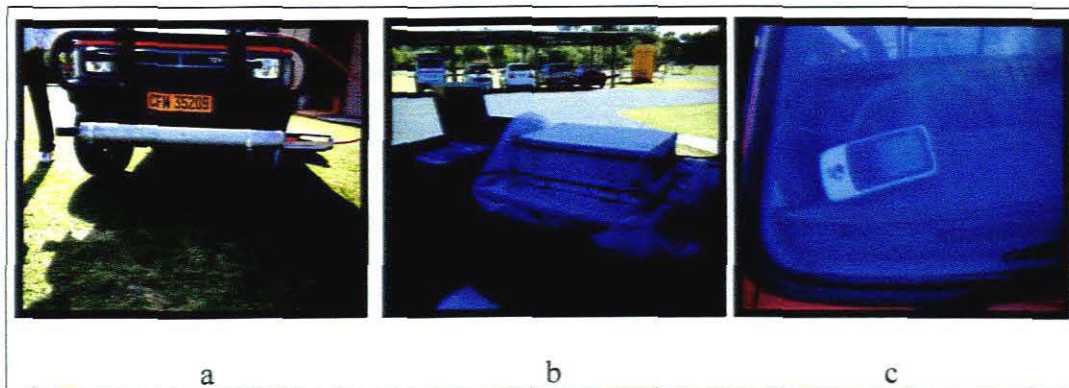


Figure 3-6: Photographs showing the setup on the 4x4 of the (a) probe, (b) Aladin box and laptop computer, and (c) GPS receiver.

The job of deploying the MS required a team of at least three people. In Figure 3-6 are shown some photos of the deployed MS of *iTL*. The probe was rested horizontally, approximately 50 cm above the ground, on brackets mounted on the front of the 4x4 vehicle (photo a). The laptop computer and the Aladin interface box were placed securely on the back of the vehicle, with ropes holding them in the secure position (photo b). The GPS device was kept in the interior of the vehicle (photo c), and was operated with its external antenna mounted directly above the detection crystal in the probe (see Figure 3-7b). The battery was used to supply the MS with required voltage via the DC/AC power inverter (Figure 3-7a). The MS was powered up, and then the MDL software program was started for data logging.

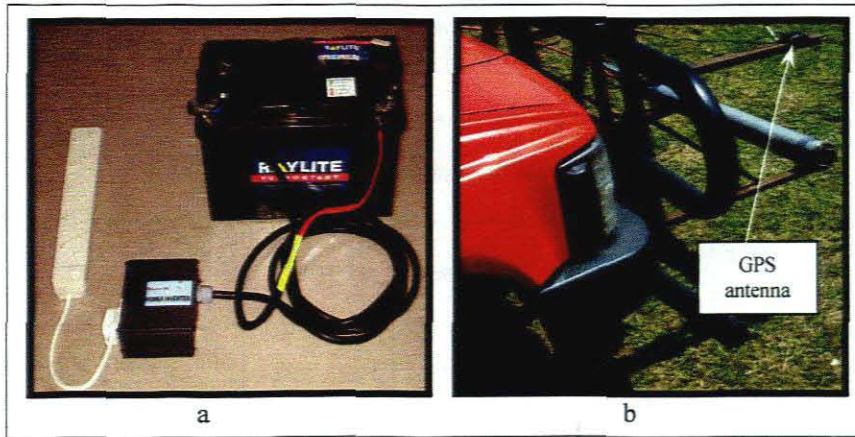


Figure 3-7: Photographs showing the (a) battery used to supply the MS with required voltage via the DC/AC power inverter, and (b) external GPS antenna mounted directly above the detection crystal in the probe.

The traversing of the *i*TL site's terrain followed a similar pattern in all the three days of surveying. The 4x4 vehicle, moving at approximately  $2 \text{ m.s}^{-1}$ , was first driven over the accessible tar road sections of the *i*TL site and data were logged for these. After the "road" sections were completed, the first "off-road" sections to be scanned were those along the perimeter of the *i*TL site. Further off-road scans then followed over the rest of the accessible portions of the site. The logging of the data was constantly being monitored via the MDL software program installed on the laptop computer. MDL allows up-to-date information on the incoming detector-plus-GPS readings to be viewed on the display. This information includes the following: the MEDUSA detection count rate, acquired  $\gamma$ -ray spectra, and a GPS spatial map.

At certain locations where enhanced count rate levels could be observed, there were done some stationary MS measurements. Other stationary MS measurements were done at the so-called calibration spots. In Table 3-1 are shown the locations where stationary MS measurements were made during the February and July 2005 surveys. Photos of some of the locations are shown in Figure 3-8.



**Table 3-1: Locations where stationary MEDUSA measurements were made during the February and July 2005 surveys. The numbers in brackets in the third column indicate the duration of each measurement (minutes).**

	Location	Location description	GPS Coordinates			Average count rate (counts/s)	MDL Files	Sampling
			Latitude	Longitude	Altitude (m)			
February 2005	Calibration Spot CS1	open field across road opposite J-Block (20)	34°01.436'S	18°43.036'E	12.5	111.0	ilts0205c.m17	5 soil
	Hot Spot HS1	next to fence across road opposite hospital (49)	34°01.396'S	18°43.160'E	15.4	994.8	ilts0205c.m08, ...m09, ...m10	5 soil & 1 grass
	Hot Spot HS2	next to hospital parallel road to MRG (10)	34°01.509'S	18°43.150'E	13.9	1225.6	ilts0205c.m13	1 soil
	Hot Spot HS3	gully of Dam 1 next to S-Block (49)	34°01.557'S	18°43.932'E	8.6	4843.8	itls0205.m11, ...m12, ilts0205c.m15	1 soil
July 2005	Calibration Spot NCS1	next to fence behind MRG building & bushes (20)	34°01.517'S	18°43.414'E	12.5	113.3	itl140705.m29, ...m30	5 soil
	Hot Spot NHS4	in front of Cyclotron building by J-Block flat (20)	34°01.457'S	18°43.066'E	16.3	959.5	itl140705.m07, ...m08	1 soil & 1 grass
	Hot Spot NHS5	next to S-Block building in front of parking lot (5)	34°01.559'S	18°43.985'E	12.5	719.5	itl140705.m17	1 soil
	MRG hotspot	lawn in front of MRG building facing hospital (5)	34°01.565'S	18°43.240'E	9.7	419.7	itl140705.m27	none
	Near-Dam 1 count	edge of Dam 1 facing J-Block & workshop buildings (5)	34°01.548'S	18°43.934'E	14.4	500.2	itl140705.m19	none
	RPG pipe count	section of pipe between cooling towers & Dam 1 (5)	34°01.540'S	18°43.960'E	13.7	1119.2	itl140705.m22	none
	Dipole magnet	in front of J-Block towards Dam 1 (5)	34°01.470'S	18°43.973'E	11.6	560.5	itl140705.m12	none
	Calibration Spot CS1	open field across road opposite J-Block (10)	34°01.436'S	18°43.036'E	12.5	97.8	itl140705.m33	none
	Hot Spot HS1	next to fence across road opposite hospital (10)	34°01.396'S	18°43.160'E	15.4	676.4	itl140705.m10	none
	Hot Spot HS2	next to hospital parallel road to MRG (5)	34°01.509'S	18°43.150'E	13.9	850.8	itl140705.m24	none
Hot Spot HS3	gully of Dam 1 next to S-Block (26)	34°01.557'S	18°43.932'E	8.6	2485.8	itl140705.m14, ...m15	none	

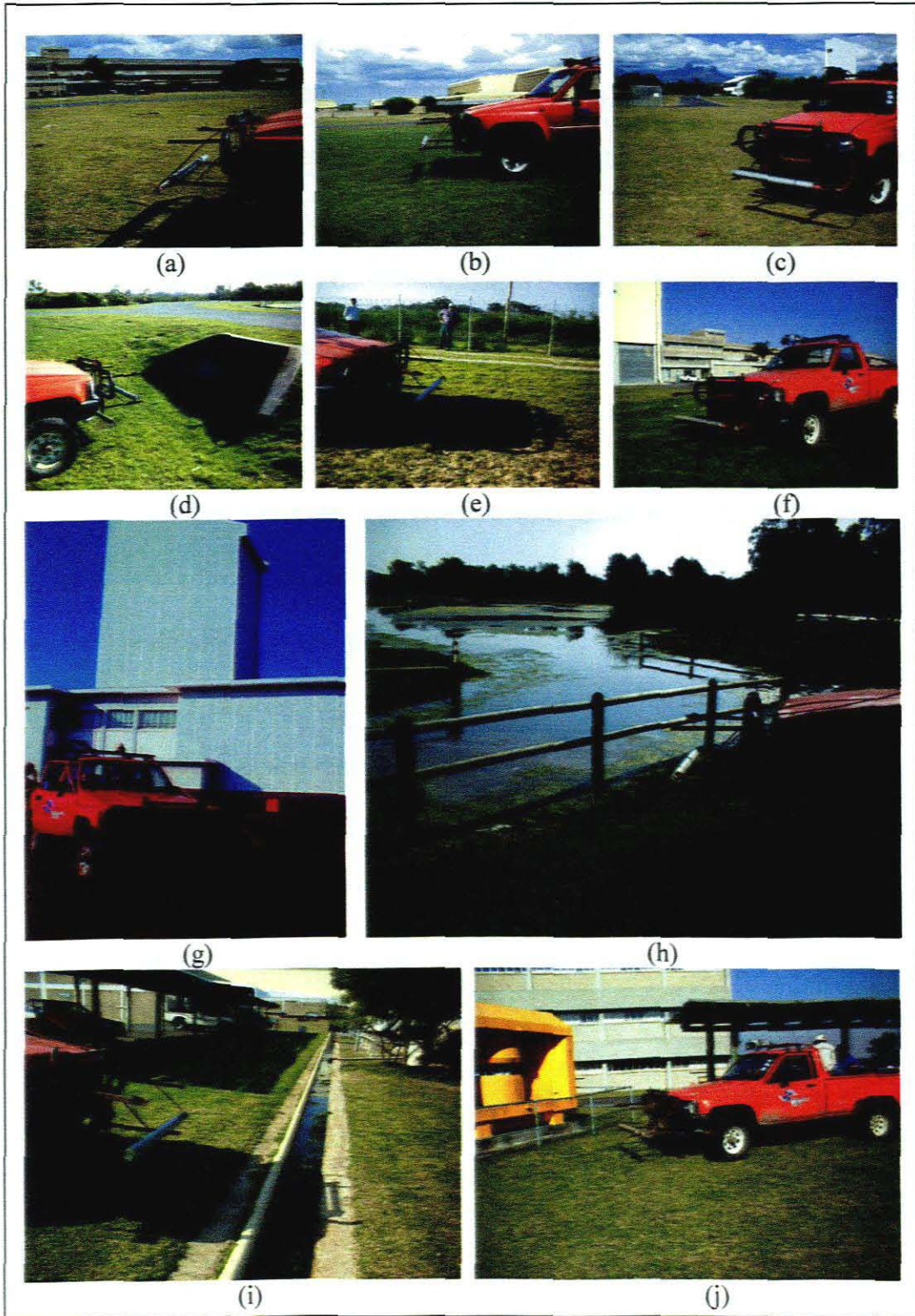


Figure 3-8: Photographs showing locations where stationary measurements were made. (a) Calibration Spot CS1, (b) Hot Spot HS1, (c) Hot Spot HS2, (d) Hot Spot HS3, (e) Calibration Spot NCS1, (f) Hot Spot NHS4 (g) MRG hotspot, (h) Near-Dam 1 count, (i) RPG pipe count, (j) Dipole magnet as listed in Table 3-1. From the photographs it can be seen that the geometry of the stationary locations was not always flatbed geometry, e.g. location (j), the dipole magnet.

### 3.3 Ex-situ procedure

Samples of soil, and sometimes grass, were taken at certain spots of interest on the surveyed field. These samples were transported in polythene bags from the field into the ERL. The ERL is equipped with a high-resolution type detector called a *High Purity Germanium* (or *HPGe*) detector, which was used to measure the radioactivity of the collected samples [Mod05].

#### 3.3.1 Overview of the ERL HPGe detector system

A lead-shielded HPGe detector, coupled with the appropriate electronics in the ERL, is set up as depicted by the schematic diagram in Figure 3-9 below. The diagram shows the interlinking between the main parts of the ERL HPGe system. The ERL HPGe detector is a closed-end coaxial Canberra p-type model GC4520 with built-in pre-amplifier. It has a crystal diameter of 62.5 mm and a length of 59.0 mm. Like all germanium detectors, the ERL HPGe detector is operated at liquid nitrogen ( $LN_2$ ) temperatures because of its small band gap [Leo87]. The detection crystal is supported on a mechanically rigid cryostat with a  $LN_2$  dewar attached to it (see Figure 3-11). The ERL HPGe  $LN_2$  dewar is routinely filled with the liquid once a week.

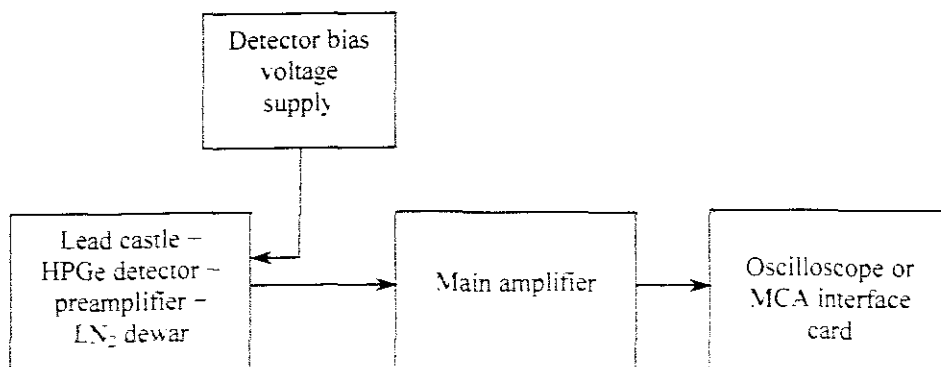


Figure 3-9: Schematic diagram showing how the components of the ERL HPGe system interlink. (Adapted from [Mal01]).

The ERL HPGe detector and the preamplifier are enclosed in the lead castle. The lead castle has appropriately shaped lead bricks (~100 mm thick) stacked onto each other for the purpose of shielding background radiation (see Figure 3-10). The lead castle also has a copper lining (~2 mm thick) in its interior in order to absorb X-rays emanating from the lead [Mal01, Mod05].

A bias voltage of 3500 V is applied across the detector junction to provide the electric field required to sweep up the charge produced in the detector crystal. The charge is collected by the preamplifier, and then the amplifier. At the amplifier, the pulse shape is changed and increased in size [Mal01]. From the amplifier, the pulses are collected and sorted by the multi-channel analyzer (MCA). The MCA then stores the sorted data, displays the data, does the pre-analysis and prepares the results for output [Mal01]. The sorted data are first digitized, and then displayed as counts vs. channel number. The ERL MCA software is called *OxfordWin-MCA* and it is installed on a desktop PC inside the ERL.

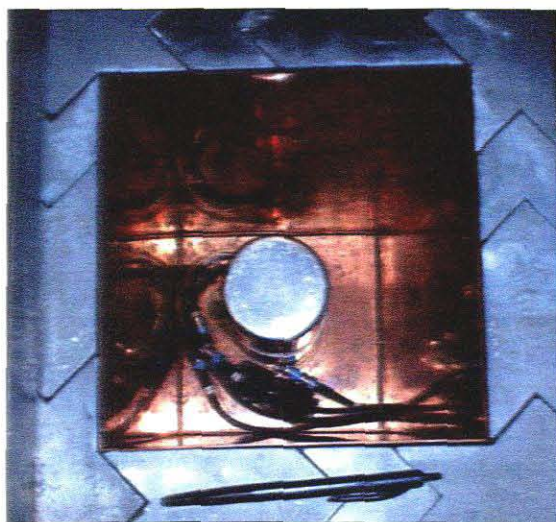


Figure 3-10: Photograph showing a top view of the ERL HPGe setup located in the ERL.

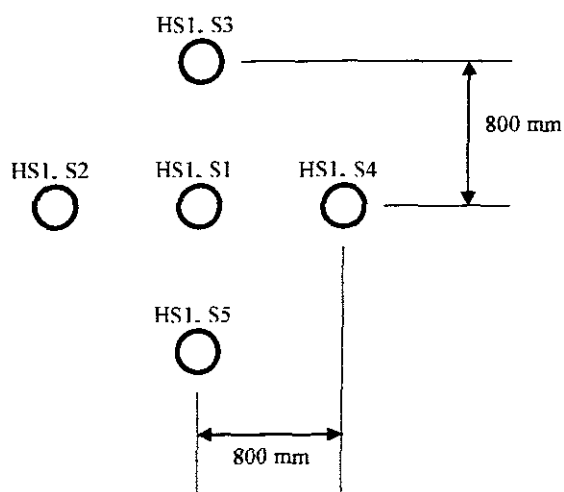


Figure 3-11: Photograph showing the lead castle of the ERL HPGe system, with the LN<sub>2</sub> dewar protruding underneath.

### 3.3.2 Sample collection, preparation, and measurements

Certain spots of interest were sampled during the surveys. Amongst these spots were those that measured higher count rates with the MEDUSA system (MS), the so-called *hotspots*, as well as those spots chosen for MS calibration, the so-called *calibration spots*. In Table 3-1 is indicated the sampling done at the different stationary measurement locations identified. At the locations where 5 samples were taken, the method of sampling used is illustrated by the diagram in Figure 3-12 below. The main idea behind the sampling strategy used was to get as much representativity [of the spot] as possible, from the samples collected. The types of samples collected were either soil (dug up to ~10 cm of depth) or grass, but most were soil. The samples

were packed into Ziploc® polythene bags, and transported to the ERL for preparation and measurement (see Table 3-2 for information about the samples collected at spots of interest).



**Figure 3-12: Schematic top-view representation of the sampling strategy used at the spots CS1, NCS1, and HSI (see Table 3-1). The circles indicate the points of sampling.**

During preparation, the soil sample was poured out of the polythene bag onto a labelled heating tray. (The tray was labelled with the name of the sample that it held). The soil and the tray were weighed on a Sartorius scale<sup>10</sup> and thereafter the soil mass was determined by subtracting the mass of the pre-weighed tray from the combined mass of the soil-plus-tray system. (This had to be done so that the soil mass before drying could be compared to the soil mass after drying and the soil's moisture content could then be determined). The soil-plus-tray system was then put into a LABOTEC Model 276 digital oven so as to dry the soil. Mostly, the soil was heated overnight, undisturbed, at a temperature of 105°C.

After heating, the soil-plus-tray system was taken out of the oven and weighed on the scale again so as to get the mass of the soil after heating. The dried soil was

<sup>10</sup> The Sartorius BP 2100 S and EA6DCE-I models are both housed in the ERL. The maximum masses that can be loaded on these are 2100 and 6000 g, respectively. Depending on the mass to be measured, both the scales were used in this study.

then ready for sieving through the wire mesh to remove organic materials, stones, and lumps [Jos05]. If the sample was made up of hardened clay and/or had a lot of lumps and roughage, then the sample was first crushed with a rod (or pestle), before sieving. After sieving, the sample was now divided into two labelled bags with sieved soil and the unwanted remains. Both the sieved soil and the remains were weighed, separately, and then their combined mass was compared with the total soil mass measured after heating; the masses had to match. The formula for calculating moisture ( $s(\%)$ ) for the soil is given by [Jos05]

$$s(\%) = \frac{(\text{sample wet weight} - \text{sample dry weight})}{\text{sample wet weight}}$$

**Equation 3-1**

The sample bags were marked as sieved and kept for further processing. The next step was to prepare the Marinelli beaker (see Figure 3-13), which is used to contain the sample and has the feature that it is able to expose the sample optimally to the HPGe detector crystal [Mod05]. The beaker (without the lid) was first weighed on the scale to get its mass. The sieved soil was then poured into the Marinelli beaker to fill it up, with constant tapping, to a volume of 1000 cm<sup>3</sup> (1 litre), as marked on the beaker. The container and its contents were weighed again, still without any lid. From this combined mass was determined the mass of the soil by taking the difference between the combined and container masses. Dividing this mass by the volume of the soil sample (1 litre) gave the density of the soil sample.

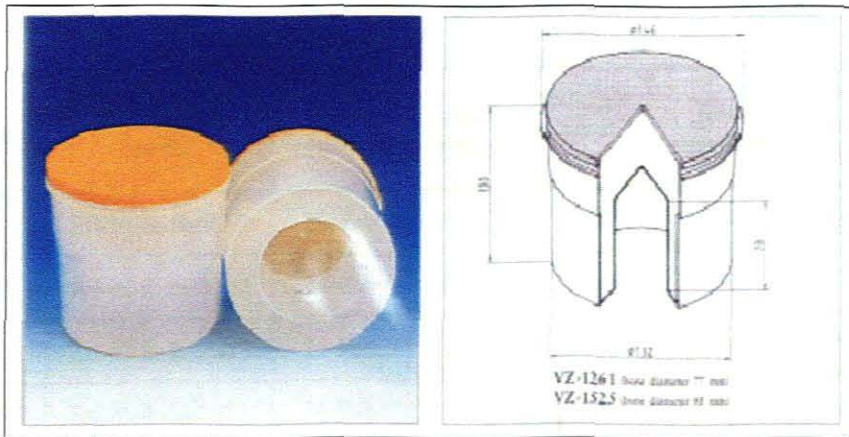


**Figure 3-13: The geometry of the Marinelli beaker used for holding environmental samples for laboratory measurements with the HPGe detector. (Manufactured by Isotrak/AEA TECHNOLOGY QSA.)**

Before the Marinelli beaker was sealed, a copper disk (~2 mm diameter [Jos05]) was used as a lid to cover the top of the soil inside the beaker. This copper lid, whose mass was pre-defined, was used as a seal to allow for secular equilibrium to occur between  $^{226}\text{Ra}$  (the parent radionuclide to radon ( $^{222}\text{Rn}$ )) and its daughter radionuclides – this done by preventing the radon gas in the uranium decay chain from escaping the soil [Jos05]. The copper lid was then sealed at the sides by lining it with a white silicone sealant (Bostik Bath type). Finally, the Marinelli beaker was sealed with its cap lined with the silicone sealant as shown in Figure 3-14. After sealing, the sample was kept in the ERL for a minimum of 21 days to allow for secular equilibrium to occur in the soil before measuring with the HPGe detector.

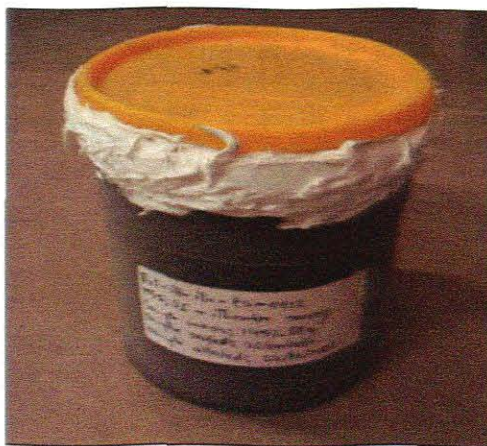


**Figure 3-14: Photograph showing the sealed soil sample in a labeled Marinelli beaker.**



**Table 3-2: Information about the samples collected at spots of interest regarding receipt, labelling, and measurement.**

	User sample code	ERL sample code	Date collected	Date sealed	Sample mass (kg)	Date measured	Preset time (hrs)	Spectrum code
February 2005	HS1, S1	Erl-itl-ih-ts-0012	24-Feb	24-Apr	1.4529	24-May	12	ihts0013
	HS1, S2	Erl-itl-ih-ts-0002	24-Feb	8-Mar	1.3064	29-Mar	10	ihts0003
	HS1, S3	Erl-itl-ih-ts-0003	24-Feb	15-Mar	1.1625	28-Apr	10	ihts0004
	HS1, S4	Erl-itl-ih-ts-0011	24-Feb	25-Apr	1.3440	23-May	12	ihts0012
	HS1, S5	Erl-itl-ih-ts-0010	24-Feb	25-Apr	1.2513	21-May	12	ihts0011
	HS1, S6	Erl-itl-ih-tg-0001	24-Feb	1-Mar	0.0794	9-Mar	5	ihtg0002
	HS2, S1	Erl-itl-ih-ts-0013	24-Feb	25-Apr	1.2815	25-May	12	ihts0014
	HS3, S1	Erl-itl-ih-ts-0009	24-Feb	25-Apr	1.0866	20-May	12	ihts0010
	CS1, S1	Erl-itl-ih-ts-0004	24-Feb	29-Mar	1.4201	29-Apr	10	ihts0005
	CS1, S2	Erl-itl-ih-ts-0005	24-Feb	29-Mar	1.3702	3-May	10	ihts0006
	CS1, S3	Erl-itl-ih-ts-0006	24-Feb	22-Apr	1.3920	17-May	12	ihts0007
	CS1, S4	Erl-itl-ih-ts-0007	24-Feb	22-Apr	1.3412	18-May	12	ihts0008
	CS1, S5	Erl-itl-ih-ts-0008	24-Feb	25-Apr	1.3203	19-May	12	ihts0009
July 2005	NCS1, S1	Erl-itl-ih-ts-0014	14-Jul	19-Jul	1.4349	11-Aug	12	ihts0015
	NCS1, S2	Erl-itl-ih-ts-0015	14-Jul	21-Jul	1.4449	12-Aug	12	ihts0016
	NCS1, S3	Erl-itl-ih-ts-0016	14-Jul	20-Jul	1.4701	15-Aug	12	ihts0017
	NCS1, S4	Erl-itl-ih-ts-0017	14-Jul	20-Jul	1.4548	16-Aug	12	ihts0018
	NCS1, S5	Erl-itl-ih-ts-0018	14-Jul	21-Jul	1.5099	17-Aug	12	ihts0019
	NHS4, S1	Erl-itl-ih-ts-0019	14-Jul	21-Jul	1.2960	18-Aug	12	ihts0020
	NHS5, S1	Erl-itl-ih-ts-0020	14-Jul	22-Jul	1.2953	19-Aug	12	ihts0021
	Ngrass3	Erl-itl-ih-tg-0021	14-Jul	22-Jul	0.1273	10-Aug	5	ihtg0003

## CHAPTER 4 DATA ANALYSIS

In this chapter are given the details on how the acquired data were analyzed in order to extract information such as the activity concentration of concerned radionuclides in this study. With this chapter is discussed the analysis of the *in-situ* and the *ex-situ* data (4.1 and 4.2, respectively), and the energy spectral analysis methods in general (4.2.1).

### 4.1 Analysis of the in-situ data

#### 4.1.1 Full-spectrum (FSA) spectral analysis method

In the FSA method, the acquired  $\gamma$ -ray spectrum is analysed by focusing on its entire shape, instead of only analyzing certain selected regions of interest, as is the case with the *windows* method of analysis [Hen01]. With FSA, the total acquired  $\gamma$ -ray spectrum is 'disintegrated' into units called *standard spectra* plus a *background spectrum*. By definition, a standard spectrum for radionuclide  $X$  is the expected response of the detector when exposed to  $1 \text{ Bq.kg}^{-1}$  activity concentration of radionuclide  $X$ , via a specific geometry [New04b]. Therefore, the sum of the standard spectra plus background spectrum (call this combination the *calculated spectrum*), multiplied by the associated activity concentrations of the featured radionuclides, equals to the acquired spectrum.

Now, let activity concentration ( $C_i$ ) be the unknown, i.e. from the acquired  $\gamma$ -ray spectrum ( $Y$ ), the sum of the standard spectra ( $X_i$ ) plus a background spectrum ( $BG$ ) has to provide values of activity concentration of the radionuclides in question. This is done by fitting the calculated spectrum to the acquired one [Hen01]. Using the chi-squared minimisation procedure ensures an optimal extraction of the activity concentration values from the acquired spectrum with

$$\chi^2 = \frac{1}{N-M} \sum_{i=1}^N \left[ Y(i) - \sum_j C_j X_j(i) - BG(i) \right]^2 / w(i)$$

Equation 4-1

where  $i$  is the channel (up to  $N$ ),  $w(i)$  is a so-called weight factor, and  $M$  represents the number of standard spectra used. Traditionally,  $w(i)$  is taken as  $Y(i)$  [Hen01].

#### 4.1.2 The actual analysis

The MEDUSA data (hereafter referred to as the data), stored in MDL files, are analysed by employing two MEDUSA software programs, namely (1) MEDUSA Data Synchronizer (MDS), and (2) MEDUSA Post Analysis (MPA). In Figure 4-1 is given a flow diagram of MEDUSA data moving from one software program to another, in different file formats, during the analysis. The flow diagram begins with the data that has been logged in and stored via the MDL program as \*.mxx files, where the xx in the file extension stands for numerical values counting as 01, for the first MDL file; 02, for the second MDL file; 03, for the third one and so on.

In its \*.mxx format, the data is in an *unsynchronized* state because of the difference in acquisition rate between that of  $\gamma$ -ray spectra data sets (every 2 seconds) and that of some auxiliary data (every second) (see Table 4-1). This requires that averaging be done over the auxiliary data sets in order to create a one-to-one correspondence between each  $\gamma$ -ray spectrum and the associated auxiliary data set. The MDS program is used to perform the latter task, which is referred to as the process of synchronization.

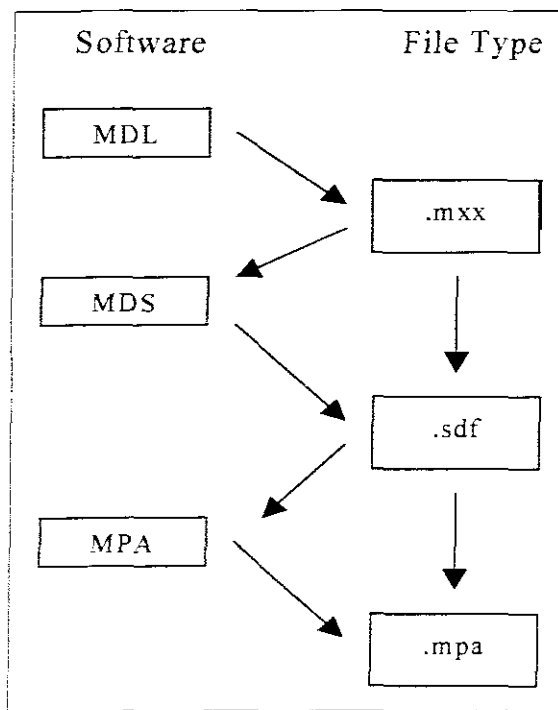


Figure 4-1: Flow diagram showing how, and in which file format, the MEDUSA-acquired data went from one software program to another during the analysis. (Adapted from [Mod05])

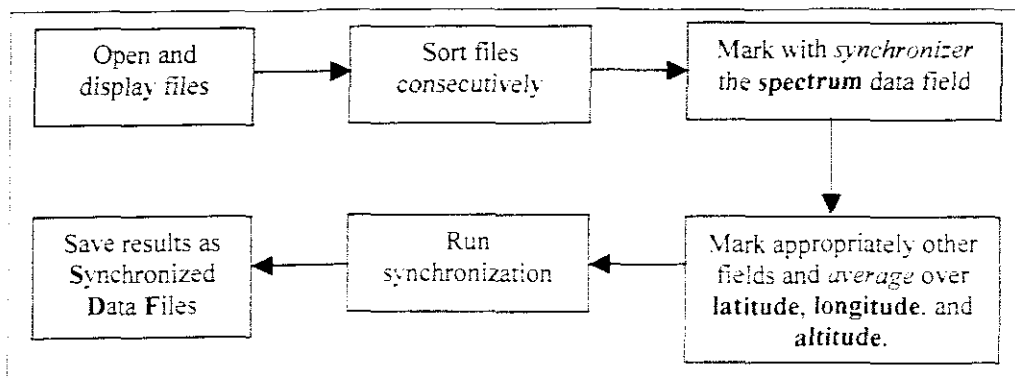


Figure 4-2: Flow diagram showing the procedure that was followed during the synchronization of the MEDUSA- acquired data of this study, using the MDS software program.

The flow diagram shown in Figure 4-2 demonstrates the steps that were followed in MDS during the synchronization of \*.mxx files for this study. The process started with every file being loaded onto MDS, and its contents displayed. The files, usually more than one, were then sorted in ascending order according to the xx values in their file extensions. At this stage the files were ready for synchronization as follows: the spectrum data field was marked with the *synchronizer* action status, while the other data fields were marked as shown in Table 4-1 (where data fields from pressure

to time were left as default)<sup>11</sup>. The synchronization was then run and the results were stored as Synchronized Data Files, in \*.sdf format, which are suitable for undergoing MPA program procedures.

**Table 4-1: MDS settings and acquisition rates of the different data sets accommodated in the MEDUSA in the MEDUSA detection system. (Adapted from [Mod05])**

<b>Data field</b>	<b>Action</b>	<b>Decimal Digits</b>	<b>Acquisition rate</b>
Spectrum	Synchronizer	-1	Every 2s
Pressure	Take the last known value	-1	Every 1s
Sound	Take the last known value	-1	Every 1s
Temperature	Take the last known value	-1	Every 1s
Total counts	Take the last known value	-1	Every 1s
Cable length	Take the last known value	-1	N/A
Cable volts	Take the last known value	-1	Every 1s
Time	Take the last known value	-1	Every 2s
Latitude	Average values	4	Every 2s
Longitude	Average values	4	Every 2s
Altitude	Average values	2	Every 2s

The \*.sdf files were loaded onto MPA, and processed as shown in the flow diagram of Figure 4-3. The ‘plug-ins’ referred to in the flow diagram are nothing other than the *standard spectra plus background spectrum* (Figure 4-4 to Figure 4-8) that are needed for performing the full-spectrum analysis (FSA) of the acquired MEDUSA  $\gamma$ -ray spectra. The standard spectra were generated by simulation with the Monte Carlo N-Particle X (MCNPX) code where a flatbed geometry was considered. The background spectrum, on the other hand, was acquired by making radiation measurements with the MEDUSA detector immersed in water at Theewaterskloof Dam near Grabouw, Western Cape [Mod05]. Chi-squared minimisation in MPA was achieved by using a tool called Manual Stabilization, which involved a manual modification of certain parameters.

<sup>11</sup> From Table 4-1, it should be noted that averaging was done over the latitude, longitude, and altitude data fields only, and not the other auxiliary data fields, because only these three were relevant to this study. It is also clear from the table that no useful change occurs from taking averages over latitude, longitude, and altitude data fields, because their acquisition rate of 2 seconds each corresponds with the spectrum acquisition rate.

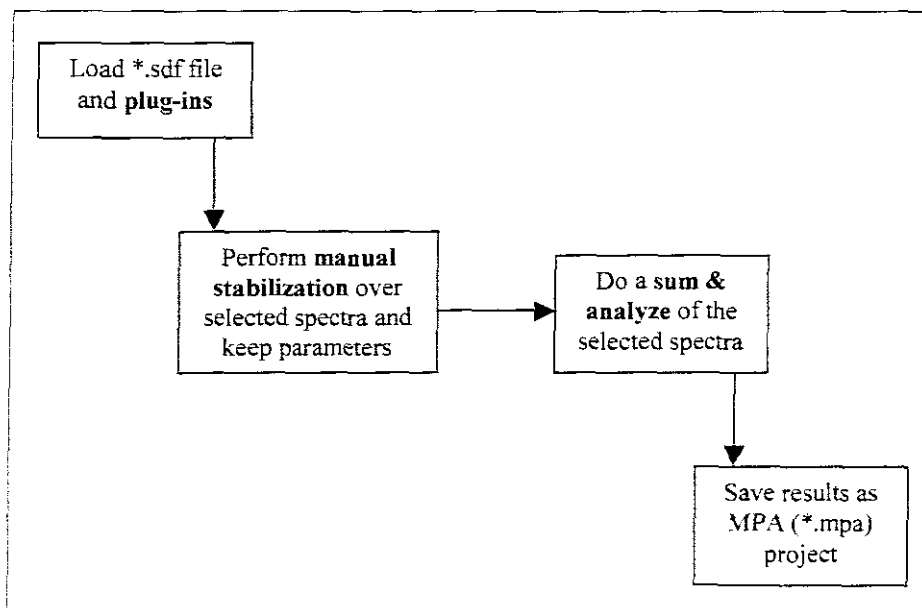


**Figure 4-3:** Flow diagram showing the procedure that was followed during the extraction of activity concentration of radionuclides from the synchronized MEDUSA data of this study, using the MPA software program.

The new parameters were kept for the next step, namely a “Sum & Analyze” operation of all acquired spectra to extract activity concentrations, plus the uncertainties thereof, for the radionuclides in question ( $^{40}\text{K}$ ,  $^{232}\text{Th}$ ,  $^{238}\text{U}$ , and  $^{22}\text{Na}$ , in this study.) According to the patent of the MEDUSA system, if  $S_i$  represents the number of  $\gamma$ -rays detected per second, who carry energy  $E_i$ , then  $\Delta S_i = \sqrt{S_i} / T$  gives the uncertainty in this number over time interval  $T$ . Here  $i = 1, 2 \dots n$  where  $n$  is a positive integer [Eur98]. The activity concentration, plus uncertainty, of the radionuclides was therefore determined from the number of detected  $\gamma$ -rays emitted by the radionuclides. The results of the MPA procedure were then saved as \*.mpa files, and referred to as MPA projects.

With MPA, the synchronized (\*.sdf) data could be plotted and viewed as maps of total count rate by using the relevant functions in the software. Each map, as seen in Figure 1-6, gave a ‘feel’ of the levels of radioactivity that is distributed along the surveyed portion of the grounds.

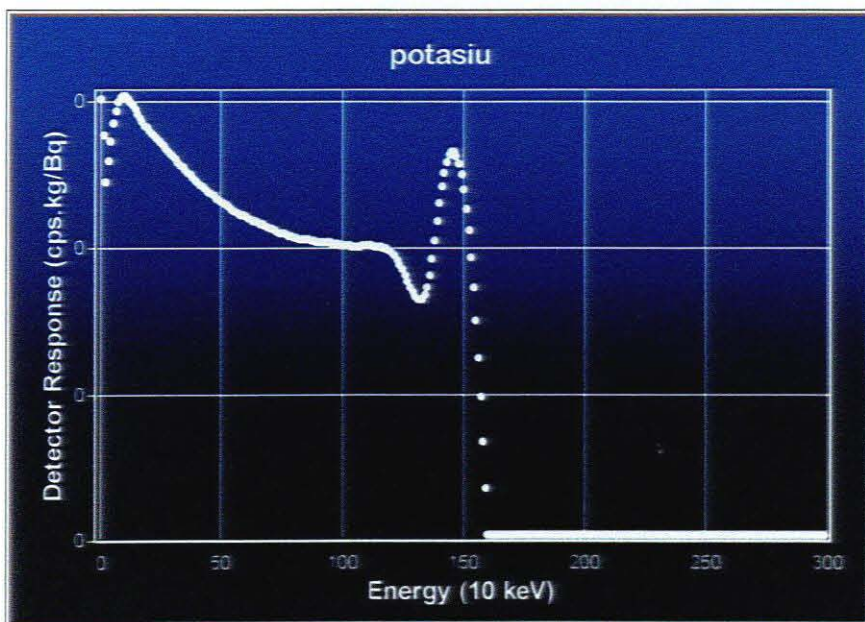


Figure 4-4: MCNPX-simulated  $\gamma$ -ray spectrum of radionuclide  $^{40}\text{K}$  used in FSA.

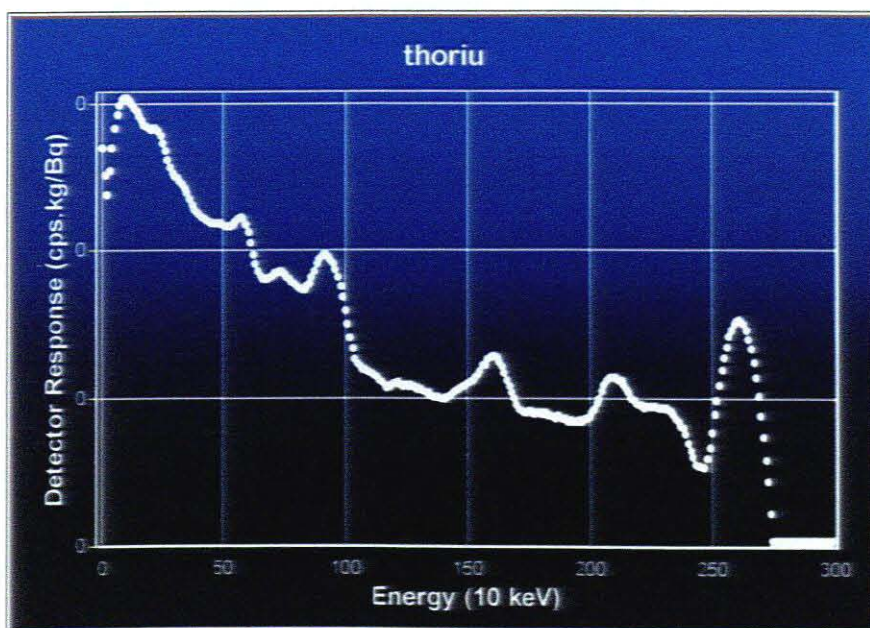


Figure 4-5: MCNPX-simulated  $\gamma$ -ray spectrum of radionuclide  $^{232}\text{Th}$  used in FSA.

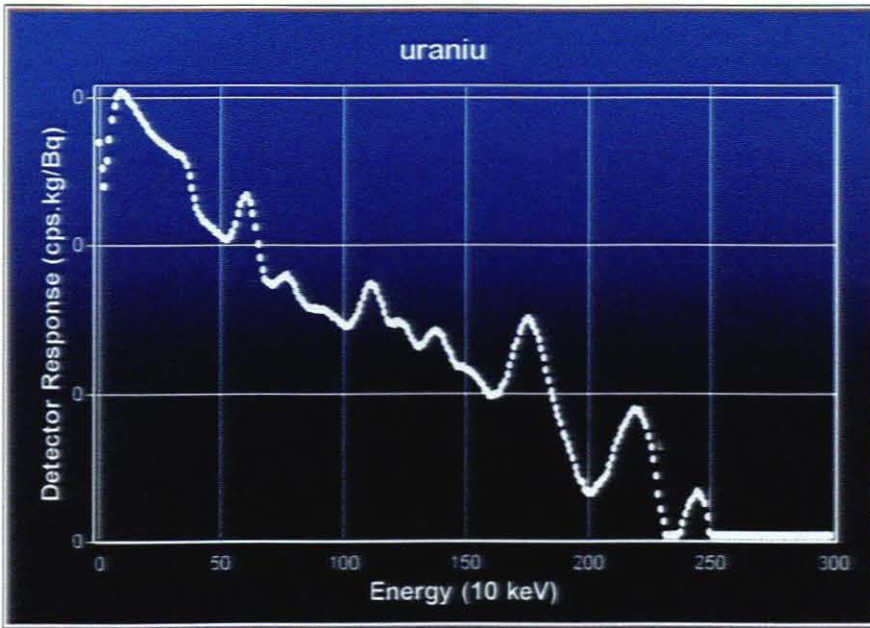


Figure 4-6: MCNPX-simulated  $\gamma$ -ray spectrum of radionuclide  $^{238}\text{U}$  used in FSA.

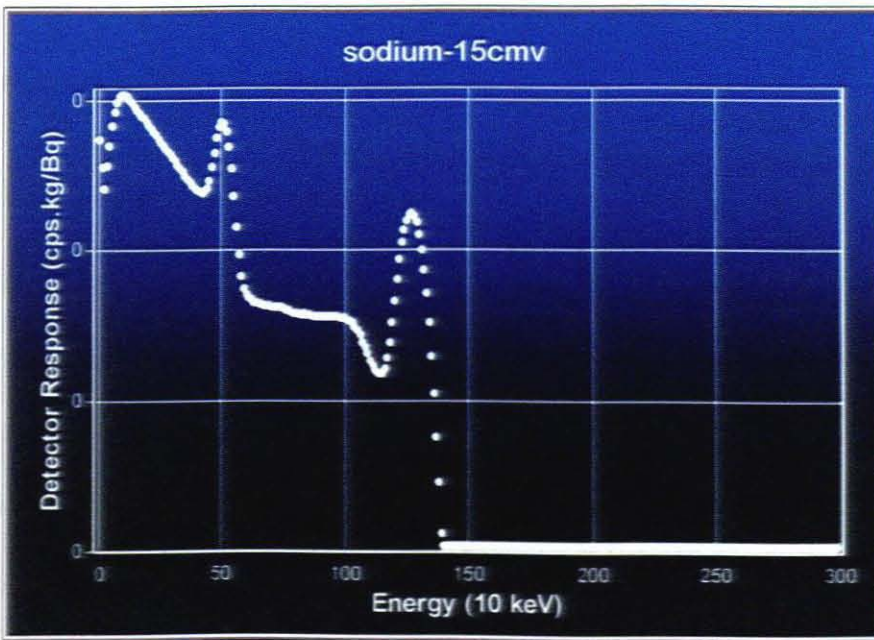


Figure 4-7: MCNPX-simulated  $\gamma$ -ray spectrum of radionuclide  $^{22}\text{Na}$  used in FSA. A source depth of 15 cm was considered in the simulation.



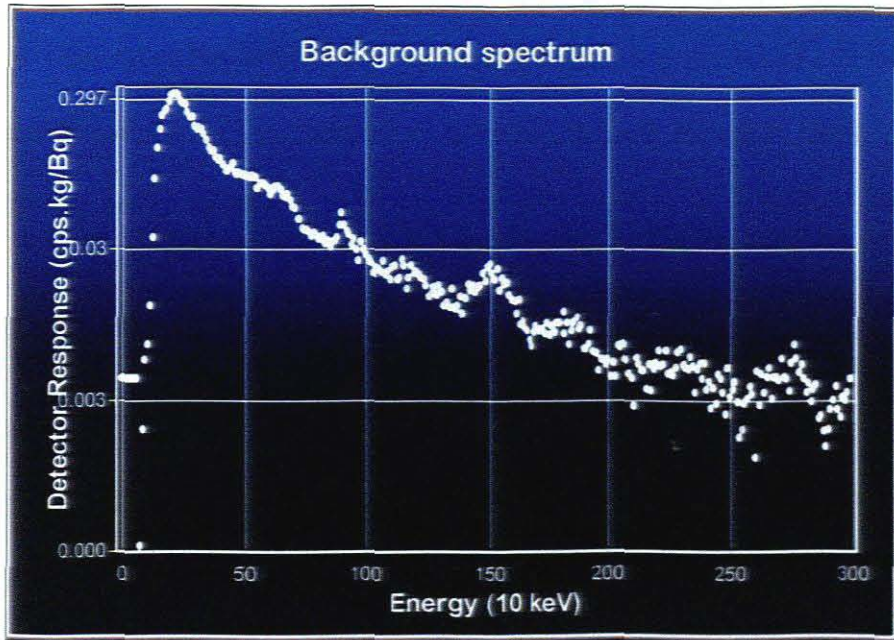


Figure 4-8: Background spectrum measured at Theewaterskloof Dam and used in FSA.

## 4.2 Analysis of the ex-situ data

### 4.2.1 Peak area analysis methods

An energy spectrum consists of *regions of interest* (ROIs) showing energy peaks indicating an enhanced level of detection of  $\gamma$ -rays belonging to particular species of radionuclides. Peak area analysis therefore uses different methods to get accurate information contained in these energy peaks. Two such methods are used in practice, namely (1) a *summation* (or *windows*) method, and (2) a *fit* method [LAN98]. Both these methods are reviewed briefly in this section.

The purpose of analyzing the energy peaks (or ROIs) is to accurately determine the net area underneath the peak [Ame93]. A summation method defines the area under the energy peak as:

$$\text{Area} = \sum_{i=\text{left}}^{\text{right}} y_i - b_i$$

Equation 4-2

where  $i$  = channel number,  $left$  = the leftmost channel of the peak region,  $right$  = the rightmost channel of the peak region,  $y_i$  = number of gross counts in channel  $i$ , and  $b_i$  = continuum contribution to channel  $i$ . A fit method, on the other hand, defines the area under the energy peak as:

$$\text{Area} = \int P(\alpha_1, \alpha_2, \alpha_3, \dots, x_i) dx$$

**Equation 4-3**

where  $P(\alpha_1, \alpha_2, \alpha_3, \dots, x_i)$  = the “best fit” mathematical function that models the assumed peak shape [LAn98]. A standard way of determining the best fit is a least squares method involving a minimization of  $\chi^2$ , where

$$\chi^2 = \sum_i w_i [y_i - b_i - P(\alpha_1, \alpha_2, \alpha_3, \dots, x_i)]^2$$

**Equation 4-4**

where  $w_i$  = the weighting applied to the  $i^{\text{th}}$  point and the  $\alpha_k$  are the free parameters of the model [LAn98].

The fit method finds application in the analysis of both the singlet and multiplet peaks. The summation method (by itself), on the other hand, is used to analyze single peaks only [LAn98]. In both these peak area analysis methods, the number of continuum counts under a peak,  $b_i$ , has to be known (see Equation 4-2 and Equation 4-4). Mathematical models for determining  $b_i$  have been assumed. There are two of these models that are normally used, namely (1) the linear background, and (2) the step background [LAn98].

Using the two methods for determining  $b_i$ , the quantity is found as follows:

By the linear model:

$$b_i = \frac{B_L}{n} + \frac{(B_R - B_L)}{n(N + 1)} i$$

**Equation 4-5**

By the step model:

$$b_i = \frac{B_L}{n} + \frac{(B_R - B_L)}{nG} \sum_{j=\text{left}}^i y_j$$

**Equation 4-6**

where

$$B_L = \sum_{j=\text{left}-n}^{\text{left}-1} y_j$$

**Equation 4-7**

and

$$B_R = \sum_{j=\text{right}+1}^{\text{right}+n} y_j$$

**Equation 4-8**

where  $n$  = the number of channels to be averaged on each side of the peak to determine the background,  $N$  = the number of channels in the peak region, and

$$G = \text{integral of the ROI} = \sum_{j=\text{left}}^{\text{right}} y_j .$$

**Equation 4-9**

When the peak is single and well-resolved, the linear background and the step background give approximately equivalent results for  $b_i$ . However, this is not always true for multiplet peaks. A graphical illustration is shown in Figure 4-9 where the linear background is less than the step background on the left side of the multiplet and greater than the step background on the right side [LAn98].

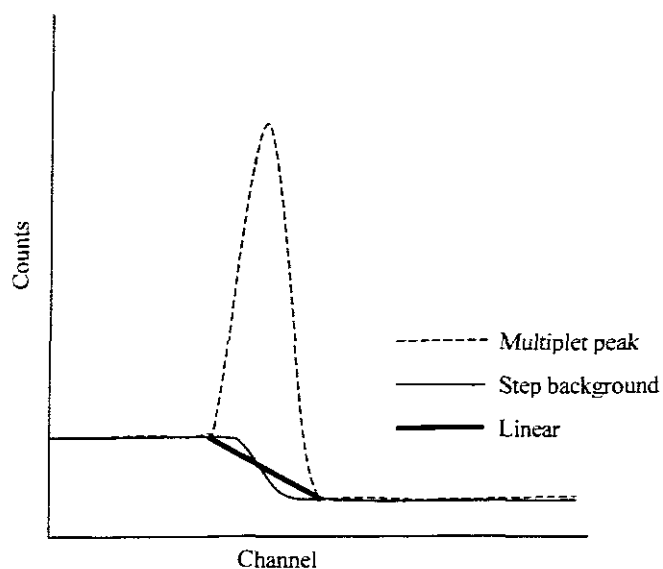


**Figure 4-9: An illustration showing the linear background being less than the step background on the left side of the multiplet and greater than the step background on the right side. (Adapted from [LAn98]).**

#### 4.2.2 The actual analysis

The HPGe spectra were analyzed using a technique known as the *peak or windows* analysis (see Appendix 1 for details on the windows analysis method). The spectra were viewed using the OxfordWin-MCA software (where MCA in the name stands for *multi-channel analyzer*) installed on a desktop computer in the ERL office (see Figure 3-5 for example of an HPGe spectrum). This software was then used to perform the windows analysis on the HPGe spectra. Figure 4-10 shows a flow diagram of the spectra analysis by means of the OxfordWin-MCA software. The diagram begins with the loading of the spectrum, which was opened as a \*.ans file, onto the OxfordWin-MCA window.

Every spectrum was re-calibrated for energy by setting ROIs over the chosen, clean and most prominent energy peaks, and then using the OxfordWin-MCA tool to do both the ‘energy by ROI centroids’ and ‘resolution,’ calibrations (see section 3.1.2.2 for details on energy and resolution calibration). By ‘clean’ peaks it is meant those peaks that do not have very close nearby peaks that may overlap on the

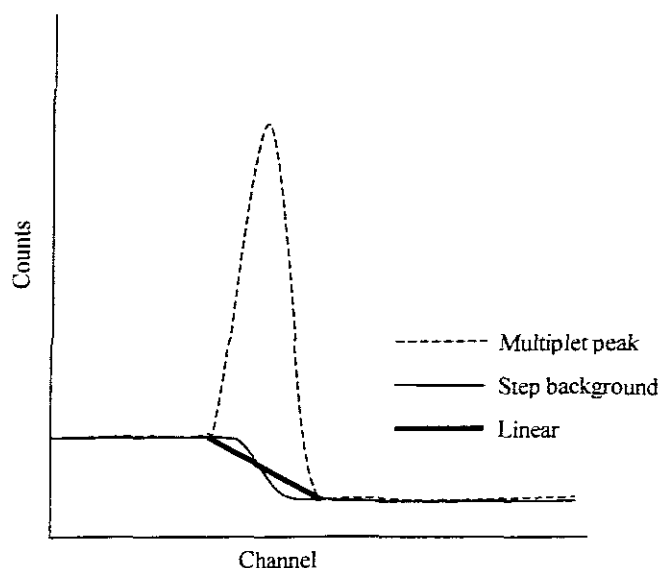


**Figure 4-9: An illustration showing the linear background being less than the step background on the left side of the multiplet and greater than the step background on the right side. (Adapted from [LAN98]).**

#### 4.2.2 The actual analysis

The HPGe spectra were analyzed using a technique known as the *peak* or *windows* analysis (see Appendix 1 for details on the windows analysis method). The spectra were viewed using the OxfordWin-MCA software (where MCA in the name stands for *multi-channel analyzer*) installed on a desktop computer in the ERL office (see Figure 3-5 for example of an HPGe spectrum). This software was then used to perform the windows analysis on the HPGe spectra. Figure 4-10 shows a flow diagram of the spectra analysis by means of the OxfordWin-MCA software. The diagram begins with the loading of the spectrum, which was opened as a \*.ans file, onto the OxfordWin-MCA window.

Every spectrum was re-calibrated for energy by setting ROIs over the chosen, clean and most prominent energy peaks, and then using the OxfordWin-MCA tool to do both the ‘energy by ROI centroids’ and ‘resolution,’ calibrations (see section 3.1.2.2 for details on energy and resolution calibration). By ‘clean’ peaks it is meant those peaks that do not have very close nearby peaks that may overlap on the

spectrum. The energy peaks used for calibration include (values in keV): 238.632 (from  $^{212}\text{Pb}$ ), 295.213 ( $^{214}\text{Pb}$ ), 351.921 ( $^{214}\text{Pb}$ ), 911.205 ( $^{228}\text{Ac}$ ), 1077.4 ( $^{68}\text{Ga}$ ), 1274.53 ( $^{22}\text{Na}$ ), 1460.83 ( $^{40}\text{K}$ ), and 2614.533 ( $^{208}\text{Tl}$ ) [Fir96]. These values were entered into the ‘energy by ROI centroids’ calibration window and a linear (1<sup>st</sup> order polynomial) curve was employed for calibration. The chosen lines were then included in the ‘resolution’ calibration window to perform the calibration linearly as well. The calibration curve parameters were recorded into the logbook.

The spectrum was thereafter saved as calibrated. The ROIs were set (or the existing ones uploaded) over the calibrated spectrum in order to extract the number of counts associated with the detected  $\gamma$ -ray energy lines. The final selection of ROIs was saved as an \*.roi file belonging to that particular spectrum. The OxfordWin-MCA software generated a report containing information about the analysis, such information as, a list of all the analyzed ROIs, their  $\gamma$ -ray energies (in keV), gross counts ( $C_g$ ), net counts ( $C_n$ ), and full-width-at-half-maximum (FWHM).

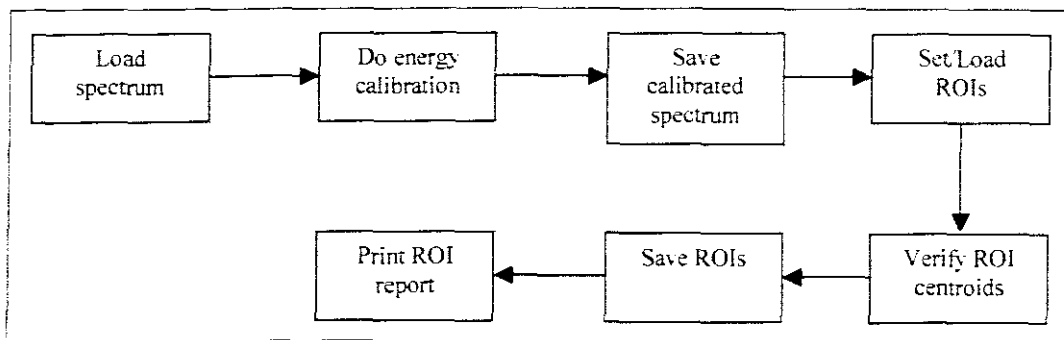


**Figure 4-10: Flow diagram showing the spectra analysis by means of the OxfordWin-MCA software in the ERL.**

The relationship between gross counts and net counts is as follows:

$$C_n = C_g - C_c$$

**Equation 4-10**

where  $C_c$  represents the continuum counts under the peak [Mod05]. In order to determine the activity concentration of radionuclides associated with every energy peak, the following formula is used:

$$A(\text{Bq / kg}) = \frac{C_s}{mTb\epsilon_{\text{det}}}$$

**Equation 4-11**

where  $A$  is the activity concentration measured in becquerel (Bq) per kilogram (kg),  $C_s$  stands for spectrum counts and equals to the sample net counts ( $C_{ns}$ ) minus the background net counts ( $C_{nb}$ ) (background here refers to the measured tap water sample),  $m$  is the mass of the sample measured in kg,  $T$  is the live time of the detector measured in seconds (s),  $b$  is the branching ratio associated with the particular  $\gamma$ -ray energy line ( $b$  gives the statistical chance that a particular  $\gamma$ -ray is emitted per decaying nucleus), and  $\epsilon_{\text{det}}$  is the detection efficiency at the  $\gamma$ -ray energy line ( $\epsilon_{\text{det}}$  equals to the ratio of the number of detected photons to the number of photons emitted by the source).

The parameters in Equation 4-11 were obtained as follows:  $C_s$  was calculated [with Microsoft Excel] directly from the OxfordWin report,  $m$  is the value that was read from the weighing scale in the ERL,  $T$  came from the report,  $b$  was quoted from [Fir96], and  $\epsilon$  was obtained as described in section 4.2.2.1 below. The uncertainties to the values of  $A$  (and all other quantities with values that had uncertainties associated with them) were calculated by employing the propagation rule

$$\sigma_z^2 = \left(\frac{\partial f}{\partial x}\right)^2 \sigma_x^2 + \left(\frac{\partial g}{\partial y}\right)^2 \sigma_y^2$$

**Equation 4-12**

for any function  $Z = f(x) - g(y)$ . In the equation, the symbols  $\sigma_x$ ,  $\sigma_y$ , and  $\sigma_z$  are uncertainties associated with variables  $x$  and  $y$ , and function  $Z$ , respectively.

#### 4.2.2.1 Determination of absolute efficiency

The absolute detection efficiency ( $\varepsilon$ ) was obtained using the following equation:

$$\varepsilon = a \left( \frac{E}{E_0} \right)^b$$

**Equation 4-13**

where  $a$  and  $b$  are constants,  $E$  is the  $\gamma$ -ray energy value, and  $E_0 = 1$  keV. The parameters  $a$  and  $b$  were obtained from the work done by [Mod05], and are listed in Table 0-1 in Appendix 3. The table shows the list of 10 parameters obtained for 10 different soil samples that were collected from Simonsig Wine Farm, in Stellenbosch. For each  $\gamma$ -ray energy line, 10 different absolute efficiency values,  $\varepsilon_1$  up to  $\varepsilon_{10}$ , were calculated by substitution into Equation 4-13. An average of the absolute efficiencies was calculated as  $\varepsilon_{ave} = (\varepsilon_1 + \varepsilon_2 + \dots + \varepsilon_9 + \varepsilon_{10})/10$ . The average absolute efficiencies were then used in the further analysis of the  $\gamma$ -ray full energy peaks (see Table 4-2 for list of absolute efficiencies used). The absolute efficiency curve is shown in Figure 4-11. To validate the method used to obtain the absolute efficiencies, the ERL re-measured an IAEA reference soil sample for comparison of their results with those recommended by the IAEA (see Table 0-2 in Appendix 3 for results).



**Table 4-2: Gamma-ray lines, their branching ratios, and their absolute efficiencies, with uncertainties, used to obtain the activity concentrations of their respective source radionuclides [Fir96].**

Series	Radionuclide	E (keV)	Branching ratio (%)	Absolute Efficiency
Uranium-238	Lead-214	295.21	18.50 ± 0.0030	0.028 ± 0.011
	Lead-214	351.92	35.80 ± 0.0080	0.024 ± 0.010
	Bismuth-214	934.06	3.03 ± 0.0005	0.012 ± 0.006
	Bismuth-214	1238.11	5.86 ± 0.0008	0.010 ± 0.005
	Bismuth-214	1377.67	3.92 ± 0.0008	0.009 ± 0.004
	Bismuth-214	1764.49	15.36 ± 0.0020	0.008 ± 0.004
	Bismuth-214	2204.21	4.86 ± 0.0009	0.007 ± 0.003
Thorium-232	Actinium-228	338.32	11.25 ± 0.0027	0.025 ± 0.010
	Bismuth-212	727.33	6.58 ± 0.0005	0.015 ± 0.006
	Actinium-228	794.95	4.34 ± 0.0011	0.014 ± 0.006
	Actinium-228	911.21	26.60 ± 0.0069	0.012 ± 0.006
	Actinium-228	966.87	21.28 ± 0.0023	0.012 ± 0.005
	Potassium-40	1460.83	10.67 ± 0.0013	0.009 ± 0.004
	Gallium-68	1077.40	3.00 ± 0.0030	0.011 ± 0.005
	Zinc-65	1115.55	50.60 ± 0.0024	0.011 ± 0.005
	Sodium-22	1274.53	99.94 ± 0.0001	0.010 ± 0.005
	Caesium-137	661.66	85.10 ± 0.0020	0.016 ± 0.007

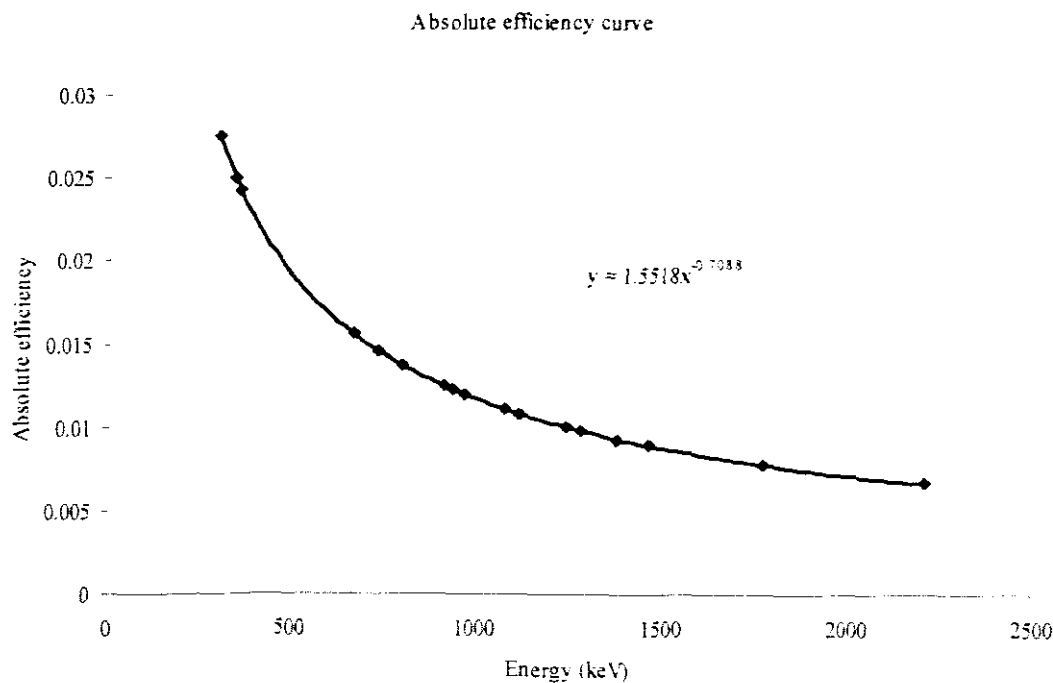


**Figure 4-11: Absolute efficiency curve for  $\gamma$ -ray energies used to identify radionuclides in this study. The average parameters  $a$  and  $b$  are 1.5518 and (-0.7088), respectively.**

### 4.3 Calculation of Dose

The analysis of the data further translated the extracted activity concentration results into effective dose to human beings on the IITL site. This step involved the use of dose conversion factors (for external exposure to  $\gamma$ -rays associated with NORM radionuclides  $^{238}\text{U}$ ,  $^{232}\text{Th}$ , and  $^{40}\text{K}$ ), the air kerma<sup>12</sup> per unit [anthropogenic] source intensity, the conversion coefficient from absorbed dose in air to effective dose, and the outdoor occupancy factor [Moh04, Sai94]. Mathematically, the equation that relates the effective dose of a person to the measurable quantity of activity concentration of radionuclides is

$$\text{Effective dose rate (mSv.y}^{-1}\text{)} = \text{Absorbed dose rate (nGy.h}^{-1}\text{)} \times 8760 \text{ h.y}^{-1} \\ \times 0.2 \times 0.7 \text{ Sv.Gy}^{-1} \times 10^{-6}$$

Equation 4-14

where 8760 h = number of hours in a year, 0.2 = outdoor occupancy factor, and 0.7 Sv.Gy<sup>-1</sup> = conversion coefficient from absorbed dose in air to effective dose [UNS00].

The absorbed dose rate ( $D$ ) of Equation 4-14 was obtained, for the NORM radionuclides, by summing the products of activity concentration and the dose conversion factors for each radionuclide as follows:

$$D(\text{nGy.h}^{-1}) = 0.462C_{\text{U}} + 0.604C_{\text{Th}} + 0.0417C_{\text{K}}$$

Equation 4-15

where 0.462, 0.604, and 0.0417 are dose conversion factors for external exposure to  $\gamma$ -rays associated with  $^{238}\text{U}$ ,  $^{232}\text{Th}$ , and  $^{40}\text{K}$ , respectively [Moh04].  $C_{\text{U}}$ ,  $C_{\text{Th}}$ , and  $C_{\text{K}}$  are activity concentrations of  $^{238}\text{U}$ ,  $^{232}\text{Th}$ , and  $^{40}\text{K}$ , respectively. The dose conversion factors for the NORM radionuclides are quoted from reference [UNS00] (see Table 4-3).

---

<sup>12</sup> Kerma is defined as the kinetic energy of charged ionising particles that are liberated per unit mass of specified material by uncharged ionising particles such as photons and neutrons. For radiation protection purposes, air kerma and tissue kerma are considered to be equal in magnitude [vRo04].

**Table 4-3: Dose conversion factors for NORM radionuclides used in this study [UNS00, Sai94].**

<b>Radionuclide</b>	<b>Conversion factor (nGy h<sup>-1</sup> per Bq kg<sup>-1</sup>)</b>
<sup>238</sup> U	0.462
<sup>232</sup> Th	0.604
<sup>40</sup> K	0.0417

For anthropogenic radionuclides, the absorbed dose was obtained via modeling. In Figure 4-12 is shown a flow diagram indicating how the units evolved during the determination of absorbed dose by anthropogenic radionuclides via the model used. The diagram begins with the assumption of the plane [anthropogenic] source<sup>13</sup> location (see Figure 4-13). The source was located at depths of 1 and 10 cm, to determine the upper and lower limits of the absorbed dose, respectively. The air (or tissue) kerma was quoted from reference [Sai94], at 1 and 10 cm depths. The area assumed for the plane was  $2\text{m} \times 2\text{m} = 4\text{m}^2$ , since the samples taken in the manner of Figure 3-12 show a spread in the distribution of the HS1 contamination, for example (see Table 0-4 in Appendix 5). The thickness assumed for the soil slab was 10 cm, since samples of this approximate depth were considered. Assuming a soil density of  $1.5 \text{g.cm}^3$ , the calculation of mass of the slab yielded 600 kg. The activity of the soil slab was determined by multiplying the mass by the activity concentration (in  $\text{Bq.kg}^{-1}$ ) of the considered anthropogenic radionuclide. By multiplying the activity of the slab by the branching ratio of the  $\gamma$ -ray used for the radionuclide, the number of photons associated with the plane area was approximated per second. The last step was to multiply the tissue kerma by the number of photons to yield the absorbed dose (in  $\text{nGy.h}^{-1}$ ) associated with the source.

---

<sup>13</sup> Here, 'source' and 'radionuclide' are used interchangeably.

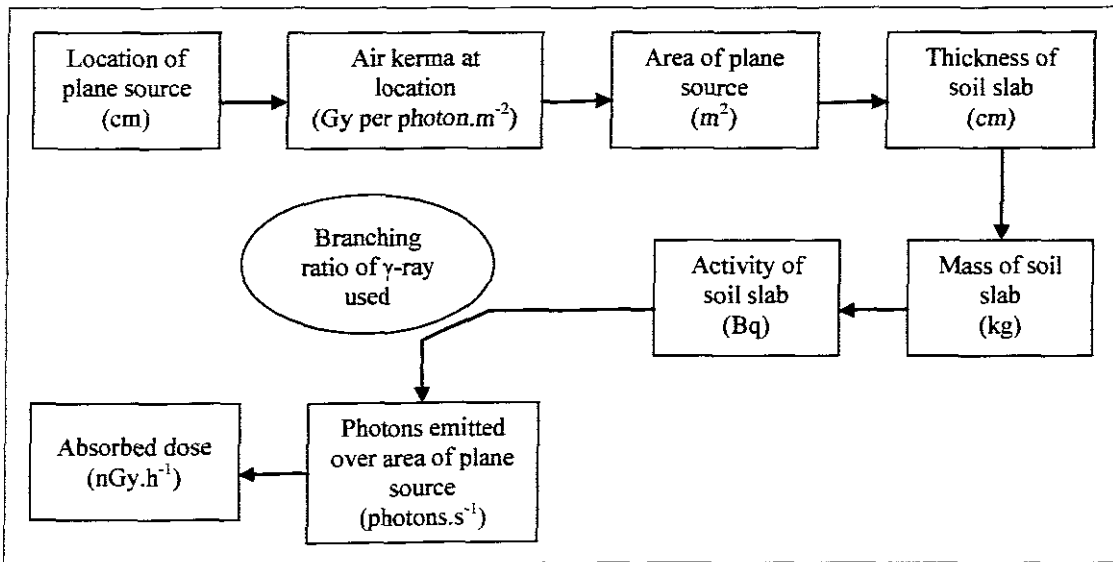


Figure 4-12: Flow diagram showing how the units evolved during the determination of absorbed dose by anthropogenic radionuclides via the model used. For radiation protection purposes, air kerma and tissue kerma are considered to be equal in magnitude [vRo04].

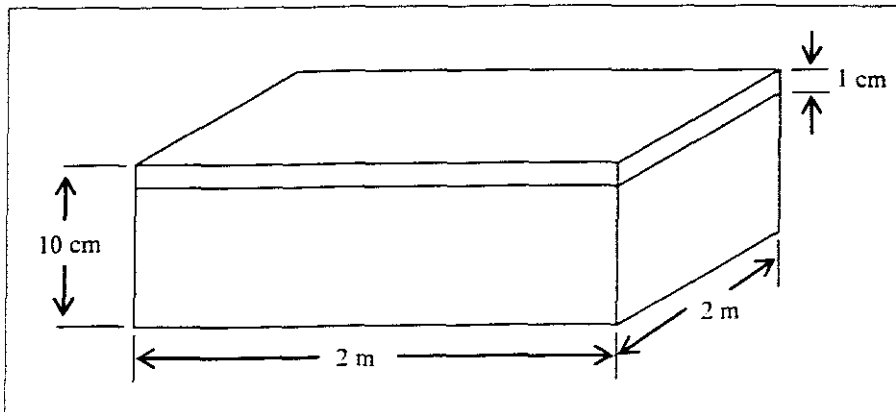


Figure 4-13: Schematic diagram showing features of the assumed slab of soil. The plane area is  $4 \text{ m}^2$ , the thickness of the soil slab is 10 cm, and the plane source locations are 1 and 10 cm.

The outdoor occupancy factor, 0.2, of Equation 4-14 gives the fraction of time spent outdoors in a year. For a hypothetical  $\bar{I}$ TL gardener working 236 shifts of 6 hours each, per year, the occupancy factor was calculated and found to be 0.16, rounded off to 0.2. The conversion coefficient from absorbed dose in air to effective dose,  $0.7 \text{ Sv.Gy}^{-1}$ , is quoted from reference [UNS00].

## CHAPTER 5 FINDINGS AND DISCUSSION

In this chapter are presented the results obtained from this study. A brief discussion of the results is given accordingly.

### **5.1 In-situ findings**

The map of the variations in the altitude on the *i*TTL site during the February 2005 survey is shown in Figure 5-1. According to the map, the altitude varied over a range of approximately 7 – 23 metres. This variation is rather large given that the accessible landscape of the *i*TTL site is not expected to vary by more than 2 metres in altitude. The magnitude of this variation indicates that there is a maximum error of ~ 15 metres associated with the altitude readings from the GPS system. The map also shows the locations of the various features of the *i*TTL site.

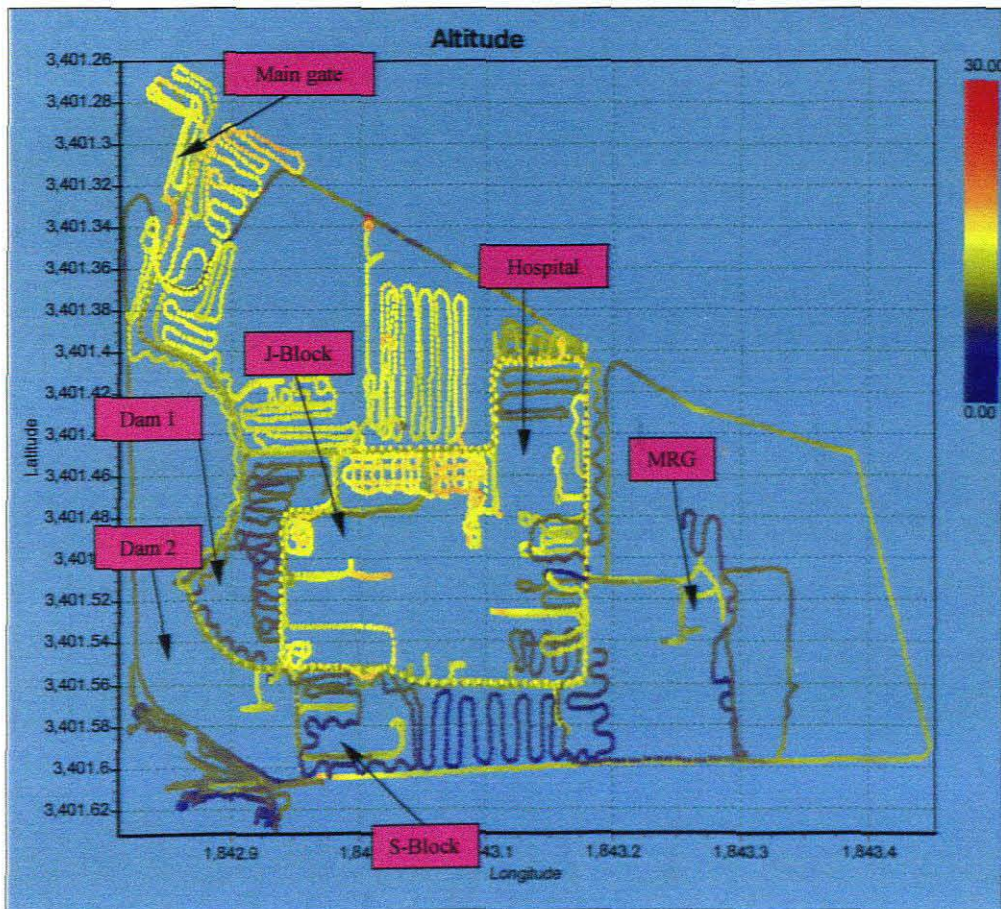


Figure 5-1: Map showing the altitude (m) of all locations surveyed in February 2005 (also in July 2005). (Note: The map shows the Latitude and Longitude coordinates in the format x,xyy.yy instead of the usual xx°yy.yy' where xx and yy.yy correspond to the degrees and minutes, respectively.)

### 5.1.1 February 2005 survey

The map of the variations in the temperature on the iTL site during the February 2005 survey is shown in Figure 5-2. According to the map, the temperature varied over a range of approximately 20 – 50 °C. The magnitude of this variation could be due to the changes in temperature for morning, day, and afternoon measurements.

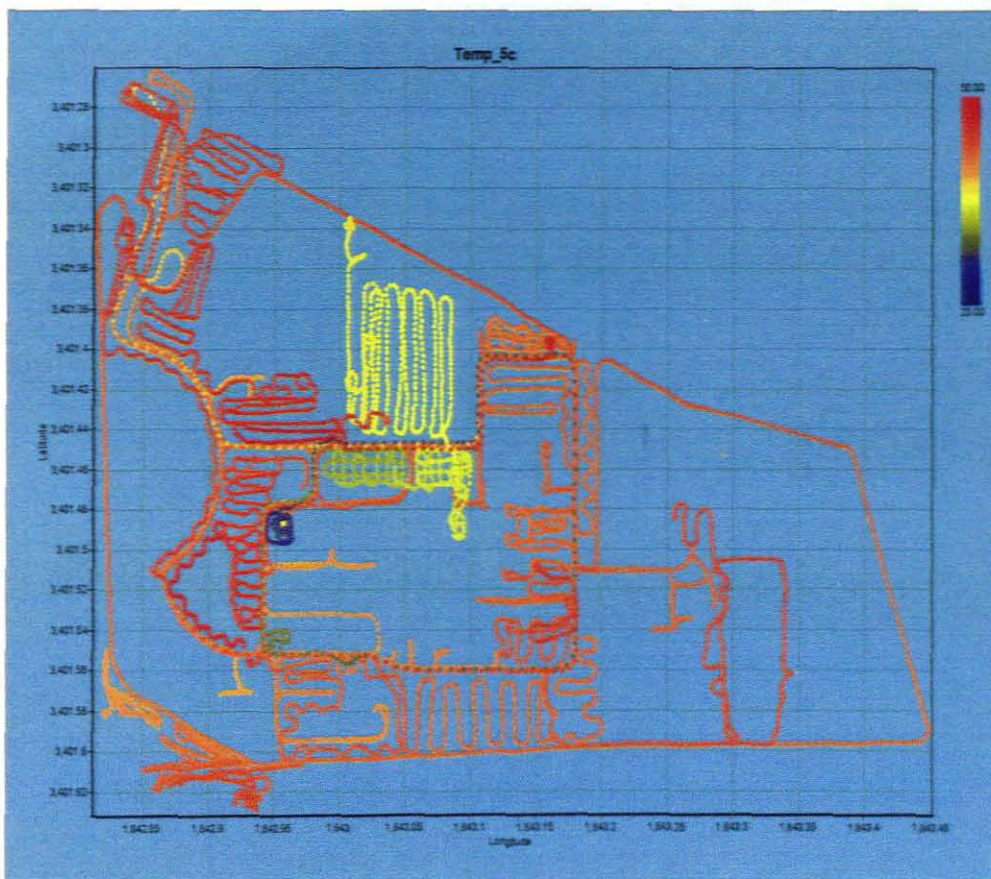


Figure 5-2: Map showing the temperature variation at sections surveyed on the site in February 2005. The range of the temperature is from 20 to 50 °C, and is shown on the top-right corner in the map.

The maps of Figure 5-3 and Figure 5-4 show the recorded variation of the count rate with the *i*TTL MEDUSA detector, during the February 2005 survey. The displayed scale of variation is only 100 – 1100 counts per second for the map, and this limitation was made so as to give better contrast with the colour-coded presentation. The maps also show the locations of the different spots of interest on the *i*TTL site.

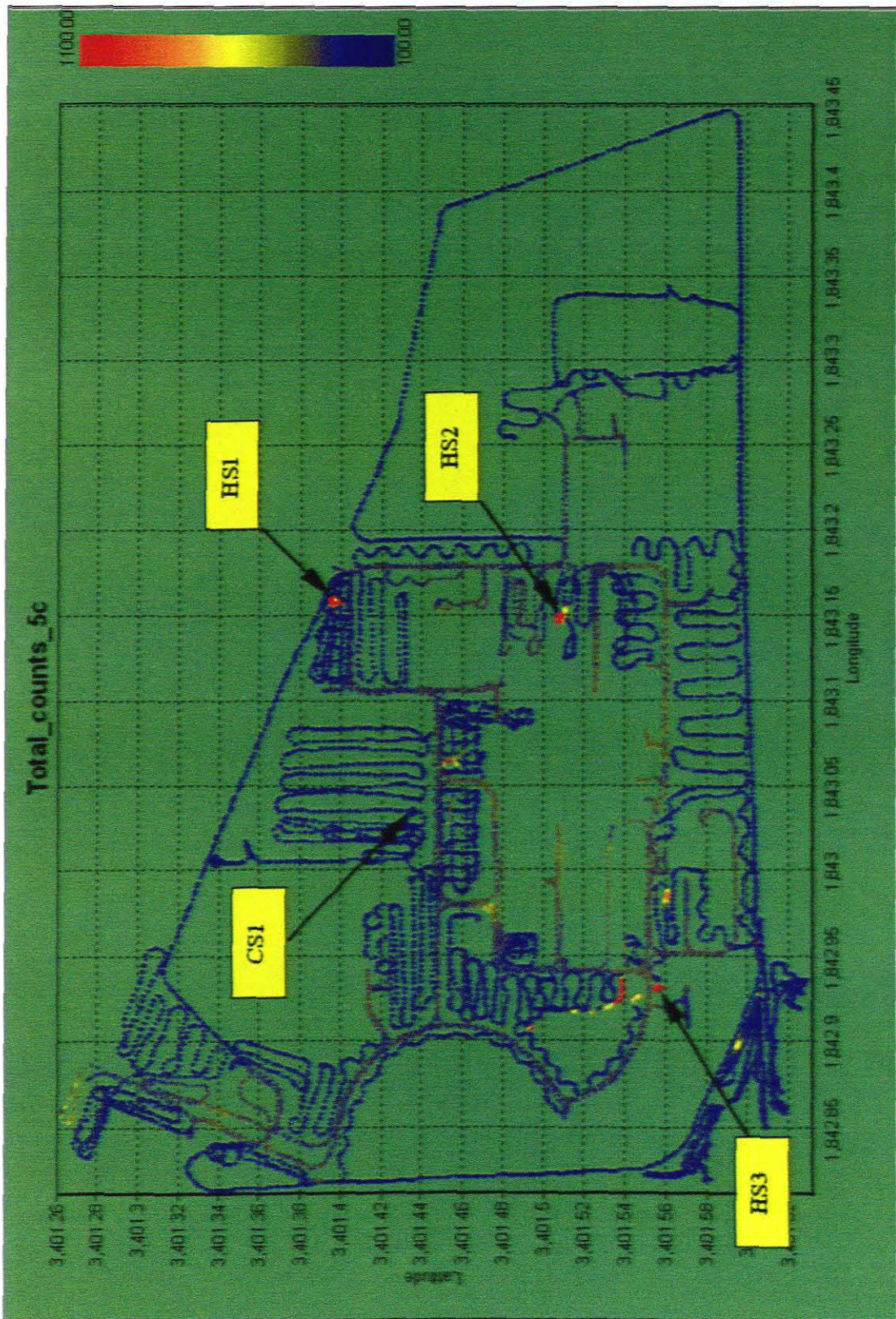


Figure 5-3: Map showing MEDUSA count rate obtained during the February 2005 survey. The range of the count rate is 100 - 1100 counts per second, and is shown on the top-right corner in the map. The GPS coordinates of the labeled locations are listed in Table 3-1.



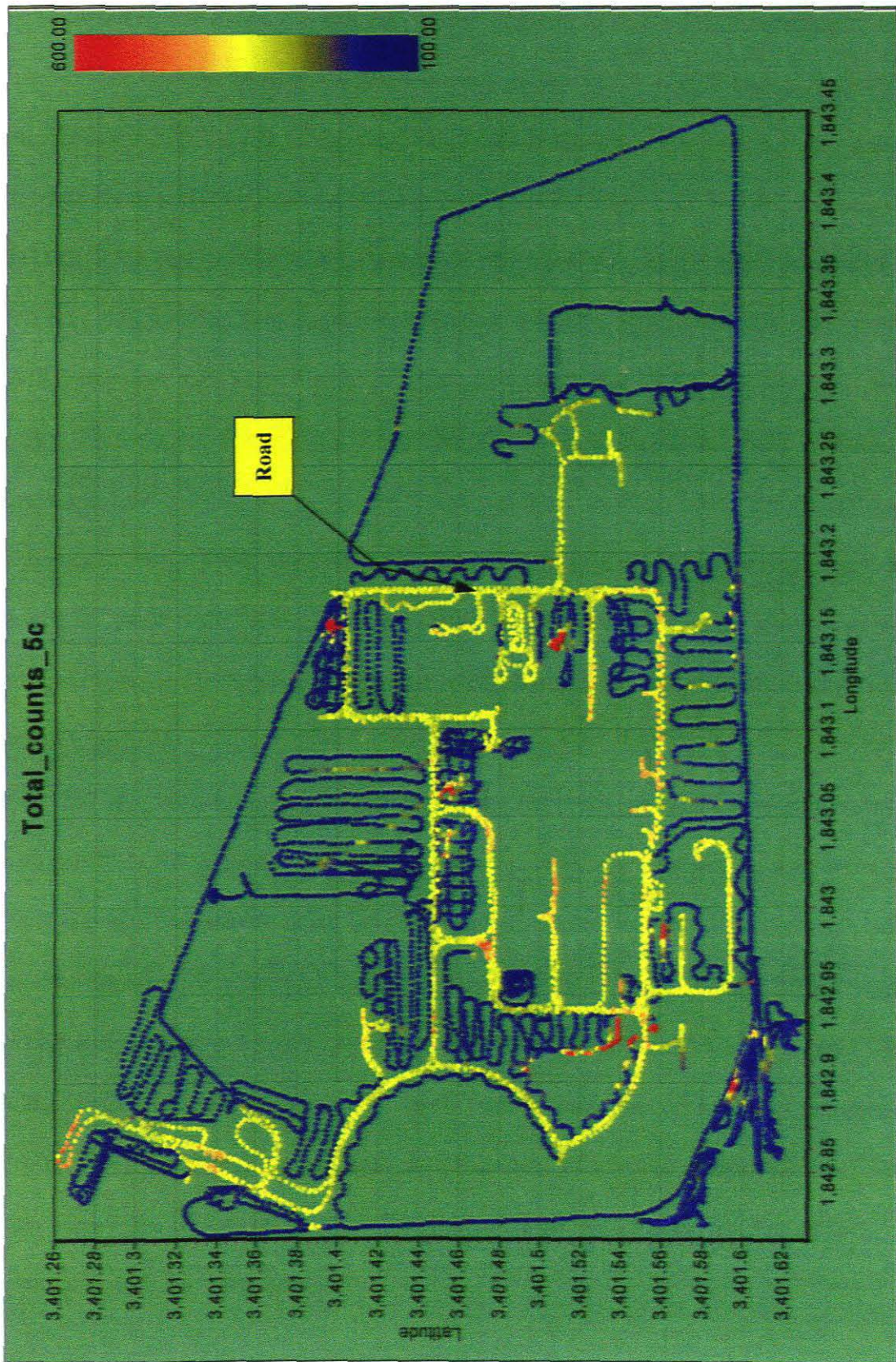


Figure 5-4: Map showing MEDUSA count rate obtained during the February 2005 survey. The range of the count rate is 100 - 600 counts per second, and is shown on the top-right corner in the map.

A list of the average count rate values is given in Table 3-1. According to the list, hotspot HS3 recorded the highest average count rate of 4843.8 counts/second in the February 2005 survey. The rest of the results in the list, in the order of decreasing average count rate levels, are as follows: 2485.8 (HS3, July), 1225.6 (HS2, February), 1119.2 (RPG pipe), 994.8 (HS1, February), 959.5 (NHS4), 850.8 (HS2, July), 719.5 (NHS5), 676.4 (HS1, February), 560.5 (Dipole magnet), 500.2 (Near-Dam 1), 419.7 (MRG hotspot), 113.3 (NCS1), 111.0 (CS1, February), and 97.8 counts/second (CS1, July). These count rate values show that for hotspot locations where stationary measurements were done in February and repeated in July 2005, the count rate obtained in July is lower than that of February 2005. This could be due to radioactive decay, or there might actually be a decline in the concentration of anthropogenic radionuclides at the hotspots due to seasonal changes, i.e. summer (February) and winter (July).

In Figure 5-5 to Figure 5-8 are shown the raw  $\gamma$ -ray spectra that were acquired with the MEDUSA detector at locations CS1, HS1, HS2, and HS3 during the February 2005 survey. The spectra were received and displayed as plots of count rate per channel number. The labeled energy peaks 1077.4, 1274.5, 1460.8, 2204.2, and 2614.5 keV in Figure 5-6 are associated with from  $^{68}\text{Ga}$ ,  $^{22}\text{Na}$ ,  $^{40}\text{K}$ ,  $^{214}\text{Bi}$ , and  $^{208}\text{Bi}$  decay, respectively. The 511.0 keV peak results from the detection of positron-electron annihilation  $\gamma$ -rays associated with the decay of positron sources such as  $^{22}\text{Na}$  (see Figure 0-3 in Appendix 2). The labeled peak 834.9 keV in Figure 5-8 is associated with the  $^{54}\text{Mn}$  decay.

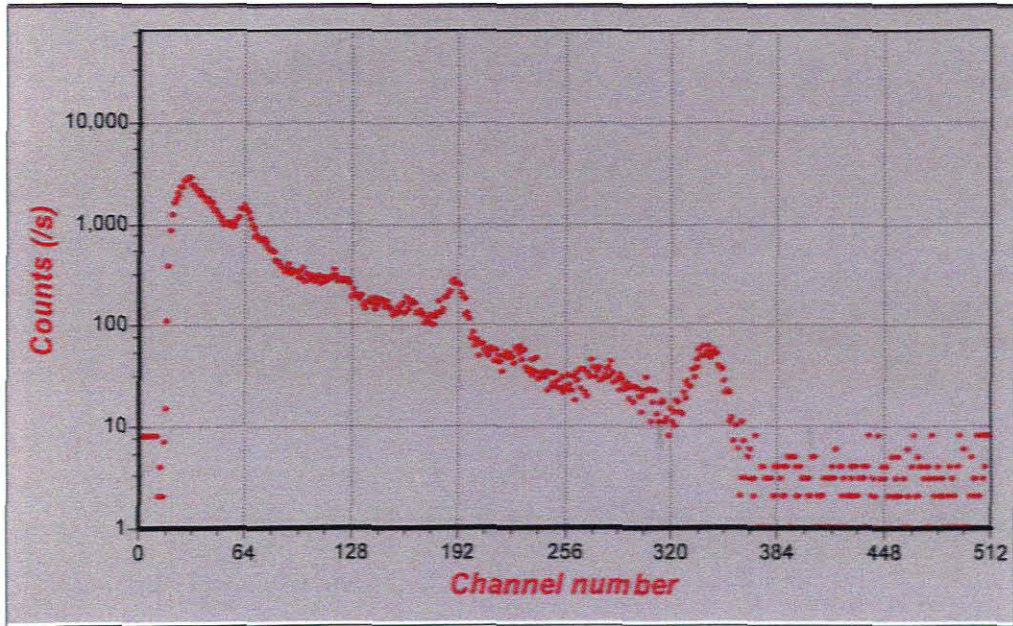


Figure 5-5: The raw *gamma*-ray spectrum acquired with MEDUSA in a stationary position over calibration spot CS1 in February 2005.

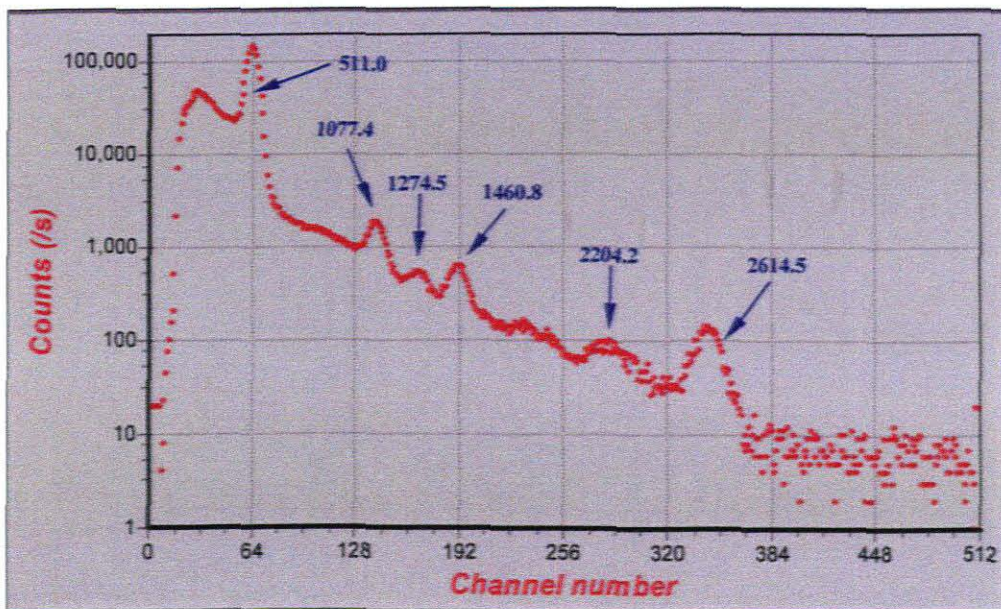


Figure 5-6: The raw *gamma*-ray spectrum acquired with MEDUSA in a stationary position over hotspot HS1 in February 2005. The labeled peaks 1077.4, 1274.5, 1460.8, 2204.2, and 2614.5 keV are associated with  $^{68}\text{Ga}$ ,  $^{22}\text{Na}$ ,  $^{40}\text{K}$ ,  $^{214}\text{Bi}$ , and  $^{208}\text{Bi}$  decay, respectively. The 511.0 keV peak results from the detection of positron-electron annihilation  $\gamma$ -rays associated with the decay of positron sources such as  $^{22}\text{Na}$ .

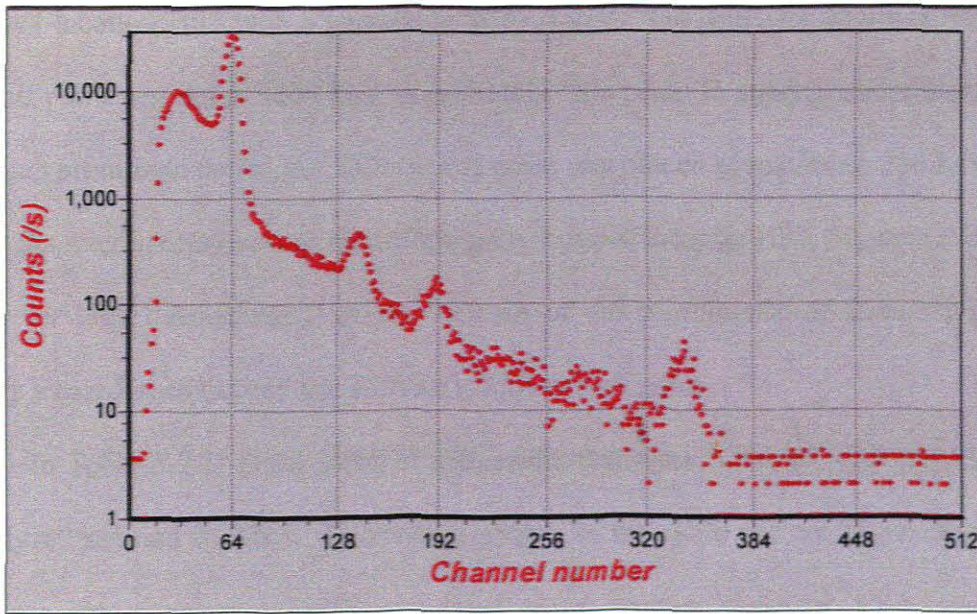


Figure 5-7: The raw *gamma*-ray spectrum acquired with MEDUSA in a stationary position over hotspot HS2 in February 2005.

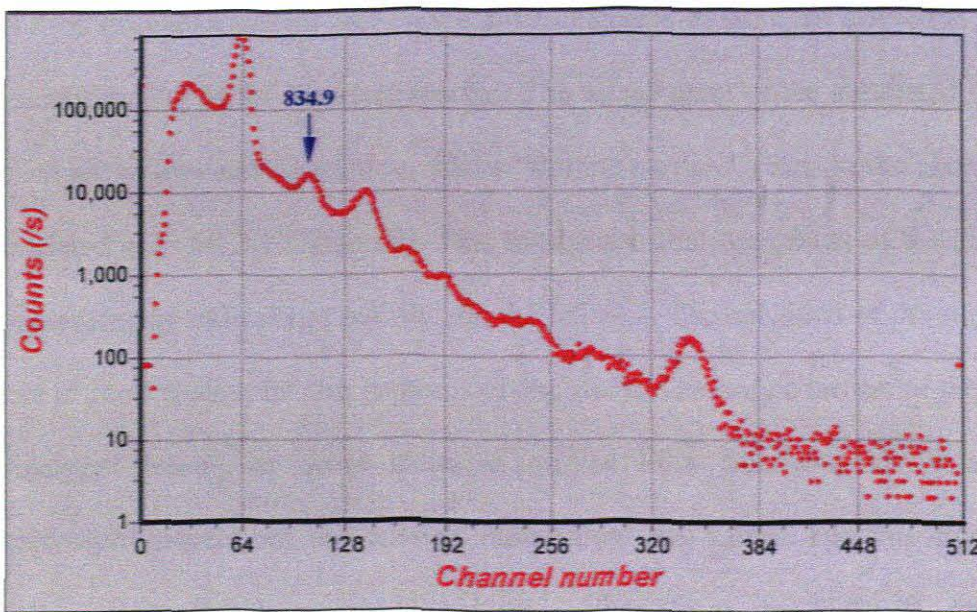


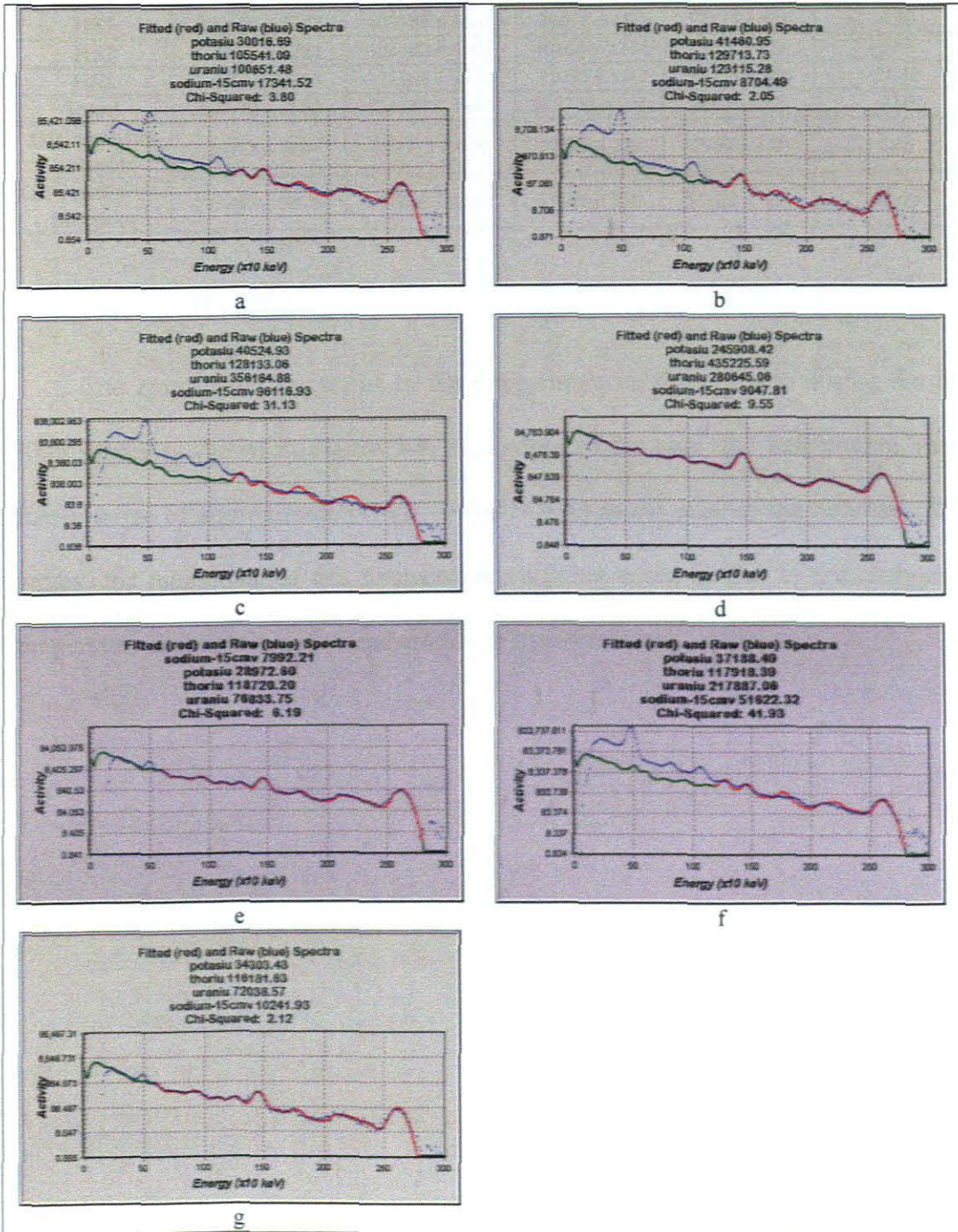
Figure 5-8: The raw *gamma*-ray spectrum acquired with MEDUSA in a stationary position over hotspot HS3 in February 2005. The labeled peak 834.9 keV is associated with the  $^{54}\text{Mn}$  decay.

The results of FSA fits, with the “Manual Stabilization” method in MPA, are listed in Table 5-1. With this MPA method, the “regions of interest” (ROIs) in the spectrum could be appropriately varied for FSA curve fitting. The reason for varying the ROIs was to obtain the best FSA fit by avoiding prominent energy peaks from anthropogenic radionuclides that had no standard spectra. For spectra such as that of

hotspot location HS1 with a prominent 1077.4 keV  $^{68}\text{Ga}$  peak, for example, the ROI cut-off point was put at 1200 keV to avoid this  $^{68}\text{Ga}$  peak. In spectra where there were no such prominent peaks, the ROI cut-off point was placed at minimum 250 keV. The FSA fits over spectra such as that of the gully hotspot location HS3, for example, gave poor (or large) chi-squared values because of the prominence of these “unfitted” peaks located even beyond the 1200 keV ROI cut-off point.

In Table 5-2 is given a list of the results that were obtained with the “Sum & Analyze” method in MPA. The results shown in the table are not given any units, because the supplied MCNPX-simulated  $\gamma$ -ray spectra used for FSA were not renormalised for use as absolute data [Hen02]. Therefore, the units shown on the left axis of the simulated spectra (see Figure 4-4 to Figure 4-8) were not arrived at during the manufacturing of the standard spectra. The actual units of the simulated spectra supplied are counts/starting particle, where “starting particle” refers to the photon that is simulated with MCNPX [Hen02]. This means also that the results of the FSA fits are misleading by indicating “activity” on the left axis. The condition of the simulated spectra is good enough for the purposes of the study. The normalisation of the “Sum & Analyze” results, or those indicated on the FSA fits, with HPGe activity concentration cancels out the missing factor from the values. For this study, the MEDUSA results that were normalised were taken from the “Sum & Analyze” procedure, instead of the FSA fits, because the former are presented with uncertainties associated with them, but the latter are not.

Table 5-1: “Manual Stabilization” fits for the February 2005 survey reported for (a) HS1, (b) HS2, (c) HS3, (d) Road, (e) Off-road-no-hotspots, (f) Off-road-with-hotspots<sup>14</sup>, and (g) CS1. The underlined location does not have flatbed geometry (see also Figure 3-8 for photos of locations). The ROIs were varied to obtain the best fit by avoiding prominent peaks from anthropogenic radionuclides that had no standard spectra.



<sup>14</sup> For 'Off-road-no-hotspots' and 'Off-road-with-hotspots' results, the data considered ranged from 0 – 150 and 511 – 6000 counts per second, respectively.

**Table 5-2: February 2005 MEDUSA “Sum & Analyze” results. The results shown are not given any units because the supplied MCNPX-simulated  $\gamma$ -ray spectra used for FSA were not renormalized for use as absolute data [Hen02].**

Location	MEDUSA: Sum & Analyze				Chi-squared
	$^{238}\text{U}$	$^{232}\text{Th}$	$^{40}\text{K}$	$^{22}\text{Na}$	
<b>CS1</b>	71566 ± 2415	115187 ± 2084	34298 ± 711	10203 ± 556	2.08
<b>HS1</b>	101658 ± 2352	103384 ± 1604	29871 ± 458	17175 ± 410	4.20
<b>HS2</b>	129977 ± 6281	124082 ± 4095	40165 ± 1244	7953 ± 921	2.69
<b>HS3</b>	356859 ± 4281	129368 ± 2231	41033 ± 686	96466 ± 980	31.40
<b>Road</b>	280690 ± 1881	434664 ± 1846	245770 ± 775	9095 ± 288	9.80
<b>Off-road-no-hotspots</b>	76413 ± 780	117712 ± 670	29007 ± 220	7959 ± 171	7.60
<b>Off-road-with-hotspots</b>	217887 ± 2076	117918 ± 1202	37188 ± 358	51622 ± 404	42.00

### 5.1.2 July 2005 survey

The map of the variations in the temperature on the *i*TTL site during the July 2005 survey is shown in Figure 5-9. According to the map, the temperature varied over a range of approximately 19.3 – 40.0 °C. As in the case of the February 2005 survey, the magnitude of this temperature variation could be due to the changes in temperature for morning, day, and afternoon measurements.

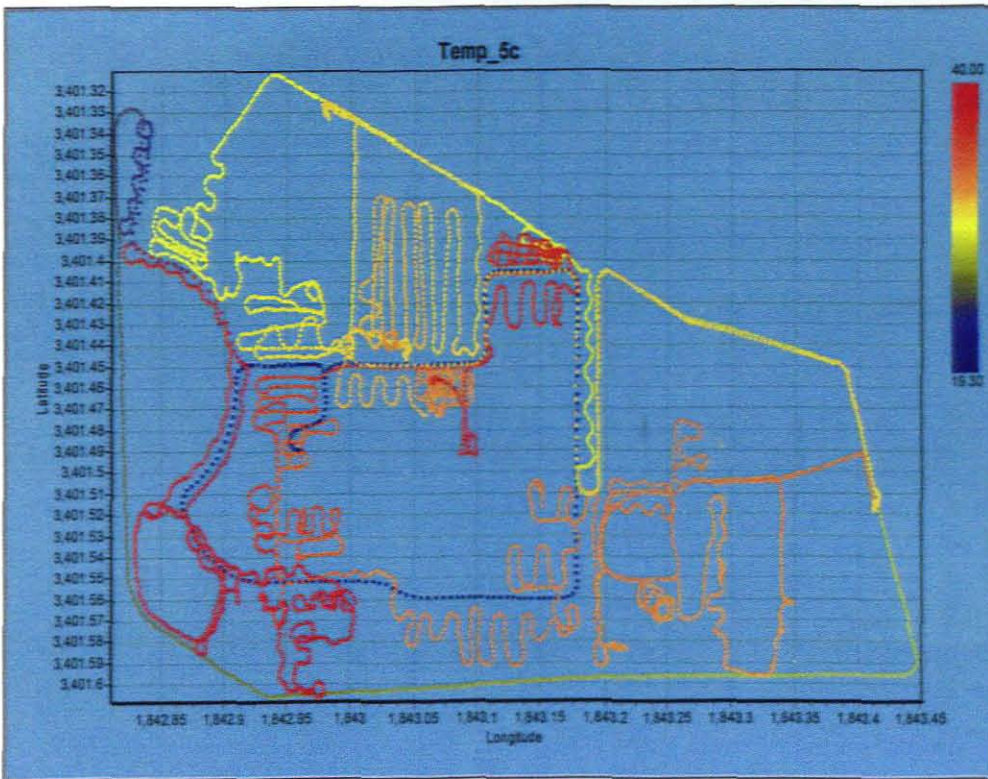


Figure 5-9: Map showing the temperature variation at sections surveyed on the site in July 2005. The range of the temperature is from 20 to 50 °C, and is shown on the top-right corner in the map.

The maps of Figure 5-10 and Figure 5-11 show the recorded variation of the count rate with the *i*TL MEDUSA detector, during the July 2005 survey. The displayed scale of variation is only 100 – 1100 counts per second for the map, and this limitation was made so as to give better contrast with the colour-coded presentation. The maps also show the locations of the different spots of interest on the *i*TL site.

In Figure 5-12 to Figure 5-13 are shown the raw  $\gamma$ -ray spectra that were acquired with the MEDUSA detector at locations NHS4 and NHS5 during the July 2005 survey.



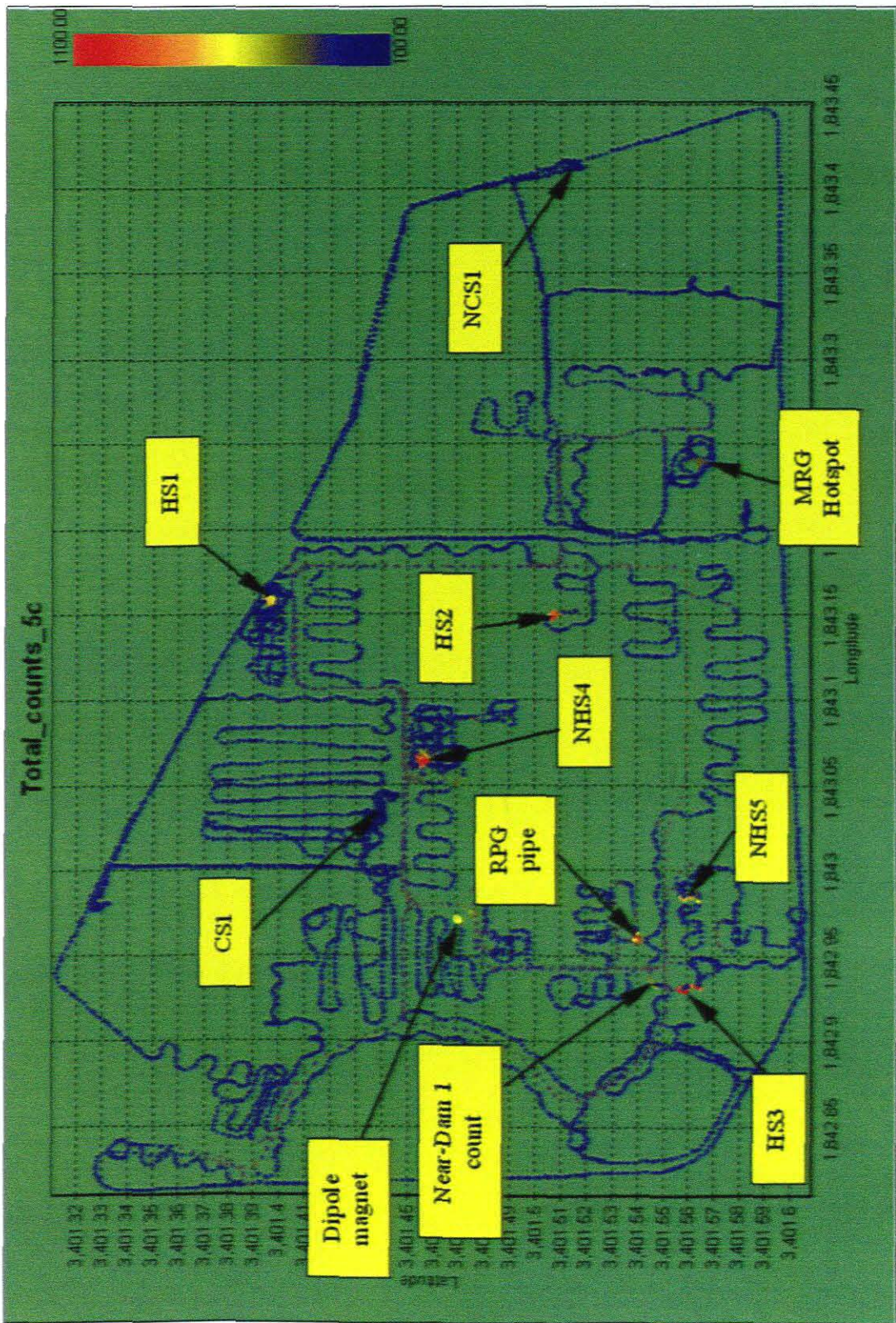


Figure 5-10: Map showing MEDUSA count rate obtained during the July 2005 survey. The range of the count rate is 100 - 1100 counts per second, and is shown on the top-right corner in the map. The GPS coordinates of the labeled locations are listed in Table 3-1.

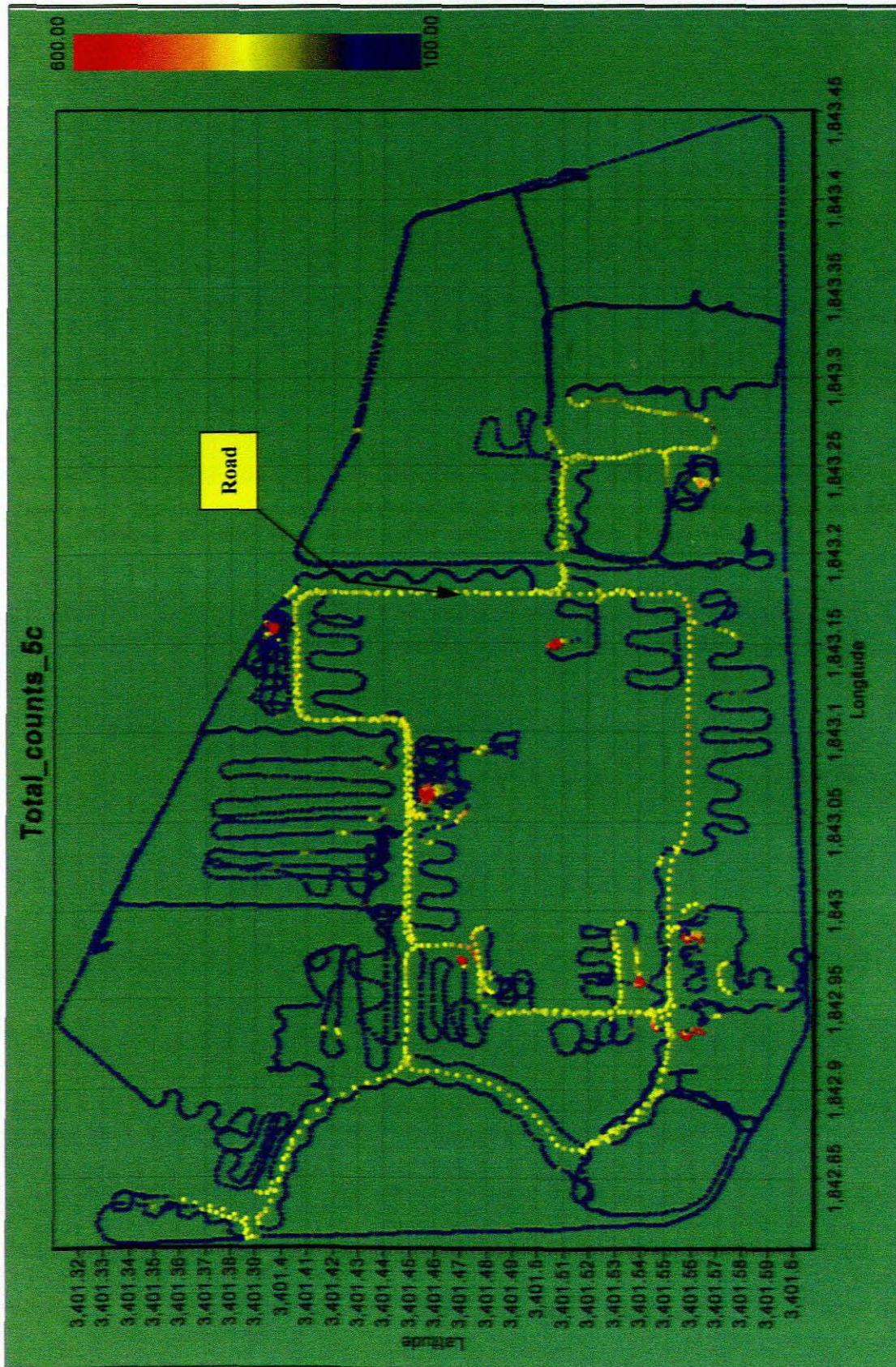


Figure 5-11: Map showing MEDUSA count rate obtained during the July 2005 survey. The range of the count rate is 100 - 600 counts per second, and is shown on the top-right corner in the map.

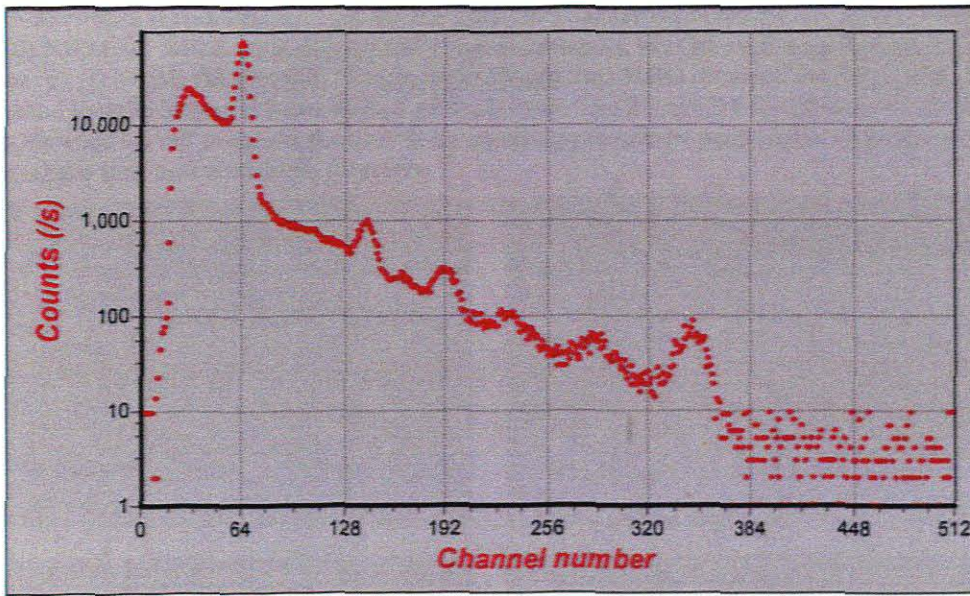


Figure 5-12: The raw gamma-ray spectrum acquired with MEDUSA in a stationary position over hotspot NHS4 in July 2005. Some of the visible peaks are labeled in Figure 5-6.

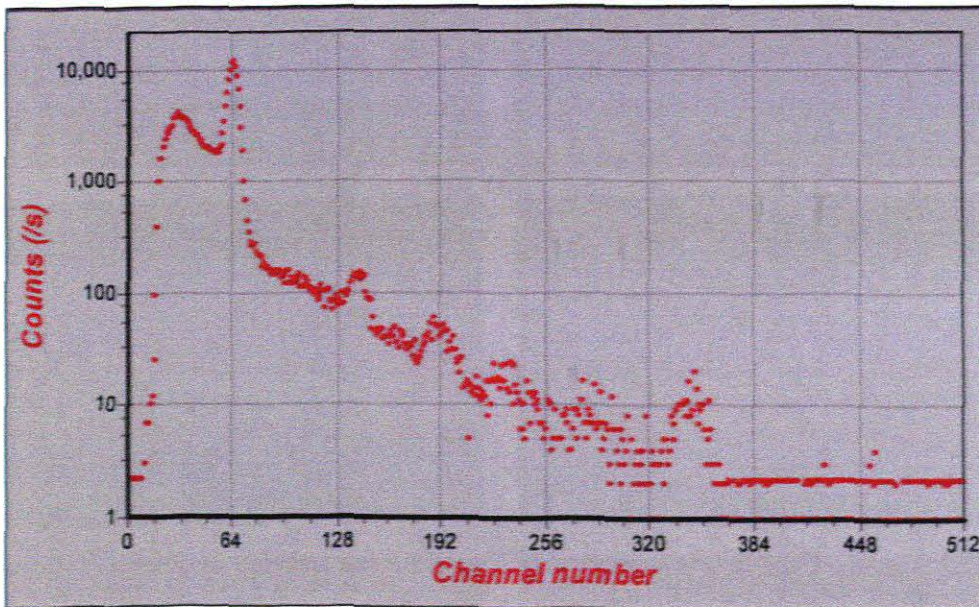
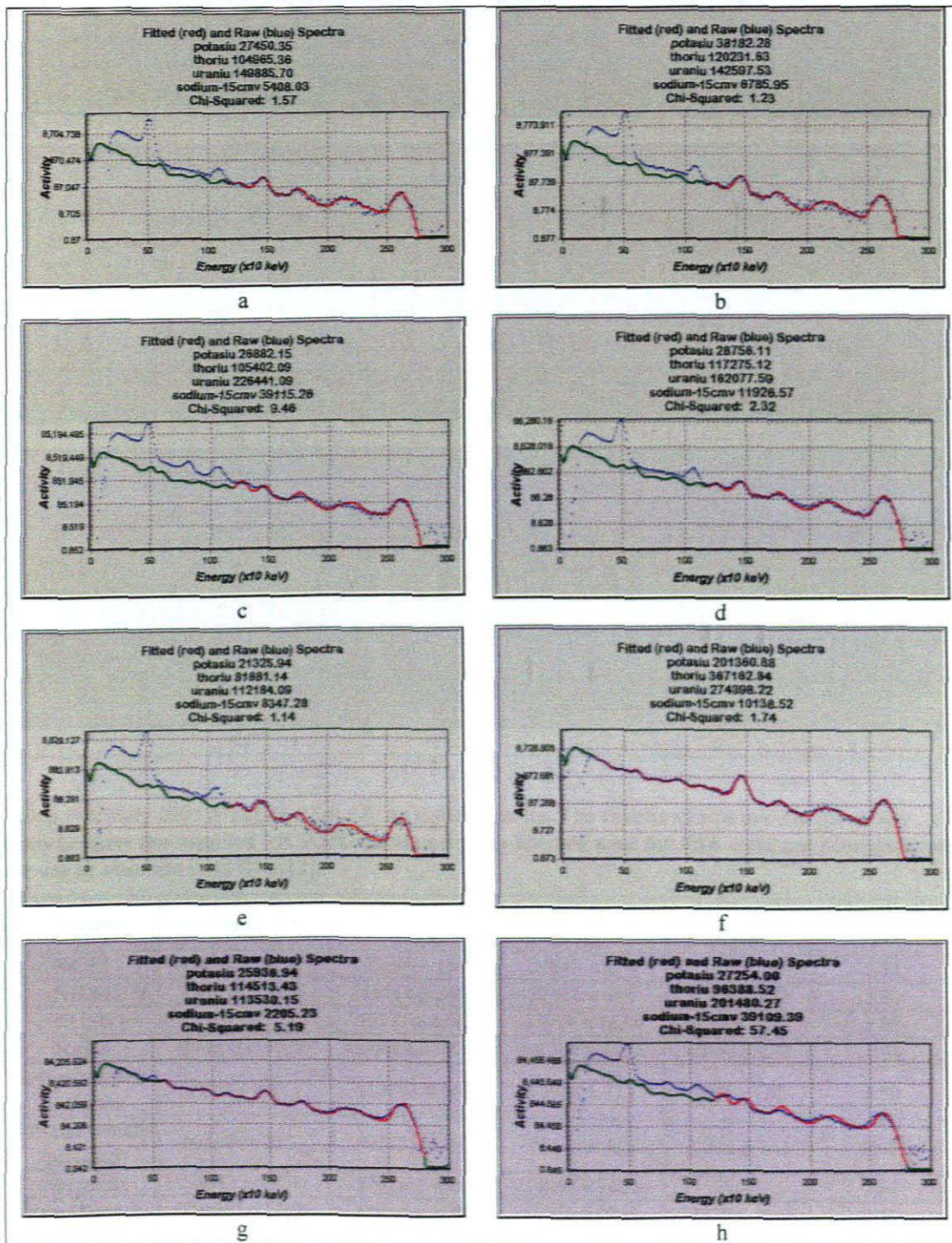


Figure 5-13: The raw gamma-ray spectrum acquired with MEDUSA in a stationary position over hotspot NHS5 in July 2005. Some of the visible peaks are labeled in Figure 5-6.

The results of FSA fits that were done are listed in Table 5-3. The spectrum obtained for a stationary measurement done next to the dipole magnet (geometry is obviously not flatbed) reveals that  $^{60}\text{Co}$   $\gamma$ -rays lines 1173.2 and 1332.5 keV are detected from the magnet. In Table 5-4 is given a list of the results that were obtained with the “Sum & Analyze” method in MPA.

Table 5-3: "Manual stabilization" fits for the July 2005 survey reported for (a) HS1, (b) HS2, (c) HS3, (d) NHS4, (e) NHS5, (f) Road, (g) Off-road-no-hotspots, (h) Off-road-with-hotspots, (i) CSI (February), (j) NCS1, (k) Magnet, (l) Dam near JBlock, (m) MRG hotspot, (n) RPG pipe. The underlined location does not have flatbed geometry (see also Figure 3-8 for photos of locations). The ROIs were varied to obtain the best fit by avoiding prominent peaks from anthropogenic radionuclides that had no standard spectra.



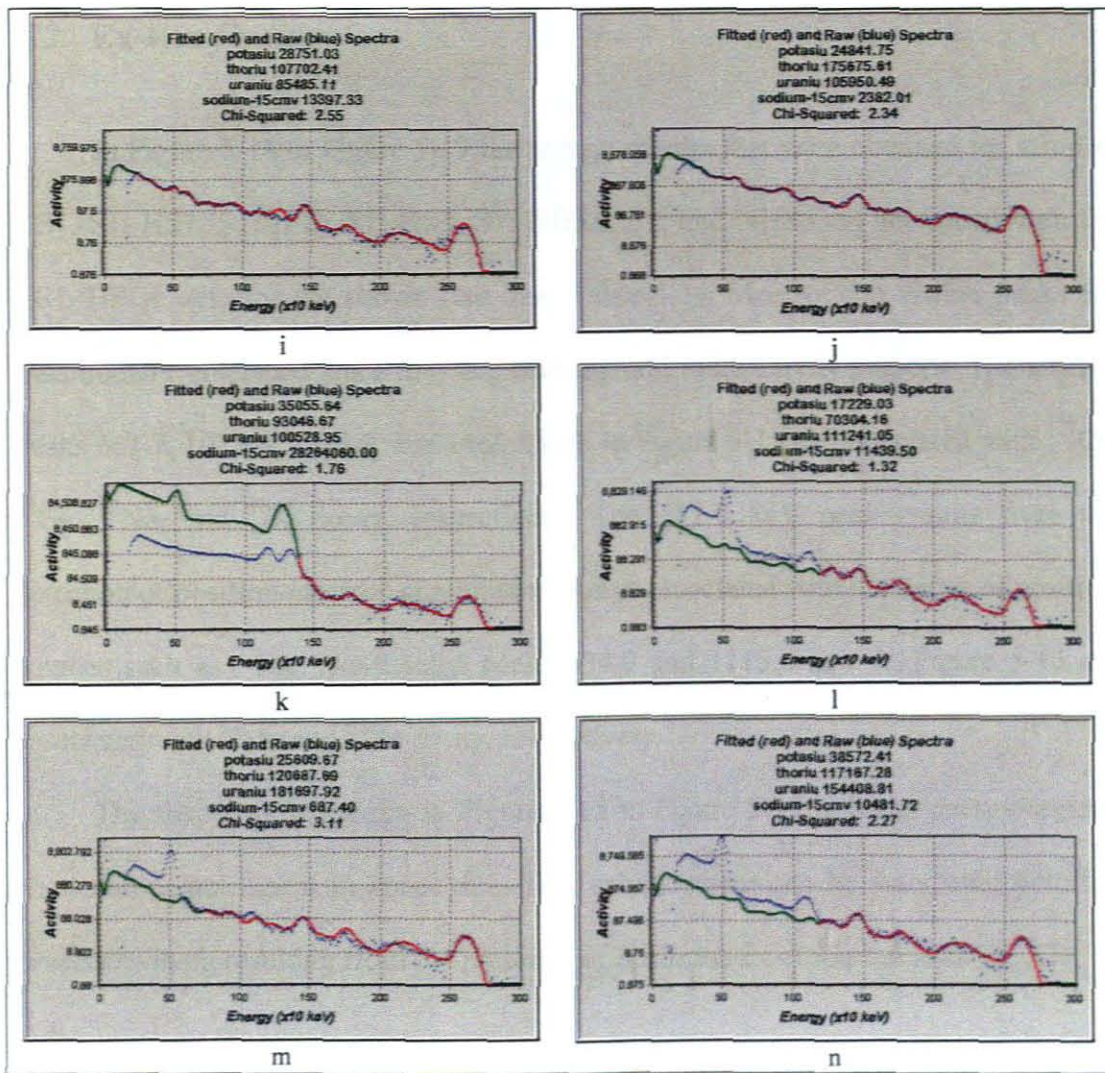


Table 5-4: July 2005 MEDUSA “Sum & Analyze” results. The results shown are not given any units because the supplied MCNPX-simulated  $\gamma$ -ray spectra used for FSA were not renormalized for use as absolute data [Hen02].

Location	MEDUSA: Sum & Analyze				Chi-squared
	$^{238}\text{U}$	$^{232}\text{Th}$	$^{40}\text{K}$	$^{22}\text{Na}$	
NCS1	105950 ± 2187	175676 ± 1949	24842 ± 579	2382 ± 276	2.34
NHS4	163414 ± 3970	115514 ± 2486	28411 ± 695	11736 ± 599	2.68
NHS5	113055 ± 7012	79777 ± 4347	21074 ± 1226	8159 ± 1049	1.39
Road	274373 ± 5379	366926 ± 5232	201294 ± 2156	10168 ± 828	1.76
Off-road-no-hotspots	112901 ± 801	113583 ± 652	25938 ± 212	2189 ± 152	6.70
Off-road-with-hotspots	204588 ± 2121	97645 ± 1162	28170 ± 349	38326 ± 382	58.00
Magnet	99862 ± 7371	92624 ± 4501	34061 ± 1627	N/A	1.62
Near-Dam 1	109567 ± 7093	67846 ± 4389	17216 ± 1233	11430 ± 1165	1.50
MRG hotspot	181218 ± 6751	120164 ± 4168	25624 ± 1341	716 ± 987	3.12
RPG pipe	159111 ± 7396	110818 ± 4594	37308 ± 1418	9684 ± 1107	2.83
CS1	85323 ± 3132	107176 ± 3130	28693 ± 977	13455 ± 538	2.69
HS1	150690 ± 5391	102361 ± 3375	27016 ± 963	5313 ± 750	1.69
HS2	143903 ± 7195	117947 ± 4580	37906 ± 1377	6524 ± 1023	1.29
HS3	225549 ± 4228	104124 ± 2356	26466 ± 680	39119 ± 766	9.20

## 5.2 Ex-situ findings

In Figure 5-14 to Figure 5-19 the energy spectra that were obtained for samples CS1, S1; HS1, S1; HS2, S1; HS3, S1; NHS4, S1; and NHS5, S1 measured with the ERL HPGe detector are shown (see also Table 3-1). Most of the visible peaks are intentionally unlabeled since they are from natural radioactivity sources. The labeled peaks 661.7, 1077.4, 1274.5, and 1460.8 keV in Figure 5-15 are associated with  $^{137}\text{Cs}$ ,  $^{68}\text{Ge}$ ,  $^{22}\text{Na}$ , and  $^{40}\text{K}$  decay, respectively. The 511.0 keV peak results from the detection of positron-electron annihilation  $\gamma$ -rays associated with the decay of positron sources such as  $^{22}\text{Na}$ . The labeled peaks 834.9 and 1115.6 keV in Figure 5-16 are associated with  $^{54}\text{Mn}$  and  $^{65}\text{Zn}$  decay, respectively.

The shape of the spectra in Figure 5-15 to Figure 5-19 at lower energy regions shows an enhancement in count rate. This enhancement can be associated with the *bremsstrahlung* resulting from the presence of positrons from sources such as  $^{68}\text{Ge}$ .

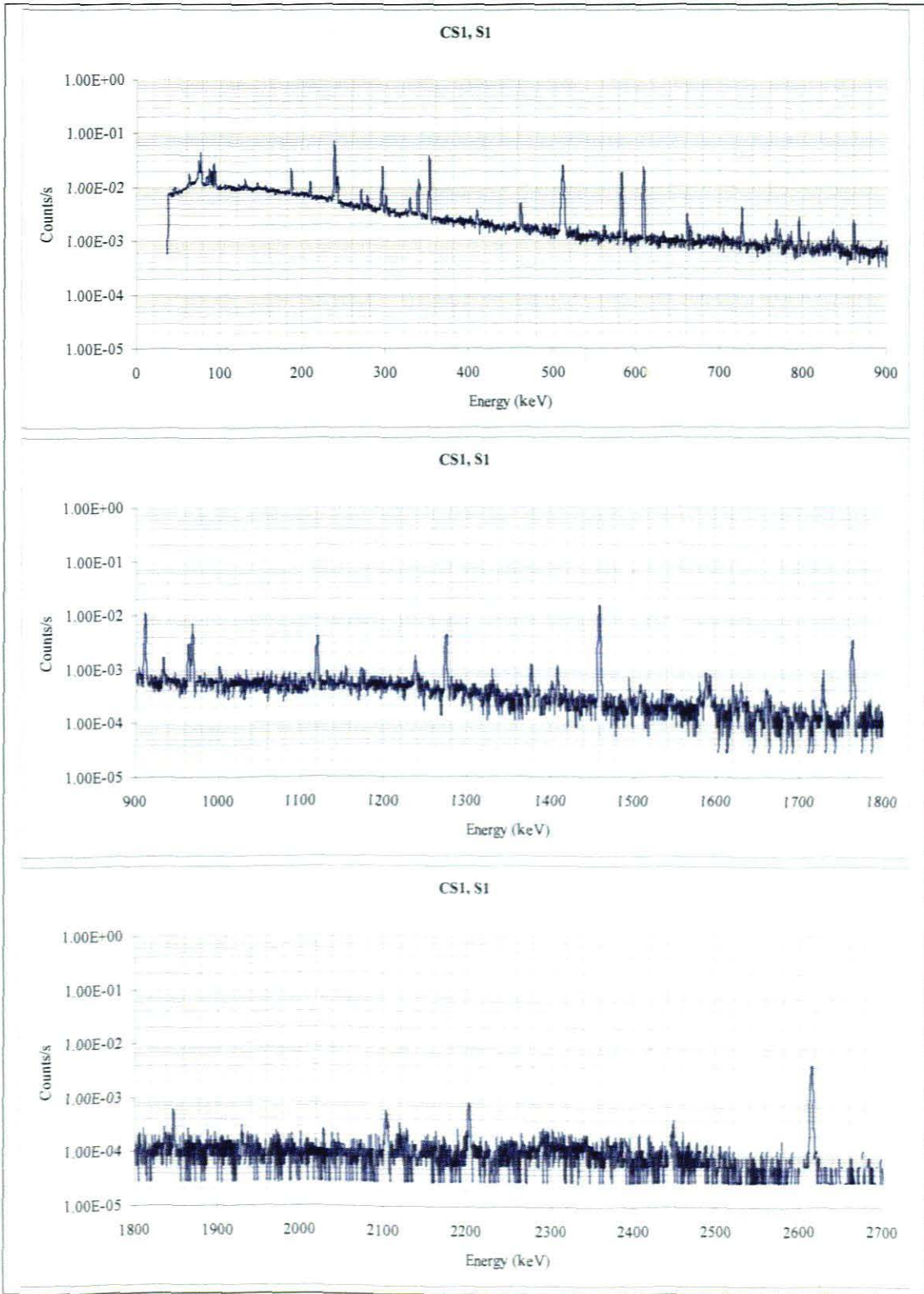


**Figure 5-14: Spectrum showing energy peaks (range = 0 – 2700 keV) identified with the HPGe detector in soil CS1, S1. The peaks are intentionally unlabeled since they are mostly from natural radioactivity sources. The peaks from anthropogenic sources are labeled in the spectra of HS1, S1 and HS3, S1, Figure 5-15 and Figure 5-17, respectively.**

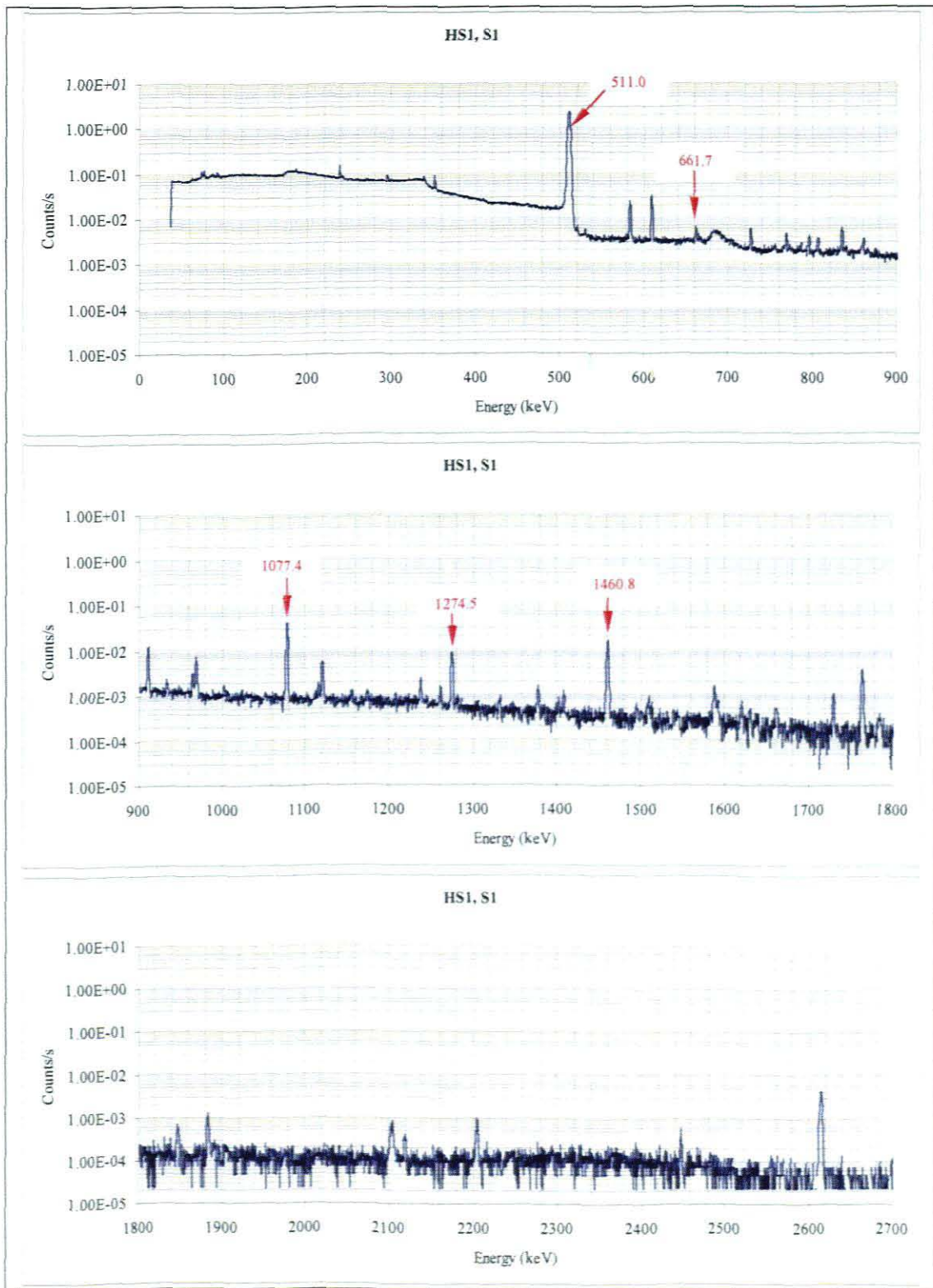


Figure 5-15: Spectrum showing energy peaks (range = 0 – 2700 keV) identified with the HPGe detector in soil HS1, S1. The labeled peaks 661.7, 1077.4, 1274.5, and 1460.8 keV are associated with  $^{137}\text{Cs}$ ,  $^{68}\text{Ge}$ ,  $^{22}\text{Na}$ , and  $^{40}\text{K}$  decay, respectively. The 511.0 keV peak results from the detection of positron-electron annihilation  $\gamma$ -rays associated with the decay of positron sources such as  $^{22}\text{Na}$ .



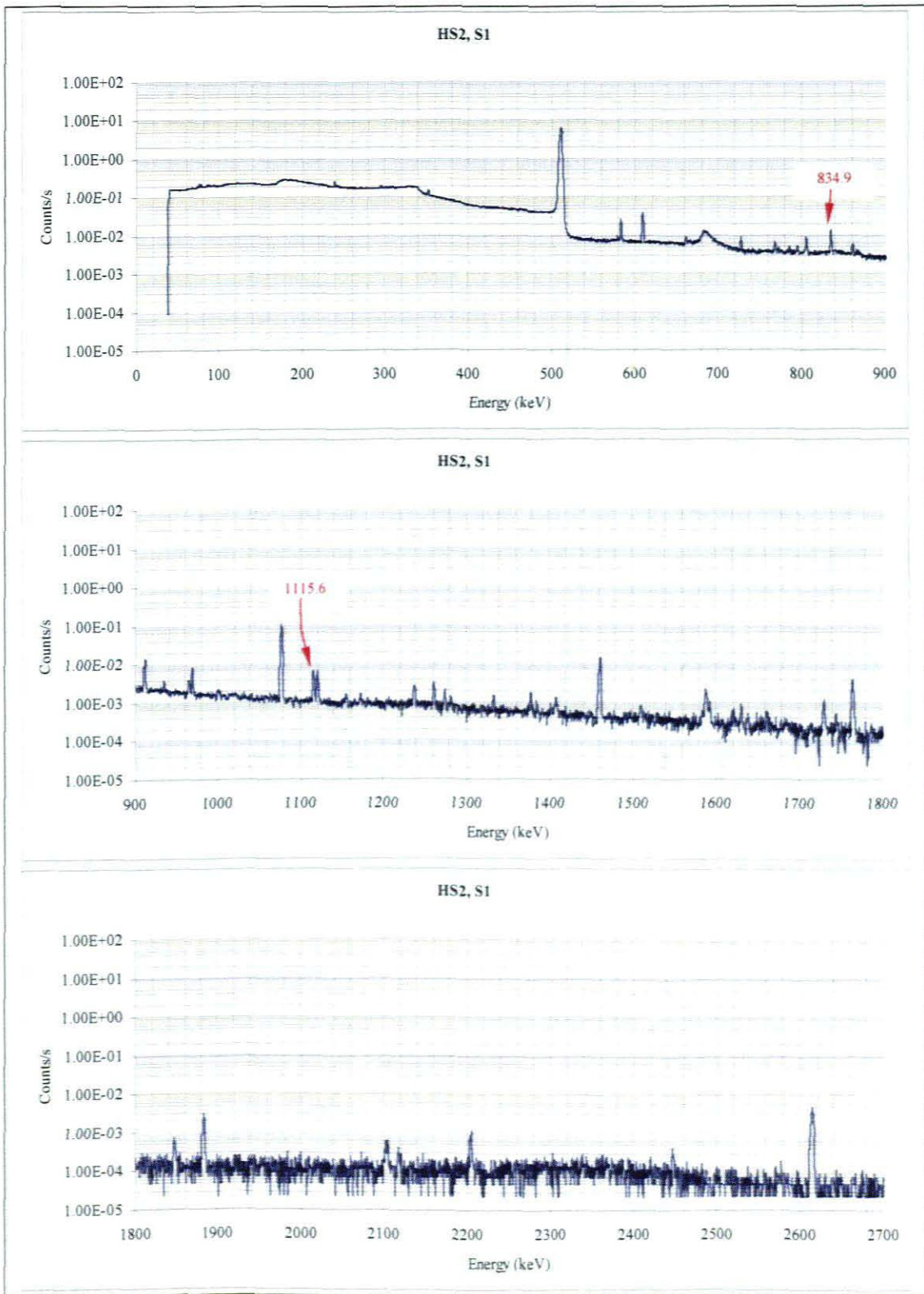
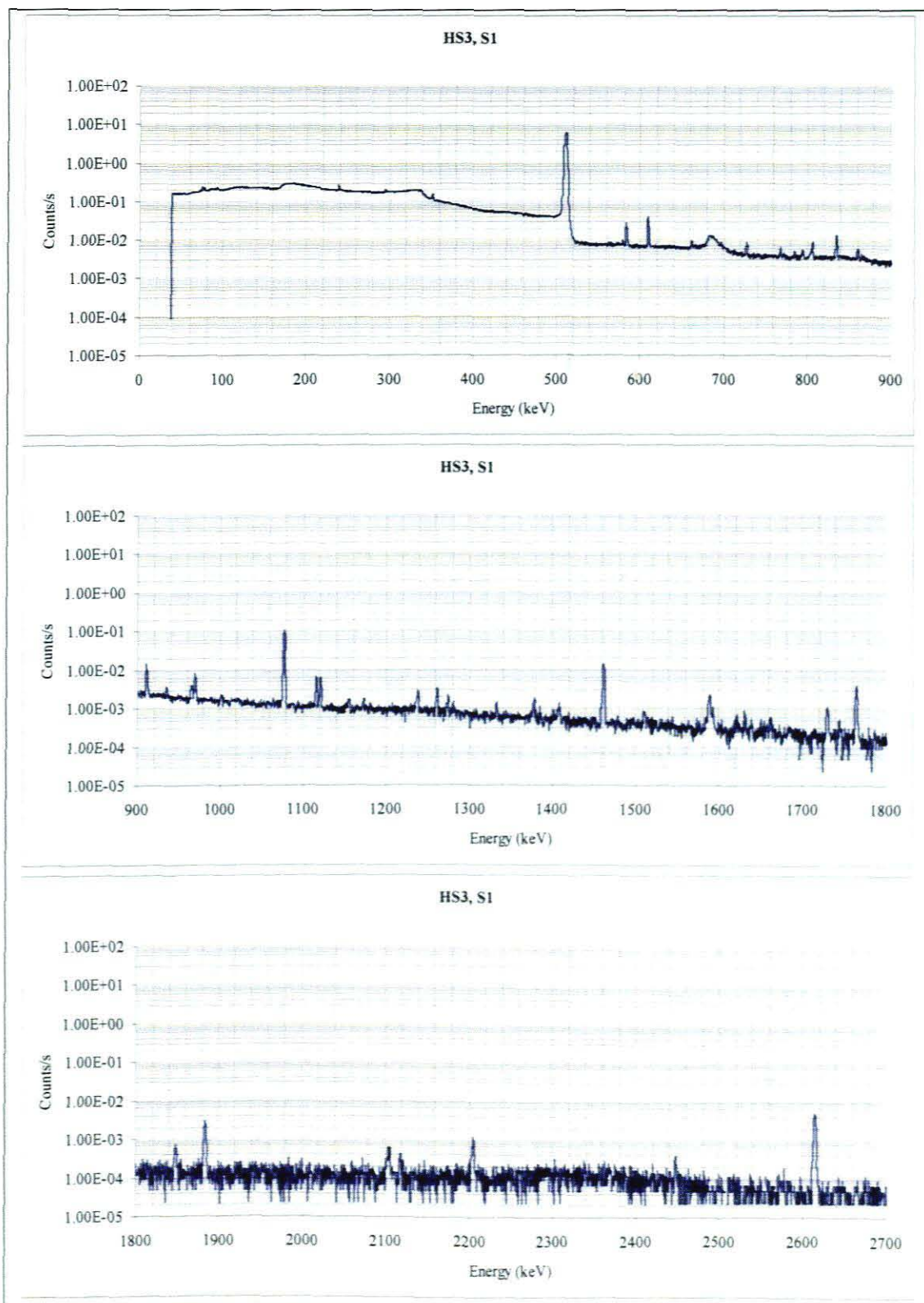
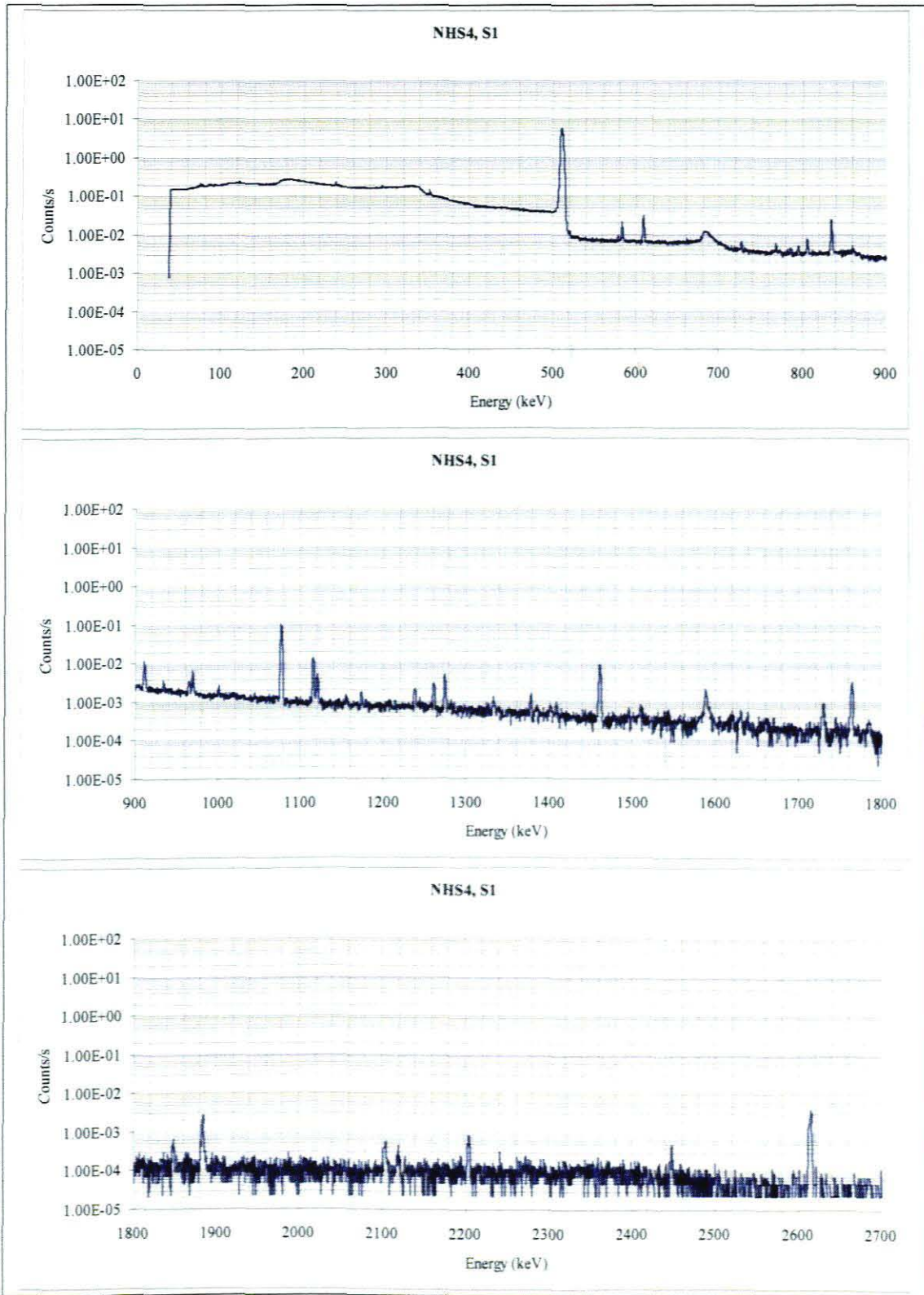


Figure 5-16: Spectrum showing energy peaks (range = 0 – 2700 keV) identified with the HPGe detector in soil HS2, S1. The labeled peaks 834.9 and 1115.6 keV are associated with  $^{54}\text{Mn}$  and  $^{65}\text{Zn}$  decay, respectively.



**Figure 5-17: Spectrum showing energy peaks (range = 0 – 2700 keV) identified with the HPGe detector in soil HS3, S1.**



**Figure 5-18: Spectrum showing energy peaks (range = 0 – 2700 keV) identified with the HPGe detector in soil NHS4, S1.**

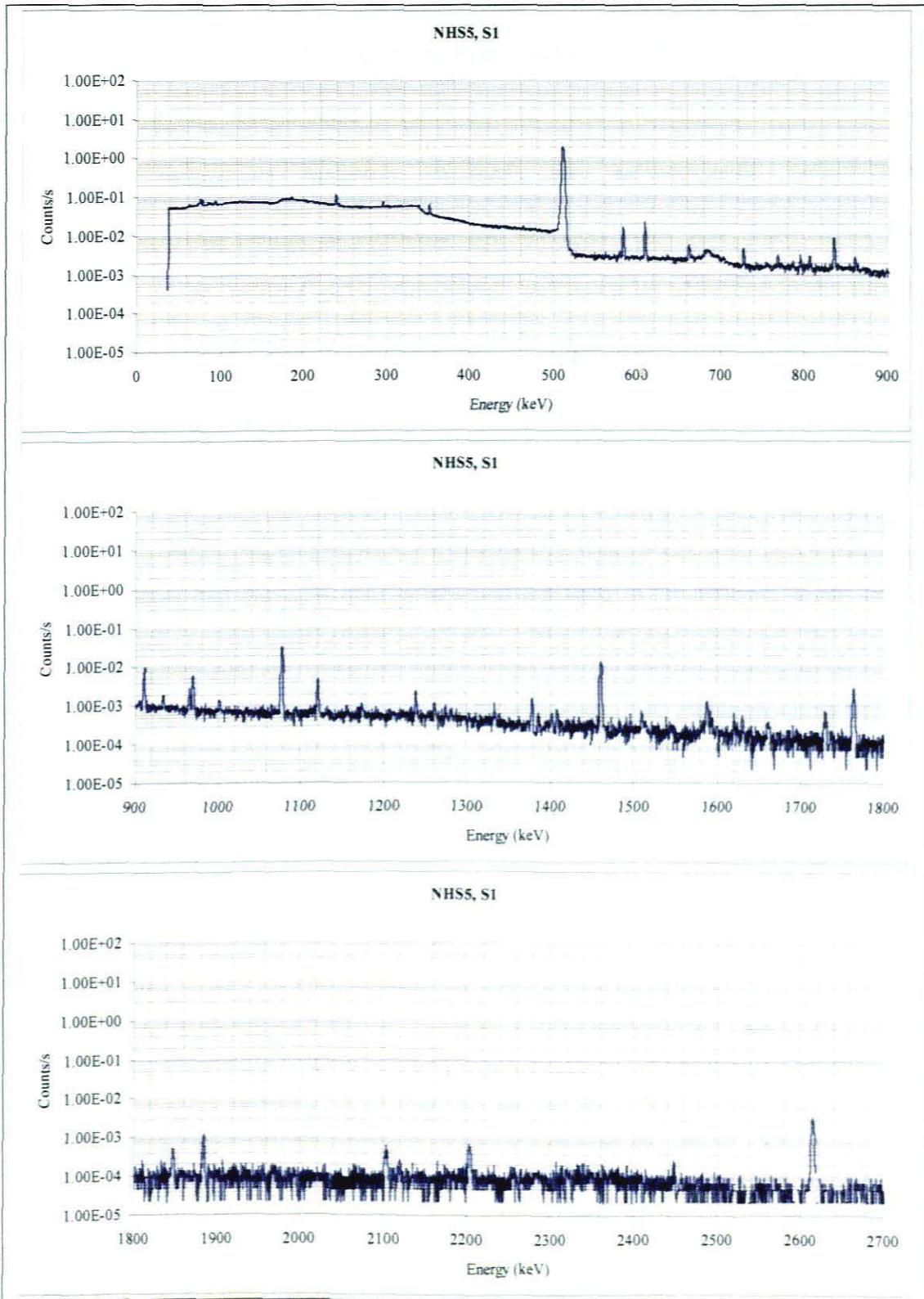


**Figure 5-19: Spectrum showing energy peaks (range = 0 – 2700 keV) identified with the HPGe detector in soil NHSS, S1.**

In Table 5-5 and Table 5-6 is listed the OxfordWin-MCA-reported HPGe count rate (in units  $\times 10^{-6}$  counts.s<sup>-1</sup>) for all the samples measured. The background counts

have been considered and subtracted for each of the  $\gamma$ -ray lines used. Tap water from the ERL was used for the background measurement. The activity concentration was calculated and the results listed in Table 5-7 and Table 5-8, for the identified naturally occurring radioactive materials (NORM) and anthropogenic radionuclides, respectively. The results of absorbed and effective dose are, from HPGe data, calculated for the NORM and anthropogenic radionuclides identified in the surveys, are listed in Table 5-9.

The results that show values with percentage uncertainties bigger than 70 % are taken as being equivalent to naught, and no percentage uncertainty is associated with them. This applies also for results with negative values. The "N/A" in some of the cells indicates that the  $\gamma$ -ray energy line was not used in the analysis of the data. A criterion of 20 % cut-off in percentage uncertainty associated with the net counts of the  $^{232}\text{Th}$  and  $^{238}\text{U}$  energy lines was used for excluding or including lines from the analyses of these radionuclides.

**Table 5-5: HPGe count rate reported for the February 2005 calibration spot and hotspot samples. Values of CS1 and HS1 are averaged over 5 samples (see Table 0-3 and Table 0-4 in Appendix 5 for results of the individual samples). The values listed here have all been corrected for background live time and are rounded off to three significant digits. The values are all quoted at the time of measurement.**

Radio-nuclide	E (keV)	Average count rate ( $\times 10^{-5}$ counts.s <sup>-1</sup> )			
		CS1	HS1	HS2, S1	HS3, S1
<sup>232</sup> Th	934.06	355 ± 60	552 ± 96	510 ± 78	728 ± 135
	1238.11	549 ± 61	805 ± 79	883 ± 80	2480 ± 161
	295.21	5820 ± 176	N/A	N/A	N/A
	351.92	10100 ± 198	13100 ± 661	11100 ± 689	17100 ± 1390
	1377.67	364 ± 52	593 ± 69	505 ± 52	1150 ± 95
	1764.49	1390 ± 68	1890 ± 79	1770 ± 73	3460 ± 109
	2204.21	359 ± 43	485 ± 45	486 ± 47	871 ± 60
<sup>238</sup> U	338.32	3280 ± 151	N/A	N/A	N/A
	727.33	1200 ± 86	1310 ± 143	1180 ± 133	2390 ± 225
	794.95	651 ± 66	847 ± 137	846 ± 217	1080 ± 390
	911.21	3800 ± 117	4750 ± 155	4670 ± 156	7470 ± 293
	966.87	2880 ± 126	3500 ± 183	3760 ± 169	5520 ± 317
<sup>40</sup> K	1460.83	6850 ± 142	7050 ± 149	6570 ± 161	5610 ± 162
<sup>68</sup> Ga	1077.40	44 ± 87	36900 ± 313	44900 ± 333	188000 ± 693
<sup>65</sup> Zn	1115.55	2 ± 42	1280 ± 83	2170 ± 91	46700 ± 525
<sup>22</sup> Na	1274.53	2070 ± 88	3610 ± 116	502 ± 105	20500 ± 258
<sup>137</sup> Cs	661.66	743 ± 74	865 ± 159	936 ± 138	923 ± 319
<sup>54</sup> Mn	834.848	285 ± 71	5820 ± 223	4100 ± 252	228000 ± 972

**Table 5-6: Average HPGe count rate reported for the July 2005 calibration spot and hotspot samples. Values of NCS1 are averaged over 5 samples (see Table 0-5 in Appendix 5 for results of the individual samples). The values listed here have all been corrected for background live time and are rounded off to three significant digits. The values are all quoted at the time of measurement.**

Radio-nuclide	E (keV)	Average count rate ( $\times 10^{-5}$ counts.s <sup>-1</sup> )		
		NCS1	NHS4, S1	NHS5, S1
<sup>232</sup> Th	934.06	701 ± 64	428 ± 87	399 ± 61
	1238.11	1100 ± 73	590 ± 66	667 ± 59
	295.21	10700 ± 216	N/A	N/A
	351.92	18600 ± 242	10600 ± 717	9000 ± 390
	1377.67	760 ± 62	366 ± 57	446 ± 52
	1764.49	2550 ± 85	1400 ± 70	1310 ± 61
	2204.21	650 ± 49	375 ± 47	346 ± 47
<sup>238</sup> U	338.32	6220 ± 167	N/A	N/A
	727.33	2290 ± 105	1080 ± 126	1020 ± 105
	794.95	1160 ± 80	454 ± 214	504 ± 165
	911.21	7350 ± 150	5680 ± 154	3240 ± 119
	966.87	5550 ± 155	2810 ± 164	2510 ± 131
<sup>40</sup> K	1460.83	8000 ± 147	3650 ± 110	5890 ± 126
<sup>68</sup> Ga	1077.40	79 ± 92	42900 ± 328	13900 ± 193
<sup>65</sup> Zn	1115.55	-17 ± 41	5610 ± 131	82 ± 43
<sup>22</sup> Na	1274.53	35 ± 63	1860 ± 119	178 ± 93
<sup>137</sup> Cs	661.66	453 ± 72	265 ± 152	1080 ± 96
<sup>54</sup> Mn	834.848	425 ± 81	7830 ± 189	2870 ± 114

**Table 5-7: Activity concentrations, from HPGe data, calculated for the naturally occurring radioactive materials (NORM) identified in the surveys. Results of CS1, HS1, and NCS1 are averaged over 5 samples (see Table 0-6 in Appendix 5 for results of the individual samples).**

		Sample code	HPGe Activity Concentration (Bq.kg <sup>-1</sup> )		
			<sup>238</sup> U	<sup>232</sup> Th	<sup>40</sup> K
February 2005	CS1	7.83 ± 0.25	8.51 ± 0.24	52.94 ± 4.23	
	HS1	11.72 ± 1.84	10.86 ± 0.83	57.45 ± 4.49	
	HS2, S1	11.13 ± 0.75	10.86 ± 0.87	54.19 ± 1.61	
	HS3, S1	26.04 ± 7.88	21.35 ± 1.52	54.53 ± 1.82	
July 2005	NCS1	13.94 ± 0.54	15.01 ± 1.29	57.78 ± 2.72	
	NHS4, S1	8.60 ± 0.75	8.66 ± 0.09	29.75 ± 0.97	
	NHS5, S1	8.57 ± 0.53	7.53 ± 0.70	48.09 ± 1.28	

**Table 5-8: Activity concentrations, from HPGe data, calculated for the anthropogenic radionuclides identified in February and July 2005. Results of CS1, HS1, and NCS1 are averaged over 5 samples (see Table 0-7 in Appendix 5 for results of the individual samples).**

		Sample code	HPGe Activity concentration (Bq.kg <sup>-1</sup> )				
			<sup>68</sup> Ge	<sup>65</sup> Zn	<sup>22</sup> Na	<sup>137</sup> Cs	<sup>54</sup> Mn
February 2005	CS1	1.23 ± 1.51	0.00 ± 0.04	1.64 ± 0.37	0.41 ± 0.08	0.19 ± 0.04	
	HS1	1056.98 ± 459.51	2.30 ± 1.37	3.01 ± 0.38	0.51 ± 0.17	4.10 ± 2.78	
	HS2, S1	1336.15 ± 267.49	4.02 ± 0.83	0.43 ± 0.13	0.56 ± 0.13	2.96 ± 1.34	
	HS3, S1	6533.49 ± 1307.30	100.77 ± 20.27	20.59 ± 4.20	0.65 ± 0.25	192.53 ± 0.25	
July 2005	NCS1	1.77 ± 0.90	-0.02 ± 0.01	0.03 ± 0.04	0.24 ± 0.16	0.24 ± 0.04	
	NHS4, S1	1097.34 ± 219.69	8.81 ± 1.78	1.51 ± 0.08	0.16 ± 0.09	4.96 ± 2.22	
	NHS5, S1	357.01 ± 71.59	0.13 ± 0.07	0.14 ± 0.07	0.63 ± 0.13	1.82 ± 0.82	

**Table 5-9: Absorbed and effective dose, from HPGe data, calculated for the NORM and anthropogenic radionuclides identified in February and July 2005. The absorbed dose results for anthropogenic radionuclides are a sum of contributions from each radionuclide.**

		NORM		Anthropogenic (Plane source at 1 cm)		Anthropogenic (Plane source at 10 cm)	
		Absorbed dose (nGy.h <sup>-1</sup> )	Effective dose (μSv.y <sup>-1</sup> )	Absorbed dose (nGy.h <sup>-1</sup> )	Effective dose (μSv.y <sup>-1</sup> )	Absorbed dose (nGy.h <sup>-1</sup> )	Effective dose (μSv.y <sup>-1</sup> )
February 2005	CS1	10.96 ± 0.21	13.45 ± 0.26	0.89 ± 0.17	1.09 ± 0.20	0.23 ± 0.04	0.29 ± 0.05
	HS1	14.37 ± 0.89	17.62 ± 1.09	13.51 ± 4.60	16.57 ± 5.64	3.38 ± 1.14	4.14 ± 1.40
	HS2, S1	13.96 ± 0.61	17.12 ± 0.74	15.00 ± 2.66	18.40 ± 3.26	3.73 ± 0.66	4.57 ± 0.81
	HS3, S1	27.20 ± 3.68	33.36 ± 4.52	152.72 ± 31.10	187.30 ± 38.14	38.08 ± 7.73	46.70 ± 9.47
July 2005	NCS1	17.92 ± 0.37	21.97 ± 0.45	0.15 ± 0.04	0.18 ± 0.05	0.04 ± 0.01	0.04 ± 0.01
	NHS4, S1	10.44 ± 0.43	12.80 ± 0.53	14.50 ± 2.29	17.78 ± 2.81	3.61 ± 0.57	4.43 ± 0.70
	NHS5, S1	10.51 ± 0.50	12.89 ± 0.62	4.30 ± 0.75	5.27 ± 0.92	1.07 ± 0.19	1.31 ± 0.23

From the results in Table 5-7 it is observed that the <sup>238</sup>U and <sup>232</sup>Th activity concentrations increase by almost a factor of 2 when moving from calibration spot CS1 to calibration spot NCS1. The results in Table 5-8 show that all the hotspot samples are contaminated with the radionuclide <sup>68</sup>Ge. The presence of <sup>68</sup>Ge in the

gully hotspot sample HS3, S1 is associated to the radioactive effluent waste released into the dam from the iTL Radionuclide Production Group (RPG). The same cannot be said about the other hotspot samples; the presence of  $^{68}\text{Ge}$  in the other hotspots does not seem to be related to the controlled waste release from RPG.

The results also show low activity concentrations (zero at calibration spots) for  $^{65}\text{Zn}$  in all the samples except HS3, S1. Low activity concentrations (zero for NCS1) are observed for  $^{22}\text{Na}$  in all samples except HS3, S1. The absence of  $^{22}\text{Na}$  at location NCS1, also confirmed by the FSA fit of Table 5-3(j), is possibly due to the absence of irrigation at this location. As expected in the case of fallout contamination, the presence of  $^{137}\text{Cs}$  is evidenced in all the samples. Contamination with  $^{54}\text{Mn}$  is seen in all the samples, although it is not expected in location NCS1 due to no irrigation there. A possible explanation for this result could be in the poorly-resolved closeness of 834.85 and 835.71 keV peaks of  $^{54}\text{Mn}$  and  $^{228}\text{Ac}$ , respectively, affecting the ROI selection. This problem of a nearby peak also affected the 1115.55 keV  $^{65}\text{Zn}$  peak, which is closely located to a prominent 1120.29 keV  $^{214}\text{Bi}$  peak (see Figure 5-20).

The results of Table 5-9 show that the highest effective dose result of 187.3  $\mu\text{Sv}\cdot\text{y}^{-1}$  is still well under 1  $\text{mSv}\cdot\text{y}^{-1}$  set as recommended dose limit on effective dose of per individual member of public [vRo04].



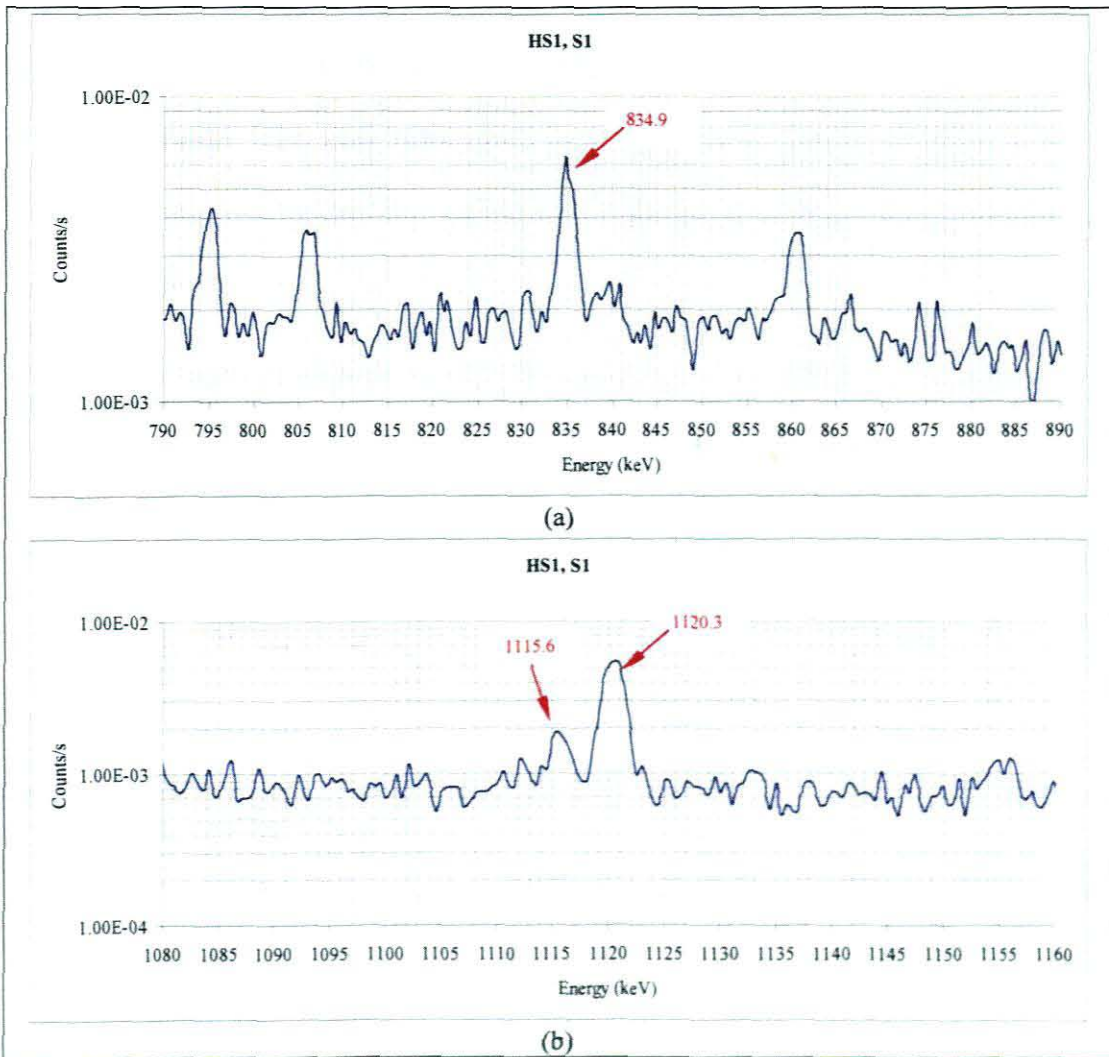


**Figure 5-20:** Spectrum showing that energy peaks (a) 834.9 and (b) 1115.5 keV, from  $^{54}\text{Mn}$  and  $^{65}\text{Zn}$ , respectively, identified with the HPGe detector in soil HS1, S1, are affected by nearby peaks.

### 5.3 Normalised in-situ findings

The normalization factors were obtained by considering the MEDUSA “Sum & Analyze” results (*MSA*) of the stationary measurement made over the spot CS1 (of February 2005), and the average HPGe activity concentration results ( $A_{\text{HPGe}}$ ) from the soil samples CS1, S1 to CS1, S5. For each radionuclide, the normalization factor was calculated as  $A_{\text{HPGe}}/MSA$ , and the results are listed in Table 5-10. A similar calculation was done considering the results from the soil samples NCS1, S1 to NCS1, S5 (of July 2005) and the results are listed in Table 0-16 in Appendix 7. After

the testing of the normalisation factors from these two calculations, those of CS1 were chosen to be used in this study (see Appendix 5).

In Table 5-11 and Table 5-12 are listed the normalized MEDUSA activity concentration results for the identified NORM and anthropogenic radionuclides, respectively.

**Table 5-10: Normalization factors used for the February and July 2005 MEDUSA activity concentration results.**

Location	Radio-nuclide	Average HPGe (Bq.kg <sup>-1</sup> )	MEDUSA	Normalisation factors (×10 <sup>-6</sup> )
CS1	<sup>238</sup> U	7.83 ± 0.25	71566 ± 2415	109.0 ± 5.0
	<sup>232</sup> Th	8.51 ± 0.24	115187 ± 2084	73.9 ± 2.4
	<sup>40</sup> K	52.94 ± 4.23	34298 ± 711	1540.0 ± 127.0
	<sup>22</sup> Na	1.64 ± 0.37	10203 ± 556	161.0 ± 37.0

**Table 5-11: Normalized activity concentrations, from MEDUSA data, extracted for the NORM radionuclides identified in the surveys.**

	Sample code	MEDUSA Activity concentration (Bq.kg <sup>-1</sup> )		
		<sup>238</sup> U	<sup>232</sup> Th	<sup>40</sup> K
February 2005	HS1	11.12 ± 0.57	7.64 ± 0.28	46.11 ± 3.87
	HS2	14.21 ± 0.95	9.17 ± 0.43	62.00 ± 5.47
	HS3	39.02 ± 1.86	9.56 ± 0.36	63.34 ± 5.34
	Road	30.69 ± 1.43	32.12 ± 1.07	379.36 ± 31.34
	Off-road-no-hotspots	8.86 ± 0.39	8.70 ± 0.29	44.77 ± 3.71
	Off-road-with-hotspots	23.83 ± 1.12	8.71 ± 0.30	57.40 ± 4.77
July 2005	NCS1	11.59 ± 0.58	12.98 ± 0.45	38.35 ± 3.29
	NHS4	17.87 ± 0.93	8.54 ± 0.34	43.85 ± 3.78
	NHS5	12.36 ± 0.96	5.90 ± 0.38	32.53 ± 3.29
	Road	30.00 ± 1.50	27.12 ± 0.98	310.71 ± 25.87
	Off-road-no-hotspots	12.35 ± 0.58	8.39 ± 0.28	40.04 ± 3.32
	Off-road-with-hotspots	22.37 ± 1.06	7.22 ± 0.25	43.48 ± 3.63

**Table 5-12: Normalized activity concentrations, from MEDUSA data, extracted for the anthropogenic radionuclides identified in the surveys. The results are for  $^{22}\text{Na}$  alone because, so far, only the standard spectrum for this radionuclide is available for data analysis.**

		Sample code	MEDUSA Activity concentration ( $\text{Bq.kg}^{-1}$ )
			$^{22}\text{Na}$
February 2005		HS1	$2.76 \pm 0.64$
		HS2	$1.28 \pm 0.33$
		HS3	$15.53 \pm 3.57$
		Road	$1.46 \pm 0.34$
		Off-road-no-hotspots	$1.28 \pm 0.30$
		Off-road-with-hotspots	$8.31 \pm 1.91$
July 2005		NCS1	$0.38 \pm 0.10$
		NHS4	$1.89 \pm 0.44$
		NHS5	$1.31 \pm 0.35$
		Road	$1.64 \pm 0.40$
		Off-road-no-hotspots	$0.35 \pm 0.08$
		Off-road-with-hotspots	$6.17 \pm 1.42$

**Table 5-13: Absorbed and effective dose, from MEDUSA data, calculated for the NORM and anthropogenic radionuclides identified in the surveys.**

		NORM		Anthropogenic (Plane source at 1 cm)		Anthropogenic (Plane source at 10 cm)	
		Absorbed dose ( $\text{nGy.h}^{-1}$ )	Effective dose ( $\mu\text{Sv.y}^{-1}$ )	Absorbed dose ( $\text{nGy.h}^{-1}$ )	Effective dose ( $\mu\text{Sv.y}^{-1}$ )	Absorbed dose ( $\text{nGy.h}^{-1}$ )	Effective dose ( $\mu\text{Sv.y}^{-1}$ )
February 2005	CS1	$10.96 \pm 0.21$	$13.45 \pm 0.26$	$0.74 \pm 0.17$	$0.91 \pm 0.21$	$0.20 \pm 0.05$	$0.24 \pm 0.06$
	HS1	$11.67 \pm 0.31$	$14.32 \pm 0.39$	$1.24 \pm 0.29$	$1.52 \pm 0.35$	$0.33 \pm 0.08$	$0.40 \pm 0.09$
	HS2	$14.69 \pm 0.50$	$18.02 \pm 0.61$	$0.58 \pm 0.15$	$0.71 \pm 0.18$	$0.15 \pm 0.04$	$0.19 \pm 0.05$
	HS3	$26.44 \pm 0.89$	$32.43 \pm 1.09$	$6.98 \pm 1.60$	$8.56 \pm 1.97$	$1.85 \pm 0.42$	$2.27 \pm 0.52$
	Road	$49.40 \pm 1.48$	$60.59 \pm 1.81$	$0.66 \pm 0.15$	$0.81 \pm 0.19$	$0.17 \pm 0.04$	$0.21 \pm 0.05$
	Off-road-no-hotspots	$10.98 \pm 0.25$	$13.47 \pm 0.30$	$0.58 \pm 0.13$	$0.71 \pm 0.16$	$0.15 \pm 0.04$	$0.19 \pm 0.04$
	Off-road-with-hotspots	$22.89 \pm 0.68$	$18.66 \pm 0.56$	$3.74 \pm 0.86$	$4.58 \pm 1.05$	$0.99 \pm 0.23$	$1.22 \pm 0.28$
July 2005	NCS1	$14.79 \pm 0.32$	$18.14 \pm 0.39$	$0.17 \pm 0.04$	$0.21 \pm 0.05$	$0.05 \pm 0.01$	$0.06 \pm 0.01$
	NHS4	$15.24 \pm 0.46$	$18.69 \pm 0.57$	$0.85 \pm 0.20$	$1.04 \pm 0.24$	$0.23 \pm 0.05$	$0.28 \pm 0.06$
	NHS5	$10.63 \pm 0.47$	$13.04 \pm 0.57$	$0.59 \pm 0.16$	$0.72 \pm 0.19$	$0.16 \pm 0.04$	$0.19 \pm 0.05$
	Road	$43.20 \pm 1.30$	$52.98 \pm 1.59$	$0.74 \pm 0.18$	$0.90 \pm 0.22$	$0.20 \pm 0.05$	$0.2 \pm 0.06$
	Off-road-no-hotspots	$12.44 \pm 0.30$	$15.26 \pm 0.37$	$0.16 \pm 0.04$	$0.19 \pm 0.05$	$0.04 \pm 0.01$	$0.05 \pm 0.01$
	Off-road-with-hotspots	$16.51 \pm 0.51$	$20.24 \pm 0.63$	$2.77 \pm 0.64$	$3.40 \pm 0.78$	$0.74 \pm 0.17$	$0.90 \pm 0.21$

The results in Table 5-11 show a high activity concentration of  $^{40}\text{K}$  in the Road. This must be related to the radionuclide content of the materials used in road construction. Compared to the world average [UNS00] of  $400 \text{ Bq.kg}^{-1}$  for  $^{40}\text{K}$ , the reported  $^{40}\text{K}$  activity concentration in the Road is still 10 and 26 % smaller for

February and July 2005, respectively. The world average values of activity concentration for  $^{238}\text{U}$  and  $^{232}\text{Th}$  in soil are 35 and 30 Bq.kg<sup>-1</sup>, respectively [UNS00].

## ***5.4 Comparison of results***

### **5.4.1 Current vs. June 2004 count rate maps**

In Figure 5-21 to Figure 5-23 are shown sections of MEDUSA count rate maps obtained during the June 2004, July 2005, and February 2005 surveys. Although the surveyed areas were not precisely the same for all the surveys, these sections still show good agreement regarding the identification and location of hotspots on the iTL site. The variation in shape and size of hotspots [for the different surveys] is partly due to the type of measurement done on the spot during that particular survey, i.e. stationary or non-stationary measurement. The purple oval labels #1, #2, and #3 in Figure 5-21 give highlight to non-stationary measurements over the RPG pipe, the gully, and boundary of Dam 1, respectively.

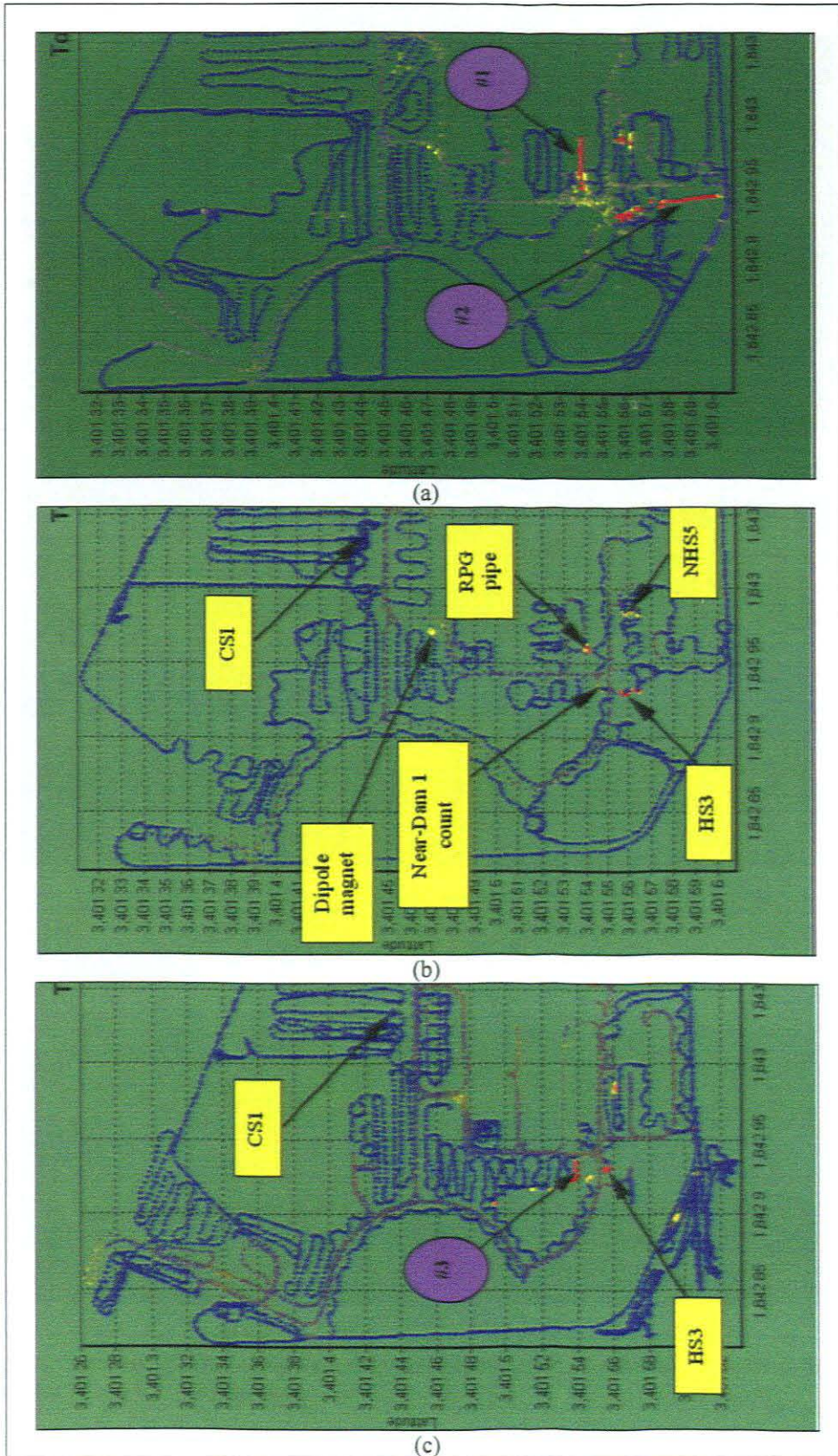


Figure 5-21: Sections of MEDUSA count rate maps obtained during the (a) June 2004, (b) July 2005, and (c) February 2005 surveys. The purple oval labels #1, #2, and #3 give highlight to non-stationary measurements over the RPG pipe, the gully, and boundary of Dam 1, respectively.

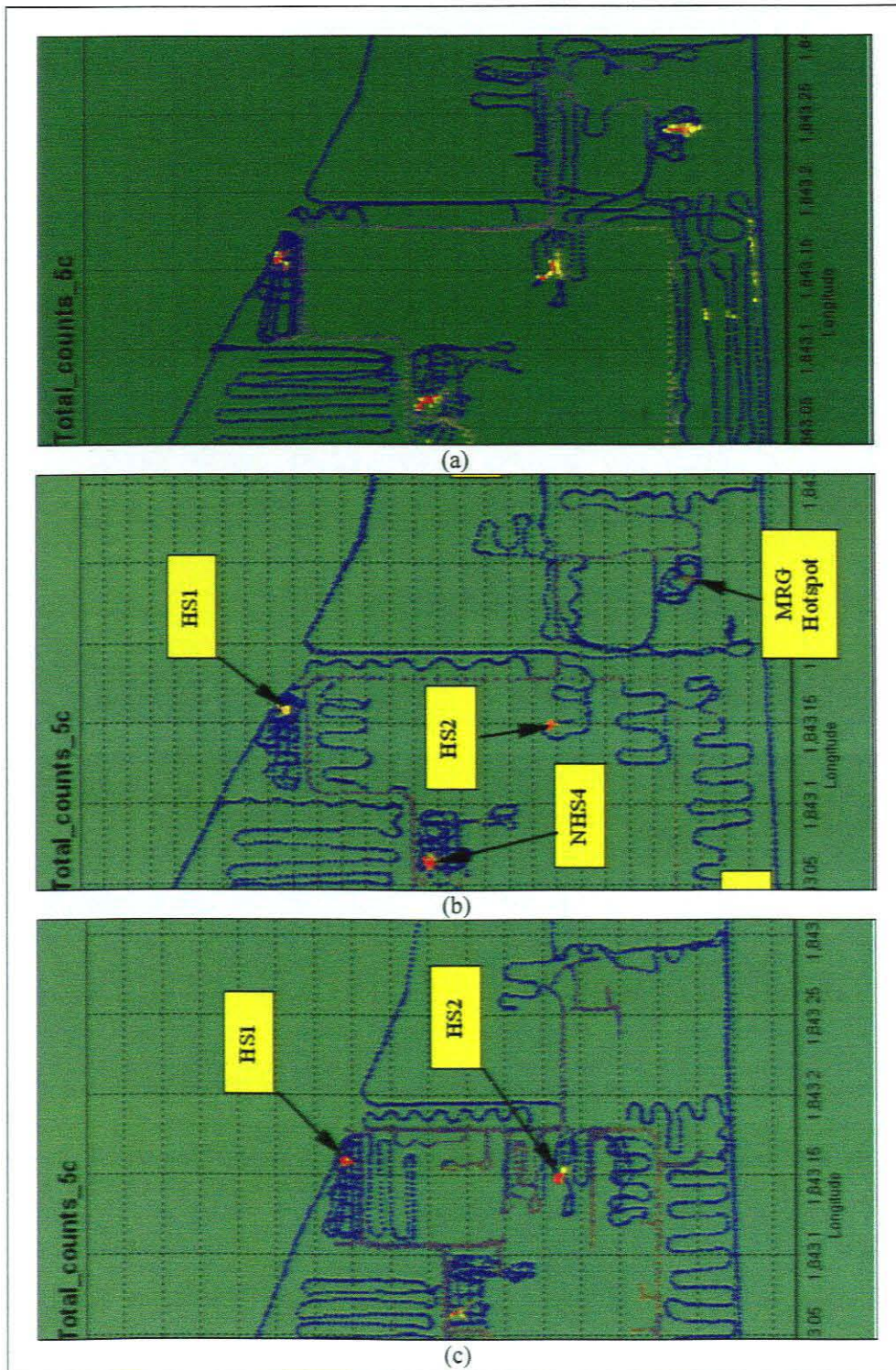


Figure 5-22: Sections of MEDUSA count rate maps obtained during the (a) June 2004, (b) July 2005, and (c) February 2005 surveys.

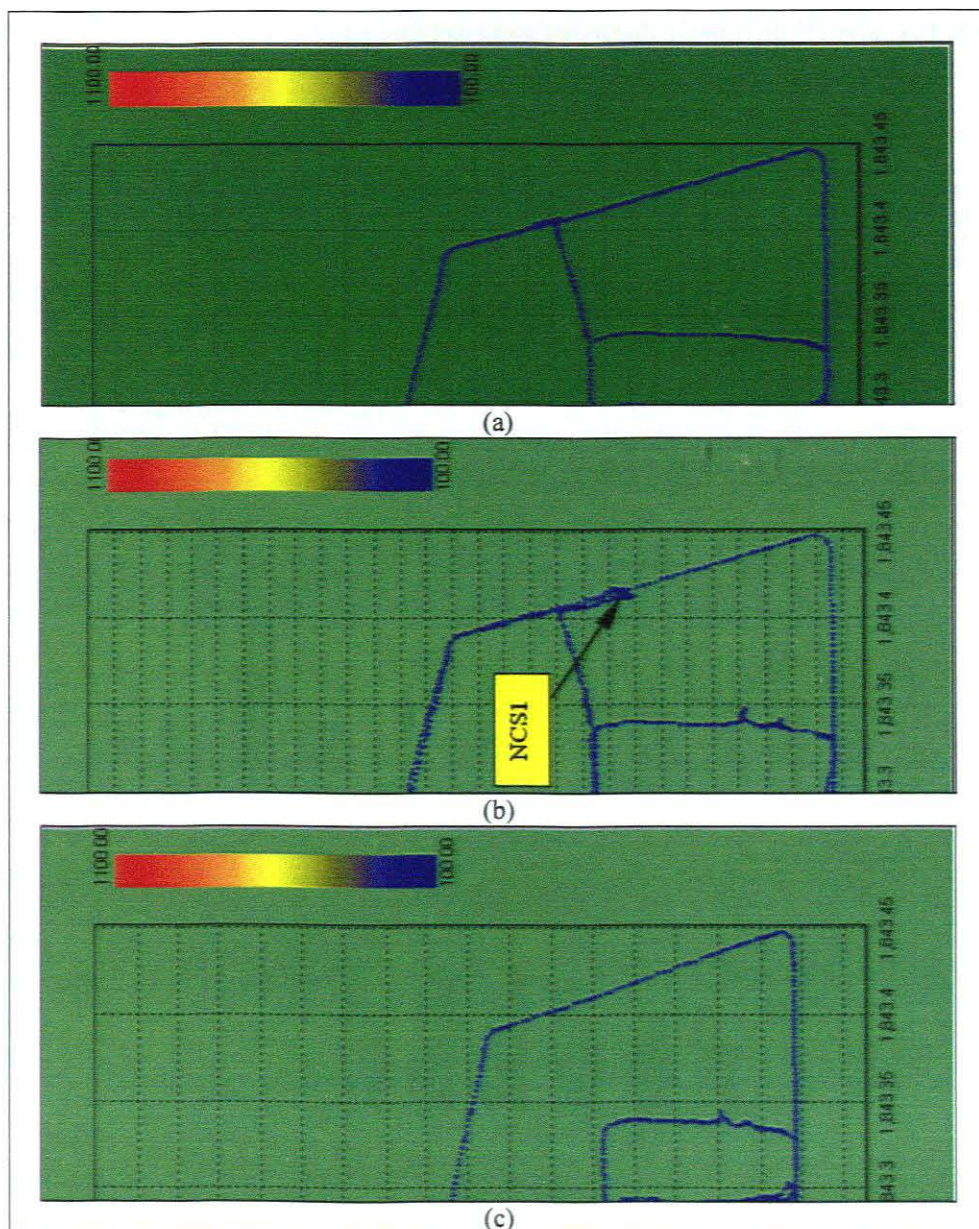


Figure 5-23: Sections of MEDUSA count rate maps obtained during the (a) June 2004, (b) July 2005, and (c) February 2005 surveys.

#### 5.4.2 HPGe vs. normalised MEDUSA

In Table 5-14 and Table 5-15 are listed the results of the comparison made between the HPGe and MEDUSA activity concentration values. In Figure 5-24 and Figure 5-25 are displayed these results in bar graphs for each radionuclide.

Table 5-14: Comparison of activity concentration results obtained with MEDUSA and HPGe for the NORM sources February and July 2005.

Location		HPGe vs. MEDUSA Activity Concentration (Bq.kg <sup>-1</sup> )					
		<sup>238</sup> U		<sup>232</sup> Th		<sup>40</sup> K	
		HPGe	Normalised MEDUSA	HPGe	Normalised MEDUSA	HPGe	Normalised MEDUSA
February 2005	HS1	11.72 ± 1.84	11.12 ± 0.57	10.86 ± 0.83	7.64 ± 0.28	57.45 ± 4.49	46.11 ± 3.87
	HS2	11.13 ± 0.75	14.21 ± 0.95	10.86 ± 0.87	9.17 ± 0.43	54.19 ± 1.61	62.00 ± 5.47
	HS3	26.04 ± 7.88	39.02 ± 1.86	21.35 ± 1.52	9.56 ± 0.36	54.53 ± 1.82	63.34 ± 5.34
July 2005	NCS1	13.94 ± 0.54	11.59 ± 0.58	15.01 ± 1.29	12.98 ± 0.45	57.78 ± 2.72	38.35 ± 3.29
	NHS4	8.60 ± 0.75	17.87 ± 0.93	8.66 ± 0.09	8.54 ± 0.34	29.75 ± 0.97	43.85 ± 3.78
	NHS5	8.57 ± 0.53	12.36 ± 0.96	7.53 ± 0.70	5.90 ± 0.38	48.09 ± 1.28	32.53 ± 3.29

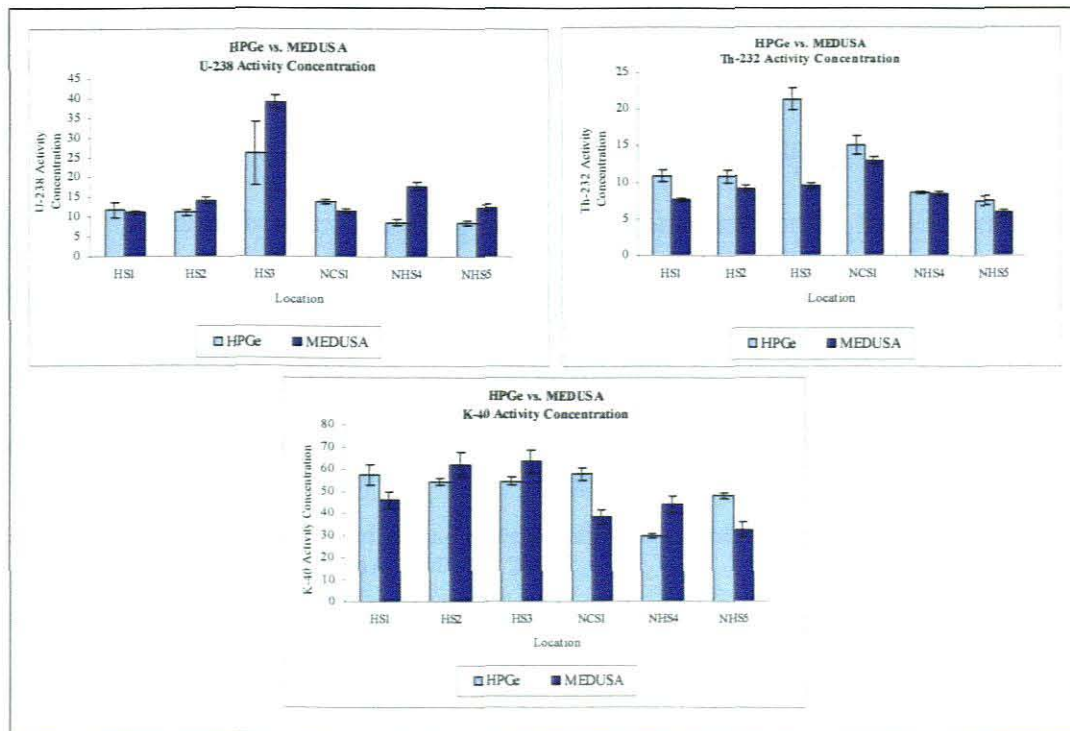
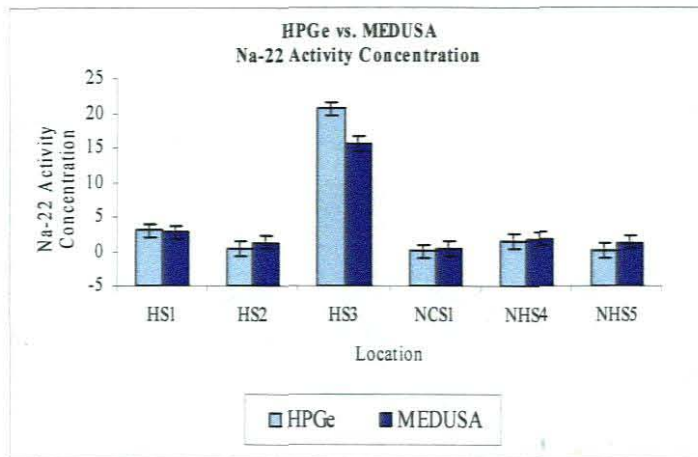


Figure 5-24: Bar graphs showing the comparison of activity concentration results obtained with MEDUSA and HPGe for the NORM sources in February and July 2005.

Table 5-15: Comparison of activity concentration results obtained with MEDUSA and HPGe for the anthropogenic sources in February and July 2005.

Location		HPGe vs. MEDUSA Activity concentration (Bq.kg <sup>-1</sup> )	
		<sup>22</sup> Na	
		HPGe	Normalized MEDUSA
February 2005	HS1	3.01 ± 0.38	2.76 ± 0.64
	HS2	0.43 ± 0.13	1.28 ± 0.33
	HS3	20.59 ± 4.20	15.53 ± 3.57
July 2005	NCS1	0.03 ± 0.04	0.38 ± 0.10
	NHS4	1.51 ± 0.08	1.89 ± 0.44
	NHS5	0.14 ± 0.07	1.31 ± 0.35





**Figure 5-25:** Bar graph showing the comparison of activity concentration results obtained with MEDUSA and HPGe for the anthropogenic sources in February and July 2005. (In this case only  $^{22}\text{Na}$  is considered since only this standard spectrum was available for FSA analysis).

In Table 5-16 are listed the results of the comparison made between the HPGe and MEDUSA absorbed and effective dose values obtained for the NORM sources. In Figure 5-26 are displayed these results in bar graphs. For the anthropogenic sources, the results of absorbed and effective dose were not compared since MEDUSA only refers to  $^{22}\text{Na}$  results in this case.

**Table 5-16:** Comparison of absorbed and effective dose results obtained with MEDUSA and HPGe for the NORM sources in February and July 2005.

	Location	HPGe vs. MEDUSA Absorbed & Effective dose			
		Absorbed Dose ( $\text{nGy}\cdot\text{h}^{-1}$ )		Effective Dose ( $\mu\text{Sv}\cdot\text{y}^{-1}$ )	
		HPGe	MEDUSA	HPGe	MEDUSA
February 2005	HS1	$14.37 \pm 0.89$	$11.67 \pm 0.31$	$17.62 \pm 1.09$	$14.32 \pm 0.39$
	HS2	$13.96 \pm 0.61$	$14.69 \pm 0.50$	$17.12 \pm 0.74$	$18.02 \pm 0.61$
	HS3	$27.20 \pm 3.68$	$26.44 \pm 0.89$	$33.36 \pm 4.52$	$32.43 \pm 1.09$
July 2005	NCS1	$17.92 \pm 0.37$	$14.79 \pm 0.45$	$21.97 \pm 0.45$	$18.14 \pm 0.39$
	NHS4	$10.44 \pm 0.43$	$15.24 \pm 0.46$	$12.80 \pm 0.53$	$18.69 \pm 0.57$
	NHS5	$10.51 \pm 0.50$	$10.63 \pm 0.47$	$12.89 \pm 0.62$	$13.04 \pm 0.57$

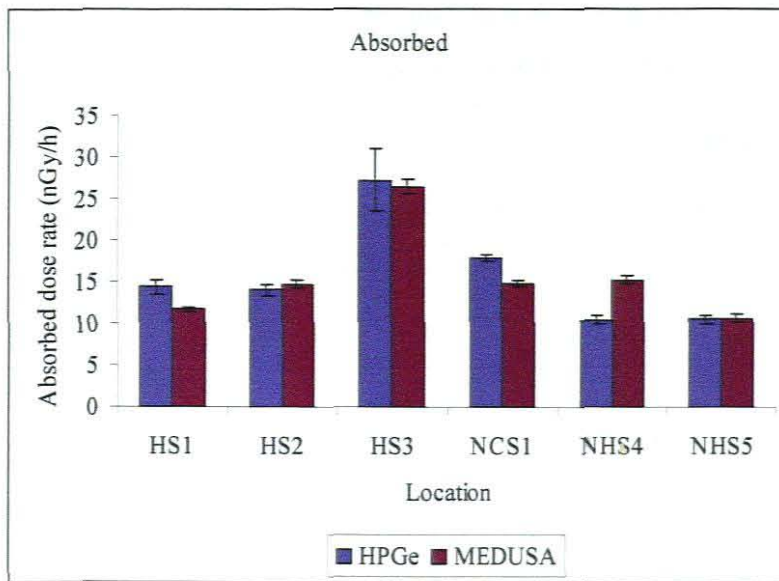


Figure 5-26: Bar graph showing the comparison of absorbed dose results obtained with MEDUSA and HPGe for the NORM sources in February and July 2005.

The results of Figure 5-24 and Figure 5-25 show considerable variations in the  $^{22}\text{Na}$  comparison between HPGe and normalised MEDUSA activity concentration results. This variation is indicated by the percentage differences<sup>15</sup> listed in Table 5-17 below. The variation has to do with the fact that MEDUSA performs average or “bulk” measurements that fail to capture detailed variations in the measured soil, whereas sampling does capture these but fails to provide full assurance for a safe extrapolation between widely spaced sampling points [Jos98]. The deviation from flatbed geometry could be one experimental error associated with the MEDUSA results. The percentage differences from the comparison of absorbed and effective dose results of Figure 5-26 are listed in Table 5-18 below.

<sup>15</sup> Let  $A > B$ . The percentage difference (%) between A and B, as used in this study, is given by

$$\left| \frac{A - B}{A} \right| \times 100.$$

**Table 5-17: Percentage differences from the comparison of activity concentration results obtained with MEDUSA and HPGe for NORM plus <sup>22</sup>Na in February and July 2005.**

		Location	Percentage Difference (%)			
			<sup>238</sup> U	<sup>232</sup> Th	<sup>40</sup> K	<sup>22</sup> Na
			HPGe vs. MEDUSA	HPGe vs. MEDUSA	HPGe vs. MEDUSA	HPGe vs. MEDUSA
February 2005	HS1	5.1	29.7	19.7	8.3	
	HS2	21.7	15.6	12.6	66.4	
	HS3	33.3	55.2	13.9	24.6	
July 2005	NCS1	16.9	13.5	33.6	92.1	
	NHS4	51.9	1.4	32.2	20.1	
	NHS5	30.7	21.7	32.4	89.3	

**Table 5-18: Percentage differences from the comparison of absorbed and effective dose results obtained with MEDUSA and HPGe for the NORM sources in February and July 2005.**

		Location	Percentage Difference (%)	
			Absorbed dose	Effective Dose
			HPGe vs. MEDUSA	HPGe vs. MEDUSA
February 2005	HS1	18.8	18.7	
	HS2	5.0	5.0	
	HS3	2.8	2.8	
July 2005	NCS1	17.5	17.4	
	NHS4	31.5	31.5	
	NHS5	1.1	1.2	

## CHAPTER 6 SUMMARY AND CONCLUSION

In this chapter are presented the summary and conclusions reached through this study, based on the hypothesis and research questions stated in Chapter 1. The presentation contains the summary, conclusion and outlook, sections 6.1, 6.2, and 6.3, respectively.

### 6.1 Summary

In February and July 2005, following up on June 2004, the site of *iThemba LABS* (*iTL*) was surveyed for environmental radioactivity by the Environmental Radioactivity Laboratory (ERL) of *iThemba LABS*. The *in-situ* and *ex-situ* measurement techniques were used to perform the surveys. The apparatus used were the ERL's Multi-Element-Detector-for-Underwater-Sediment-Activity (or MEDUSA) and high purity germanium (or HPGe) detector systems, to make *in-situ* and *ex-situ* measurements, respectively.

The MEDUSA system consists of a CsI(Na) crystal (length 15 cm, diameter 7 cm) for  $\gamma$ -ray detection. During the surveys the detector was mounted  $\sim 0.5$  m above the ground on the front of a 4x4 vehicle to traverse [at  $\sim 2$  m.s<sup>-1</sup>] the accessible portions of the *iTL* grounds. The spatial data (via a handheld GPS receiver mounted above the crystal) were acquired every 1 s, and  $\gamma$ -ray spectra (0 –3 MeV) every 2 s. Soil samples ( $\sim 10$  cm deep), at times also the grass, were collected from spots of interest. A 20-minute MEDUSA calibration measurement was made at one of the spots that were sampled. The samples were oven-dried (at 105 °C), sealed into Marinelli beakers, and then measured (after a minimum of 21 days) using the lead-shielded HPGe detector (Canberra p-type model with built-in pre-amplifier, crystal diameter 62.5 mm, length 59.9 mm) in the ERL.

The MEDUSA data are analysed as follows: (1) MEDUSA Data Synchronizer (MDS) creates a one-to-one correspondence between each spectrum obtained every 2 s and the associated auxiliary data obtained every 1 s, (2) the synchronized data are analysed by MEDUSA Post Analysis (MPA), which performs Full-Spectrum Analysis (FSA) of the spectra and extracts activity concentrations. FSA involves fitting standard spectra of associated radionuclides (in this study only  $^{238}\text{U}$ ,  $^{232}\text{Th}$ ,  $^{40}\text{K}$ , and  $^{22}\text{Na}$  spectra were available) plus background to the MEDUSA spectrum by means of a *chi-square minimisation procedure*. The HPGe data were analysed by setting regions of interest (ROIs) over the  $\gamma$ -ray energies peaks detected, and extracting net counts detected for the peaks in order to calculate the activity concentration of the associated radionuclides. Using the data from the 20-minute calibration measurement, the ratios of HPGe over MEDUSA were calculated for activity concentration of  $^{238}\text{U}$ ,  $^{232}\text{Th}$ ,  $^{40}\text{K}$ , and  $^{22}\text{Na}$ , and these ratios were used to normalise MEDUSA activity concentrations. Using the activity concentration results from both the HPGe and normalised MEDUSA data, the absorbed and effective doses to the public were calculated.

The HPGe activity concentration results that were obtained for the naturally occurring radioactive materials (NORM) have the ranges 7.8 – 26.0, 7.5 – 21.4, and 29.8 – 57.8  $\text{Bq.kg}^{-1}$  for  $^{238}\text{U}$ ,  $^{232}\text{Th}$ , and  $^{40}\text{K}$ , respectively. The percentage uncertainties associated with these HPGe activity concentration results have the ranges 3.2 – 30.3, 1.0 – 9.3, and 2.7 – 8.0 %, respectively. The absorbed and effective dose results [with HPGe data] that were obtained for the NORM radionuclides have the ranges 10.4 – 27.2  $\text{nGy.h}^{-1}$  and 12.8 – 33.4  $\mu\text{Sv.y}^{-1}$ , respectively. The percentage uncertainties associated with these HPGe absorbed and effective dose results both have the range 1.9 – 13.5 %.

The normalised MEDUSA activity concentration results for NORM have the ranges 11.1 – 39.0, 5.9 – 13.0, and 32.5 – 63.3 Bq.kg<sup>-1</sup>, with associated percentage uncertainties of ranges 3.2 – 7.8, 2.8 – 6.4, and 8.0 – 10.1 % for <sup>238</sup>U, <sup>232</sup>Th, and <sup>40</sup>K, respectively. The absorbed and effective dose results [with normalised MEDUSA data] that were obtained for the NORM radionuclides have the ranges 10.6 – 26.4 nGy.h<sup>-1</sup> and 13.0 – 32.4 μSv.y<sup>-1</sup>, respectively. The percentage uncertainties associated with these MEDUSA absorbed and effective dose results both have the range 1.9 – 4.4 %.

In addition to the results from the sampled spots, the average normalised MEDUSA results (from February and July 2005) for the *i*TL road are 30.3, 29.6, and 345.0 Bq.kg<sup>-1</sup>, with associated percentage uncertainties of 2.5, 2.4, and 5.9 % for <sup>238</sup>U, <sup>232</sup>Th, and <sup>40</sup>K, respectively. When averaging over the “off-road” sections of the *i*TL site, and excluding data from high activity spots (“hotspots”), then the average normalised MEDUSA results obtained are 10.6, 8.5, and 42.4 Bq.kg<sup>-1</sup>, with associated percentage uncertainties of 3.3, 2.4, and 5.9 %. When averaging over the “off-road” sections of the *i*TL site, and also including data from the hotspots, the average normalised MEDUSA results are 23.1, 8.0, and 50.4 Bq.kg<sup>-1</sup>, with associated percentage uncertainties of 3.3, 2.5, and 5.9 %.

The HPGe activity concentration results that were obtained for the anthropogenic radionuclides have the ranges 1.2 – 6533.5, 0 – 100.8, 0 – 20.6, 0 – 0.7, and 0.2 – 192.5 Bq.kg<sup>-1</sup>, with associated percentage uncertainties of ranges of 20.0 – 43.5, 0 – 59.6, 5.3 – 30.2, 19.5 – 66.7, and 0.1 – 67.8 % for <sup>68</sup>Ga, <sup>65</sup>Zn, <sup>22</sup>Na, <sup>137</sup>Cs, and <sup>54</sup>Mn, respectively. The absorbed and effective dose by anthropogenic sources was calculated for two plane source depth locations, namely, 1 and 10 cm. The absorbed and effective dose results [with HPGe data] that were obtained at 1 cm plane source depth have the ranges 0.2 – 152.7 nGy.h<sup>-1</sup> and 0.2 – 187.3 μSv.y<sup>-1</sup>, and both

have associated percentage uncertainties of range 15.8 – 34.0 %. The absorbed and effective dose results [with HPGe data] that were obtained at 10 cm plane source depth have the ranges 0 – 38.1 nGy.h<sup>-1</sup> and 0 – 46.7 μSv.y<sup>-1</sup>, with associated percentage uncertainties of ranges 15.8 – 33.7 and 15.8 – 33.8 %, respectively.

The normalised MEDUSA activity concentration results that were obtained for the anthropogenic radionuclides are given for <sup>22</sup>Na only. The results have the range 0.4 – 15.5 Bq.kg<sup>-1</sup>, and have a percentage uncertainty range 22.6 – 26.7 % associated with them. The average normalised MEDUSA results for <sup>22</sup>Na are 1.6, 0.8, and 7.2 Bq.kg<sup>-1</sup> for “road”, “off-road-no-hotspot”, and “off-road-with-hotspots” sections, respectively. For these sections, the results have percentage uncertainties of 16.9, 19.0, and 16.4 % associated with them. Again, the absorbed and effective dose by anthropogenic sources (only <sup>22</sup>Na) was calculated for two plane source depth locations, namely, 1 and 10 cm. The absorbed and effective dose results [with normalised MEDUSA data] that were obtained at 1 cm plane source depth have the ranges 0.2 – 7.0 nGy.h<sup>-1</sup> and 0.2 – 8.6 μSv.y<sup>-1</sup>, with associated percentage uncertainties of ranges 22.4 – 27.1 and 22.5 – 26.4 %, respectively. The absorbed and effective dose results [with normalised MEDUSA data] that were obtained at 10 cm plane source depth have the ranges 0 – 1.9 nGy.h<sup>-1</sup> and 0 – 2.3 μSv.y<sup>-1</sup>, with associated percentage uncertainties of ranges 20.0 – 26.7 and 16.7 – 30.0 %, respectively.

The HPGe and normalised MEDUSA activity concentration results were compared [for February and July 2005] and the percentage uncertainties obtained have ranges 5.1 – 51.9, 1.4 – 55.2, and 12.6 – 33.6 % for <sup>238</sup>U, <sup>232</sup>Th, and <sup>40</sup>K, respectively. The range is 8.3 – 92.1 % for <sup>22</sup>Na. The comparison of absorbed and effective dose results [with HPGe data] for the assumed plane source locations of 1

and 10 cm showed that there is an average drop of 75 % when moving the source from 1 cm to 10 cm depth location. The comparison of absorbed and effective dose results [with normalised MEDUSA data] for the assumed plane source locations of 1 and 10 cm showed that there is an average drop of range 73 - 74 % when moving the source from 1 cm to 10 cm depth location.

## **6.2 Conclusion**

From the findings of this study, it is unquestionable that indeed the maximum effective dose to humans on the *iThemba LABS* grounds as a result of external exposure to natural and anthropogenic radionuclides is well below the regulatory 1 mSv per year per member of public.

In attempting to answer the main research questions posed in section 1.3, the following was concluded through this study:

- in terms of the activity concentration of the identified radionuclides, the radioactivity level due to natural  $\gamma$ -ray emitting radionuclides on the *iThemba LABS* grounds is below the world average of 35, 30, and 400 Bq.kg<sup>-1</sup> for <sup>238</sup>U, <sup>232</sup>Th, and <sup>40</sup>K, respectively. The radioactivity level due to anthropogenic  $\gamma$ -ray emitting radionuclides has a maximum activity concentration of 6533.5 bq.kg<sup>-1</sup> (see section 6.1).
- The six hotspots are clearly located on count rate maps of the grounds, and the hotspots consistently appear at the same locations for June 2004, and February and July 2005 maps.
- The radionuclides that contribute to the radiation in these hotspots are summarized in Table 6-1 below.



- The activity concentrations of the radionuclides are thoroughly outlined in Chapter 5.
- There is uncertainty as to whether MEDUSA has managed to precisely resolve the spatial outline of the hotspots given the possible variation in the positioning of the detection crystal [over the hotspot] in February and July 2005. This variation gives room for inaccurate spatial location of  $\gamma$ -rays. Therefore it is not clear at this stage whether the “hotspot” spatial distribution changes with time.
- The associated effective doses from the “hotspots” to humans on the site are outlined in Chapter 5. As already mentioned, the maximum effective dose obtained in this study is below the regulatory 1 mSv per year per individual member of public.

**Table 6-1: A summary of the radionuclide contamination identified on the TLL grounds. The codes of the “hotspot” locations are shown, and the anthropogenic radionuclides that were identified in the locations are indicated with the “x” sign. The red sign indicates the radionuclide(s) with high activity concentration.**

Hotspot location	Identified anthropogenic radionuclides					
	<sup>68</sup> Ga	<sup>65</sup> Zn	<sup>22</sup> Na	<sup>137</sup> Cs	<sup>54</sup> Mn	<sup>60</sup> Co
HS1	x	x	x	x	x	
HS2	x	x	x	x	x	
HS3	x	x	x	x	x	
NHS4	x	x	x	x	x	
NHS5	x	x	x	x	x	
MRG hotspot	x					
Near-Dam 1	x		x			
RPG pipe	x					
Dipole magnet						x

Other conclusions outside the focus of the research questions can be noted as follows:

- The comparison of MEDUSA count rate obtained in February and July 2005 for stationary measurements in some locations showed that there might be a decline in the concentration of anthropogenic radionuclides at the hotspots due to seasonal

changes. The increase in self-absorption by the  $\gamma$ -rays due to wet weather conditions in July, as different from those in February, is a possible explanation for this decline.

- The scatter in the locations of the identified hotspots on the *i*TTL grounds suggests that there should be another way (in addition to irrigation) by which the contamination reached those locations. Another possibility is that the matter state (liquid or solid) of the radioactive material was different at the time of irrigation. The latter possibility is more plausible considering that the origin of  $^{68}\text{Ge}$ -contaminated spots is believed to be associated with the shattering of two germanium (Ge) targets in the Horizontal Beam Target Station of *i*TTL in 2004. There is a possibility that small fragments of  $^{68}\text{Ge}$  were transferred to the holding dam via the liquid effluent system, and then distributed around the site by some mechanisms [McG07].

### 6.3 Outlook

The findings of this study show that there is scope for a thorough radiological risk assessment that could be carried out in the future for interpreting the results even further. It is recommended that standard spectra should be acquired for all the identified anthropogenic radionuclides for improved work with the *i*TTL MEDUSA system in the future. Work could also be done of assessing the dose due to the beta ionizing radiation type, which is characteristic of the decay of some of the radionuclides identified in this study.

The questions that still require answers from the findings of this kind of work are:

- (a) how wide and deep is the radionuclide contamination at the identified “hotspots”? and

(b) does the hotspot spatial distribution change with time?

In Figure 6-1 is shown a photograph taken of some of the wild animals that live, and eat of the grass on the *i*TL site. In Figure 6-2 is shown the evidence of uptake of radionuclides by the grass sampled at location NHS4 during the July 2005 survey. The result underscores the need to further study the impact of anthropogenic radionuclides (present on the *i*TL grounds) on the non-human biota.



Figure 6-1: A photograph showing some of the wild animals that live, and eat of the grass on the *i*TL site.

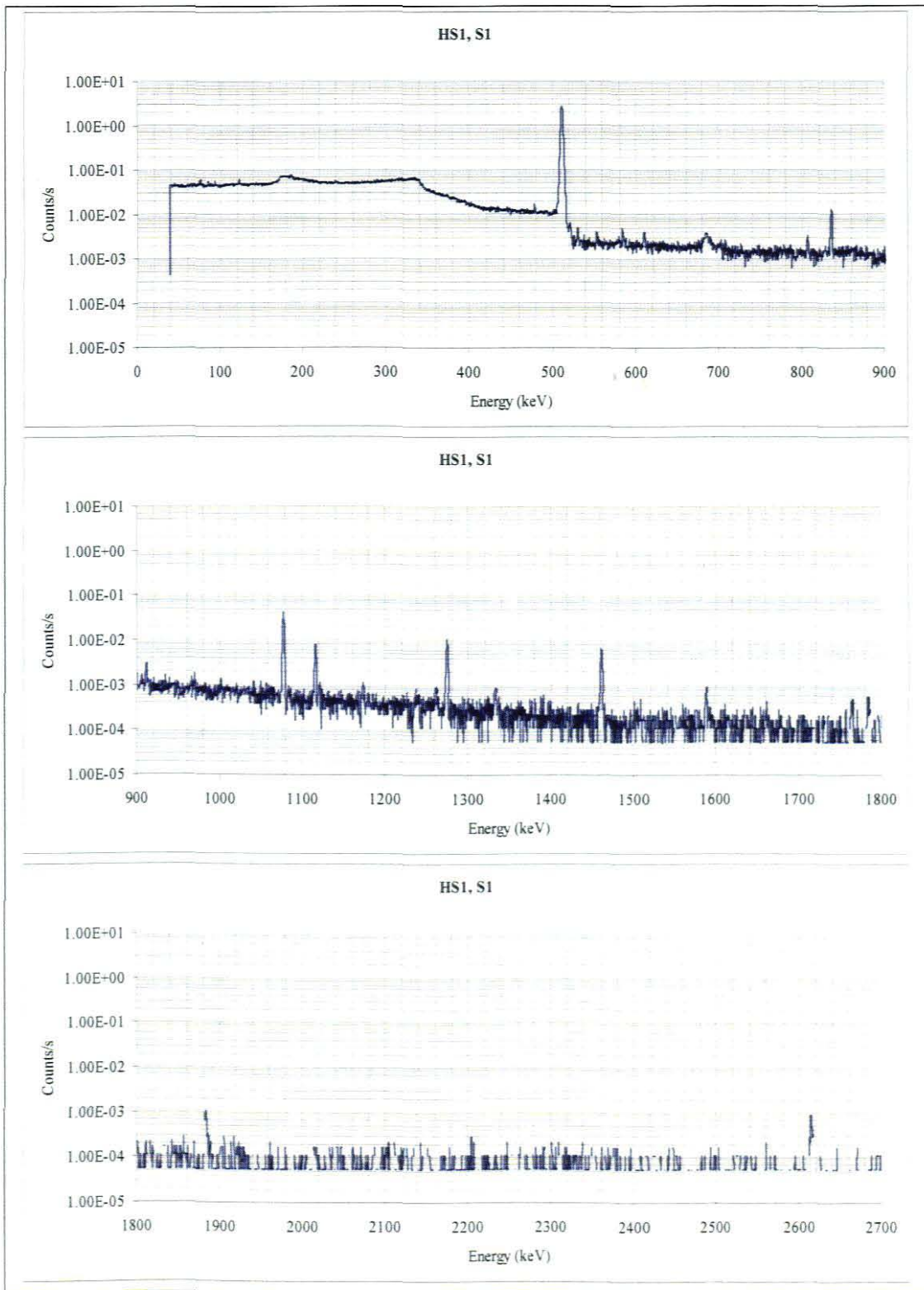


Figure 6-2: Spectrum showing energy peaks (range = 0 – 2700 keV) in grass sample taken from location NHS4 during the July 2005 survey.

# APPENDICES

## APPENDIX 1

### *Overview of the patent of the MEDUSA system*

The diagram in Figure 0-1 represents the MEDUSA system according to the invention as patented by the Nuclear Geophysics Division (NGD) of the Nuclear Accelerator Institute (abbreviated KVI, which stands for Kernfysisch Versneller Instituut) at the University of Groningen (RuG) in the Netherlands [Eur98]. This section seeks to cover, briefly, the components (represented by numbered boxes in the diagram) that are contained in the MEDUSA system and their respective functions, according to the invention.

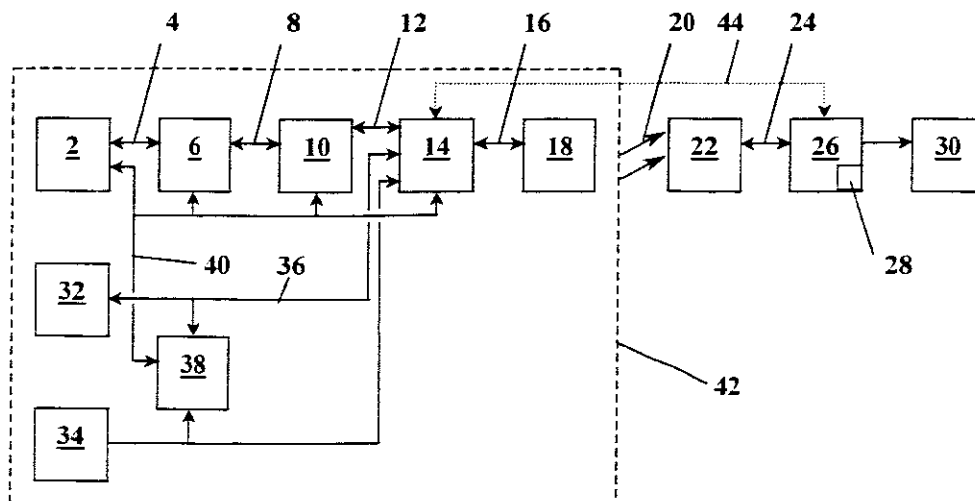


Figure 0-1: Schematic diagram showing the components of the MEDUSA system according to the invention as patented by the Nuclear Geophysics Division (NGD) of the KVI. (Adapted from [Eur98])

Beginning with component numbered 2, it is a scintillation detector, which uses the BGO (Bismuth Germanium Oxide) crystal for detection, in this example. The scintillation crystal generates a light flash for every photon of radiation that falls on it. The light flashes are sent, via line 4, to photomultiplier 6. The photomultiplier then

converts the received light flashes into electrical pulses of amplitudes that correspond to the levels of energy that were carried by the received radiation. Line 8 is used to transport these electrical pulses to pulse height analyzer 10. From the pulse height analyzer, information regarding the height of the pulse, and hence the energies of the received radiation photons, is obtained and sent as electrical signals via line 12. The information about the number of radiation photons detected per unit time, i.e. the measure of radiation intensity, is also made available on line 12. The electrical signals are digitized by A/D (analog-to-digital) converter 14.

From the A/D converter 14, the line 16 is used to transport the digitized signal to a transmitter/receiver unit 18 where it gets radiated via the modulated carrier numbered 20. Another transmitter/receiver unit 22 features in this example, and its function is to receive and demodulate the signal sent by unit 18. Via line 24, unit 22 sends a digital signal that corresponds to the one received from the A/D converter, to the first computer unit 26. This computer unit then uses the digital information contained in the received digital spectrum to produce an energy spectrum of the form shown in the example of Figure 0-2, below. The features of the energy spectrum reveal three energy peaks that belong to radionuclides  $^{40}\text{K}$ ,  $^{238}\text{U}$ , and  $^{232}\text{Th}$ .

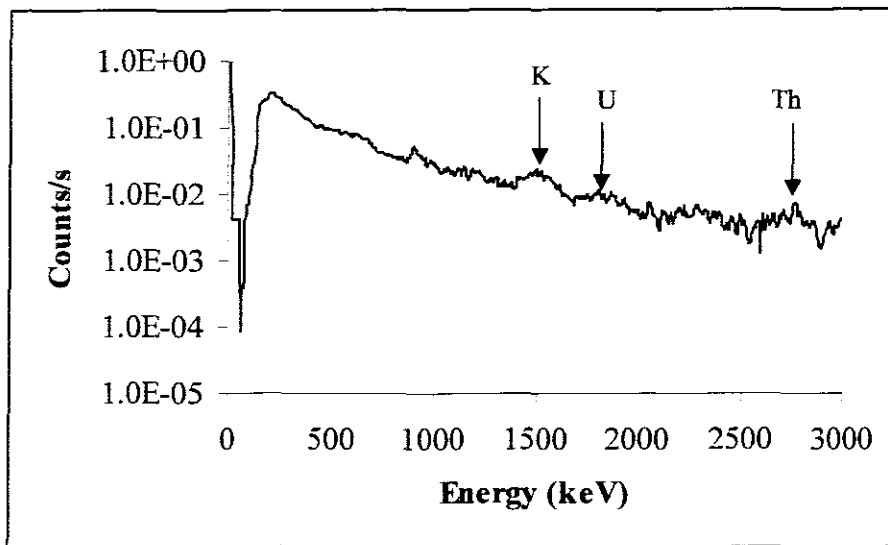


Figure 0-2: A plot of count rate versus energy showing the spectrum of energy peaks as produced in computer unit 26.

Memory 28 contains *standard spectra* of  $^{40}\text{K}$ ,  $^{238}\text{U}$ , and  $^{232}\text{Th}$ , with which the first computer unit 26 is able to ‘disintegrate’ the energy spectrum of Figure 0-2 to extract, by means of a *first algorithm*, the activity concentrations of the radionuclides in question. The first algorithm should preferably use the entire energy spectrum during the analysis. Memory 28 also stores information about known minerals and the activity concentrations of the radionuclides contained in these minerals. From the *measured activity concentration data*, the first computer unit 26 uses the available information about minerals to determine, using a *second algorithm*, the ratio in which the groups of minerals have been detected. The results of this work are passed on to a data output system 30, for further processing.

In the example of Figure 0-1, the MEDUSA system contains additional sensors 32 and 34, representing temperature sensor, and motion detector, respectively. The sensor 32 uses line 36 to send its signals to the A/D converter 14, which in turn digitizes the signals and transmits them to the transmitter/receive unit via line 16. On line 16, multiplex techniques or coding techniques can be used to distinguish the latter signals from those coming from the pulse height analyzer 10. Depending on whether

the first and/or second algorithm contains any temperature-dependent parameters, the first computer unit 26 will again perform these algorithms with the digitized temperature-representing signals. A similar process holds also for the motion sensor 34.

The example of Figure 0-1 further incorporates a second computer unit 38, which also handles output signals from the sensors 32 and 34. Using the *third algorithm*, unit 38 determines the way in which setting parameters of other units like the *photomultiplier 6, pulse height analyzer 10 and/or A/D converter 14, can be regulated via line 40*. This means, for instance, that the gain of the units 6, 10, 14 can be regulated depending on the temperature. Since, according to a highly beneficial model, the units 2, 6, 10, 14, and 18 (as well units 32, 34, and 38 if present) are assembled in a casing 42 to comprise a probe, then the probe can be placed directly and regulated based on the direct environment of the probe as measured by the sensors 32 and 34.

As can be seen in the diagram in Figure 0-1, there are more possible models of the invention of the MEDUSA system, other than the one described above. An example is that of a replacement of transmitter/receiver units 18 and 22 with a direct connection by means of line 44. Another would be to replace particular lines in the model of Figure 0-1, with pairs of transmitter/receiver units [Eur98].



## APPENDIX 2

### Decay schemes of the anthropogenic radionuclides identified on the iThemba LABS site

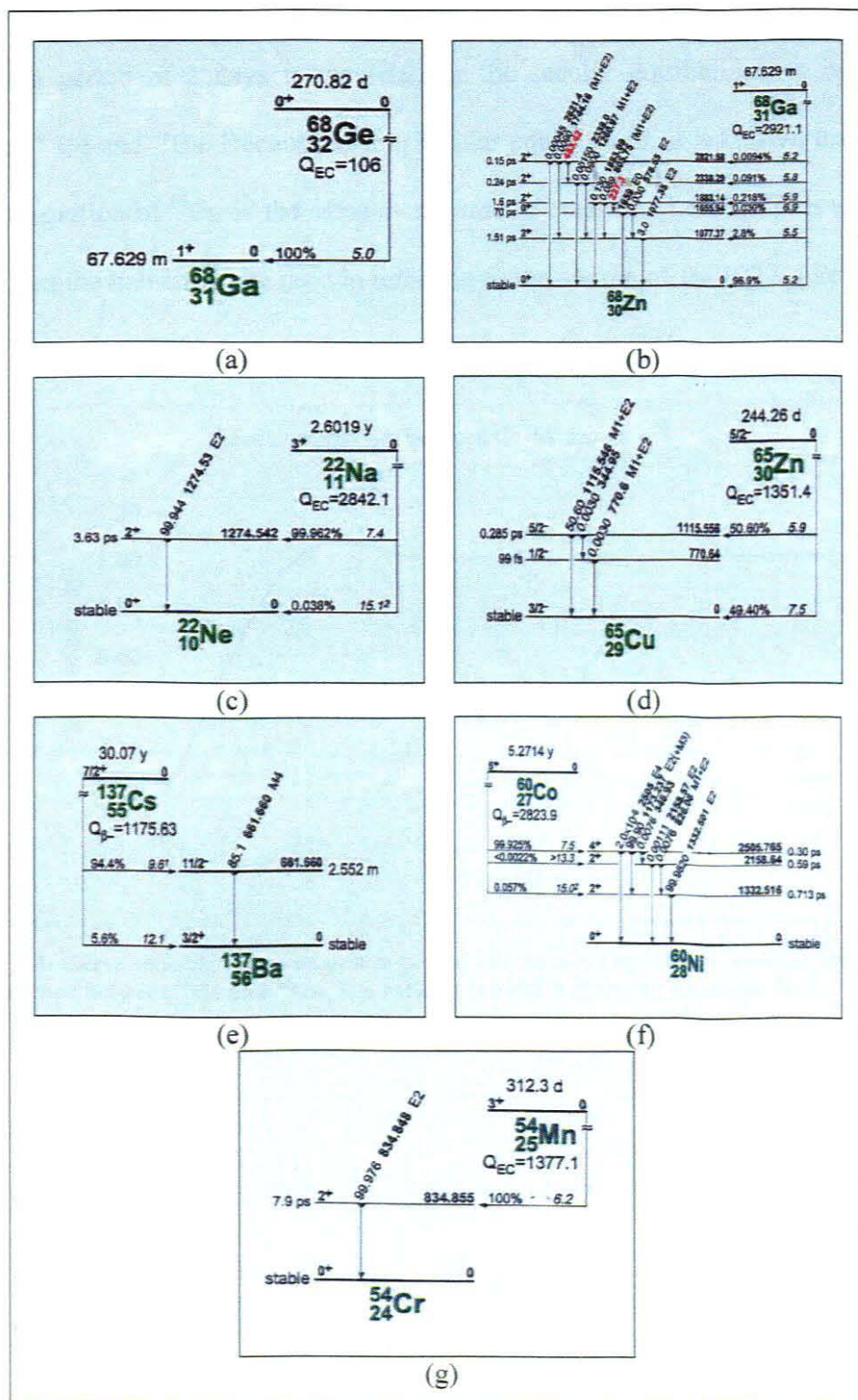


Figure 0-3: Decay schemes [Fir96] of the anthropogenic radionuclides identified in the surveys, namely, (a)  $^{68}\text{Ge}$ , (b)  $^{68}\text{Ga}$ , (c)  $^{22}\text{Na}$ , (d)  $^{65}\text{Zn}$ , (e)  $^{137}\text{Cs}$ ,  $^{60}\text{Co}$ , and  $^{54}\text{Mn}$ .

## APPENDIX 3

### *<sup>68</sup>Ge-<sup>68</sup>Ga secular equilibrium*

In Figure 0-4 is shown a curve of the ratio of Equation 2-10 indicating that a minimum period of 2 days is required for the secular equilibrium to be reached between <sup>68</sup>Ge and <sup>68</sup>Ga. Because of this secular equilibrium, it is known that the rate of disintegration of <sup>68</sup>Ga is the same as the rate of creation [Leo87]. This essentially means that the half-life to be used in referring to the source of the 1077.4 keV  $\gamma$ -ray is that of <sup>68</sup>Ge, the 270.82 days, and not the 67.63 minutes of <sup>68</sup>Ga.

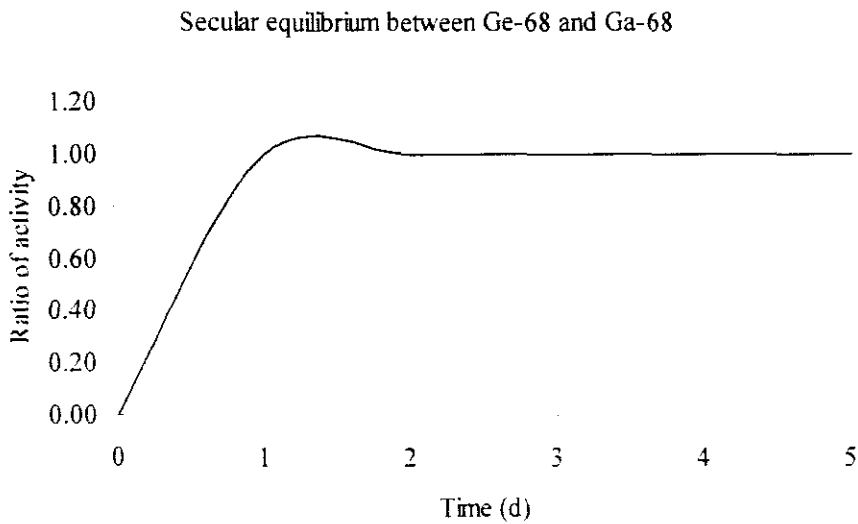


Figure 0-4: Curve showing that a minimum period of 2 days is required for secular equilibrium to be reached between <sup>68</sup>Ge and <sup>68</sup>Ga. The ratio of activity is given by Equation 2-10.

## APPENDIX 4

### *Absolute efficiency parameters and the IAEA intercomparison*

The parameters  $a$  and  $b$  of Equation 4-13 were obtained from the 10 parameters listed in Table 0-1 that were obtained for 10 different soil samples that were collected from Simonsig Wine Farm, in Stellenbosch during the work of [Mod05].

**Table 0-1: Parameters ( $a$  and  $b$ ) and their uncertainties for the absolute FEP efficiency for Simonsig Wine Farm samples. (Adapted from [Mod05]).**

Sample Code	Parameter a	Parameter b
NCP	$1.522 \pm 0.002$	$-0.707 \pm 0.038$
NSP4	$1.450 \pm 0.002$	$-0.700 \pm 0.035$
NSP11	$0.817 \pm 0.001$	$-0.620 \pm 0.029$
NSP17	$2.235 \pm 0.003$	$-0.759 \pm 0.058$
NSP18	$1.441 \pm 0.003$	$-0.698 \pm 0.066$
NSP18D	$4.199 \pm 0.007$	$-0.845 \pm 0.110$
PCP	$0.777 \pm 0.008$	$-0.614 \pm 0.042$
PSP14	$2.247 \pm 0.008$	$-0.759 \pm 0.211$
PSP18	$1.167 \pm 0.001$	$-0.671 \pm 0.026$
PSP30	$1.320 \pm 0.008$	$-0.686 \pm 0.037$

The validity of the absolute efficiencies obtained with the method outlined in section 4.2.2.1 was checked by re-measuring an IAEA reference soil sample [in the ERL], and then calculating the activity concentrations of  $^{232}\text{Th}$ ,  $^{40}\text{K}$ , and  $^{137}\text{Cs}$  using the obtained absolute efficiencies. The ERL activity concentration results for the radionuclides were then compared with those recommended by the IAEA as shown in Table 0-2. The comparison results show good agreement, within the uncertainties, between the ERL and the IAEA-recommended values. The percentage differences of the compared activity concentration values are 6.5, 2.7, and 0.9 % for  $^{232}\text{Th}$ ,  $^{40}\text{K}$ , and  $^{137}\text{Cs}$ , respectively.

**Table 0-2: Results of the comparison of the ERL to the IAEA-recommended activity concentrations, for the validation of the method used in this study to obtain absolute efficiencies.**

Sample Code	ERL vs. IAEA Activity Concentration (Bq.kg <sup>-1</sup> )					
	<sup>232</sup> Th		<sup>40</sup> K		<sup>137</sup> Cs	
	95% confidence interval		95% confidence interval		95% confidence interval	
	19.2 - 21.9		417.0 - 432.0		5200.0 - 5360.0	
	ERL	IAEA	ERL	IAEA	ERL	IAEA
<b>IAEA-375</b>	21.9 ± 1.4	20.5	412.7 ± 19.2	424.0	5231.7 ± 298.1	5280.0

## APPENDIX 5

### *HPGe count rate, activity concentration, and dose in each sample*

In Table 0-3 to Table 0-1 are shown the HPGe count rate results for the individual  $\gamma$ -ray energy values. The results are shown for each of the 5 samples collected at locations CS1, HS1, and NCS1 during the February and July 2005 surveys. The values listed here have all been corrected for background live time and are rounded off to three significant digits. The values are reported at the time of measurement.

**Table 0-3: HPGe count rate reported for the 5 locations of calibration spot CS1 in February 2005. The values listed here have been corrected for background live time and are rounded off to three significant digits. The values are reported at the time of measurement.**

Radio-nuclide	E (keV)	Count rate ( $\times 10^{-5}$ counts.s <sup>-1</sup> )				
		CS1, S1	CS1, S2	CS1, S3	CS1, S4	CS1, S5
<sup>232</sup> Th	934.06	325 ± 60	306 ± 60	463 ± 57	352 ± 61	331 ± 61
	1238.11	529 ± 60	540 ± 67	624 ± 61	543 ± 57	509 ± 61
	295.21	6350 ± 179	5460 ± 173	5840 ± 182	5680 ± 168	5800 ± 179
	351.92	10600 ± 207	9960 ± 205	10200 ± 196	10500 ± 192	9570 ± 192
	1377.67	369 ± 59	316 ± 51	401 ± 45	355 ± 52	382 ± 52
	1764.49	1520 ± 73	1340 ± 70	1350 ± 65	1470 ± 68	1280 ± 63
	2204.21	379 ± 48	390 ± 48	333 ± 45	347 ± 36	345 ± 38
<sup>238</sup> U	338.32	3470 ± 157	3170 ± 154	3180 ± 156	3330 ± 143	3260 ± 147
	727.33	1220 ± 90	1060 ± 93	1320 ± 84	1190 ± 82	1220 ± 82
	794.95	584 ± 65	745 ± 68	561 ± 63	721 ± 66	644 ± 68
	911.21	3910 ± 123	3780 ± 120	3920 ± 116	3860 ± 112	3540 ± 112
	966.87	3250 ± 132	2770 ± 129	2760 ± 120	2710 ± 120	2910 ± 131
<sup>40</sup> K	1460.83	6690 ± 148	6280 ± 143	6800 ± 138	7240 ± 140	7210 ± 140
<sup>68</sup> Ga	1077.40	0 ± 91	22 ± 88	0 ± 88	76 ± 85	120 ± 83
<sup>65</sup> Zn	1115.55	-20 ± 40	28 ± 45	3 ± 43	-20 ± 40	20 ± 43
<sup>22</sup> Na	1274.53	1980 ± 92	1730 ± 87	2760 ± 95	1620 ± 79	2290 ± 86
<sup>137</sup> Cs	661.66	633 ± 85	655 ± 74	894 ± 76	905 ± 73	625 ± 64
<sup>54</sup> Mn	834.848	266 ± 62	233 ± 60	293 ± 52	362 ± 59	272 ± 123

**Table 0-4: HPGe count rate reported the 5 locations of hotspot HS1 in February 2005. The values listed here have been corrected for background live time and are rounded off to three significant digits. The values are reported at the time of measurement.**

Radio-nuclide	E (keV)	Count rate ( $\times 10^{-5}$ counts.s <sup>-1</sup> )				
		HS1, S1	HS1, S2	HS1, S3	HS1, S4	HS1, S5
<sup>232</sup> Th	934.06	457 ± 71	499 ± 93	600 ± 107	699 ± 115	505 ± 94
	1238.11	672 ± 73	639 ± 82	799 ± 84	947 ± 82	969 ± 75
	295.21	N/A	N/A	N/A	N/A	N/A
	351.92	1300 ± 462	1200 ± 636	12800 ± 785	14300 ± 767	13200 ± 654
	1377.67	536 ± 57	537 ± 70	513 ± 84	816 ± 73	565 ± 61
	1764.49	1810 ± 72	1770 ± 81	1770 ± 81	2180 ± 80	1930 ± 82
	2204.21	397 ± 40	408 ± 43	507 ± 46	582 ± 47	533 ± 50
<sup>238</sup> U	338.32	N/A	N/A	N/A	N/A	N/A
	727.33	1330 ± 112	1210 ± 109	1390 ± 160	1280 ± 177	1360 ± 156
	794.95	861 ± 87	1040 ± 184	713 ± 129	795 ± 142	826 ± 142
	911.21	4470 ± 130	4600 ± 154	45600 ± 171	5140 ± 166	4980 ± 154
	966.87	3340 ± 152	3330 ± 177	3350 ± 205	3840 ± 199	3670 ± 185
<sup>40</sup> K	1460.83	7290 ± 145	7080 ± 154	6680 ± 152	6750 ± 148	7460 ± 147
<sup>68</sup> Ga	1077.40	16500 ± 210	29000 ± 299	46800 ± 375	52700 ± 364	39700 ± 317
<sup>65</sup> Zn	1115.55	472 ± 59	895 ± 76	2270 ± 106	1610 ± 91	1170 ± 82
<sup>22</sup> Na	1274.53	3510 ± 105	3250 ± 115	3530 ± 123	3760 ± 119	3980 ± 117
<sup>137</sup> Cs	661.66	1200 ± 112	883 ± 132	1070 ± 204	464 ± 180	707 ± 166
<sup>54</sup> Mn	834.848	1640 ± 103	2660 ± 240	5670 ± 266	11000 ± 326	8110 ± 182

**Table 0-5: HPGe count rate reported for the 5 locations of calibration spot NCS1 in July 2005. The values listed here have been corrected for background live time and are rounded off to three significant digits. The values are reported at the time of measurement.**

Radio-nuclide	E (keV)	Count rate ( $\times 10^{-5}$ counts.s <sup>-1</sup> )				
		NCS1, S1	NCS1, S2	NCS1, S3	NCS1, S4	NCS1, S5
<sup>232</sup> Th	934.06	646 ± 59	748 ± 61	607 ± 68	766 ± 64	736 ± 68
	1238.11	1120 ± 75	976 ± 73	1100 ± 70	1020 ± 70	1260 ± 77
	295.21	10700 ± 214	9990 ± 216	10600 ± 202	10600 ± 221	11700 ± 226
	351.92	18400 ± 233	17200 ± 233	18600 ± 240	18400 ± 242	20300 ± 261
	1377.67	785 ± 63	723 ± 63	753 ± 56	811 ± 59	730 ± 66
	1764.49	2530 ± 84	2340 ± 82	25800 ± 86	2550 ± 84	277 ± 88
	2204.21	720 ± 49	558 ± 45	639 ± 49	655 ± 49	676 ± 49
<sup>238</sup> U	338.32	6220 ± 168	5600 ± 163	5610 ± 159	6670 ± 172	7020 ± 170
	727.33	2340 ± 112	1990 ± 98	2220 ± 103	2360 ± 107	2530 ± 107
	794.95	1120 ± 84	1010 ± 77	1050 ± 75	1300 ± 86	1290 ± 80
	911.21	7200 ± 146	6670 ± 149	6710 ± 144	7990 ± 158	8150 ± 153
	966.87	5340 ± 152	5040 ± 145	5130 ± 152	6100 ± 161	6130 ± 163
<sup>40</sup> K	1460.83	7910 ± 147	7530 ± 142	7640 ± 144	8230 ± 149	8700 ± 154
<sup>68</sup> Ga	1077.40	0 ± 92	127 ± 88	88 ± 90	111 ± 95	67 ± 95
<sup>65</sup> Zn	1115.55	-20 ± 40	-20 ± 40	-20 ± 40	-20 ± 40	-6 ± 43
<sup>22</sup> Na	1274.53	95 ± 65	4 ± 59	-14 ± 61	106 ± 63	-14 ± 65
<sup>137</sup> Cs	661.66	426 ± 76	838 ± 91	651 ± 80	294 ± 71	56 ± 44
<sup>54</sup> Mn	834.848	559 ± 93	369 ± 82	374 ± 66	411 ± 62	413 ± 103

In Table 0-6 to Table 0-8 are shown the activity concentrations, absorbed and effective dose, from HPGe data, calculated for the NORM as well as the

anthropogenic radioactive materials identified in the surveys. The results are shown for all the samples where 5 spots were sampled.

**Table 0-6: Activity concentrations, absorbed and effective dose, from HPGe data, calculated for the naturally occurring radioactive materials (NORM) identified in the surveys. Results are shown for all the samples where 5 spots were sampled.**

	Sample code	HPGe Activity Concentration (Bq.kg <sup>-1</sup> )			Absorbed dose (nGy.h <sup>-1</sup> )	Effective dose (μSv.y <sup>-1</sup> )
		<sup>238</sup> U	<sup>232</sup> Th	<sup>40</sup> K		
February 2005	CS1, S1	7.76 ± 1.15	8.41 ± 0.86	49.81 ± 10.36	10.74 ± 0.71	13.17 ± 0.87
	CS1, S2	7.48 ± 1.08	8.39 ± 0.47	48.45 ± 10.08	10.54 ± 0.66	12.93 ± 0.81
	CS1, S3	8.12 ± 0.52	8.24 ± 1.12	51.64 ± 10.73	10.89 ± 0.55	13.35 ± 0.68
	CS1, S4	7.98 ± 0.90	8.79 ± 0.50	57.09 ± 11.85	11.38 ± 0.65	13.95 ± 0.80
	CS1, S5	7.79 ± 0.77	8.72 ± 0.62	57.71 ± 11.98	11.28 ± 0.63	13.83 ± 0.77
	HS1, S1	9.31 ± 1.12	9.52 ± 0.40	53.04 ± 11.02	12.26 ± 0.70	15.04 ± 0.86
	HS1, S2	10.28 ± 1.13	10.99 ± 1.70	57.28 ± 11.91	13.77 ± 0.79	16.89 ± 0.97
	HS1, S3	12.82 ± 0.83	11.54 ± 0.90	60.77 ± 12.64	15.43 ± 0.67	18.92 ± 0.83
	HS1, S4	13.70 ± 1.70	10.72 ± 0.86	53.10 ± 11.04	15.02 ± 0.92	18.42 ± 1.13
HS1, S5	12.48 ± 0.88	11.55 ± 0.40	63.04 ± 13.09	15.37 ± 0.69	18.85 ± 0.84	
July 2005	NCS1, S1	14.34 ± 1.15	15.14 ± 1.38	58.26 ± 12.09	18.20 ± 0.78	22.32 ± 0.95
	NCS1, S2	13.18 ± 0.98	13.56 ± 1.02	55.08 ± 11.43	16.58 ± 0.68	20.33 ± 0.84
	NCS1, S3	13.58 ± 1.24	13.82 ± 1.33	54.90 ± 11.40	16.91 ± 0.79	20.74 ± 0.96
	NCS1, S4	14.17 ± 1.04	16.34 ± 0.72	59.77 ± 12.40	18.91 ± 0.72	23.19 ± 0.88
	NCS1, S5	14.41 ± 0.96	16.20 ± 1.11	60.91 ± 12.64	18.98 ± 0.72	23.28 ± 0.88

**Table 0-7: Activity concentrations, from HPGe data, calculated for the anthropogenic radioactive materials identified in the surveys. Results are shown for all the samples where 5 spots were sampled.**

	Sample code	HPGe Activity concentration (Bq.kg <sup>-1</sup> )				
		<sup>68</sup> Ga	<sup>65</sup> Zn	<sup>22</sup> Na	<sup>137</sup> Cs	<sup>54</sup> Mn
February 2005	CS1, S1	0.00 ± 1.94	-0.03 ± 0.05	1.50 ± 0.30	0.34 ± 0.08	0.16 ± 0.08
	CS1, S2	0.59 ± 1.95	0.04 ± 0.06	1.36 ± 0.27	0.36 ± 0.08	0.15 ± 0.08
	CS1, S3	0.00 ± 1.91	0.01 ± 0.06	2.16 ± 0.42	0.49 ± 0.10	0.19 ± 0.09
	CS1, S4	2.14 ± 1.96	-0.03 ± 0.06	1.31 ± 0.26	0.51 ± 0.11	0.25 ± 0.12
	CS1, S5	3.43 ± 1.99	0.03 ± 0.06	1.89 ± 0.37	0.36 ± 0.08	0.19 ± 0.12
	HS1, S1	433 ± 69.1	0.77 ± 0.14	2.64 ± 0.51	0.63 ± 0.13	1.04 ± 0.47
	HS1, S2	731 ± 135	1.39 ± 0.27	2.61 ± 0.53	0.51 ± 0.12	1.66 ± 0.76
	HS1, S3	1435 ± 244	4.31 ± 0.74	3.26 ± 0.64	0.70 ± 0.19	4.26 ± 1.92
	HS1, S4	1489 ± 238	2.83 ± 0.46	3.06 ± 0.59	0.26 ± 0.11	7.58 ± 3.40
	HS1, S5	1197 ± 192	2.20 ± 0.37	3.47 ± 0.67	0.43 ± 0.13	5.95 ± 2.67
July 2005	NCS1, S1	0.00 ± 1.95	-0.03 ± 0.05	0.07 ± 0.05	0.23 ± 0.06	0.31 ± 0.15
	NCS1, S2	2.88 ± 1.91	-0.03 ± 0.05	0.00 ± 0.04	0.44 ± 0.10	0.21 ± 0.10
	NCS1, S3	1.97 ± 1.89	-0.03 ± 0.05	-0.01 ± 0.04	0.34 ± 0.08	0.21 ± 0.10
	NCS1, S4	2.52 ± 2.02	-0.03 ± 0.05	0.08 ± 0.05	0.15 ± 0.05	0.23 ± 0.11
	NCS1, S5	1.47 ± 1.92	-0.01 ± 0.05	-0.01 ± 0.04	0.03 ± 0.02	0.22 ± 0.11

**Table 0-8: Absorbed and effective dose, from HPGe data, calculated for the anthropogenic radioactive materials identified in the surveys. Results are shown for all the samples where 5 spots were sampled.**

	Sample code	(Plane source at 1 cm)		(Plane source at 10 cm)	
		Absorbed dose (nGy.h <sup>-1</sup> )	Effective dose (μSv.y <sup>-1</sup> )	Absorbed dose (nGy.h <sup>-1</sup> )	Effective dose (μSv.y <sup>-1</sup> )
February 2005	CS1, S1	0.79 ± 0.15	0.96 ± 0.18	0.21 ± 0.04	0.25 ± 0.05
	CS1, S2	0.74 ± 0.13	0.91 ± 0.16	0.19 ± 0.04	0.24 ± 0.04
	CS1, S3	1.13 ± 0.21	1.38 ± 0.25	0.29 ± 0.05	0.36 ± 0.07
	CS1, S4	0.78 ± 0.13	0.96 ± 0.16	0.20 ± 0.04	0.25 ± 0.04
	CS1, S5	1.02 ± 0.18	1.25 ± 0.22	0.27 ± 0.05	0.33 ± 0.06
	HS1, S1	6.01 ± 0.90	7.37 ± 1.10	1.51 ± 0.22	1.85 ± 0.27
	HS1, S2	9.20 ± 1.48	11.28 ± 1.81	2.30 ± 0.37	2.82 ± 0.45
	HS1, S3	17.74 ± 2.90	21.75 ± 3.56	4.43 ± 0.72	5.43 ± 0.88
	HS1, S4	18.93 ± 3.13	23.22 ± 3.84	4.72 ± 0.78	5.79 ± 0.96
	HS1, S5	15.66 ± 2.52	19.20 ± 3.09	3.91 ± 0.63	4.88 ± 0.77
July 2005	NCS1, S1	0.17 ± 0.06	0.21 ± 0.07	0.04 ± 0.01	0.05 ± 0.02
	NCS1, S2	0.18 ± 0.05	0.22 ± 0.06	0.04 ± 0.01	0.05 ± 0.01
	NCS1, S3	0.14 ± 0.05	0.17 ± 0.06	0.03 ± 0.01	0.04 ± 0.01
	NCS1, S4	0.16 ± 0.05	0.20 ± 0.06	0.04 ± 0.01	0.05 ± 0.01
	NCS1, S5	0.09 ± 0.05	0.11 ± 0.06	0.02 ± 0.01	0.03 ± 0.01

In Table 0-9 to Table 0-11 are shown activity concentrations results, from HPGe data, for the individual  $\gamma$ -ray energy values used for the thorium and uranium series. The results are shown for each of the 5 samples collected at locations CS1, HS1, and NCS1 during the February and July 2005 surveys.

**Table 0-9: Activity concentrations, from HPGe data for the 5 locations of calibration spot CS1, shown for the individual energy lines used for the thorium and uranium series.**

Radio-nuclide	E (keV)	Activity concentration (Bq.kg <sup>-1</sup> )				
		CS1, S1	CS1, S2	CS1, S3	CS1, S4	CS1, S5
<sup>232</sup> Th	934.06	6.21 ± 1.14	6.05 ± 1.18	9.03 ± 1.11	7.12 ± 1.24	6.81 ± 1.26
	1238.11	6.37 ± 0.72	6.75 ± 0.84	7.68 ± 0.75	6.94 ± 0.72	6.60 ± 0.79
	295.21	8.76 ± 0.25	7.81 ± 0.25	8.23 ± 0.26	8.30 ± 0.25	8.61 ± 0.27
	351.92	8.54 ± 0.18	8.35 ± 0.18	8.38 ± 0.17	8.98 ± 0.18	8.32 ± 0.18
	1377.67	7.16 ± 1.15	6.36 ± 1.03	7.95 ± 0.90	7.30 ± 1.07	8.00 ± 1.09
	1764.49	8.97 ± 0.43	8.19 ± 0.43	8.16 ± 0.40	9.18 ± 0.43	8.12 ± 0.40
	2204.21	8.27 ± 1.05	8.83 ± 1.09	7.43 ± 1.00	8.03 ± 0.83	8.11 ± 0.90
<sup>238</sup> U	338.32	8.69 ± 0.40	8.23 ± 0.40	8.12 ± 0.40	8.82 ± 0.38	8.78 ± 0.40
	727.33	8.99 ± 0.66	8.11 ± 0.71	9.89 ± 0.64	9.32 ± 0.64	9.71 ± 0.65
	794.95	6.95 ± 0.77	9.20 ± 0.84	6.82 ± 0.77	9.09 ± 0.83	8.26 ± 0.87
	911.21	8.37 ± 0.27	8.39 ± 0.28	8.56 ± 0.27	8.74 ± 0.27	8.14 ± 0.27
	966.87	9.06 ± 0.37	8.01 ± 0.38	7.84 ± 0.34	8.00 ± 0.36	8.73 ± 0.40



**Table 0-10: Activity concentrations, from HPGe data for the 5 locations of hotspot HS1, shown for the individual energy lines used for the thorium and uranium series.**

Radio-nuclide	E (keV)	Activity concentration (Bq.kg <sup>-1</sup> )				
		HS1, S1	HS1, S2	HS1, S3	HS1, S4	HS1, S5
<sup>232</sup> Th	934.06	8.54 ± 1.32	10.36 ± 1.93	14.01 ± 2.50	14.11 ± 2.32	10.94 ± 2.03
	1238.11	7.92 ± 0.86	8.38 ± 1.07	11.78 ± 1.25	12.07 ± 1.05	13.26 ± 1.03
	295.21	N/A	N/A	N/A	N/A	N/A
	351.92	10.29 ± 0.38	10.51 ± 0.57	12.66 ± 0.78	12.22 ± 0.66	12.07 ± 0.61
	1377.67	10.19 ± 1.08	11.35 ± 1.49	12.18 ± 2.01	16.76 ± 1.51	12.48 ± 1.36
	1764.49	10.47 ± 0.43	11.37 ± 0.53	12.79 ± 0.60	13.62 ± 0.51	12.94 ± 0.56
	2204.21	8.47 ± 0.86	9.69 ± 1.02	13.52 ± 1.22	13.44 ± 1.10	13.20 ± 1.24
<sup>238</sup> U	338.32	N/A	N/A	N/A	N/A	N/A
	727.33	9.61 ± 0.81	9.70 ± 0.88	12.48 ± 1.44	9.96 ± 1.38	11.34 ± 1.31
	794.95	10.03 ± 1.01	13.47 ± 2.39	10.37 ± 1.88	10.01 ± 1.80	11.17 ± 1.93
	911.21	9.34 ± 0.29	10.70 ± 0.37	11.91 ± 0.46	11.61 ± 0.39	12.09 ± 0.40
	966.87	9.10 ± 0.42	10.09 ± 0.54	11.39 ± 0.70	11.30 ± 0.59	11.60 ± 0.59

**Table 0-11: Activity concentrations, from HPGe data for the 5 locations of calibration spot NCS1, shown for the individual energy lines used for the thorium and uranium series.**

Radio-nuclide	E (keV)	Activity concentration (Bq.kg <sup>-1</sup> )				
		NCS1, S1	NCS1, S2	NCS1, S3	NCS1, S4	NCS1, S5
<sup>232</sup> Th	934.06	12.22 ± 1.12	14.05 ± 1.16	11.20 ± 1.26	14.30 ± 1.19	13.23 ± 1.23
	1238.11	13.40 ± 0.90	11.57 ± 0.86	12.78 ± 0.82	12.04 ± 0.83	14.33 ± 0.88
	295.21	14.57 ± 0.32	13.55 ± 0.31	14.16 ± 0.29	14.28 ± 0.32	15.24 ± 0.32
	351.92	14.74 ± 0.24	13.68 ± 0.23	14.52 ± 0.24	14.56 ± 0.24	15.44 ± 0.25
	1377.67	15.11 ± 1.23	13.81 ± 1.22	14.14 ± 1.07	15.39 ± 1.13	13.34 ± 1.21
	1764.49	14.80 ± 0.51	13.59 ± 0.49	14.74 ± 0.51	14.69 ± 0.50	15.39 ± 0.51
	2204.21	15.57 ± 1.08	11.98 ± 0.97	13.49 ± 1.05	13.97 ± 1.06	13.89 ± 1.03
<sup>238</sup> U	338.32	15.40 ± 0.45	13.76 ± 0.42	13.55 ± 0.41	16.28 ± 0.46	16.51 ± 0.44
	727.33	17.09 ± 0.82	14.41 ± 0.72	15.81 ± 0.74	16.99 ± 0.78	17.54 ± 0.75
	794.95	13.25 ± 1.00	11.80 ± 0.91	12.08 ± 0.87	15.14 ± 1.02	14.48 ± 0.91
	911.21	15.24 ± 0.36	14.02 ± 0.35	13.86 ± 0.34	16.68 ± 0.39	16.40 ± 0.37
	966.87	14.73 ± 0.43	13.82 ± 0.41	13.81 ± 0.42	16.60 ± 0.46	16.06 ± 0.45

In Table 0-12 are shown activity concentrations results, from HPGe data, for the individual  $\gamma$ -ray energy values used for the thorium and uranium series. The results are shown for samples collected at hotspots HS2, HS3, NHS4, and NHS5 during the February and July 2005 surveys.

**Table 0-12: Activity concentrations, from HPGe data for the rest of the hotspots, shown for the individual energy lines used for the thorium and uranium series.**

Radio-nuclide	E (keV)	Activity concentration (Bq.kg <sup>-1</sup> )			
		HS2, S1	HS3, S1	NHS4, S1	NHS5, S1
<sup>232</sup> Th	<b>934.06</b>	10.79 ± 1.65	18.18 ± 3.38	8.96 ± 1.82	8.36 ± 1.29
	<b>1238.11</b>	11.81 ± 1.07	39.15 ± 2.60	7.80 ± 0.87	8.82 ± 0.78
	<b>295.21</b>	N/A	N/A	N/A	N/A
	<b>351.92</b>	9.91 ± 0.62	18.02 ± 1.48	9.37 ± 0.64	7.98 ± 0.35
	<b>1377.67</b>	10.89 ± 0.08	29.32 ± 2.46	7.79 ± 1.21	9.50 ± 1.11
	<b>1764.49</b>	11.62 ± 0.49	26.69 ± 0.91	9.05 ± 0.46	8.48 ± 0.40
	<b>2204.21</b>	11.77 ± 1.15	24.85 ± 1.74	8.97 ± 1.13	8.28 ± 1.13
<sup>238</sup> U	<b>338.32</b>	N/A	N/A	N/A	N/A
	<b>727.33</b>	9.61 ± 1.09	23.05 ± 2.17	8.76 ± 1.02	8.26 ± 0.85
	<b>794.95</b>	11.16 ± 2.86	16.87 ± 6.08	5.93 ± 2.80	6.58 ± 2.16
	<b>911.21</b>	11.06 ± 0.39	20.88 ± 0.87	8.62 ± 0.37	7.60 ± 0.29
	<b>966.87</b>	11.61 ± 0.53	20.12 ± 1.17	8.59 ± 0.50	7.68 ± 0.40

## APPENDIX 6

### *Half-life prediction decay curves*

In Table 0-13 to Table 0-15 are shown count rate results obtained for the different measuring durations and decay periods of soil sample HS1, S1 to predict the half-lives of radionuclides associated with the 1077.4, 1115.6, and 834.8 keV  $\gamma$ -ray energies. In Figure 0-5 to Figure 0-7 the results are shown as plots of count rate versus decay period. The predicted half-lives correspond to those of  $^{68}\text{Ge}$ ,  $^{65}\text{Zn}$ , and  $^{54}\text{Mn}$ , with percentage differences of 2.3, 14.0, and 14.4 % for 1077.4, 1115.6, and 834.8 keV energies, respectively.

**Table 0-13: Half-life prediction results from decay measurements of the 1077.4 keV line of  $^{68}\text{Ga}$  in hotspot sample HS1, S1. The predicted half-live corresponds to that of  $^{68}\text{Ge}$  because of secular equilibrium.**

Decay period (d)	Net counts	Live time (s)	Count rate (counts.s <sup>-1</sup> )	Predicted half-life (d)	Actual half-life (d)
89	7120	43107.80	0.165	277.26	270.82
138	9574	65372.70	0.146		
182	5610	43125.06	0.130		
369	3568	43148.43	0.083		
464	9756	152725.30	0.064		
524	3410	62229.32	0.055		

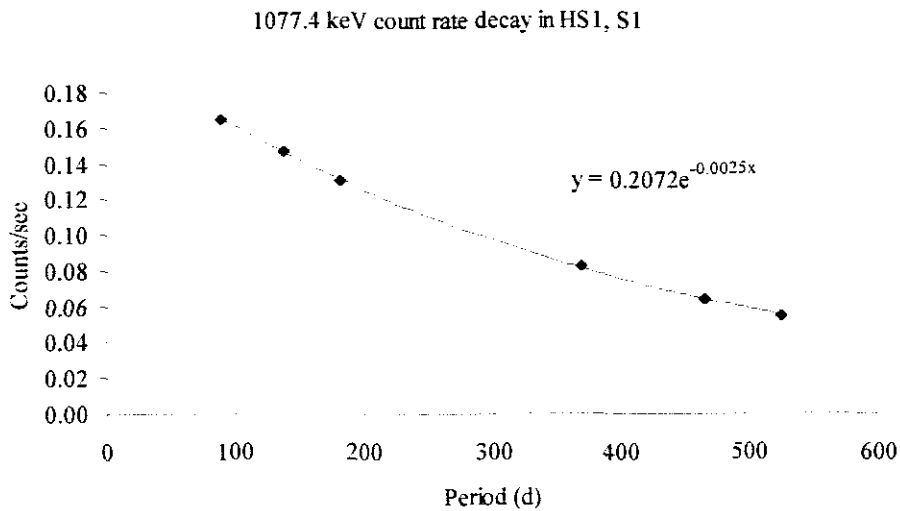


**Figure 0-5:** Count rate decay curve of the 1077.4 keV line measured and re-measured in hotspot sample HS1, S1.

**Table 0-14:** Half-life prediction results from decay measurements of the 1115.55 keV line of <sup>65</sup>Zn in hotspot sample HS1, S1.

Decay period (d)	Net counts	Live time (s)	Count rate (counts.s <sup>-1</sup> )	Predicted half-life (d)	Actual half-life (d)
89	212	43107.80	0.005	210.04	244.26
138	227	65372.70	0.003		
182	147	43125.06	0.003		
369	84	43148.43	0.002		
464	222	152725.30	0.001		
524	63	62229.32	0.001		

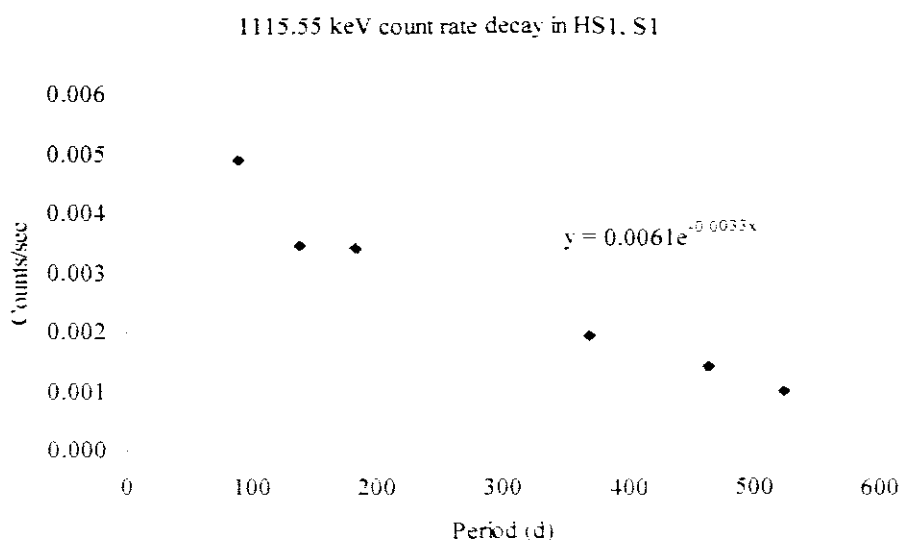


**Figure 0-6:** Count rate decay curve of the 1115.55 keV line measured and re-measured in hotspot sample HS1, S1.

**Table 0-15: Half-life prediction results from decay measurements of the 834.848 keV line of <sup>54</sup>Mn in hotspot sample HS1, S1.**

Decay period (d)	Net counts	Live time (s)	Count rate (counts.s <sup>-1</sup> )	Predicted half-life (d)	Actual half-life (d)
89	726	43107.80	0.017	364.81	312.3
138	887	65372.70	0.014		
182	600	43125.06	0.014		
369	392	43148.43	0.009		
464	1171	152725.30	0.008		
524	469	62229.32	0.008		

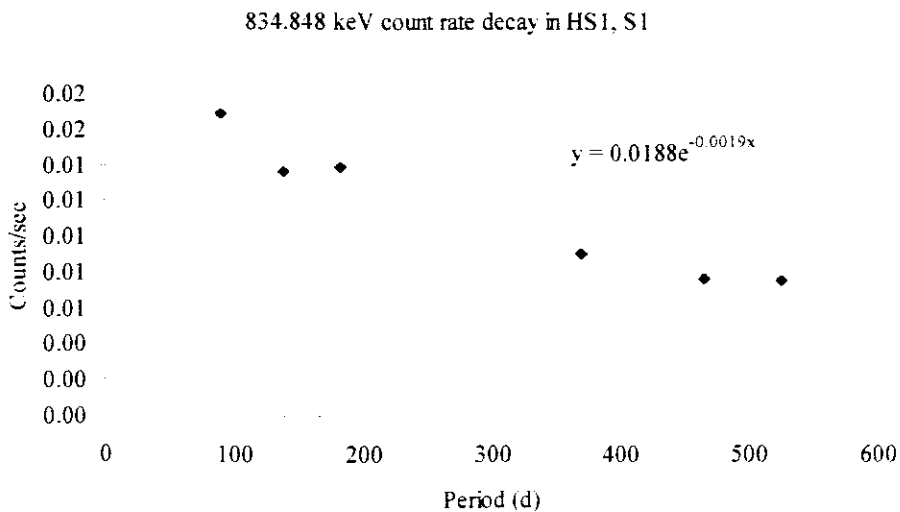


**Figure 0-7: Count rate decay curve of the 834.848 keV line measured and re-measured in hotspot sample HS1, S1.**

## APPENDIX 7

### *Testing of normalisation factors*

In Table 0-16 are shown the normalisation factors obtained with HPGe and MEDUSA activity concentration results for calibration spot NCS1 of the July 2005 survey. These NCS1 normalisation factors were tested by using them to normalise the MEDUSA activity concentration results of calibration spot CS1 from the February 2005 survey. The results of this test are shown in Table 0-17, where results of a similar test done with CS1 normalisation factors are also shown.

These tests were done in order to decide on the best normalisation factors to be used [for all the results] in this study. In Figure 0-8 are shown the results of the tests in bar graphs, which both indicate a percentage difference of range 16.9 – 93.3 %. Other similar tests were carried out with data from other locations, and based on those results, the CS1 normalisation factors were chosen for use in this study.

**Table 0-16: Normalisation factors obtained from calibration spot NCS1.**

Location	Radio-nuclide	Average HPGe (Bq.kg <sup>-1</sup> )	MEDUSA	Normalisation factors ( $\times 10^{-6}$ )
NCS1	<sup>238</sup> U	13.94 $\pm$ 0.54	105950 $\pm$ 2187	132.0 $\pm$ 6.0
	<sup>232</sup> Th	15.01 $\pm$ 1.29	175676 $\pm$ 1949	85.0 $\pm$ 7.0
	<sup>40</sup> K	57.78 $\pm$ 2.72	24842 $\pm$ 579	2326.0 $\pm$ 122.0
	<sup>22</sup> Na	0.03 $\pm$ 0.04	2382 $\pm$ 276	11.0 $\pm$ 18.0

**Table 0-17: Results obtained for normalisation of CS1 and NCS1 MEDUSA results using NCS1 and CS1 normalisation factors, respectively. (see Table 5-10 for CS1 normalisation factors).**

Radio-nuclide	CS1		NCS1	
	Average HPGe (Bq.kg <sup>-1</sup> )	Normalised MEDUSA	Average HPGe (Bq.kg <sup>-1</sup> )	Normalised MEDUSA
<sup>238</sup> U	7.83 ± 0.25	9.41 ± 0.52	13.94 ± 0.54	11.59 ± 0.58
<sup>232</sup> Th	8.51 ± 0.24	9.84 ± 0.87	15.01 ± 1.29	12.98 ± 0.45
<sup>40</sup> K	52.94 ± 4.23	79.78 ± 4.50	57.78 ± 2.72	38.35 ± 3.29
<sup>22</sup> Na	1.64 ± 0.37	0.11 ± 0.19	0.03 ± 0.04	0.38 ± 0.10

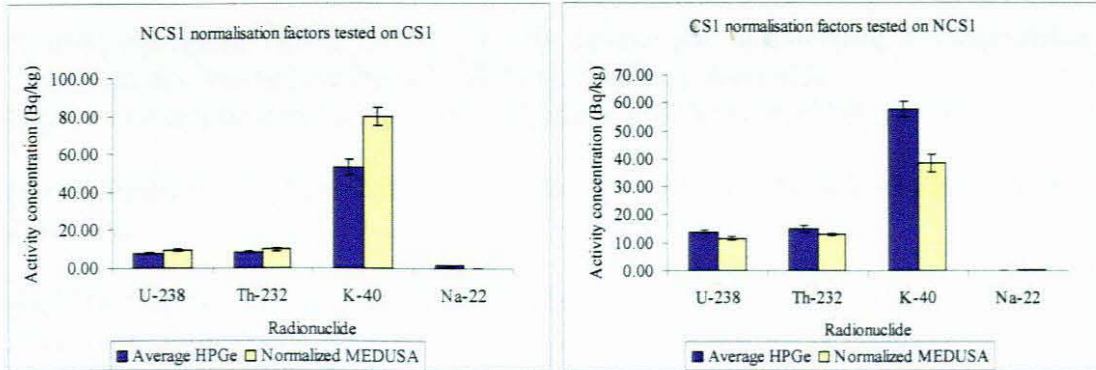


**Figure 0-8: Bar graphs showing results obtained for normalisation of CS1 and NCS1 MEDUSA results using NCS1 and CS1 normalisation factors, respectively.**

## REFERENCES

- [Ame93] American Nuclear Systems. (1993-1997). OxfordWin-MCA and Assayer software, Version 3.80. User's manual.
- [Can96] Canberra. (1996). *In Situ Gamma Spectroscopy Systems for Soil and Surface Activity Measurements*. Application Note. [Online]. Available <http://www.canberra.com/pdf/Literature/can0015.pdf>
- [deM97] De Meijer, R. J. (1997). Heavy Minerals: From 'Edelstein' to Einstein. *Journal of Geochemical Exploration*, 62(1-3): 81-103.
- [Eur98] European Patent Office. (1998). *System for determining a composition of radionuclides*, Patent Number US5744804. [Online]. Available <http://v3.espacenet.com/textdoc?DB=EPODOC&IDX=US6057542&F=0>
- [Fir96] Firestone, R. B. (1996). *Table of Isotopes (8<sup>th</sup> Ed.)*. New York: John Wiley & Sons, Inc.
- [Hal97] Halliday, D., Resnick, R., & Walker, J. (1997). *Fundamentals of physics*. New York: John Wiley & Sons, Inc.
- [Hen01] Hendriks, P. H. G. M. *et. al.* (2001). Full-spectrum analysis of  $\gamma$ -ray spectra. *Journal of Environmental Radioactivity*, 53 (2001): 365-380.
- [Hen02] Hendriks, P. H. G. M. *et. al.* (2002). MCNP modeling of scintillation-detector  $\gamma$ -ray spectra from natural radionuclides. *Applied Radiation and Isotopes*, 57 (2002): 449-457.
- [Jon94] Jones, D. G. (1994). Towed Seabed Gamma Ray Spectrometer: 'Eel' Is Radiometric Instrument for Wide Range of Offshore, Mineral Exploration, Environmental Survey Applications. *Sea Technology*, August 1994 edition; 89 – 93.
- [Jos98] Josten, N. E. & Gehrke, R. (1998). *In-situ Radiation Mapping for Assessment of Distributed Radioactive Contamination*. [Online]. Available [http://tech.inel.gov/documents/teb/calcium\\_fluoride\\_detector\\_array/insitu\\_mapping\\_spectrum98.pdf](http://tech.inel.gov/documents/teb/calcium_fluoride_detector_array/insitu_mapping_spectrum98.pdf)
- [Jos05] Joseph, A. D. (2005). *Radiometric Study of Soil: The Systematic Effects*. Unpublished Master's thesis. Bellville: University of the Western Cape.
- [Kat84] Kathren, R. L. (1984). *Radioactivity in the environment*. New York: Harwood Academic Publishers.
- [LAn98] L'Annunziata M. F. (1998). *Handbook of radioactivity analysis*. California: Academic Press.
- [Leo87] Leo, W. R. (1987). *Techniques for Nuclear and Particle Physics Experiments*. New York: Springer-Verlag.



[Lim00] J. Limburg & de Meijer R.J. (2000). The Nuclear Geophysics Division at KVI in Groningen: *Past, Present and Future*. FKPE 5th Workshop "Bohrlochgeophysik und Gesteinsphysik", Hannover, October 7-8 1999 Sonderband III/2000: 52-55.

[Lon04] Long, S. *et al.* (2004). Development and performance of the vehicle-mounted radiation monitoring equipment used in the Maralinga rehabilitation project. *Journal of Environmental Radioactivity* 76 (2004), 207-223.

[McG07] McGee, D. (2007). Manager, Radiation Safety & Environment Division, Radionuclide Production Group, iThemba LABS. Private communication.

[Mal01] Maleka P. P. (2001). *Calibration of germanium detectors for applications of radiometric methods in South Africa*. Unpublished Master's thesis. Bellville: University of the Western Cape.

[Map04] Maphoto, K. P. (2004). *Determination of Natural Radioactivity Concentration in Soil: a comparative study of Windows and Full Spectrum Analysis*. Unpublished Master's thesis. Bellville: University of the Western Cape.

[Mar79] Martin, A., Harbison, S. A. (1979). *An introduction to radiation protection (2<sup>nd</sup> Ed.)*. London: Chapman and Hall Ltd.

[Mil94] Miller, M. *et al.* (1994). *In-situ gamma-ray spectrometry for the measurement of uranium in surface soils*. *Health Physics*, 67: 140-150.

[Mod05] Modisane, T. J. D. (2005). *Correlations between natural radionuclide concentrations in soils and vine-growth potential*. Unpublished Master's thesis. Mafikeng: North West University.

[Moh04] Mohanty, A. K. *et al.* (2004). Natural radioactivity and radiation exposure in the high background area at Chhatrapur beach placer deposit of Orissa, India. *Journal of Environmental Radioactivity* 75 (2004), 15-33.

[Mud04] Mudau, A. E. (2004). *MEDUSA data Synchronization and Analysis manual*. Environmental Radioactivity Lab, Physics Group, iThemba LABS, private communication.

[New04a] PRELIMINARY (2004). *Preliminary results from 1<sup>st</sup> MEDUSA gamma-ray mapping of the iThemba LABS site on 22 June 2004*. Microsoft PowerPoint Slides (hard copy). Newman, R. T. *et al.*, Environmental Radioactivity Laboratory, Physics Group, iThemba LABS. Private communication.

[New04b] Newman, R. T., *et al.* (2004). *Report on in-situ gamma-ray mapping of Paarl, Report no.: ERL/04/UWC/02*. Environmental Radioactivity Lab, Physics Group, iThemba LABS.

[New04c] PROPOSAL (2004). *Proposal: use of MEDUSA technology for rapid, high-density mapping of (gamma-ray emitting) environmental radioactivity on the iThemba*

*LABS site*. Microsoft PowerPoint Slides. Newman, R. T. *et. al.*, Environmental Radioactivity Laboratory, Physics Group, *iThemba LABS*. Private communication.

[Sai94] Saito, K. & Jacob P. (1994). Gamma ray fields in the air due to sources in the ground. *Radiation Protection Dosimetry* 58 (1995), 29-45.

[Sed03] Sedumedi, L. (2003). *Radiometry of milk and mineral water from the Western Cape*. Unpublished Masters thesis. Limpopo: University of North-West.

[Tso83] Tsoulfanidis, N. (1983). *Measurement and Detection of Radiation*. USA: Hemisphere Publishing Corporation.

[Tyk95] Tykva, R., Sabol, J. (1995). *Low-level Environmental Radioactivity: Sources and Evaluation*. Pennsylvania: Technomic Publishing Company, Inc.

[Tyl04] Tyler, A. N. (2004). High accuracy *in situ* radiometric mapping. *Journal of Environmental Radioactivity* 72 (2004), 195-202.

[UNS00] UNSCEAR. (2000). *Sources and Effects of Ionizing Radiation*. United Nations Scientific Committee on the Effect of Atomic Radiation, United Nations, New York. [Online]. Available [www.unscear.org/docs/reports/annexb.pdf](http://www.unscear.org/docs/reports/annexb.pdf)

[Ven00] Venema, L. B., de Meijer, R. J. (2000). Natural radionuclides as tracers of the dispersal of dredge spoil dumped at sea. *Journal of Environmental Radioactivity*, 55 (2001): 221 – 239.

[vRo04] THE SCIENCE (2004). *The Science of Radiation Protection*. Van Rooyen, J., Radiation Protection Division, *iThemba LABS*. Training notes.

[Www01] [www.sa-venues.com](http://www.sa-venues.com)

[Www02] [www.futureharvest.org/about/glossary.shtml](http://www.futureharvest.org/about/glossary.shtml).

[Www03] National Safety Council. [www.nsc.org/ehc/glossary.htm#e](http://www.nsc.org/ehc/glossary.htm#e)

[Www04] [www.epa.gov/OCEPAterms/iterms.html](http://www.epa.gov/OCEPAterms/iterms.html)